

AT&T  
BELL LABORATORIES

February 1984  
Vol. 63 No. 2

# TECHNICAL JOURNAL

A JOURNAL OF THE AT&T COMPANIES

Corrugated-Waveguide Transformer

Digital Filters

Power Amplifiers

Picture Coding

Signal Clipping

Voice/Data Services

Bubble Memory

Coatings on Laser Facets

Optical Fibers

## EDITORIAL COMMITTEE

|                                 |   |                           |
|---------------------------------|---|---------------------------|
|                                 | A. A. PENZIAS, <sup>1</sup> <i>Committee Chairman</i> |                           |
| M. M. BUCHNER, JR. <sup>1</sup> | D. HIRSCH <sup>4</sup>                                | R. L. MARTIN <sup>1</sup> |
| R. P. CLAGETT <sup>2</sup>      | S. HORING <sup>1</sup>                                | J. S. NOWAK <sup>1</sup>  |
| R. P. CREAN <sup>2</sup>        | R. A. KELLEY <sup>1</sup>                             | B. B. OLIVER <sup>5</sup> |
| B. R. DARNALL <sup>1</sup>      | R. W. LUCKY <sup>1</sup>                              | J. W. TIMKO <sup>3</sup>  |
| B. P. DONOHUE, III <sup>3</sup> | J. F. MARTIN <sup>2</sup>                             |                           |

<sup>1</sup>AT&T Bell Laboratories    <sup>2</sup>AT&T Technologies    <sup>3</sup>AT&T Information Systems

<sup>4</sup>AT&T Consumer Products    <sup>5</sup>AT&T Communications

## EDITORIAL STAFF

|                                    |                                       |
|------------------------------------|---------------------------------------|
| B. G. KING, <i>Editor</i>          | L. S. GOLLER, <i>Assistant Editor</i> |
| P. WHEELER, <i>Managing Editor</i> | H. M. PURVIANCE, <i>Art Editor</i>    |
| B. G. GRUBER, <i>Circulation</i>   |                                       |

AT&T BELL LABORATORIES TECHNICAL JOURNAL (ISSN0005-8580) is published by AT&T, 550 Madison Avenue, New York, NY 10022; C. L. Brown, Chairman and Chief Executive Officer; W. M. Ellinghaus, President; V. A. Dwyer, Vice President and Treasurer; T. O. Davis, Secretary.

The Journal is published ten times each year. The Computing Science and Systems section and the special issues are included as they become available. Subscriptions: United States—1 year \$35; 2 years \$63; 3 years \$84; foreign—1 year \$45; 2 years \$73; 3 years \$94. A subscription to the Computing Science and Systems section only is \$10 (\$12 foreign). Single copies of most issues of the Journal are available at \$5 (\$6 foreign). Payment for foreign subscriptions or single copies must be made in United States funds, or by check drawn on a United States bank and made payable to the Technical Journal and sent to AT&T Bell Laboratories, Circulation Dept., Room 1E335, 101 J. F. Kennedy Pky, Short Hills, NJ 07078.

Single copies of material from this issue of the Journal may be reproduced for personal, noncommercial use. Permission to make multiple copies must be obtained from the Editor.

Comments on the technical content of any article or brief are welcome. These and other editorial inquiries should be addressed to the Editor, AT&T Bell Laboratories Technical Journal, Room 1J319, 101 J. F. Kennedy Pky, Short Hills, NJ 07078. Comments and inquiries, whether or not published, shall not be regarded as confidential or otherwise restricted in use and will become the property of AT&T. Comments selected for publication may be edited for brevity, subject to author approval.

Printed in U.S.A. Second-class postage paid at Short Hills, NJ 07078 and additional mailing offices. Postmaster: Send address changes to the AT&T Bell Laboratories Technical Journal, Room 1E335, 101 J. F. Kennedy Pky, Short Hills, NJ 07078.

Copyright © 1984 AT&T.

AT&T Bell Laboratories

# Technical Journal

VOL. 63

FEBRUARY 1984

NO. 2

Copyright © 1984 AT&T. Printed in U.S.A.

|  |     |
|--|-----|
| <b>Quarter-Wave Corrugated Transformer for Broadband Matching of a Corrugated Feed</b>                           | 207 |
| C. Dragone and W. E. Legg  |     |
| <b>Moment Calculations by Digital Filters</b>  | 217 |
| Z. L. Budrikis and M. Hatamian   |     |
| <b>Wideband Operation of Nonlinear Solid-State Power Amplifiers—Comparisons of Calculations and Measurements</b> | 231 |
| J. B. Minkoff  |     |
| <b>Conditional Variable-Length Coding for Gray-Level Pictures</b>  | 249 |
| H. Gharavi   |     |
| <b>Signals Designed for Recovery After Clipping—I. Localization of Infinite Products</b>                         | 261 |
| B. F. Logan, Jr.   |     |
| <b>Signals Designed for Recovery After Clipping—II. Fourier Transform Theory of Recovery</b>                     | 287 |
| B. F. Logan, Jr.   |     |
| <b>Integrated Voice/Data Services on Fasnnet</b>   | 307 |
| J. W. Mark and J. O. Limb  |     |
| <b>Experimental Ion-Implanted Bubble Memory Device With 16-<math>\mu\text{m}^2</math> Cell</b>                   | 337 |
| T. J. Nelson, D. J. Muehlner, V. V. S. Rana, B. J. Roman, and G. P. Vella-Coleiro                                |     |
| <b>Theoretical Design of Single-Layer Antireflection Coatings on Laser Facets</b>                                | 357 |
| G. Eisenstein  |     |
| <b>Polarization Quality of High-Birefringence Single-Mode Fibers</b>   | 365 |
| F. M. Sears and J. R. Simpson  |     |
| <br>   |     |
| PAPERS BY AT&T BELL LABORATORIES AUTHORS   | 373 |
| CONTENTS, MARCH ISSUE  | 377 |



## Quarter-Wave Corrugated Transformer for Broadband Matching of a Corrugated Feed

By C. DRAGONE\* and W. E. LEGG\*

(Manuscript received June 3, 1983)

This paper describes a broadband technique for obtaining the transformation  $TE_{11} \rightarrow HE_{11}$  at the input of a corrugated feed. Usually, this transformation is obtained by operating the feed in the vicinity of a frequency,  $\omega_1$ , corresponding to one of the zeroes of the input surface reactance since the feed input reflection,  $\rho_t$ , vanishes at  $\omega_1$ . Here we use a matching transformer to produce  $\rho_t \approx 0$  at two frequencies simultaneously, i.e., at  $\omega_1$  and a much lower frequency,  $\omega_0$ . Using two sections of corrugated waveguides, with a total of eight teeth and  $\omega_0 \approx 0.63 \omega_1$ , the measured reflection,  $\rho_t$ , is about  $-40$  dB in the vicinity of both frequencies  $\omega_0$  and  $\omega_1$ , and it remains less than  $-30$  dB over the entire frequency range  $0.60 \omega_1 < \omega < 1.04 \omega_1$ . This makes the corrugated feed suitable for simultaneous operation at the 4- and 6-GHz terrestrial microwave radio bands.

### I. INTRODUCTION

Corrugated feeds are usually characterized by a relatively large input reflection,<sup>1-3</sup> which vanishes only at certain frequencies corresponding to the zeroes of the surface reactance due to the input corrugations. In this article we describe a simple technique for reducing considerably this reflection over a wide range of frequencies. The reflection in question arises at the input of the feed as shown in Fig. 1, where a corrugated waveguide is directly connected to an uncorrugated waveguide of circular cross sections. The reflection,  $\rho_t$ , due to the discon-

---

\* AT&T Bell Laboratories.

---

Copyright © 1984 AT&T. Photo reproduction for noncommercial use is permitted without payment of royalty provided that each reproduction is done without alteration and that the Journal reference and copyright notice are included on the first page. The title and abstract, but no other portions, of this paper may be copied or distributed royalty free by computer-based and other information-service systems without further permission. Permission to reproduce or republish any other portion of this paper must be obtained from the Editor.

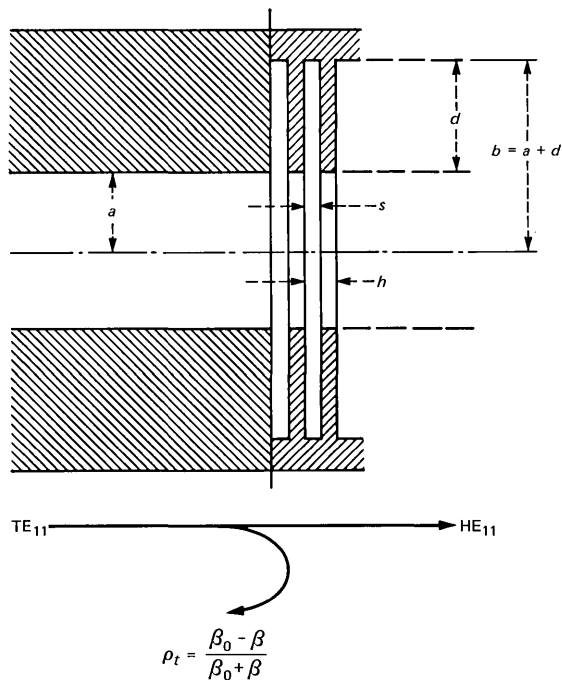


Fig. 1—Junction between two circular waveguides, one with corrugations of depth,  $d$ . The reflection,  $\rho_t$ , is given accurately by eq. (1).

tinuity in surface reactance between the two waveguides, is given accurately by the formula<sup>2</sup>

$$\rho_t = \frac{\beta_0 - \beta}{\beta_0 + \beta}, \quad (1)$$

relating  $\rho_t$  to the propagation constants ( $\beta_0$  and  $\beta$ ) of the dominant modes ( $TE_{11}$  and  $HE_{11}$ ) of the two waveguides. The two propagation constants coincide only at certain isolated frequencies, corresponding to the zeroes of the surface reactance of the input corrugations. The feed is normally operated in the vicinity of the first zero, which is the frequency,  $\omega_1$ , determined by the condition

$$d = \frac{\lambda_r(\omega_1)}{2}, \quad (2)$$

where  $d$  is the depth of the corrugations and  $\lambda_r(\omega)$  is the wavelength for the radial waves excited in the grooves at an input frequency,  $\omega$ . Using eq. (1), one can readily determine, as in Refs. 2 and 3, the variation of  $\rho_t$  with frequency, in the vicinity of  $\omega_1$ .

One finds a rapid increase in  $\rho_t$ , with  $|\omega - \omega_1|$  causing, under the

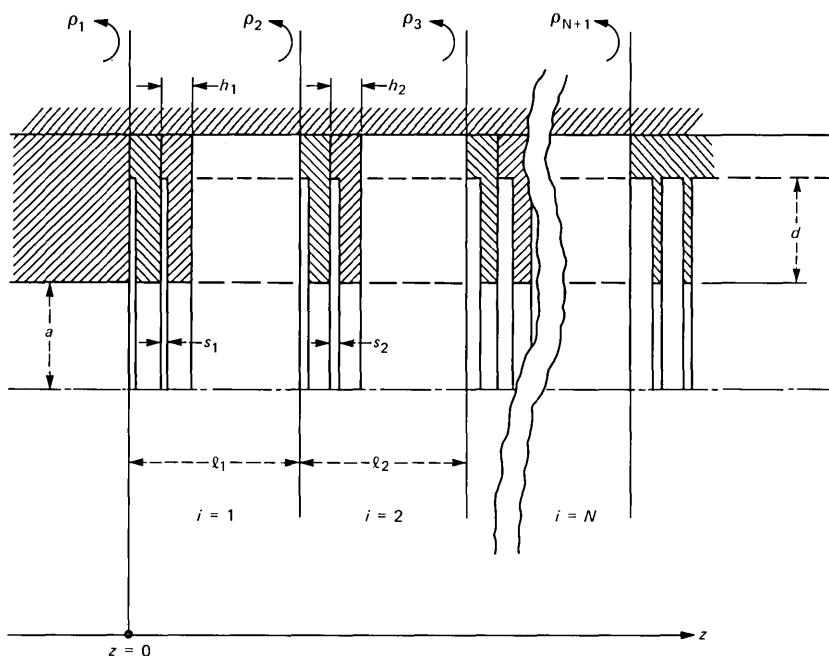


Fig. 2—The two waveguides of Fig. 1 are matched by using  $N$  sections of waveguides with corrugations of the same depth,  $d$ , but different  $s_i/h_i$ .

conditions of Ref. 2,\* reflections greater than  $-30$  dB for  $\omega < 0.832 \omega_1$ . Thus, the junction of Fig. 1 is unsuitable for applications requiring negligible  $|\rho_t|^2$  at widely spaced frequencies, such as, for instance, 4 and 6 GHz, as required in terrestrial radio systems.†

In this article we place a matching transformer between the two waveguides of Fig. 1 to cause  $\rho_t \approx 0$  also in the vicinity of a frequency  $\omega_0$  appreciably lower than  $\omega_1$ . The transformer, shown in Fig. 2, consists of two sections of corrugated waveguide having the same  $d$  but different gaps  $s_i$  between successive teeth in each section. Since all corrugations have the same depth,  $d$ , the total reflection,  $\rho_t$ , vanishes for  $\omega = \omega_1$ . To obtain  $\rho_t \approx 0$  in the vicinity of  $\omega_0$ , the lengths,  $l_i$ , of the various sections and the values of  $s_i$  are chosen by the same procedure commonly used for multisection quarter-wave matching transformers.<sup>4</sup> By properly choosing the parameters  $l_i$  and  $s_i$ , one can cause  $\rho_t$  to have  $N$  zeroes in the vicinity of  $\omega_0$ . Here we make these zeroes coincide with  $\omega_0$  to obtain a maximally flat characteristic in the

\* Notice a misprint in Ref. 2. The frequency  $\omega_1 = 17.5$  GHz, given correctly on page 878, is given incorrectly as 19 GHz on pp. 810 and 876.

† The TD and TH bands correspond to the intervals (3.7, 4.2) and (5.925, 6.325) in GHz.

vicinity of  $\omega = \omega_0$ . As a result, the reflection,  $\rho_t$ , is very small at frequencies close to  $\omega_0$  and  $\omega_1$ . Furthermore, we shall see that  $\rho_t$  is also small in the entire interval  $(\omega_0, \omega_1)$ .

Section III describes a transformer with inside radius  $a$  with a measured reflection of less than  $-30$  dB for values of  $ka$  in the interval  $(2.437, 4.22)$ , and less than  $-35$  dB in  $(2.437, 2.766)$  and  $(3.69, 4.22)$ . This performance is obtained using two sections with ordinary teeth, as in Fig. 2. Moreover, it can be further improved by increasing the number of sections or by using special teeth, as in Ref. 5.

Equation (1) was derived in eq. (2) by a perturbation analysis that assumes that the difference  $\beta_0 - \beta$  is small. Recently,  $\rho_t$  has been derived<sup>6</sup> without this restriction for the special case where one of the two waveguides is uncorrugated, as in Fig. 1, and a more general derivation is given in Ref. 7. By letting  $\beta_0 - \beta \rightarrow 0$  in the results of Refs. 6 and 7, we obtain eq. (1). For the purpose of this analysis, however, eq. (1) is more than adequate since all reflections,  $\rho_i$ , are small.

Reflections of less than  $-30$  dB were reported in Ref. 8 over a band  $2.7 < ka < 3.8$ , using only five slots. A mode-matching technique was used to accurately determine the transformer scattering matrix. Here, however, we are interested in a ratio  $\omega_1/\omega_0$ , which is much greater than  $3.8/2.7$ . Experimental and theoretical results on the problem of minimizing the input reflection of a feed using slots of varying depth were reported in Ref. 9, and excellent performance was obtained using ring-loaded slots, which greatly reduced excitation of the  $HE_{12}$  mode. We also mention the very low cross-polarization levels obtained in Ref. 10 using a curved-aperture corrugated horn.

## II. APPROXIMATE DERIVATION OF $\rho_t, s_i$

In this section we minimize the total reflection,  $\rho_t$ , in Fig. 2 in the vicinity of  $\omega_0$ . We assume that only the  $HE_{11}$  mode propagates for  $z > 0$  and that the  $TE_{11}$  mode is incident from the left. Let  $M_i$  be the number of corrugations in the  $i$ th section, and let  $\lambda_{gi}$  be the wavelength for the  $HE_{11}$  mode. The reflection,  $\rho_i$ , at the  $i$ th junction will be determined approximately using eq. (1), which is strictly valid only if  $\rho_i$  is small and

$$M_i \gg 1, \quad (3)$$

implying  $h_i \ll \lambda_{gi}$ , where  $h_i$  is the teeth separation in the  $i$ th section.

The propagation constant,  $\beta$ , of a mode is related to its transverse wave number,  $\sigma$ ,

$$\beta a = \sqrt{(ka)^2 - u^2}, \quad (4)$$

where  $u = \sigma a$  and  $k$  is the free-space propagation constant. For the  $TE_{11}$  mode,

$$u = u_0 = 1.8411. \quad (5)$$

For the  $HE_{11}$  mode in a corrugated waveguide,  $u$  is determined by  $s/h$  and  $d$ , and it can be calculated as in Refs. 1 and 3.

Assume the reflections,  $\rho_i$ , in Fig. 2 are small, and let the frequency dependence of  $\rho_i$  and  $\beta_i/k$  be neglected. Then, for a maximally flat passband characteristic,<sup>4</sup>

$$\rho_i = \frac{1}{2^N} \frac{N!}{(N-1)!i!} \rho_t, \quad (6)$$

where  $N$  is the number of sections and

$$\rho_t = \sum \rho_i. \quad (7)$$

The reflection,  $\rho_i$ , is related<sup>3</sup> to the propagation constants  $\beta_{i-1}$  and  $\beta_i$  of the waveguides at the  $i$ th junction,

$$\rho_i = \frac{\beta_{i-1} - \beta_i}{\beta_{i-1} + \beta_i}, \quad (8)$$

and, therefore, using eqs. (4), (6), and (8) one can determine  $u_1, u_2$ , etc., if  $u_0$  and  $u_{N+1}$  are given. Once the  $u_i$  are known, the values of  $s_i/h_i$  can be determined approximately as in Refs. 1 and 3. Notice the length,  $l_i$ , of the  $i$ th section must be chosen so that

$$l_i = \frac{\lambda_{gi}}{4}, \quad \text{at } \omega_0. \quad (9)$$

In the following section the corrugated waveguide at the input of the feed (see Fig. 1) will be characterized by

$$\frac{b}{a} = 1.789, \quad \frac{h}{s} = 1.256, \quad (10)$$

which can be shown to give

$$ka = 4.03, \quad \text{at } \omega = \omega_1. \quad (11)$$

Then, if one chooses

$$\omega_0 = .63 \omega_1, \quad (12)$$

one finds

$$u_N = u_3 = 2.114, \quad \text{for } \omega = \omega_0. \quad (13)$$

Therefore, eqs. (4), (6), and (8) give

$$u_1 = 1.928, \quad u_2 = 2.056, \quad \text{for } \omega = \omega_0.$$

This requires

$$\frac{h_1}{s_1} = 16.8, \quad \frac{h_2}{s_2} = 3.15, \quad (14)$$

taking into account that  $u_0 = 1.841$  in the input guide.

### III. EXPERIMENTAL RESULTS

The values of eq. (14) will not produce exactly a maximally flat characteristic because of the frequency dependence of  $\rho_i$  and  $\beta_i/k$ . Furthermore, in the experiment each section was realized using only four corrugations, in which case the values calculated for  $\rho_i$  and  $u_i$  in the preceding section for  $\omega = \omega_0$  are not expected to be accurate since condition (3) is violated (a consequence of this is pointed out in the appendix of Ref. 3). Thus, taking into account the difficulty involved in accurately determining the dependence of  $\rho_i$  on  $h_i/s_i$ , the optimum values of  $h_i/s_i$  were determined experimentally, and they are

$$\frac{h_1}{s_1} = 15.23, \quad \frac{h_2}{s_2} = 2.492,$$

assuming the conditions in (10).

The experiment was carried out choosing

$$a = 0.651", \quad d = 0.514", \quad (15)$$

which implies  $\omega_0 = 7.18$  GHz and  $\omega_1 = 11.455$  GHz. The two sections were constructed using eight rings assembled as indicated in Fig. 2. The output corrugated waveguide was realized by the technique of Ref. 2. The input circular waveguide was connected to a rectangular waveguide using a long transition, and the input reflection,  $\rho_t$ , was measured as in Fig. 3, using a commercial directional coupler. The measured reflection, shown in Figs. 4(a), (b), and (c), includes a component due to small reflections from the directional coupler and the transition. This component, of about  $-45$  dB, is responsible for the fast ripples in Fig. 4. Also shown in Fig. 4 are the values of  $\rho_t$ , calculated using eq. (8), for  $h_i/s_i$  given by eq. (8), assuming condition

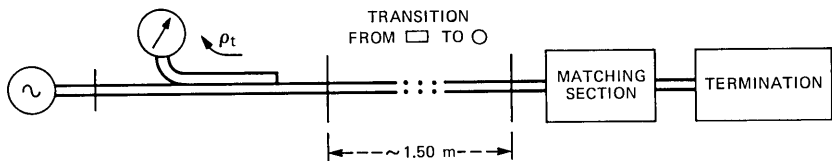


Fig. 3—Apparatus used to measure the reflection,  $\rho_t$ .

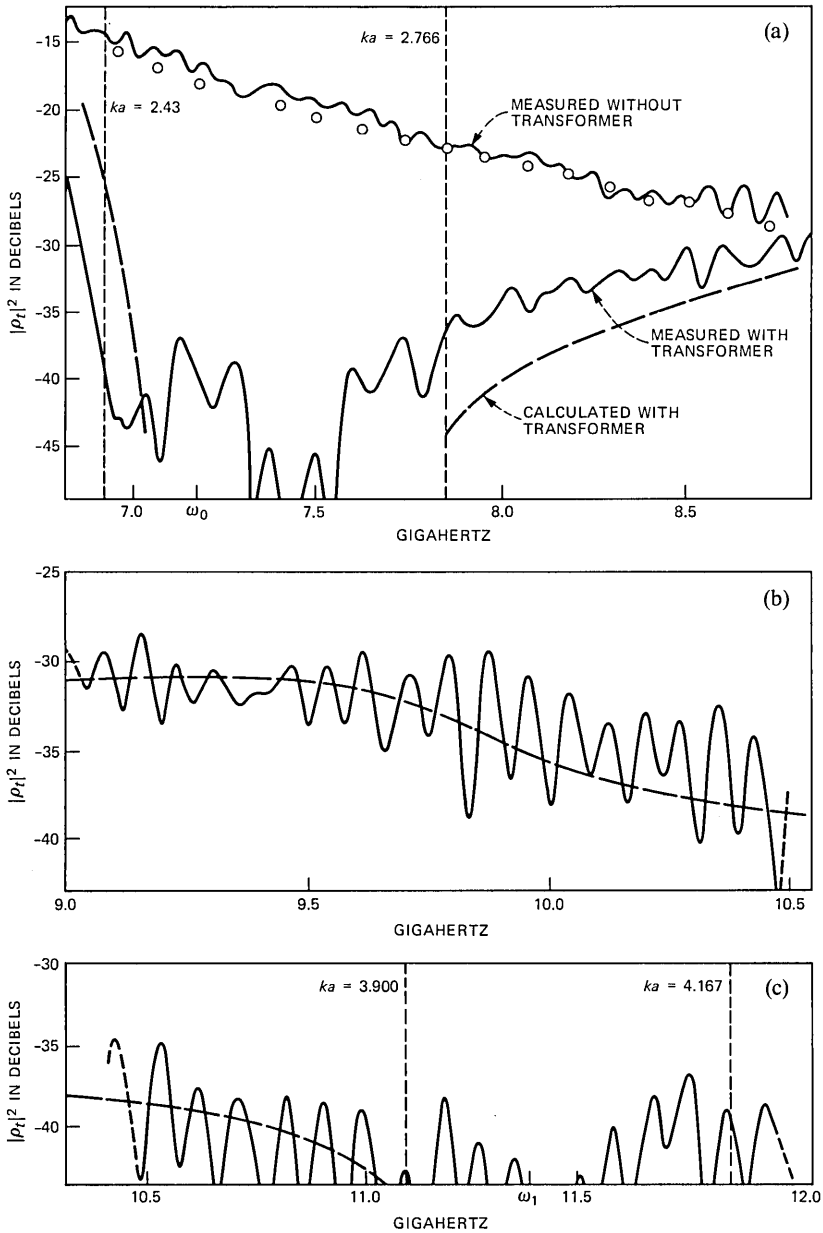


Fig. 4—Reflection,  $\rho_t$ , measured with and without transformer from (a)  $ka = 2.4$  to 3.0, (b)  $ka = 3.0$  to 3.7, and (c)  $ka = 3.7$  to 4.2.

(3) but without neglecting the frequency dependence of  $\beta_i/k$  and  $\rho_i$ . There is considerable discrepancy for  $\omega \approx \omega_0$ , as expected in view of the relatively large values of  $h_i/\lambda_{gi}$ . Also shown in Fig. 4 for comparison is the reflection  $\rho_t$  measured without matching section.

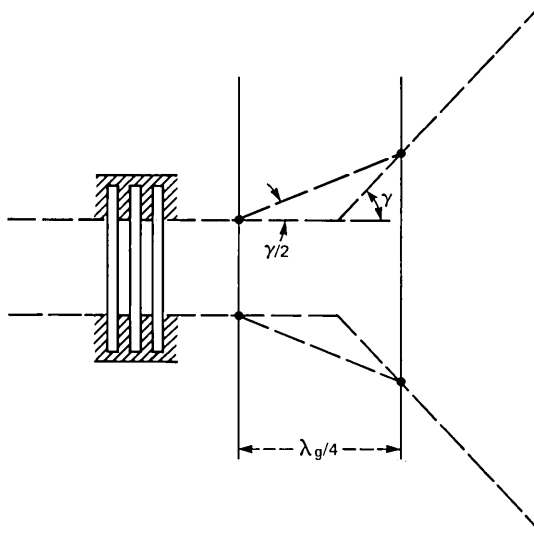


Fig. 5—The reflection at the throat of a horn can be matched by a suitable quarter-wave transformer.

#### IV. CONCLUSIONS

The input reflection,  $\rho_t$ , in Fig. 4 is less than about  $-30$  dB for values of  $ka$  in the band (2.43, 4.22) and less than  $-35$  dB over the two bands (2.43, 2.766) and (3.69, 4.22). Over most of these two bands,  $|\rho_t|^2$  is less than  $-40$  dB. The transformer is simple to realize, consisting of eight rings assembled as shown in Fig. 2.

Over part of the above frequency range, the input waveguide can be shown to be multimoding because of the  $TM_{11}$  mode, which propagates for  $ka > 3.8317$ . Also, the output waveguide is multimoding over approximately the same frequency range. However, one can show, using the approximate formulae of Ref. 3, that the transformer greatly reduces generation of this mode, which should therefore be negligible. For this reason, and also because of the difficulty in precise measurements of the conversion coefficients, the mode in question was ignored here.

Finally, in a feed, the input reflection includes a contribution from the throat of the horn.<sup>9,10</sup> This contribution is determined by the angle  $\gamma$  in Fig. 5, and it can be eliminated by using a suitable matching transformer as shown in Fig. 5. This is pointed out in Ref. 9.

#### REFERENCES

1. P. J. B. Clarricoats and P. K. Saha, "Propagation and Radiation Behavior of Corrugated Feeds; Part 1—Corrugated Waveguide Feed," Proc. IEEE, 118, No. 9 (September 1971), pp. 1167-76.

2. C. Dragone, "Characteristics of a Broadband Corrugated Feed: A Comparison Between Theory and Experiment," *B.S.T.J.*, 56, No. 6 (July-August 1977), pp. 869-88.
3. C. Dragone, "Reflection, Transmission, and Mode Conversion in a Corrugated Feed," *B.S.T.J.*, 56, No. 6 (July-August 1977), pp. 835-67.
4. R. E. Collin, *Foundations for Microwave Engineering*, New York, NY: McGraw-Hill, 1966.
5. Fumio Takeda and Tsutomu Hashimoto, "Broadbanding of Corrugated Conical Horns by Means of the Ring-Loaded Corrugated Waveguide Structure," *IEEE Trans. Ant. and Propag.*, *AP-24*, No. 6 (November 1976), pp. 786-91.
6. V. G. Daniele, I. Montrosset, and R. S. Zich, "Wiener-Hopf Solution for the Junction Between a Smooth and a Corrugated Cylindrical Waveguide," *Radio Sci.*, 14, No. 6 (November-December 1979) pp. 943-55.
7. C. Dragone, unpublished work.
8. G. L. James, "Analysis and Design of  $TE_{11}$ -to- $HE_{11}$  Corrugated Cylindrical Waveguide Mode Converters," *IEEE Trans. Microw. Theory Tech.*, *MTT-29*, No. 10 (October 1981), pp. 1059-66.
9. G. L. James, " $TE_{11}$ -to- $HE_{11}$  Mode Converters for Small Angle Corrugated Horns," *IEEE Trans. Ant. and Propag.*, *AP-30*, No. 6 (November 1982), pp. 1057-62.
10. B. MacA. Thomas and K. J. Greene, "A Curved-Aperture Corrugated Horn Having Very Low Cross-Polar Performance," *IEEE Trans. Ant. and Propag.*, *AP-30*, No. 6 (November 1982), pp. 1068-72.

## AUTHORS

**Corrado Dragone**, Laurea in E.E., 1961, Padua University (Italy); Libera Docenza, 1968, Ministero della Pubblica Istruzione (Italy); AT&T Bell Laboratories, 1961—. Mr. Dragone has been engaged in experimental and theoretical work on microwave antennas and solid-state power sources. He is currently concerned with problems involving electromagnetic wave propagation and microwave antennas.

**W. E. Legg**, Rutgers University, 1945-1949; AT&T Bell Laboratories, 1945-1980. Mr. Legg has worked on dielectric lenses and microwave antennas for radio relay systems. He was involved in the development of Project Echo and Telstar tracking equipment and participated in mobile radio telephone experiments. He was also engaged in antenna measurements for satellite communication and terrestrial microwave repeaters in the Radio Research Laboratory.



## Moment Calculations by Digital Filters

By Z. L. BUDRIKIS\* and M. HATAMIAN†

(Manuscript received May 25, 1983)

We present a simple recursive algorithm for computing moments of two-dimensional integer arrays. It uses only additions and can be implemented for high-speed and real-time computation at video rates. We describe Complementary Metal-Oxide Semiconductor (CMOS), Very Large-Scale Integrated (VLSI) implementation of the algorithm in a single chip that can calculate the 16 moments  $\mu^{ij}$  ( $i, j = 0, 1, 2, 3$ ) (i.e., up to the sixth-order moment) on  $512 \times 512$  array of 8-bit integers in real time (at video rate). Such a chip can have potential applications in image processing, graphics, and robotics. The basic building block of the system is a single-pole digital filter that is implemented by recursive addition. The complexities involved in designing the chip, as well as its area, are significantly reduced by taking advantage of the fact that the column samples of the data array can be processed at a much slower rate than the row samples. An estimate of the chip area obtained from the layout design of the individual cells is given.

### I. INTRODUCTION

Moments are familiar from statistics and mechanics, and are finding applications in other areas, among them video processing.<sup>1,2</sup> The mean, or first moment, is a particularly robust estimator of the 'center' of a distribution. Similarly, the centroid is a good single indication of the location of an extended object. We want to use it for pinpointing the position of a light pen.<sup>3</sup>

A possible brake on calculating moments, particularly in real-time applications, may well have been the computational burden that they

---

\* University of Western Australia. † AT&T Bell Laboratories.

---

Copyright © 1984 AT&T. Photo reproduction for noncommercial use is permitted without payment of royalty provided that each reproduction is done without alteration and that the Journal reference and copyright notice are included on the first page. The title and abstract, but no other portions, of this paper may be copied or distributed royalty free by computer-based and other information-service systems without further permission. Permission to reproduce or republish any other portion of this paper must be obtained from the Editor.

appear to entail. It would seem that the calculation calls for exponentiations and multiplications, as well as additions. However, given real-world measurements that are finite in precision, range, and number, and are at regular intervals, the calculation of moments can involve much less effort than at first seems necessary.

One scheme has already been reported<sup>4</sup> in which the multiplying coefficients are generated without exponentiation and in which the multiplications are distributed over the individual bits of the measurements and are therefore accomplished by single AND gates. An even simpler approach is possible, requiring less computation by an order of magnitude, and is reported here.

Our approach comes about from recognizing that Infinite Impulse Response (IIR) digital filters with impulse responses  $h(n) = u(n)$ , or  $nu(n)$  or  $n^2u(n)$  or  $n^i u(n)$ , with  $u(n)$  the unit step sequences, will calculate respectively the zeroth-, first-, second-, and  $i$ th-order moments of their input sequence. It is a straightforward matter to extend this to arrays in the plane and higher dimensionality, since the computations along the different dimensions are separable from each other.

The poles of the required filters can be very easily realized by first-order sections, and these are nothing more than recursions with unity feedback. Thus, if only the poles, and not zeros, of these filters are realized, the computation between successive sample points is just one addition and can be instrumented to take place in real time on picture data from standard television. The basic building block of the system, then, will be a first-order stage, and the resulting filter will have a highly regular and recursive structure that is extremely attractive for Very Large-Scale Integrated (VLSI) implementation.

As will be seen in Section III, the consequence of discarding the zeros of these filters is that the output of, say, the  $m$ th stage, rather than being the  $m$ th-order moment itself, is a linear combination of first through  $m$ th-order moments. This, however, does not create any major difficulty because the coefficients of this linear combination are exactly known, and therefore starting from zeroth-order moment, at each stage the effect of previous moments can be removed by subtraction in a post-processing step.

We describe a design for a custom Integrated Circuit (IC) in Complementary Metal-Oxide Semiconductor (CMOS) technology that can calculate the 16 moments,  $\mu^{ij}$  ( $i, j = 0, 1, 2, 3$ ), of a  $512 \times 512$ , 8 bits/pixel image in real time (i.e., at conventional video rate).

## II. THE TASK

Given the array  $x(n, m)$  ( $n = 0, 1, \dots, N$ ,  $m = 0, 1, \dots, M$ ) of integer values, the moments about  $m = 0$ ,  $n = 0$  are

$$\begin{aligned}\mu_0^{i,j} &= \sum_{n=0}^N \sum_{m=0}^M n^i m^j x(n, m) \\ &= \sum_{n=0}^N n^i \left( \sum_{m=0}^M m^j x(n, m) \right).\end{aligned}\quad (1)$$

Only the innermost computations, corresponding to along line in television, have to be at speed. The outer computations are at lower rate by a factor of  $M$ . The choice of  $n = 0, m = 0$  as the pivot for the moments is arbitrary. Well-known expressions relate the moments about one pivot to those about another. The pivot point about which we chose to do the computations is  $n = N, m = M$ , i.e.,

$$\mu^{i,j} = \sum_{n=0}^N (N - n)^i \sum_{m=0}^M (M - m)^j x(n, m).\quad (2)$$

### III. THE ALGORITHM

We first consider the one-dimensional case. Consider a sequence  $x(n)$   $n = 0, 1, \dots, N$ ; if this sequence is applied to the input of a digital filter with impulse response  $h(n) = n^i u(n)$ , then from the well-known convolution theorem the output will be

$$\begin{aligned}y(n) &= \sum_{k=0}^N x(k)h(n - k) \\ &= \sum_{k=0}^N x(k)(n - k)^i.\end{aligned}\quad (3)$$

If this output is evaluated at  $n = N$ , then we will have

$$y(N) = \sum_{k=0}^N x(k)(N - k)^i,\quad (4)$$

which is the  $i$ th-order moment of  $x(n)$  about the point  $n = N$ . Figure 1 shows the filter for  $i = 0$ . This is a single-pole filter with the transfer function  $1/z - 1$  in  $z$ -transform domain. Its implementation is trivial, just an adder with one sample delay and a feedback, or basically an accumulator. For higher-order moments ( $i = 1, 2, \dots$ ) the filter will have both poles and zeros. In general, for the  $i$ th-order moment we have  $i$  zeros and a pole of order  $i + 1$  located at  $z = 1$ . The first and

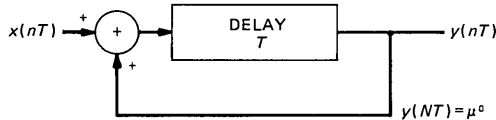


Fig. 1—Single-pole filter for generating zeroth-order moment.

Table I—Impulse response and transfer function of moment filters

| Moment Order, $i$ | Impulse Response, $h(n)$ | Transfer Function, $H(z)$     | All-Pole Transfer Function, $\hat{H}(z)$ | All-Pole Impulse Response, $\hat{h}(n)$                             |
|-------------------|--------------------------|-------------------------------|--|---|
| 0                 | $u(n)$                   | $\frac{1}{z-1}$               | $\frac{1}{z-1}$                          | $u(n)$  |
| 1                 | $nu(n)$                  | $\frac{z}{(z-1)^2}$           | $\frac{1}{(z-1)^2}$                      | $(n-1)u(n-1)$   |
| 2                 | $n^2u(n)$                | $\frac{z(z+1)}{(z-1)^3}$      | $\frac{1}{(z-1)^3}$                      | $1/2 (n-2)^2u(n-2)$<br>$+ 1/2 (n-2)u(n-2)$                          |
| 3                 | $n^3u(n)$                | $\frac{z(z^2+4z+1)}{(z-1)^4}$ | $\frac{1}{(z-1)^4}$                      | $1/6 (n-3)^3u(n-3)$<br>$+ 1/2 (n-3)^2u(n-3)$<br>$+ 1/3 (n-3)u(n-3)$ |

second columns of Table I, respectively, show the impulse response and transfer function of the moment filters for  $i = 0, 1, 2, 3$ . If we discard the zeros of the transfer function, then for the  $i$ th-order moment we obtain the all-pole filter

$$\hat{H}_i(z) = \frac{1}{(z-1)^{i+1}} \tag{5}$$

This filter can be very easily implemented by cascading  $i + 1$  first-order stages similar to the one shown in Fig. 1. Obviously, the output of the filter without zeros will no longer be just the  $i$ th-order moment of its input signal except for  $i = 0$ . We examine this next.

Starting from  $i = 0$  with the  $z$ -transform pair,

$$\hat{H}_0(z) = \frac{1}{z-1} \Leftrightarrow \hat{h}_0(n) = u(n),$$

and, using the differentiation property of the  $z$  transform, we can progressively derive the impulse responses  $\hat{h}_i(n)$  corresponding to  $\hat{H}_i(z) = 1/(z-1)^{i+1}$  for all values of  $i$ . The results for  $i = 0, 1, 2, 3$  are shown in the fourth column of Table I. To see the effect of zero elimination, let us consider the case for  $i = 3$  as an example. From Table I we have:

$$\begin{aligned} \hat{h}_3(n) = \frac{1}{6} (n-3)^3u(n-3) + \frac{1}{2} (n-3)^2u(n-3) \\ + \frac{1}{3} (n-3)u(n-3). \end{aligned} \tag{6}$$

Convolving this impulse response with the input  $x(n)$  and evaluating the output at  $n = N + 3$  will result in:

$$\begin{aligned}
 y_3(N+3) &= \frac{1}{6} \sum_{k=0}^N x(k)(N-k)^3 + \frac{1}{2} \sum_{k=0}^N x(k)(N-k)^2 \\
 &\quad + \frac{1}{3} \sum_{k=0}^N x(k)(N-k) \\
 &= \frac{1}{6} \mu^3 + \frac{1}{2} \mu^2 + \frac{1}{3} \mu^1,
 \end{aligned} \tag{7}$$

which is a linear combination of first-, second-, and third-order moments. Similarly, for an arbitrary value of  $i$ , the output of the filter evaluated at  $n = N + i$  will be a linear combination of first through  $i$ th-order moments, i.e.:

$$y_i(N+i) = \sum_{\ell=1}^i k_\ell \mu^\ell. \tag{8}$$

Conversely, the moments  $\mu^i$  ( $i = 0, 1, \dots$ ) can be expressed as a linear combination of the filter outputs  $y_i(N+i)$ ; in matrix notation,

$$\tilde{\mu} = \mathbf{C} \tilde{Y}, \tag{9}$$

where

$$\tilde{\mu} = \begin{bmatrix} \mu^0 \\ \mu^1 \\ \mu^2 \\ \vdots \end{bmatrix} \quad \tilde{Y} = \begin{bmatrix} y_0(N) \\ y_1(N+1) \\ y_2(N+2) \\ \vdots \end{bmatrix}.$$

The coefficient matrix  $\mathbf{C}$  can be easily derived from the impulse responses  $\hat{h}_i(n)$ . For  $i = 5$ , this matrix is:

$$\mathbf{C} = \begin{bmatrix} 1 & 0 & 0 & 0 & 0 & 0 \\ 0 & 1 & 0 & 0 & 0 & 0 \\ 0 & -1 & 2 & 0 & 0 & 0 \\ 0 & 1 & -6 & 6 & 0 & 0 \\ 0 & -1 & 14 & -36 & 24 & 0 \\ 0 & 1 & -30 & 150 & -240 & 120 \end{bmatrix}. \tag{10}$$

Figure 2 shows the complete filter structure for generating zeroth-through third-order moments. The delay introduced on the output of each stage is necessary for synchronizing the output before performing the matrix operation.

So far in this section we have been discussing the moment calculation problem for a one-dimensional sequence  $x(n)$ ; extending the algorithm to two or higher dimensions is a straightforward matter. This is true because the computations along the different directions are separable. Consider an array of integers  $x(n, m)$  ( $n = 0, 1, \dots, N$ ,  $m = 0, 1, \dots, M$ ), which can, for example, be the digitized samples

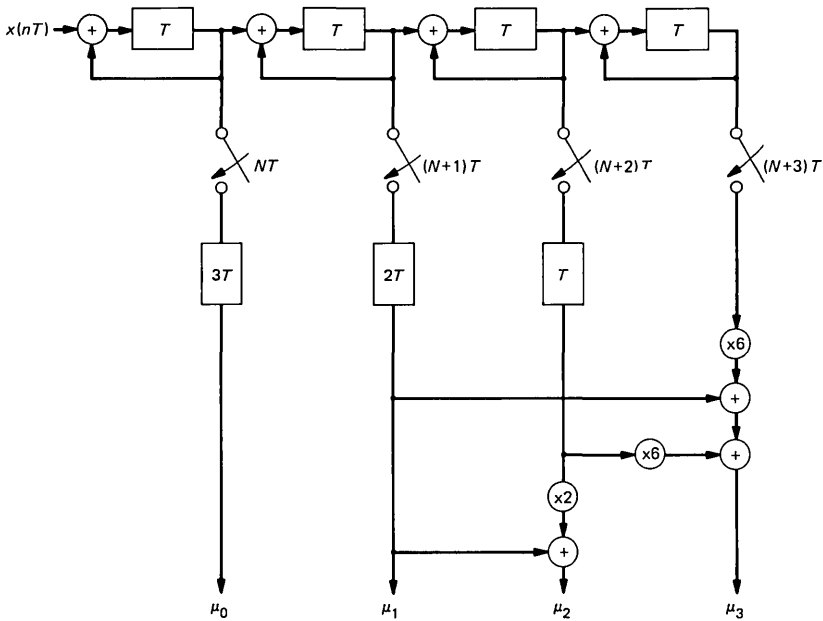


Fig. 2—Moment filter for generating zeroth- through third-order moments.

of a video image. As mentioned in Section II, the moments  $\mu^{ij}$  [i.e.,  $(i + j)$ th order] of this array can be computed from

$$\begin{aligned} \mu^{ij} &= \sum_{n=0}^N (N - n)^i \sum_{m=0}^M (M - m)^j x(n, m) \\ &= \sum_{n=0}^N (N - n)^i y_j(n). \end{aligned} \quad (11)$$

The inner summation,  $y_j(n)$ , represents the  $j$ th-order moment of the  $n$ th row ("along-line moment") which, as discussed previously, can be computed by filtering the samples on that row with a filter with the impulse response  $m^j u(m)$  (row filter) and evaluating the output at  $m = M$ .

Now  $\mu^{ij}$  is equal to the  $i$ th-order moment of the sequence  $y_j(n)$  and can be computed using a filter with impulse response  $n^i u(n)$  (column filter). Figure 3 shows the filter block diagram for generating  $\mu^{ij}$ . The input to the column filter implementing eq. (11) is updated every  $M$  samples of the input signal, corresponding to one row of the array  $x(n, m)$ ; the row filter is also reset at this time. If the array  $x(n, m)$  represents the digitized samples of a video image, then for real-time operation, the sampling rate will be equal to the pixel frequency for the row filter and line frequency for the column filter. As we will see

in Section IV, this fact greatly reduces the complexity of implementation.

The column filters can be realized with single-pole stages in exactly the same manner as was previously discussed in this section. There are two alternatives. One is to use the filter structure shown in Fig. 2, which includes the dematrixing operation, for the column filters as well and make it a building block for implementing the two-dimensional filter. The block diagram of Fig. 4 illustrates this approach. In this case the outputs of the two-dimensional filter will be the true moments  $\mu^{i,j}$ . The other alternative is to use the original single-pole stage shown in Fig. 1 as the building block for constructing the two-dimensional filter. In this case the outputs of the filter will be a linear combination of the moments; to obtain the actual moments  $\mu^{i,j}$ , a dematrixing operation has to be done at the end of the process (i.e., after the last row of the input array has passed through the filter). Figure 5 shows the complete two-dimensional structure implementing this latter filter configuration. From the implementation point of view this structure is more attractive than the former realization. (More on this in the following section.) The relationship between the array  $x(n, m)$  in Fig. 5 and the input signal is determined by the sampling strategy. For example, if  $f(t)$  is a sequentially scanned signal to be filtered, then

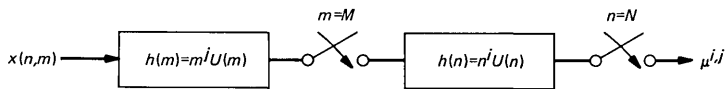


Fig. 3—Block diagram of the filter for generating  $\mu^{ij}$ .

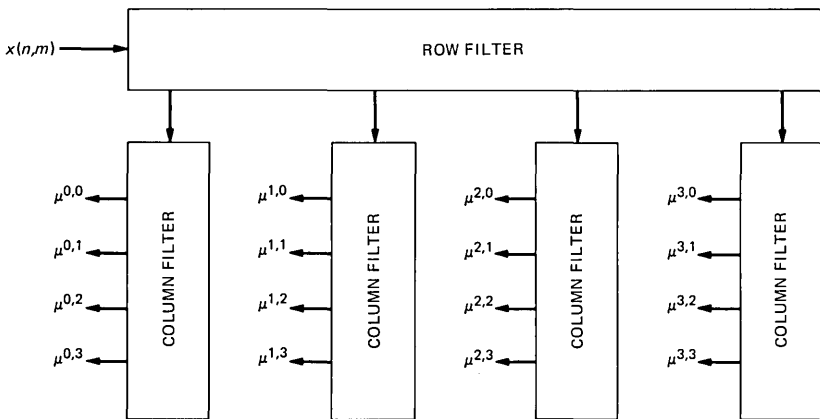


Fig. 4—Moment filter for generating  $\mu^{ij}$  ( $i, j = 0, 1, 2, 3$ ) using the filter shown in Fig. 2 as a building block.

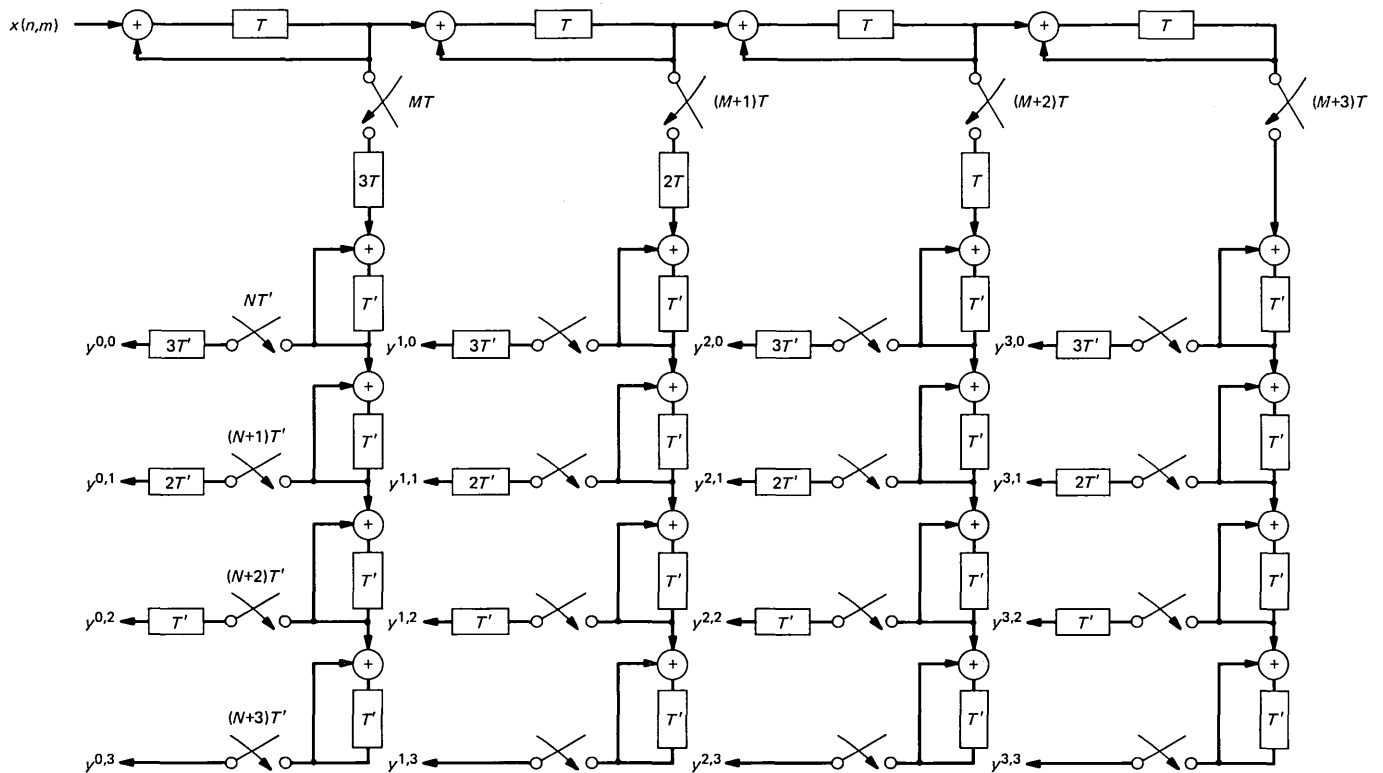


Fig. 5—Moment filter for generating  $\mu^{ij}$  ( $i, j = 0, 1, 2, 3$ ) using the single-pole stage as a building block;  $T' = MT$ .

$$x(n, m) = f(mT + nT'),$$

where  $T$  is the pixel period and  $T'$  is the line period.

#### IV. VLSI IMPLEMENTATION

In this section we describe VLSI design for implementation of our two-dimensional filtering algorithm, which can calculate the moments  $\mu^{ij}$  ( $i = 0, 1, 2, 3, j = 0, 1, 2, 3$ ) of a  $512 \times 512$ , 8 bits/pixel image in real time (i.e., at conventional video rate). We consider a maximum chip size of  $6 \text{ mm} \times 6 \text{ mm}$ . To meet the speed requirement the picture element (pel) processing time should be less than 125 ns.

We examine the two filter structures shown in Figs. 4 and 5 for possible VLSI implementation. The boxes labeled 'row filter' and 'column filter' in Fig. 4 could be made identical, and each could be realized by one chip. Then the two-dimensional filter would be constructed by putting five of these chips together. This may at first seem a reasonable approach, but in fact, it is not: the speed requirements are set by the calculations that are performed in the 'row filter', while the size of the accumulators is dictated by the 'column filters'. The result would be very large accumulators (up to 64 bits) operating at the high rate of at least 8 MHz. Moreover, that implementation would preclude any possibility of having all calculations done on a single chip.

With the structure of Fig. 5, all mismatches of speed and size can be avoided. What is more, the whole system can be put on a single chip with an area occupancy only slightly greater than needed for a single filter of Fig. 4. The only shortcoming of the system of Fig. 5 compared to that of Fig. 4 is that it is the poles-only realization and requires external dematrixing. That, however, is only minor, for those calculations involve only a few multiplications and additions, and can be readily performed by the host processor that would use the computed moments.

The basic building block of the filter in Fig. 5 is an accumulator functioning as a single-pole digital filter. The maximum word lengths that may appear as outputs and hence determine minimum accumulator sizes increase with order. For 8-bit input data samples in a  $512 \times 512$  array, the accumulations along the row section may progressively reach 17, 25, 33, and 41 bits, and those in the last column section, progressively 48, 55, 62, and 68 bits.

To achieve the required speed in the row section, we have decided to use look-ahead carry adders. The column sections could be implemented with simple ripple carry adders occupying much less area and obviously making it possible to accommodate all circuits on the available chip area. In fact, we do even better than that by using serial

additions. Conversion to serial streams when passing data from the top row into the columns is in any case indicated by wiring considerations.

If given parallel operations in both row and columns, there would be inordinate numbers of wires that would have to pass down vertically, presenting a difficult routing problem. To alleviate this, we decided to use a parallel-to-serial convertor on the output of each stage of the row filter and transfer serially the outputs to the column heads. Note that the along-row and down-to-column transfers take place at different times, the latter only once every line during the horizontal-blanking interval, and that the horizontal connections remain in parallel without any sacrifice in speed. To achieve the dual feed-out, the output registers of the along-row accumulators are designed as parallel in parallel/serial out shift registers.

Once given serial streams into the columns, there is no point in converting back to parallel operation or using ripple carry adders: the accumulations can be done equally well serially, using for each stage a one-bit full adder and a shift register. The block diagram of Fig. 6 illustrates this final design. The upper portion of this figure shows the four stages of the row filter. The lower portion is divided into four sections that correspond to the four column filters and receive their input from the serial output of the shift registers of the row-filter accumulators.

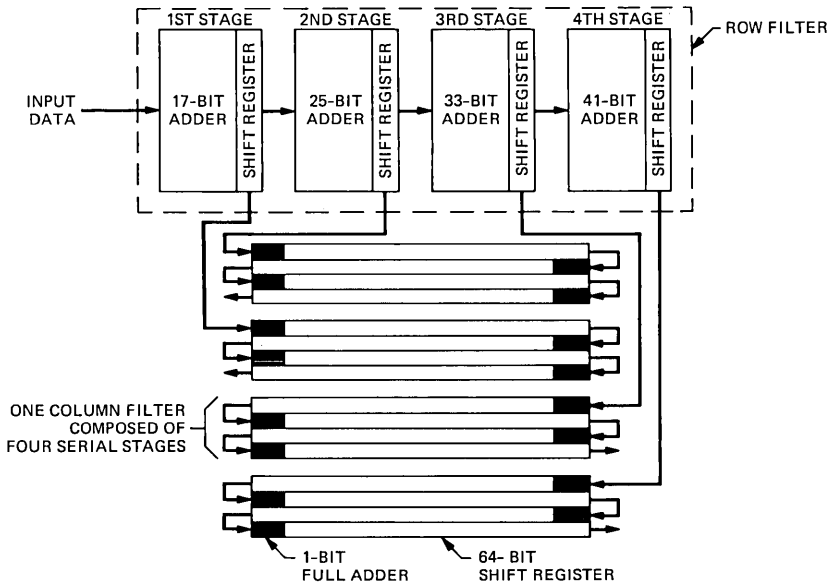


Fig. 6—Block diagram of a VLSI design for single-chip implementation of the two-dimensional moment-generating filter.

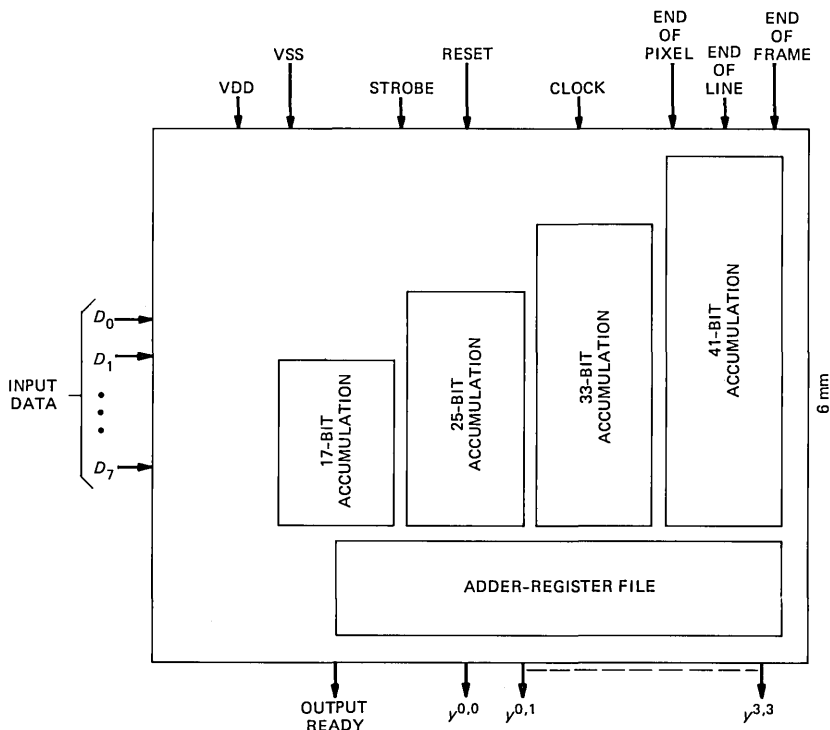


Fig. 7—Floor plan and input/output pins for the design shown in Fig. 6.

Each section consists of four stages stacked on top of each other, each containing a one-bit full adder (the dark area) and a 64-bit shift register composing a 64-bit serial accumulator. The feedback path for the accumulator is not shown in the figure.

The design of the chip is not complete yet, but a conservative estimate of the size has been obtained from the design of the individual cells. The design is for CMOS technology with a two-micrometer design rule. Figure 7 shows the result of the size estimate in a floor plan block diagram drawn in proportion to the 6 mm  $\times$  6 mm boundary. Each section of the floor plan is drawn 15-percent larger in both dimensions than the layout size estimated from individual cell designs. As can be seen from Fig. 7, there is still plenty of silicon area left for adding the timing and control section and, if desired, one or two more column stages for generating higher-order moments. The anticipated input/output pins for this chip are also shown in Fig. 7. The chip operation is synchronized with the input image data through three synch pulses: End of Pixel (EOP), End of Line (EOL), and End of Frame (EOF). After the output data ready signal is asserted, the host processor should read the 16 outputs,  $y^{0,0}, y^{0,1}, \dots, y^{3,3}$ , in serial format.

## V. CONCLUSION

We have described a simple and powerful algorithm for computing moments of a two-dimensional array of integers using digital filters. The algorithm involves only addition operation and is very suitable for real-time implementation. A two-dimensional digital filter with a separable impulse response,  $h(n, m) = n^i u(n) m^j u(m)$ , can generate the  $(i + j)$ th order moment of its input. Realization of an all-pole version of such a filter results in a filter with a highly regular structure capable of producing all the moments, from zeroth to  $(i + j)$ th order, of a two-dimensional input data array. We have shown that the consequence of eliminating the zeros of the filter and using an all-pole version is that the outputs will be a linear combination of the moments rather than the direct moments themselves. But this does not create any difficulty because the constant coefficients of the linear combination are known and a simple dematrixing operation at the end of the process will recover the actual moments. The basic building block of our moment filter is a single-pole digital filter that can be easily implemented by an accumulator. We have proposed a VLSI design for single chip implementation of this moment calculation algorithm. The preliminary results obtained from the layout design of the individual cells for 2-micrometer CMOS technology indicate that on a single 6 mm  $\times$  6 mm chip, we can certainly implement a filter for generating the 16 moments  $\mu^{i,j}$  ( $i, j = 0, 1, 2, 3$ ) of a 512  $\times$  512, 8 bits/pixel image in real time.

## VI. ACKNOWLEDGMENTS

We would like to thank Neil Weste for providing the information on the size and the speed of the look-ahead adder circuits.

## REFERENCES

1. R. C. Gonzalez and P. A. Wintz, *Digital Image Processing*, Reading, MA: Addison-Wesley, 1977.
2. U. K. Hu, "Visual Pattern Recognition by Moment Invariants," *IRE Trans. Info. Theory*, IT-8 (February 1962), pp. 179-87.
3. Z. L. Budrikis and A. N. Netravali, private communication.
4. R. L. Andersson, private communication.

## AUTHORS

**Zigmantas L. Budrikis**, B.Sc., 1955, and B.E. (Electrical Engineering, Hons I), 1957, University of Sydney; Ph.D., 1970, University of Western Australia; Research Laboratories of Telecom Australia, 1958-1960; Aeronautical Research Laboratories, 1961; on Faculty at University of Western Australia since 1962. In 1968 Mr. Budrikis was Visiting Lecturer at the University of California at Berkeley, and since 1972 he has been a recurrent visitor, as MTS or Consultant, at AT&T Bell Laboratories. He is interested in communications

and electromagnetics. Member, IEEE, Optical Society of America, NY Academy of Science. Fellow, IE Australia.

**Mehdi Hatamian**, B.S.E.E., 1977, Ary-Mehr University of Technology, Tehran; M.S. and Ph.D. (Electrical Engineering), University of Michigan, Ann Arbor, in 1978 and 1982, respectively; AT&T Bell Laboratories, 1982—. From 1979 to 1982 Mr. Hatamian was a Research Assistant on a NASA project working on the design and development of hardware and software for one of the Space Shuttle experiments. His research interests are in real-time signal processing, circuit design, image processing, and VLSI design. Member, IEEE, Sigma Xi.



## Wideband Operation of Nonlinear Solid-State Power Amplifiers—Comparisons of Calculations and Measurements

By J. B. MINKOFF\*

(Manuscript received June 29, 1983)

Calculations of intermodulation (IM) noise and input/output power-transfer characteristics for a number of different nonlinear Solid-State Power Amplifiers (SSPAs) are found to be in very good agreement with measurements. The calculations are based on the measured AM/AM and AM/PM characteristics, and include results of a computer simulation, and analytical results based on modeling the SSPA as an ideal envelope limiter. The results demonstrate that the calculations predict wideband performance characteristics of nonlinear amplifiers for arbitrary input signal configurations and operating conditions, as well as provide a basis for comparison against which anomalous behavior can be identified. Earlier results, in which anomalous behavior of an SSPA was observed to result in significant performance degradation, are discussed in the light of these new results. A simple analytical criterion is developed for evaluating measurements to identify such degradation. The effect of AM/PM conversion is investigated and found to cause significant degradation in IM performance only at low power levels for typical SSPAs. In the vicinity of saturation, and above, the contribution to IM noise due to AM/PM conversion is found to be very small in comparison with that due to the saturating AM/AM characteristic.

### I. INTRODUCTION

Two important considerations that arise in the design of nonlinear power amplifiers such as those used in satellite and terrestrial radio

---

\* AT&T Bell Laboratories.

---

Copyright © 1984 AT&T. Photo reproduction for noncommercial use is permitted without payment of royalty provided that each reproduction is done without alteration and that the Journal reference and copyright notice are included on the first page. The title and abstract, but no other portions, of this paper may be copied or distributed royalty free by computer-based and other information-service systems without further permission. Permission to reproduce or republish any other portion of this paper must be obtained from the Editor.

systems are the input/output power-transfer efficiency, and the amount of intermodulation (IM) noise produced as a function of input and output power levels. The former of these is related to what is termed the power-added efficiency of the device and the latter is a measure of its range of linearity. An earlier paper presented some results of analyses of these aspects of a nonlinear multistage Solid-State Power Amplifier (SSPA) under wideband excitation.<sup>1</sup> The results revealed a significant discrepancy between the calculated and measured power-transfer characteristics of the SSPA. In particular, measured output power levels in the vicinity of saturation were found to require approximately 3 dB more input power above predicted values based on AM/AM and AM/PM measurements. Ideally, the measured single-tone AM/AM and AM/PM characteristics of a nonlinear amplifier uniquely specify how it will perform in operation with wideband signals. The results of Ref. 1, however, have shown that anomalous cases—in which the single-tone measurements are not sufficient for predicting measured wideband behavior—can occur, with significant degradation in performance. It is therefore necessary to have a basis for comparison against which measurements of wideband power-transfer efficiency, IM performance, and possibly other performance criteria can be evaluated. In following up these initial results, the techniques originally developed in Ref. 1 have been extended and applied to a number of additional nonlinear SSPAs with newly measured performance data.<sup>2</sup> As we will see from the results presented below, calculations of this kind provide such a basis for any arbitrary input signal configuration and, essentially, any set of operating conditions.

Numerical results are obtained by means of computer simulation and an analytical closed-form expression for the wideband power-transfer characteristics. In the analysis, the multicarrier signal is assumed to be Gaussian, which is a very good approximation for the signals of interest here. In all cases it is assumed that the devices under consideration are memoryless or instantaneous. The initial results in Ref. 1 were obtained for a multistage SSPA, referred to as MS-1. The additional SSPAs for which comparisons of calculations and measurements have been made include a single-stage SSPA, referred to as SS-1, of which six such stages were employed in MS-1, another multistage SSPA, referred to as MS-2, which also employed six SS-1's, and three additional multistage SSPAs.

In all cases, measured and calculated results presented below for these SSPAs are in very close agreement, differing for the most part by fractions of a decibel. This demonstrates that the methods presented herein can be used to accurately determine what the operating characteristics of nonlinear SSPAs under wideband excitation should

be, and that they are sufficiently reliable to reveal anomalous behavior and to help pinpoint the sources of such anomalies. Specifically, the anomalous behavior of MS-1 was identified by comparison of the measured power-transfer characteristics with calculated values. Furthermore, the good agreement between measurements and calculations for SS-1 and MS-2 shows that, in general, the transistors employed in MS-1 can be expected to perform as predicted both singly as well as in a multistage configuration. Thus, the anomalous behavior observed with MS-1 has been clearly identified as being a peculiarity of the particular device. Possible reasons for this include one or more malfunctioning individual stages, and peculiarities in the overall design configuration, including possible saturation of early stages.

In the above discussion we have used the term “anomalous behavior” to indicate an observed discrepancy between measurements and predictions based on AM/AM and AM/PM characteristics. It is of interest to consider possible connections between predictable performance and optimal design. Kaye, George, and Eric have conjectured, but not proved, that, from the point of view of minimizing IM noise as a function of output power, the optimum nonlinear power amplifier has AM/AM characteristics that exhibit exact linearity up to the saturation level, with constant power output thereafter, and zero AM/PM conversion.<sup>3</sup> These characteristics are referred to as those of an Ideal Envelope Limiter (IEL). Reference 4 proves part of Kaye, George, and Eric’s conjecture, namely that AM/PM conversion can only degrade, never improve, IM performance for multicarrier input signals. Since, in practice, some degree of AM/PM conversion can be expected, it is of interest to investigate how the shape of the AM/PM characteristic affects the extent of the degradation.

For SSPA’s, the AM/PM measurements examined thus far indicate that the phase shifts at low power levels are relatively small (i.e., a few degrees), and increase very gradually up to saturation. At this point they abruptly begin to increase much more rapidly, reaching perhaps 25 to 30 degrees a few decibels above saturation; an example of such a characteristic is presented below. The larger and more rapidly increasing phase shifts at and above saturation, however, are less important to the overall IM performance than the phase shifts at lower power levels (e.g., ~6 to 10 dB back-off). This has been determined by calculating the IM performance of the SSPA with and without AM/PM conversion, which is easily done in the computer simulation. It is found near saturation that the AM/AM characteristic dominates the IM production to the extent that the difference with and without AM/PM conversion is of the order of 1 dB or less. On the other hand, for low power levels, because the AM/AM characteristic seen by the signal is effectively much more linear, relatively small

phase variations can make a very significant difference in IM performance—up to 6 dB is observed here. This indicates that, assuming that some degree of AM/PM conversion cannot be avoided, the design goal would be to have it as small as possible below saturation, while in the vicinity of saturation and above, much greater leeway in the shape of the characteristics could be tolerated. This could be of practical significance in the design of networks for compensating for AM/PM conversion. That is, the results indicate that it is more important to compensate for the small, slowly varying phase shifts below saturation than for the large, rapidly varying phase shifts at and above saturation, where the compensation is presumably more difficult and where requirements on the performance of phase-compensation networks could be relaxed with little degradation in IM performance.

With regard to the ideal AM/AM characteristics, to date no violations or counter examples to Kaye, George, and Eric's conjecture seem to have been found. AM/PM conversion has no effect on input/output total power-transfer characteristics.<sup>4</sup> Furthermore, based on comparisons of measurements with eq. (6), below, it is found that, excluding anomalous cases, SSPAs exhibit power-transfer characteristics that are nearly identical to those of an IEL, which under Kaye, George, and Eric's conjecture can be considered optimal. Thus, it should be possible for the AM/PM to be adjusted or compensated as necessary for minimum IM noise without affecting or sacrificing ideal power-transfer efficiency. With the use of eq. (6), a simple analytical criterion is developed for evaluating the extent to which SSPA wideband power-transfer measurements meet this ideal performance.

Section II summarizes the analytical results relevant to this work, including the optimal power-transfer characteristics of an IEL. Section III describes the computer simulation, Section IV compares measurements and calculations, and a summary of results and conclusions is presented in Section V.

## II. SUMMARY OF ANALYTICAL RESULTS

The multicarrier signals of interest here can, to a very good approximation, be represented as bandpass Gaussian noise in the form

$$n(t) = x(t)\cos \omega_0 t + y(t)\sin \omega_0 t, \quad (1)$$

where  $\omega_0$  is the filter center frequency. Equation (1) is the narrowband representation of Gaussian noise, in which the low-pass functions  $x(t)$  and  $y(t)$  are required to be slowly varying with respect to  $\omega_0$ . In the cases of interest (e.g., satellite communications), the bandwidth of  $x(t)$  and  $y(t)$  is nominally 40 MHz and  $f_0$  is 4 GHz, satisfying this requirement by a very large margin. Equation (1) can also be written as

$$n(t) = r(t)\cos(\omega_0 t + \theta(t)), \quad (2)$$

where  $r(t) = (x^2(t) + y^2(t))^{1/2}$  is the envelope, and  $\theta(t) = \tan^{-1}y(t)/x(t)$  is the phase. Since  $x(t)$  and  $y(t)$  are Gaussian,  $r(t)$  has a Rayleigh distribution:

$$\frac{r}{\sigma^2} e^{-r^2/2\sigma^2}, \quad (3)$$

where  $\sigma^2 = E(x^2(t)) = E(y^2(t))$  is the input-signal power.

The output of the nonlinearity will include an infinite number of harmonics of  $\omega_0$ . We are interested only in the principal zone, including only the first harmonic and a neighboring frequency range sufficiently wide to encompass all the IM noise produced ( $\sim 200$  MHz) (see Section III). For an instantaneous system, the principal-zone output can be written as:

$$A(r)\cos(\omega_0 t + \theta(t) + v(r)), \quad (4)$$

where  $A(r)$  and  $v(r)$  vary in time as  $r(t)$ , and, as functions of  $r$ , represent the AM/AM and AM/PM characteristics of the nonlinearity.

As Ref. 4 shows, the total output power in the principal zone is just  $1/2\langle A^2(r) \rangle$ , independent of  $v(r)$ . For all the SSPAs studied, the AM/AM characteristics very closely resemble those of an IEL and excluding anomalous cases, the power-transfer characteristics are also found to be essentially identical to those of an IEL. To calculate the output power for an IEL, referring to Fig. 1 we write:

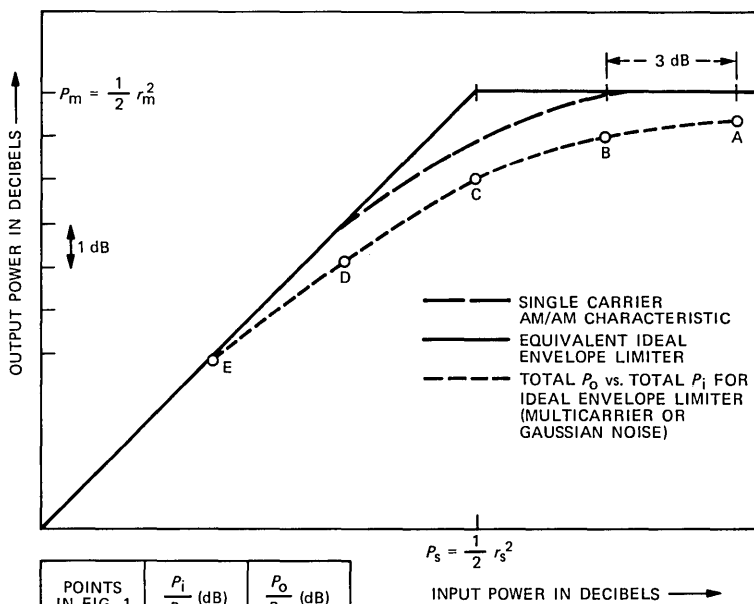
$$E\left(\frac{1}{2}A^2(r)\right) = \int_{r \leq r_s} E(A^2(r)/2)P(r)dr + \int_{r > r_s} E(A^2(r)/2)P(r)dr, \quad (5)$$

where  $r_s$  is the value of the input envelope  $r$  necessary to drive the limiter into saturation and  $P(r)$  is given by (3). In the saturated region,  $r > r_s$ , we have  $A(r) = r_m$ , the maximum saturated value of the output envelope, and in the linear region,  $r \leq r_s$ , we have  $A(r) = kr$ , where the constant  $k$  is  $r_m/r_s$ . Under these conditions the integrals in (5) are easily evaluated and, denoting the output power,  $1/2\langle A^2(r) \rangle$ , as  $P_0$ , and  $P_s = 1/2r_s^2$ ,  $P_m = 1/2r_m^2$ , it is found that

$$P_0 = P_m \frac{1 - e^{-P_s/P_i}}{P_s/P_i}, \quad (6)$$

where in (6) we have redesignated the input power as  $P_i$ .

Equation (6) provides a convenient means for quickly evaluating SSPA wideband power-transfer measurements in order to determine whether the device is performing as it should. As diagramed in Fig. 1, the IEL equivalent to a given SSPA is defined by extending the linear and saturated portions of the AM/AM characteristic to the point of



| POINTS IN FIG. 1 | $\frac{P_i}{P_s}$ (dB) | $\frac{P_o}{P_m}$ (dB) |
|------------------|------------------------|------------------------|
| A                | +6                     | -0.53                  |
| B                | +3                     | -1.04                  |
| C                | 0                      | -1.99                  |
| D                | -3                     | -3.64                  |
| E                | -6                     | -6.01                  |

Fig. 1—SSPA AM/AM characteristics with equivalent IEL and IEL power-transfer characteristics.

intersection that defines  $P_s$  and  $P_m$ . Using these values of  $P_s$  and  $P_m$ , the theoretically correct values of  $P_0$  as given by (6) can be easily plotted by noting that, starting with a value of  $P_i$  6 dB above  $P_s$  and stepping down in 3-dB increments to 6 dB below  $P_s$ , the corresponding values of output power are very nearly 0.5, 1, 2, 3.6, and 6 dB below  $P_m$ ; the exact values are given in the table insert in Fig. 1. Using this method, measurements of power-transfer characteristics for a number of SSPAs are compared in Section IV to theoretical values and found to be in almost exact agreement, which demonstrates the usefulness of this approach. It should be noted that this method is not valid for traveling-wave tubes, which do not have IEL-like AM/AM characteristics.

### III. COMPUTER SIMULATION

Figure 2 presents a block diagram of the computer simulation used in these analyses, and Ref. 1 gives a description of the calculation

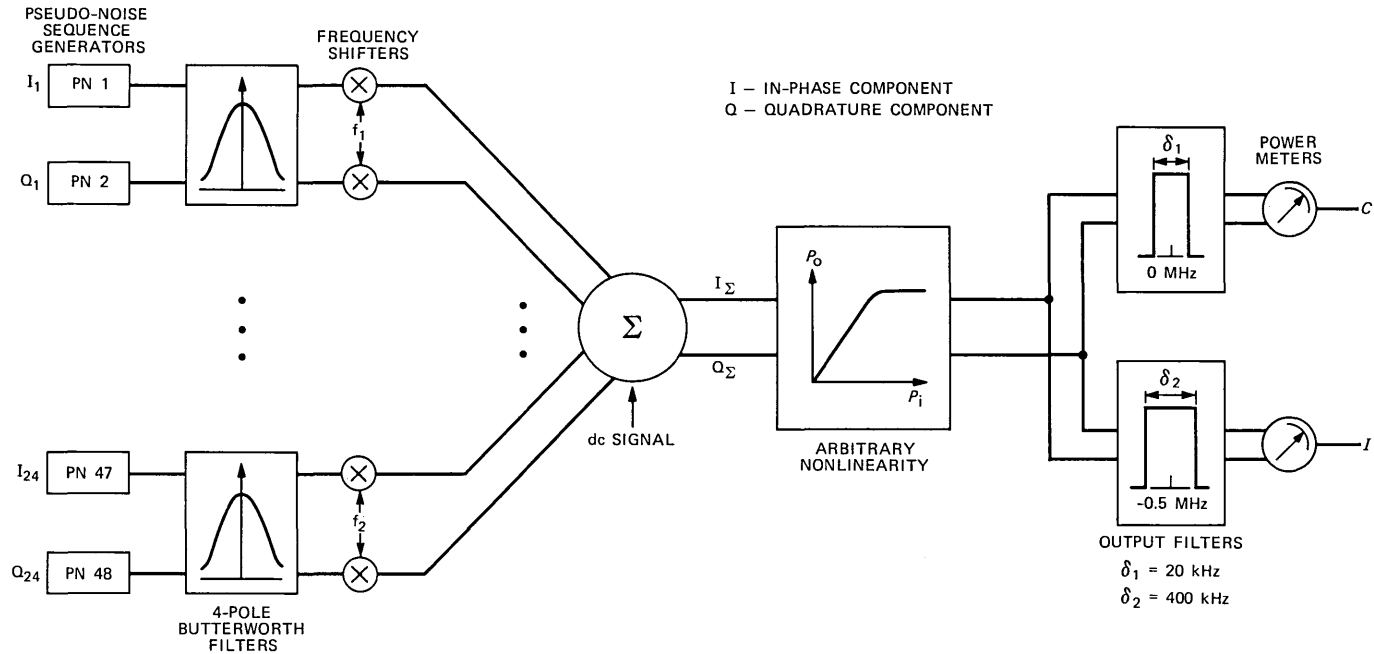


Fig. 2—Block diagram of simulation.

procedures. In the laboratory measurements, the input waveform consisted of 24 equal-power, filtered, Quadrature Phase-Shift Keying (QPSK) signals spaced on either side of an unmodulated carrier at band center (4 GHz) by the frequency increments shown in Table I (from Ref. 2). The power in the unmodulated tone was adjusted at the input to be equal to that of a single QPSK signal.

In simulating this waveform, a complex baseband formulation was employed. The simulated input consists of the outputs of 48 (24 pairs of) independent, equal-power, Pseudo-Noise (PN) sequence generators. The outputs of each pair of generators are formed into a complex number, which, in the baseband formulation, represents a QPSK signal, with the real part representing the in-phase component and the imaginary part, the quadrature component. Each QPSK signal is then passed through a four-pole Butterworth filter with a 3-dB (positive-frequency) bandwidth of 0.5 MHz. This is essentially the same filtering employed at the output of each QPSK signal generator in the 24-channel laboratory test set. The pulse duration employed in the simulation is 1.3  $\mu$ s, corresponding to  $0.772 \times 10^6$  symbols/s, or a DS-1 rate of  $1.544 \times 10^6$  bits/s.

After filtering, each QPSK signal is shifted in frequency on either side of zero by the same increments used in the measurements (see Table I). The 4-GHz carrier in the laboratory measurements is represented in the simulation by a dc signal adjusted in power to be equal at the input to a single QPSK signal. The spectrum of the input signal employed in the simulation is shown in Fig. 3.

This signal is then input to the nonlinear system under consideration. The nonlinearity is specified by entering tables of the measured AM/AM and AM/PM values into the program to which the simulation fits continuous curves. An example of the spectrum at the output of the nonlinearity, for input power in the vicinity of saturation, is presented in Fig. 4. For evaluating IM performance, the laboratory

Table I—Frequencies used in simulation

| Channel | Frequencies (MHz) | Channel | Frequencies (MHz) |
|---------|-------------------|---------|-------------------|
| -12     | -16.65            | 1       | 1.40              |
| -11     | -15.33            | 2       | 2.70              |
| -10     | -14.03            | 3       | 4.03              |
| -9      | -12.70            | 4       | 5.33              |
| -8      | -11.40            | 5       | 6.63              |
| -7      | -9.35             | 6       | 7.95              |
| -6      | -8.05             | 7       | 9.25              |
| -5      | -6.73             | 8       | 11.30             |
| -4      | -5.43             | 9       | 12.60             |
| -3      | -4.13             | 10      | 13.93             |
| -2      | -2.80             | 11      | 15.23             |
| -1      | -1.50             | 12      | 16.55             |
| 0       | 0                 |         |                   |

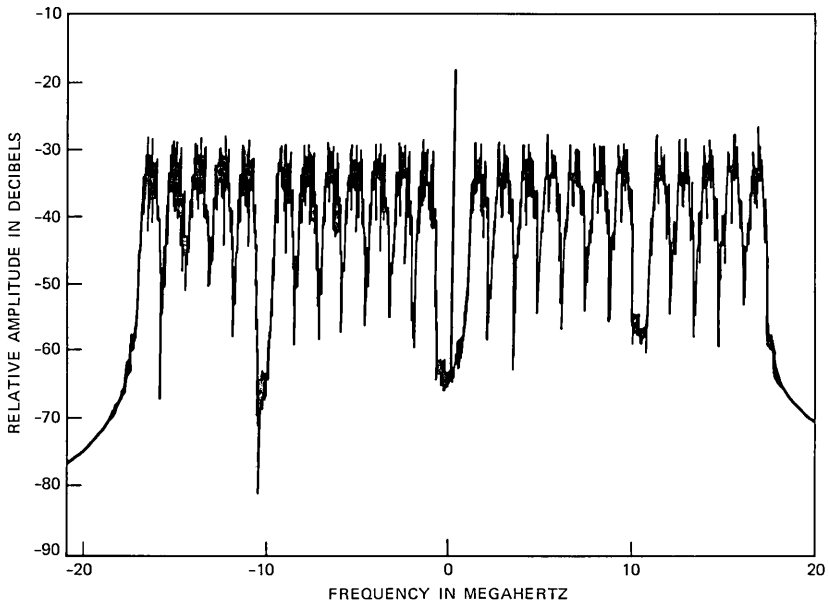


Fig. 3—Input signal spectrum showing 24 T-1 signal plus unmodulated tone at band center.

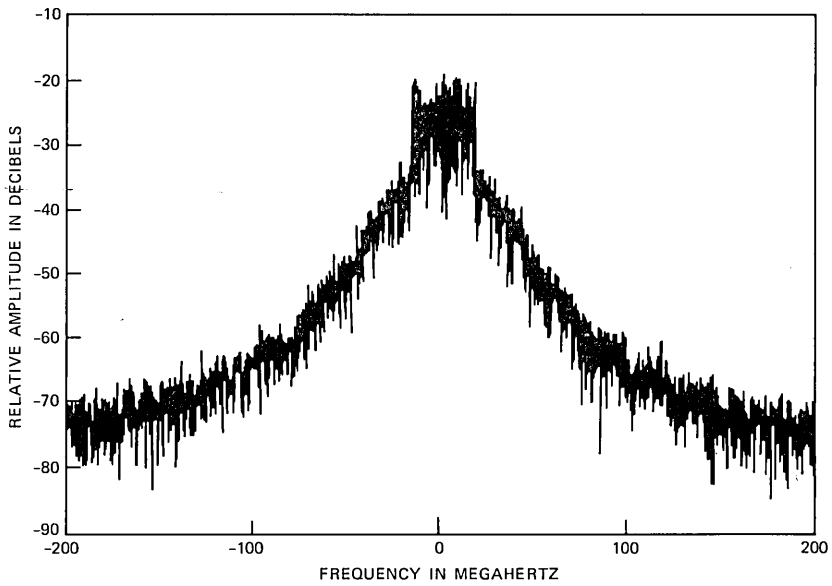


Fig. 4—MS-2 output spectrum with amplifier saturated.

measurements employed a narrowband filter in the notch at 4-GHz for measuring the output unmodulated carrier power, and a number of narrowband filters located in the notch between the 4-GHz carrier and the neighboring QPSK signals for measuring IM power; the individual IM-power measurements were averaged. Correspondingly, the simulation employs a narrowband filter at zero frequency for measuring unmodulated output dc power, and a filter for measuring IM power centered between zero and  $-1.5$  MHz.

For determining power-transfer characteristics, the total output power, including all the IM as well as signal power, is the measured quantity. Figure 4 shows that the saturated output power becomes negligible outside of  $\pm 100$  MHz, indicating that terms higher than fifth order are negligible in describing the nonlinearity. In any case, we are safe in assuming that a filter bandwidth of, say, 200 MHz will be sufficient for measuring total output power. This procedure was followed in the computer calculations and in the laboratory measurements in which the bandwidth of the detector used to measure total output power was nominally 300 MHz.

#### IV. COMPARISONS OF MEASUREMENTS AND CALCULATIONS

In plotting the laboratory data, the procedure adopted was to normalize the measurement by dividing the average measured IM power by the noise bandwidth of the filter, thereby obtaining IM power per 1-Hz frequency interval. Denoting this as  $I$  and the output unmodulated carrier power as  $C$ , the results were plotted as  $C/I$ , in dB-Hz, vs. output power, in dBm. In practice, the quantity of interest is the ratio of signal power to IM power in any given band,  $S/N_{\text{IM}}$ . Since the signal and IM spectra are essentially flat, this is equal to the ratio of the signal and IM spectral densities, and for a large number of equal-power carriers equally spaced by  $\Delta$ Hz we have:

$$\frac{S}{N_{\text{IM}}} = \frac{C}{I\Delta} \quad (7)$$

For these data, eq. (7) can be used with  $\Delta$  set equal to the nominal intercarrier spacing of 1.5 MHz.

Results of the computer calculations are also plotted in terms of  $C/I$ . In measuring IM power, an eight-pole Butterworth filter with 400 kHz, 3-dB bandwidth was used; the measured noise bandwidth in this case was 420 kHz. The bandwidth was chosen to be as wide as possible, in order to allow for averaging, and also to be able to fit into the notch in between the unmodulated dc tone and the QPSK signal at  $-1.5$  MHz. In measuring the power in the dc tone at the output of the nonlinearity, an eight-pole Butterworth filter with a 20-kHz, 3-dB bandwidth was used, which was similar to that used in the laboratory

measurements. The following subsections discuss the results for the different devices studied.

#### 4.1 Single-stage SSPA, SS-1

This single-stage SSPA used the same transistor as that used in the multistage MS-1 and MS-2 SSPAs. In this case, AM/PM characteristics for the particular amplifier that was studied were not available. A set of AM/PM characteristics typical of this type of single-stage amplifier is presented in Fig. 5, in which the phase shifts are seen to be very small. For this reason, as will be seen, unavailability of the exact set of AM/PM characteristics for this device had a negligible effect on the results. Calculations of  $C/I$  vs. output power are presented in Fig. 6 along with the measured values. For the three largest values of output power, which correspond to input saturation, 3- and 6-dB input back-off ( $\sim 35$ -,  $\sim 34$ -, and  $\sim 32$ -dBm output power), the calculated values differ from the measurements by the order of tenths of a dB. For the lowest point—13-dB input back-off,  $\sim 26$ -dBm output power—the measurement included significant thermal noise, which contributed to the difference of 2.5 dB from the calculated value. For the point at 10-dB input back-off (29-dBm output power), the difference is 1.5 dB, which may also include some nonnegligible effects of thermal noise.

In considering  $C/I$  performance, it is of interest to determine how much of the IM noise is due to AM/PM conversion, which is easily done in the simulation by setting AM/PM equal to zero. In this case

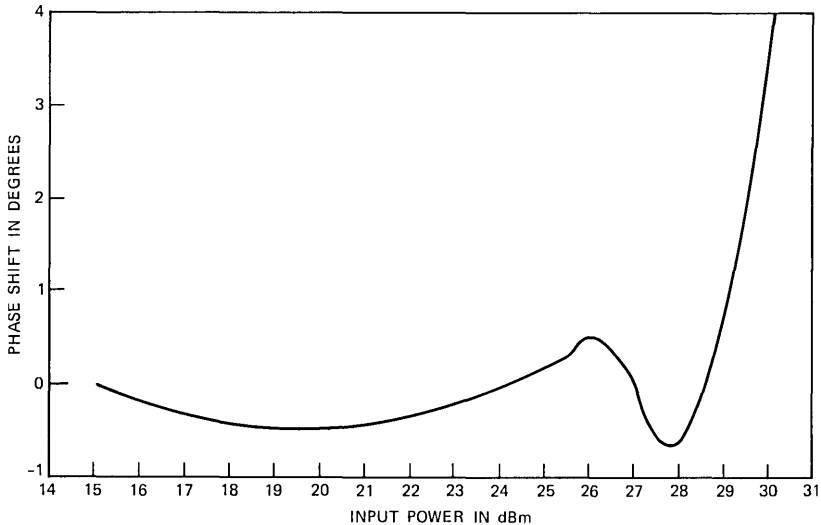


Fig. 5—Typical AM/PM characteristics for single-stage SSPA.

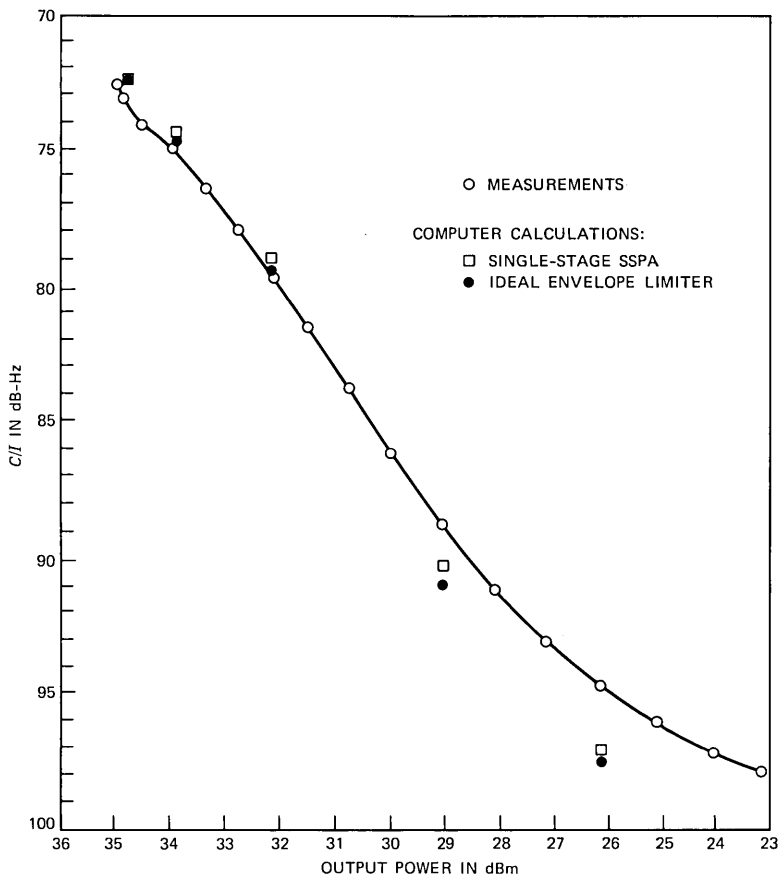


Fig. 6— $C/I$  for single-stage SSPA.

the AM/AM characteristics were modeled as those of the equivalent IEL, which is a very good approximation. The results for the IEL are also presented in Fig. 6 and seen to be only slightly different from those of the single-stage SSPA *with* AM/PM conversion, which demonstrates that phase shifts of the magnitude of those in Fig. 5, below saturation, are essentially negligible, and that the sharp increase in slope and larger phase values at and above saturation are also negligible in comparison with the effect of the saturating AM/AM characteristic.

The AM/AM characteristics used in the calculation of  $C/I$  in Fig. 6 are presented in Fig. 7, along with measurements and calculations of total power in vs. power out, and a plot of (6). The computer calculations are seen to fall exactly on the curve of measured values, with the exception of the point at saturation where the difference is  $\sim 0.2$  dB.

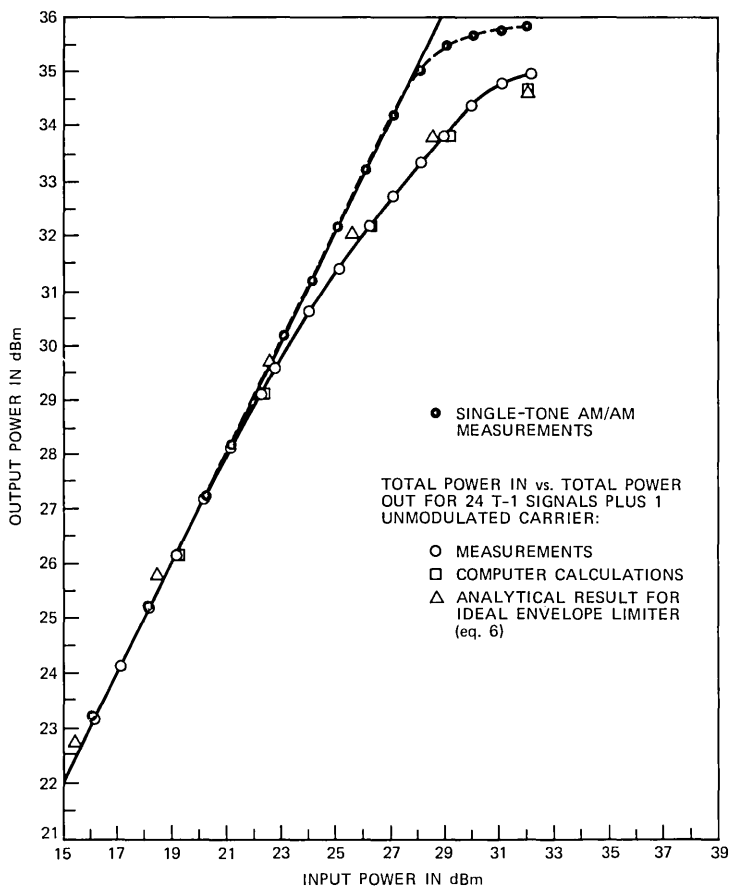


Fig. 7—AM/AM measurements and total power-transfer characteristics for single-stage SSPA.

The IEL power-transfer characteristics of (6) are also seen to be within tenths of a decibel of the measurements and the computer calculations.

#### 4.2 Multistage SSPA, MS-2

Figure 8 presents calculated and measured values of  $C/I$ . For input saturation, 3-dB input back-off and 6-dB input back-off (~36-, ~35-, and ~34-dBm output power), the differences are fractions of a decibel. The largest difference is at 10-dB input back-off (~31-dBm output power), where the difference is ~1 dB. In this case the thermal noise in the measurements was negligible, as evidenced by the falloff in  $C/I$  below ~27-dBm output power. The computer calculations have

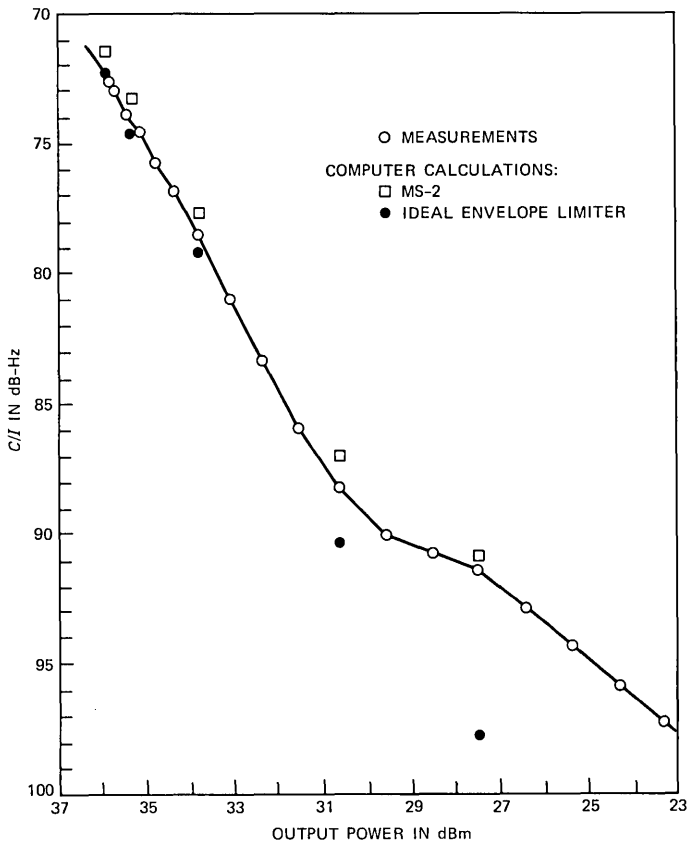


Fig. 8— $C/I$  for MS-2.

reproduced the irregular shape of the measured  $C/I$  curve in this region.

The source of this irregular shape was determined to be the somewhat irregular AM/PM characteristics for MS-2 shown in Fig. 9. As shown, the phase shift increases and then decreases somewhat in between  $-27$ - and  $-21$ -dBm input power. When the AM/PM was set equal to zero, the flattening in the  $C/I$  curve between 31 and 27 dBm output power disappeared, as shown by the equivalent IEL results in Fig. 8.

We also note that although the phase shifts are largest and vary most rapidly near and above saturation ( $\sim -22$ -dBm input power,  $\sim 37$ -dBm output power) (see Fig. 10), their effect on production of IM noise in Fig. 8 is of the order of 1 dB or less. However, although the phase shifts are much smaller and slower varying for low power levels, the differences between the  $C/I$  values for MS-2 with AM/PM

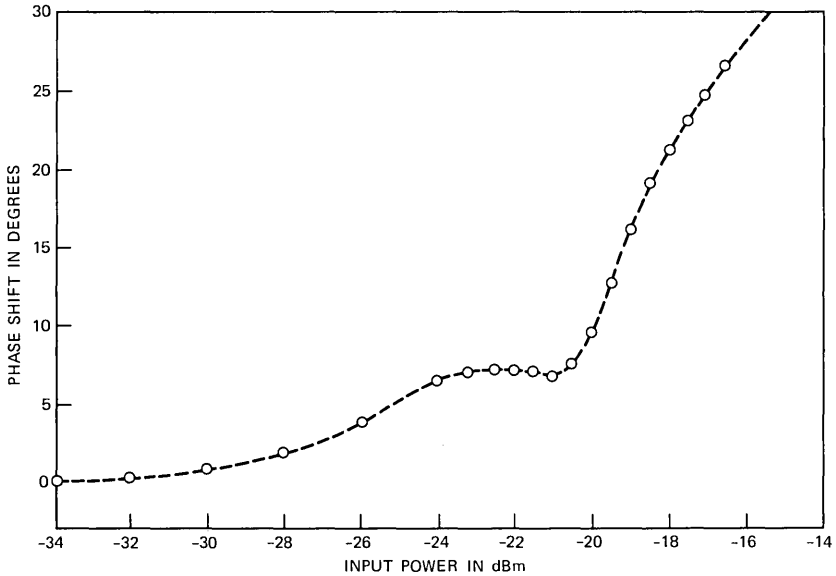


Fig. 9—AM/PM measurements for MS-2.

and the equivalent IEL, with zero AM/PM, are much larger (e.g.,  $\sim 6$  dB at  $\sim 27.5$ -dBm output power). The reasons for this, in terms of the relative importance of the AM/AM and AM/PM characteristics as a function of input power level, and the implications in terms of SSPA design and AM/PM compensation, have been discussed in Section I.

The AM/AM characteristics for MS-2 are presented in Fig. 10, along with measurements and calculations of total power in vs. power out and a plot of (6). As for the single-stage SSPA, the differences between measurements, computer simulation results, and results based on (6) are negligible. It is of interest to note that the slope of the AM/AM characteristics differs slightly from strict linearity in the gain-expansion region near saturation, which evidently has a negligible effect.

For the remaining three multistage SSPAs that were studied, AM/PM measurements were not available and  $C/I$  calculations not possible. The comparisons were therefore restricted to total power in vs. power out. In these cases the laboratory measurements were compared with calculated values using the five-point approximation method discussed at the end of Section II. Differences between calculated and measured values were found to be negligible; in the interest of brevity, plots of these results are not presented. For convenience we present in Fig. 11 the earlier result for MS-1 from Ref. 1, showing

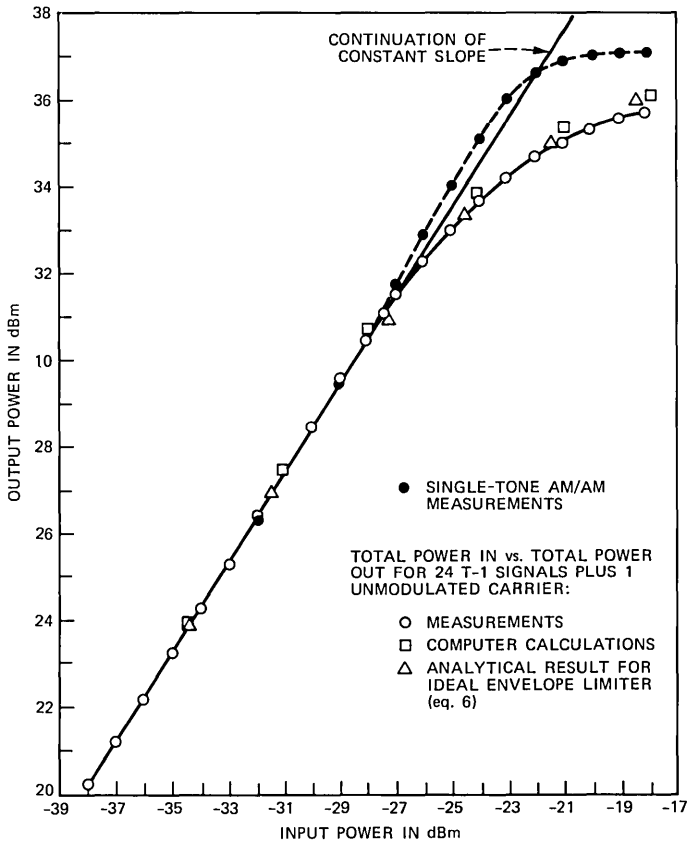


Fig. 10—AM/AM measurements and total power-transfer characteristics for MS-2.

the significant discrepancy between calculated and measured power-transfer characteristics. The significant body of data in which almost exact agreement between measurements and calculations has been obtained clearly indicates that the MS-1 device represents an anomalous case.

### V. SUMMARY AND CONCLUSIONS

A number of SSPAs have been studied, for which very good agreement has been observed between calculated and measured wideband power-transfer characteristics and IM noise performance. The calculations include results of a computer simulation developed for this purpose, with which any arbitrary input signal and any set of operating conditions can be investigated, and an analytical result that describes the wideband power-transfer characteristics of typical SSPAs. In all

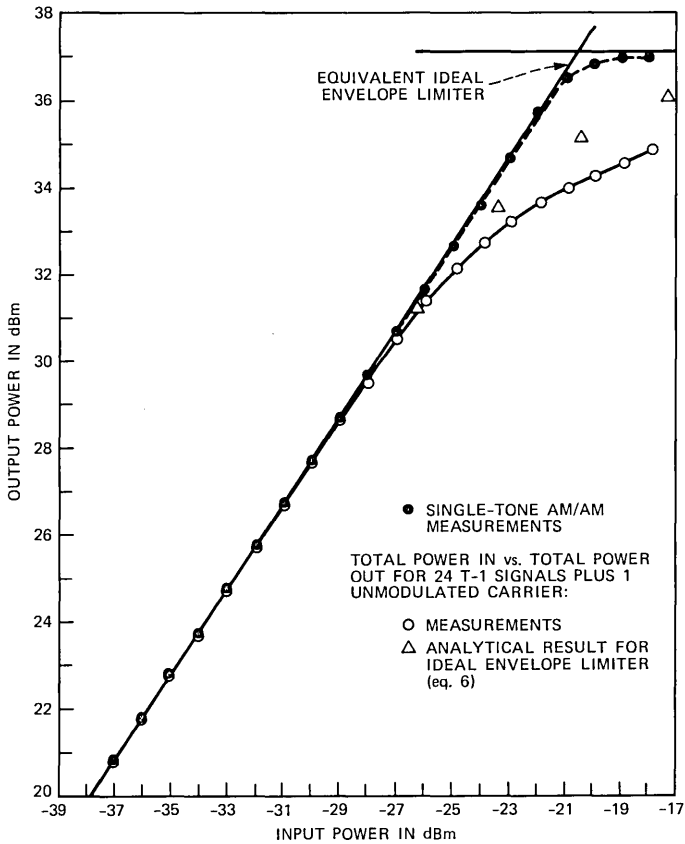


Fig. 11—AM/AM measurements and total power-transfer characteristics for MS-1, showing power-transfer anomaly.

these calculations, the devices are characterized by their measured AM/AM and AM/PM characteristics; for power-transfer calculations AM/PM is, of course, irrelevant.

The number of cases in which agreement has been obtained demonstrates the usefulness of calculations of this kind as means for predicting the performance of nonlinear power amplifiers, as well as for providing a tool with which possible anomalous behavior can be identified. Such behavior, in which the single-tone AM/AM and AM/PM measurements are not sufficient for characterizing the operation of the amplifier under wideband excitation, which can result in severe performance degradation, can, in the case of power-transfer anomalies, be identified by comparing measured data with results predicted by (6). An example of anomalous behavior, in which a

significant degradation in power-transfer efficiency was identified by means of comparison with theoretical predictions, has been discussed.

SSPAs in nonanomalous cases have been shown to generally exhibit power-transfer characteristics essentially identical to those of an ideal envelope limiter which, under the conjecture of Kaye, George, and Eric, are optimal. Part of Kaye, George, and Eric's conjecture has been proved; namely, that AM/PM conversion can only degrade, never improve, IM performance. It has been shown that degradation due to AM/PM conversion is significantly more severe at low power levels than in the vicinity of saturation where, based on available AM/PM measurement data, the phase shifts are much larger and more rapidly varying; the reasons for this have been discussed. This could be of practical importance in the design of compensation networks for AM/PM conversion, since requirements on network performance at saturating power levels could be relaxed with little degradation in IM performance.

Power-transfer characteristics are independent of AM/PM conversion. Ideally, this independence could permit the AM/PM characteristics to be adjusted or compensated to maximize IM performance without sacrificing ideal power-transfer efficiency. Using an analytical expression for power transfer in an IEL, a simple criterion has been developed for evaluating measurements to determine whether ideal power-transfer efficiency has been achieved.

## VI. ACKNOWLEDGMENT

I would like to thank R. Standley for numerous helpful discussions related to these data and measurements.

## REFERENCES

1. J. B. Minkoff, "Intermodulation Noise in Solid-State Power Amplifiers for Wideband Signal Transmission," Proc. of AIAA 9th Communications Satellite System Conference, March 1982.
2. R. Standley, private communication.
3. A. R. Kay, L. A. George, and M. J. Eric, "Analysis and Compensation of Bandpass Nonlinearities for Communications," *IEEE Trans. Commun.* (October 1972), pp. 965-72.
4. J. B. Minkoff, "The Role of AM/PM Conversion in Memoryless Nonlinear Systems," Proc. of Globecom '83, San Diego, CA, November 1983.

## AUTHOR

**John B. Minkoff**, B.S., M.S., and Ph.D. (Electrical Engineering), Columbia University, 1962, 1963, and 1967, respectively; Columbia University Electronics Research Laboratories, 1964-1977; AT&T Bell Laboratories, 1977—. At the Columbia University Electronics Research Laboratories (which became Riverside Research Institute in December 1967), Mr. Minkoff worked in the fields of electro-optical and radar systems, and ionospheric radar and radio-frequency phenomena. From 1977 to 1983 he was in the Satellite Transmission Laboratory at AT&T Bell Laboratories. He is currently in the Military Systems Division.

## Conditional Variable-Length Coding for Gray-Level Pictures

H. GHARAVI\*

(Manuscript received May 25, 1983)

This paper presents a new variable-length coding algorithm for bit-rate reduction of digital images. The coding scheme is based on the fact that by taking into account the local conditional statistics of the picture, the coding efficiency can be improved considerably. Results of computer simulations are presented in terms of picture quality and required bit rate. Simulations show that for various Differential Pulse Code Modulation (DPCM) coded pictures, coding efficiency is such that a bit rate below the entropy of the DPCM quantizer output is attained. For a 3-bit DPCM encoded picture, a bit rate of 1.64 bits/picture element is achieved.

### I. INTRODUCTION

Two popular methods for reducing bit rates of pictures are Differential Pulse Code Modulation (DPCM)<sup>1</sup> and transform coding.<sup>2</sup> When these methods are applied, their reconstructed signals are not exactly the same as the original Pulse Code Modulation (PCM) input because of the quantization noise. Consequently, these encoders are often referred to as nonreversible encoders. Bit-rate reduction can also be achieved by reversible encoders. These methods are based on the fact that it is not necessary to assign an equal number of bits to quantized samples that are not equiprobable. Therefore, it may be advantageous to design variable-length code words in which the length of the code

---

\*AT&T Bell Laboratories; present affiliation Bell Communications Research, Inc.

---

Copyright © 1984 AT&T. Photo reproduction for noncommercial use is permitted without payment of royalty provided that each reproduction is done without alteration and that the Journal reference and copyright notice are included on the first page. The title and abstract, but no other portions, of this paper may be copied or distributed royalty free by computer-based and other information-service systems without further permission. Permission to reproduce or republish any other portion of this paper must be obtained from the Editor.

words are matched to the Probability Distribution Function (PDF) of the source by using very simple procedures. One such procedure has been devised by Shannon<sup>3</sup> and Fano and another by Huffman.<sup>4</sup> Another reversible coding method is run-length coding, in which a sequence of identical symbols is replaced by a code indicating the length and symbol of the sequence. Run-length codes are useful whenever the long runs are highly probable. This method has been widely used for compression of bilevel pictures.<sup>5</sup>

With the above-mentioned reversible coding methods, the entropy obtained from the PDF of a digital image gives a target for the minimum bit rate necessary to describe the source, ignoring the conditional statistics of the picture. If, by some efficient scheme, conditional statistics can be considered, it may be possible to lower this target to a figure that can be described by conditional entropy. One such method has recently been devised by Gharavi et al. for encoding the gray-level pictures using CCITT one-dimensional run-length codes.<sup>6</sup> In this scheme the run-length statistics of the picture are changed in such a way as to provide a signal that has long bit runs.

In this paper we introduce a similar strategy by developing a scheme in which the picture can be directly coded by the variable-length codes. The code words are designed according to the local conditional statistics of the picture using the Huffman procedure. For example, the picture element (pel) values that are expected to occur most frequently, given the local PDF, are assigned to the shortest code words in accordance. The mathematical model and the details of the coding algorithm are given in the following section.

## II. BASIC MODEL

The  $n$ -bit PCM coded picture can be described mathematically as a random sequence of  $2^n$  possible outcomes with certain statistical properties, which are given in terms of probabilities. From these probabilities we can calculate the entropy of one pel, which represents a lowest theoretical bound for the one-dimensional memoryless model. The entropy of pictures can be presented as:

$$H_{\text{pel}} = - \sum_{i=1}^{2^n} P_i \text{Log}_2 P_i,$$

where  $P_i$  is the probability of the  $i$ th outcome ( $i$ th level). In the case of an  $m$ th-order Markov model, the luminance level of each pel,  $x_i$ , is considered to be dependent on the level of  $m$  previous surrounding pels. Therefore, the conditional entropy based on the  $m$  previous elements is given by:

$$H_c = - \sum_{x_{i-m}}^{2^n} \cdots \sum_{x_{i-1}}^{2^n} \sum_{x_i}^{2^n} P(x_{i-m}x_{i-m-1} \cdots x_i) \cdot \text{Log}_2 P(x_i/x_{i-1}, x_{i-2} \cdots x_{i-m}), \quad (1)$$

where  $P(x_{i-m}x_{i-m-1} \cdots x_i)$  is the joint probability of  $x_i \cdots x_{i-m}$  and  $P(x_i/x_{i-1}, x_{i-1} \cdots x_{i-m})$  is the conditional probability of  $x_i$ , given  $m$  previous pels  $x_{i-1}, x_{i-2} \cdots x_{i-m}$ . Equation (1) can be rewritten as

$$H_c = - \sum_{x_{i-m}}^{2^n} \cdots \sum_{x_{i-1}}^{2^n} P(x_{i-m}, x_{i-m-1} \cdots x_{i-1}) \cdot \sum_{x_i}^{2^n} P(x_i/x_{i-1}, x_{i-2} \cdots x_{i-m}) \text{Log}_2 P(x_i/x_{i-1}, x_{i-2} \cdots x_{i-m}) \quad (2)$$

and, on defining  $H_L$  as a local entropy,

$$H_L = - \sum_{x_i}^{2^n} P(x_i/x_{i-1}, x_{i-2} \cdots x_{i-m}) \text{Log}_2 P(x_i/x_{i-1}, \cdots x_{i-m}). \quad (3)$$

We express the conditional entropy as

$$H_c = \sum \sum \cdots \sum P(x_{i-m}, x_{i-m-1} \cdots x_{i-1}) H_L. \quad (4)$$

Equation (4) shows that the conditional entropy depends not only on the local entropy but also on its distribution over  $(2^n)^m$  independent states. This model leads to the new coding scheme proposed here.

### 2.1 Coding algorithm

The first step is to use the  $m$  previous pels to construct a table of  $(2^n)^m$  independent states of picture statistics. For each state, a set of code words is designed according to the probability distribution of the  $2^n$  outcomes of the quantized values. These code words can be derived by employing optimum coding procedures, such as Huffman, or Shannon and Fano, in which a shorter code is assigned to a more probable level. Then, for a given state, each incoming pel is coded by selecting an appropriate code word corresponding to its quantized value.

## III. DPCM CODING

In the previous section it is apparent that the total number of states is heavily dependent on the number of quantization levels. For example, for input pictures of 256 levels corresponding to 8 bits/pel, there are  $256^m$  ( $m$  is the number of reference elements) states. This figure is rather high, and a simple reduction of the number of quantizing levels would lead to annoying contouring effects. Thus, to convert an 8-bit picture into fewer bits while maintaining approximately the same

quantizer noise, a DPCM encoder is employed. In the DPCM encoder used here, a linear predictor constructs its predicted pel as the weighted summation of previous pels (see Fig. 1); thus

$$\bar{x} = 0.5A + 0.25(B + C), \quad (5)$$

where  $\bar{x}$  is the prediction of the present pel. The prediction error is then quantized by a symmetric seven-level quantizer with the transfer characteristics given in Fig. 2. Applying the above coder to the  $512 \times 512$ , 8-bit/pel picture shown in Fig. 3 results in the seven-level DPCM coded picture shown in Fig. 4.

### 3.1 Subsampling and interpolation

Subsampling at a factor of 2:1 gives approximately a 2:1 bit-rate reduction. This results in some degradation of pictures, which can be minimized by an efficient interpolation scheme. Figure 5 shows the 2:1 horizontal subsampling pattern employed here. The interpolation is based on averaging the luminance levels of the four surrounding pels. The subsampled picture is DPCM encoded, in which the present pel  $D$  (see Fig. 5) is predicted by

$$\text{Prediction of } D = 0.3B + (C + F)0.35.$$

Figure 6 shows the interpolated picture where 2:1 subsampling was employed.

## IV. COMPUTER SIMULATIONS

Experiments were carried out by means of computer simulation. Figure 7 shows the transmitter and receiver block diagrams. In our

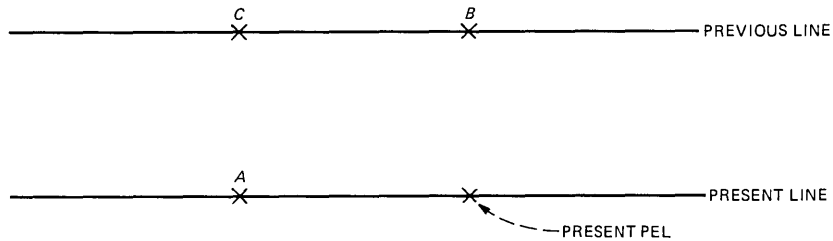


Fig. 1—Configuration of pels used for prediction.

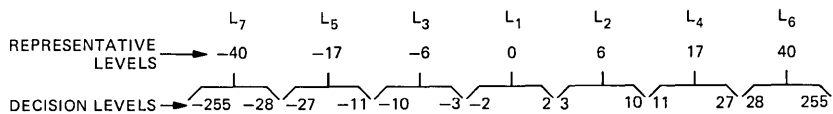


Fig. 2—Transfer characteristics of the quantizer.



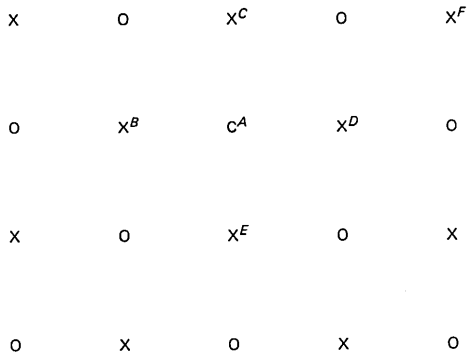
Fig. 3—Original picture.

simulation, for a set of seven-level DPCM coded pictures, tables of 49 and 343 states were constructed by observing the quantized values of two and three previous elements, respectively ( $A$ ,  $B$  and  $A$ ,  $B$ ,  $C$  of Fig. 8). As a matter of convenience only, the table of 49 states with the corresponding code words is shown in Table I. For each state, the seven code words are obtained from the probability distribution function of the seven outcomes, using the standard Huffman procedure.

As Fig. 7a shows, the input signal is first DPCM encoded to generate a 3-bit DPCM coded picture. The coded picture is then applied to the conditional variable coder, which uses the line and sample delay to represent the values of neighbors  $B$  and  $A$ , respectively. These values, along with current pel value, comprise the input for the encoder Look Up Table (LUT). The encoder LUT uses this information to give the bits of the appropriate variable-length code word, as shown in Table I. The output is smoothed by a buffer to allow for the uniform bit rate in the transmission channel. In the receiver, the transmitted variable-length code words are received from the channel and applied to a buffer and then to the decoder LUT (see Fig. 7b). The conditional variable-length decoder LUT also receives the decoded sample and line-delayed signals to represent the values of neighbors  $B$  and  $A$ , respectively. Based on this information, the decoder determines



Fig. 4—Three-bit DPCM coded picture.



X : SAMPLE SELECTED FOR TRANSMISSION  
 O : SAMPLE DROPPED

$$\text{INTERPOLATION OF } A = (B+C+D+E) / 4$$

Fig. 5—Subsampling pattern used for interpolation and prediction.

whether the current pel code word is the one expected to occur most frequently, second most frequently, and so on, as specified in Table I. The output of these is then applied to the DPCM decoder, which serves as the receiver output signal.



Fig. 6—Subsampled and interpolated picture.

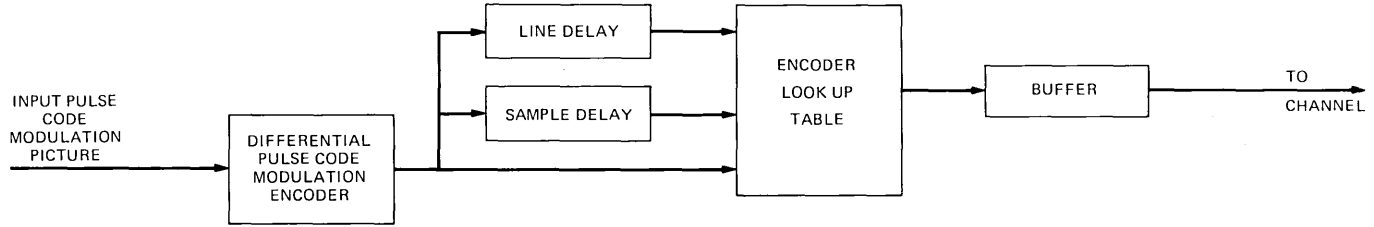
#### 4.1 Results

Table II presents the bit-rate results of the variable-length encoder with the corresponding entropies and conditional entropies. The results of variable-length coding based on the statistics of the quantizer output (ignoring the conditional statistics) are also included in Table II as a reference.

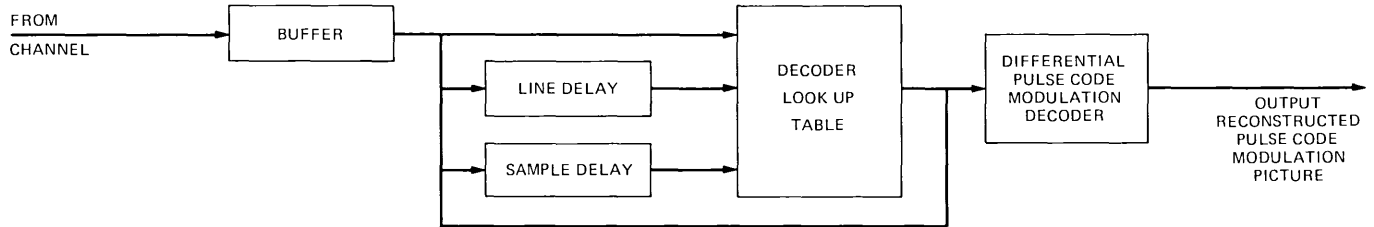
By looking at the tabulated results, it is clear that a considerable improvement is obtained by using this conditional variable-length algorithm compared with a nonconditional variable-length encoder. An even better improvement is obtained by increasing the number of reference elements from two to three (third row of Table II) at the expense of complexity, as the number of states is increased from 49 to 343. In the case of 2:1 subsampling, a 2:1 bit-rate reduction is unobtainable. This is due to the lower spatial correlation as a result of an increased distance between neighboring pels, as compared to a non-subsampled case. However, the most important conclusion from Table II is that bit rates below the entropy of the DPCM quantizer output are achievable.

#### V. CONCLUSION

A new concept for a variable-length coding scheme has been pre-



(a)



(b)

Fig. 7—Block diagram of (a) transmitter and (b) receiver.

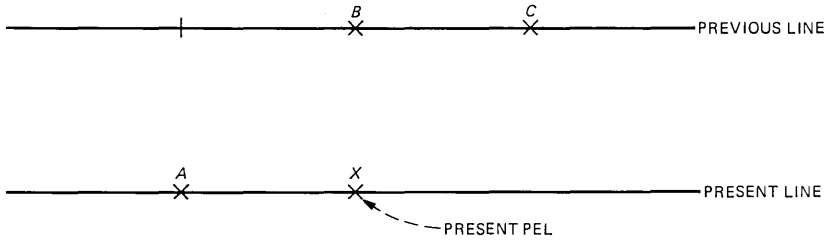


Fig. 8—Configuration of reference elements used for conditional variable-length coding.

Table 1—Table of variable-length code words

| State | Neighbors      |                | Code Words           |                       |                        |                         |                          |                          |                          |
|-------|----------------|----------------|----------------------|-----------------------|------------------------|-------------------------|--------------------------|--------------------------|--------------------------|
|       | A              | B              | L <sub>1</sub>       | L <sub>2</sub>        | L <sub>3</sub>         | L <sub>4</sub>          | L <sub>5</sub>           | L <sub>6</sub>           | L <sub>7</sub>           |
| 1     | L <sub>1</sub> | L <sub>1</sub> | L <sub>1</sub><br>1  | L <sub>2</sub><br>01  | L <sub>3</sub><br>001  | L <sub>4</sub><br>00001 | L <sub>5</sub><br>000001 | L <sub>6</sub><br>000001 | L <sub>7</sub><br>000000 |
| 2     | L <sub>1</sub> | L <sub>2</sub> | L <sub>1</sub><br>0  | L <sub>2</sub><br>11  | L <sub>3</sub><br>101  | L <sub>4</sub><br>1001  | L <sub>5</sub><br>10001  | L <sub>6</sub><br>100001 | L <sub>7</sub><br>100000 |
| 3     | L <sub>1</sub> | L <sub>3</sub> | L <sub>1</sub><br>0  | L <sub>3</sub><br>11  | L <sub>2</sub><br>101  | L <sub>5</sub><br>1001  | L <sub>4</sub><br>10001  | L <sub>6</sub><br>100001 | L <sub>7</sub><br>100000 |
| 4     | L <sub>1</sub> | L <sub>4</sub> | L <sub>2</sub><br>11 | L <sub>1</sub><br>10  | L <sub>4</sub><br>01   | L <sub>3</sub><br>001   | L <sub>7</sub><br>0001   | L <sub>5</sub><br>00001  | L <sub>6</sub><br>00000  |
| 5     | L <sub>1</sub> | L <sub>5</sub> | L <sub>3</sub><br>11 | L <sub>5</sub><br>10  | L <sub>1</sub><br>01   | L <sub>2</sub><br>001   | L <sub>6</sub><br>0001   | L <sub>4</sub><br>00001  | L <sub>7</sub><br>00000  |
| 6     | L <sub>1</sub> | L <sub>6</sub> | L <sub>5</sub><br>1  | L <sub>6</sub><br>01  | L <sub>3</sub><br>0011 | L <sub>2</sub><br>0010  | L <sub>7</sub><br>0000   | L <sub>1</sub><br>00011  | L <sub>4</sub><br>00010  |
| 7     | L <sub>1</sub> | L <sub>7</sub> | L <sub>7</sub><br>1  | L <sub>1</sub><br>01  | L <sub>2</sub><br>0011 | L <sub>6</sub><br>0010  | L <sub>5</sub><br>0000   | L <sub>3</sub><br>00011  | L <sub>4</sub><br>00010  |
| 8     | L <sub>2</sub> | L <sub>1</sub> | L <sub>1</sub><br>0  | L <sub>3</sub><br>11  | L <sub>2</sub><br>101  | L <sub>4</sub><br>1001  | L <sub>5</sub><br>10001  | L <sub>7</sub><br>100001 | L <sub>6</sub><br>100000 |
| 9     | L <sub>2</sub> | L <sub>2</sub> | L <sub>1</sub><br>0  | L <sub>2</sub><br>11  | L <sub>3</sub><br>101  | L <sub>4</sub><br>1001  | L <sub>5</sub><br>10001  | L <sub>7</sub><br>100001 | L <sub>6</sub><br>100000 |
| 10    | L <sub>2</sub> | L <sub>3</sub> | L <sub>3</sub><br>0  | L <sub>1</sub><br>11  | L <sub>2</sub><br>101  | L <sub>5</sub><br>1001  | L <sub>4</sub><br>10001  | L <sub>6</sub><br>100001 | L <sub>7</sub><br>100000 |
| 11    | L <sub>2</sub> | L <sub>4</sub> | L <sub>2</sub><br>11 | L <sub>4</sub><br>10  | L <sub>1</sub><br>01   | L <sub>3</sub><br>001   | L <sub>7</sub><br>0001   | L <sub>5</sub><br>00001  | L <sub>6</sub><br>00000  |
| 12    | L <sub>2</sub> | L <sub>5</sub> | L <sub>3</sub><br>11 | L <sub>5</sub><br>10  | L <sub>1</sub><br>01   | L <sub>2</sub><br>001   | L <sub>6</sub><br>0001   | L <sub>4</sub><br>00001  | L <sub>7</sub><br>00000  |
| 13    | L <sub>2</sub> | L <sub>6</sub> | L <sub>6</sub><br>0  | L <sub>5</sub><br>01  | L <sub>7</sub><br>0011 | L <sub>3</sub><br>0010  | L <sub>4</sub><br>0000   | L <sub>1</sub><br>0011   | L <sub>2</sub><br>00010  |
| 14    | L <sub>2</sub> | L <sub>7</sub> | L <sub>7</sub><br>0  | L <sub>4</sub><br>01  | L <sub>6</sub><br>0011 | L <sub>1</sub><br>0010  | L <sub>2</sub><br>0000   | L <sub>3</sub><br>0011   | L <sub>5</sub><br>00010  |
| 15    | L <sub>3</sub> | L <sub>1</sub> | L <sub>1</sub><br>0  | L <sub>2</sub><br>11  | L <sub>3</sub><br>101  | L <sub>4</sub><br>1001  | L <sub>5</sub><br>10001  | L <sub>6</sub><br>100001 | L <sub>7</sub><br>100000 |
| 16    | L <sub>3</sub> | L <sub>2</sub> | L <sub>1</sub><br>0  | L <sub>2</sub><br>11  | L <sub>3</sub><br>101  | L <sub>4</sub><br>1001  | L <sub>5</sub><br>10001  | L <sub>7</sub><br>100001 | L <sub>6</sub><br>100000 |
| 17    | L <sub>3</sub> | L <sub>3</sub> | L <sub>1</sub><br>0  | L <sub>3</sub><br>11  | L <sub>2</sub><br>101  | L <sub>5</sub><br>1001  | L <sub>4</sub><br>10001  | L <sub>6</sub><br>100001 | L <sub>7</sub><br>100000 |
| 18    | L <sub>3</sub> | L <sub>4</sub> | L <sub>2</sub><br>0  | L <sub>1</sub><br>11  | L <sub>4</sub><br>101  | L <sub>3</sub><br>1001  | L <sub>7</sub><br>10001  | L <sub>5</sub><br>100001 | L <sub>6</sub><br>100000 |
| 19    | L <sub>3</sub> | L <sub>5</sub> | L <sub>3</sub><br>11 | L <sub>1</sub><br>10  | L <sub>5</sub><br>01   | L <sub>2</sub><br>001   | L <sub>6</sub><br>0001   | L <sub>4</sub><br>00001  | L <sub>7</sub><br>00000  |
| 20    | L <sub>3</sub> | L <sub>6</sub> | L <sub>6</sub><br>0  | L <sub>5</sub><br>01  | L <sub>3</sub><br>0011 | L <sub>2</sub><br>0010  | L <sub>1</sub><br>0000   | L <sub>7</sub><br>00011  | L <sub>4</sub><br>00010  |
| 21    | L <sub>3</sub> | L <sub>7</sub> | L <sub>7</sub><br>0  | L <sub>6</sub><br>111 | L <sub>4</sub><br>110  | L <sub>2</sub><br>100   | L <sub>2</sub><br>1010   | L <sub>5</sub><br>10111  | L <sub>1</sub><br>10110  |

Table I—Continued

| State | Neighbors      |                | Code Words           |                       |                        |                         |                         |                          |                          |
|-------|----------------|----------------|----------------------|-----------------------|------------------------|-------------------------|-------------------------|--------------------------|--------------------------|
|       | A              | B              |                      |                       |                        |                         |                         |                          |                          |
| 22    | L <sub>4</sub> | L <sub>1</sub> | L <sub>3</sub><br>0  | L <sub>1</sub><br>11  | L <sub>2</sub><br>101  | L <sub>5</sub><br>1001  | L <sub>4</sub><br>10001 | L <sub>7</sub><br>100001 | L <sub>6</sub><br>100000 |
| 23    | L <sub>4</sub> | L <sub>2</sub> | L <sub>2</sub><br>11 | L <sub>1</sub><br>10  | L <sub>3</sub><br>01   | L <sub>4</sub><br>001   | L <sub>5</sub><br>0001  | L <sub>7</sub><br>00001  | L <sub>6</sub><br>00000  |
| 24    | L <sub>4</sub> | L <sub>3</sub> | L <sub>3</sub><br>0  | L <sub>1</sub><br>11  | L <sub>5</sub><br>101  | L <sub>2</sub><br>1001  | L <sub>4</sub><br>10001 | L <sub>7</sub><br>100001 | L <sub>6</sub><br>100000 |
| 25    | L <sub>4</sub> | L <sub>4</sub> | L <sub>4</sub><br>0  | L <sub>2</sub><br>11  | L <sub>1</sub><br>101  | L <sub>7</sub><br>1001  | L <sub>3</sub><br>10001 | L <sub>5</sub><br>100001 | L <sub>6</sub><br>100000 |
| 26    | L <sub>4</sub> | L <sub>5</sub> | L <sub>5</sub><br>0  | L <sub>3</sub><br>111 | L <sub>1</sub><br>110  | L <sub>2</sub><br>100   | L <sub>6</sub><br>1010  | L <sub>4</sub><br>10111  | L <sub>7</sub><br>10110  |
| 27    | L <sub>4</sub> | L <sub>6</sub> | L <sub>6</sub><br>11 | L <sub>7</sub><br>10  | L <sub>5</sub><br>01   | L <sub>4</sub><br>001   | L <sub>2</sub><br>0001  | L <sub>1</sub><br>00001  | L <sub>3</sub><br>00000  |
| 28    | L <sub>4</sub> | L <sub>7</sub> | L <sub>7</sub><br>0  | L <sub>4</sub><br>11  | L <sub>2</sub><br>101  | L <sub>3</sub><br>1001  | L <sub>6</sub><br>10001 | L <sub>1</sub><br>100001 | L <sub>5</sub><br>100000 |
| 29    | L <sub>5</sub> | L <sub>1</sub> | L <sub>2</sub><br>11 | L <sub>1</sub><br>10  | L <sub>3</sub><br>01   | L <sub>5</sub><br>001   | L <sub>4</sub><br>0001  | L <sub>6</sub><br>00001  | L <sub>7</sub><br>00000  |
| 30    | L <sub>5</sub> | L <sub>2</sub> | L <sub>2</sub><br>0  | L <sub>1</sub><br>111 | L <sub>4</sub><br>110  | L <sub>3</sub><br>100   | L <sub>5</sub><br>1010  | L <sub>6</sub><br>10111  | L <sub>7</sub><br>10110  |
| 31    | L <sub>5</sub> | L <sub>3</sub> | L <sub>3</sub><br>11 | L <sub>1</sub><br>10  | L <sub>2</sub><br>01   | L <sub>5</sub><br>001   | L <sub>4</sub><br>0001  | L <sub>6</sub><br>00001  | L <sub>7</sub><br>00000  |
| 32    | L <sub>5</sub> | L <sub>4</sub> | L <sub>4</sub><br>11 | L <sub>2</sub><br>10  | L <sub>7</sub><br>01   | L <sub>1</sub><br>001   | L <sub>3</sub><br>0001  | L <sub>5</sub><br>00001  | L <sub>6</sub><br>00000  |
| 33    | L <sub>5</sub> | L <sub>5</sub> | L <sub>5</sub><br>11 | L <sub>3</sub><br>10  | L <sub>6</sub><br>01   | L <sub>1</sub><br>001   | L <sub>2</sub><br>0001  | L <sub>4</sub><br>00001  | L <sub>7</sub><br>00000  |
| 34    | L <sub>5</sub> | L <sub>6</sub> | L <sub>6</sub><br>0  | L <sub>5</sub><br>11  | L <sub>3</sub><br>101  | L <sub>1</sub><br>1001  | L <sub>2</sub><br>10001 | L <sub>7</sub><br>100001 | L <sub>4</sub><br>100000 |
| 35    | L <sub>5</sub> | L <sub>7</sub> | L <sub>6</sub><br>0  | L <sub>7</sub><br>11  | L <sub>4</sub><br>101  | L <sub>5</sub><br>1001  | L <sub>2</sub><br>10001 | L <sub>1</sub><br>100001 | L <sub>3</sub><br>100000 |
| 36    | L <sub>6</sub> | L <sub>1</sub> | L <sub>1</sub><br>11 | L <sub>6</sub><br>10  | L <sub>7</sub><br>011  | L <sub>3</sub><br>010   | L <sub>2</sub><br>000   | L <sub>5</sub><br>0011   | L <sub>4</sub><br>0010   |
| 37    | L <sub>6</sub> | L <sub>2</sub> | L <sub>6</sub><br>11 | L <sub>7</sub><br>01  | L <sub>2</sub><br>00   | L <sub>4</sub><br>1011  | L <sub>5</sub><br>1010  | L <sub>1</sub><br>1001   | L <sub>3</sub><br>1000   |
| 38    | L <sub>6</sub> | L <sub>3</sub> | L <sub>1</sub><br>0  | L <sub>6</sub><br>110 | L <sub>2</sub><br>101  | L <sub>3</sub><br>1111  | L <sub>5</sub><br>1110  | L <sub>7</sub><br>1001   | L <sub>4</sub><br>1000   |
| 39    | L <sub>6</sub> | L <sub>4</sub> | L <sub>7</sub><br>11 | L <sub>6</sub><br>10  | L <sub>4</sub><br>01   | L <sub>2</sub><br>001   | L <sub>1</sub><br>0001  | L <sub>3</sub><br>00001  | L <sub>5</sub><br>00000  |
| 40    | L <sub>6</sub> | L <sub>5</sub> | L <sub>5</sub><br>11 | L <sub>6</sub><br>10  | L <sub>3</sub><br>01   | L <sub>1</sub><br>001   | L <sub>2</sub><br>0001  | L <sub>4</sub><br>00001  | L <sub>7</sub><br>00000  |
| 41    | L <sub>6</sub> | L <sub>6</sub> | L <sub>6</sub><br>1  | L <sub>5</sub><br>01  | L <sub>3</sub><br>0011 | L <sub>7</sub><br>0010  | L <sub>1</sub><br>0000  | L <sub>4</sub><br>00011  | L <sub>2</sub><br>00010  |
| 42    | L <sub>6</sub> | L <sub>7</sub> | L <sub>6</sub><br>0  | L <sub>7</sub><br>11  | L <sub>5</sub><br>101  | L <sub>4</sub><br>1001  | L <sub>2</sub><br>10001 | L <sub>3</sub><br>100001 | L <sub>1</sub><br>100000 |
| 43    | L <sub>7</sub> | L <sub>1</sub> | L <sub>7</sub><br>0  | L <sub>5</sub><br>110 | L <sub>3</sub><br>101  | L <sub>4</sub><br>1111  | L <sub>6</sub><br>1110  | L <sub>2</sub><br>1001   | L <sub>1</sub><br>1000   |
| 44    | L <sub>7</sub> | L <sub>2</sub> | L <sub>7</sub><br>11 | L <sub>2</sub><br>10  | L <sub>3</sub><br>011  | L <sub>4</sub><br>010   | L <sub>1</sub><br>000   | L <sub>5</sub><br>0011   | L <sub>6</sub><br>0010   |
| 45    | L <sub>7</sub> | L <sub>3</sub> | L <sub>7</sub><br>0  | L <sub>5</sub><br>111 | L <sub>6</sub><br>110  | L <sub>4</sub><br>100   | L <sub>3</sub><br>1010  | L <sub>1</sub><br>10111  | L <sub>2</sub><br>10110  |
| 46    | L <sub>7</sub> | L <sub>4</sub> | L <sub>4</sub><br>11 | L <sub>7</sub><br>10  | L <sub>2</sub><br>01   | L <sub>3</sub><br>001   | L <sub>1</sub><br>0001  | L <sub>6</sub><br>00001  | L <sub>5</sub><br>00000  |
| 47    | L <sub>7</sub> | L <sub>5</sub> | L <sub>7</sub><br>11 | L <sub>6</sub><br>10  | L <sub>5</sub><br>011  | L <sub>3</sub><br>010   | L <sub>4</sub><br>000   | L <sub>2</sub><br>0011   | L <sub>1</sub><br>0010   |
| 48    | L <sub>7</sub> | L <sub>6</sub> | L <sub>7</sub><br>1  | L <sub>6</sub><br>01  | L <sub>4</sub><br>000  | L <sub>5</sub><br>00111 | L <sub>3</sub><br>00110 | L <sub>2</sub><br>00101  | L <sub>1</sub><br>00100  |
| 49    | L <sub>7</sub> | L <sub>7</sub> | L <sub>7</sub><br>1  | L <sub>4</sub><br>01  | L <sub>2</sub><br>000  | L <sub>1</sub><br>00111 | L <sub>3</sub><br>00110 | L <sub>6</sub><br>00101  | L <sub>5</sub><br>00100  |

Table II—Performance of variable-length coding algorithms for 512 x 512 pictures

| Variable-Length Encoder                               | DPCM Encoder | Entropy of Quantizer Output (bits/pel) | Conditional Entropy (bits/pel) | Bit Rate (bits/pel) |
|---|--------------|--|--------------------------------|---------------------|
| Based on quantizer output                             | Nonsampled   | 1.84                                   | —                              | 1.94                |
| Based on conditional statistics ref. elements A, B    | Nonsampled   | 1.84                                   | 1.64                           | 1.73                |
| Based on conditional statistics ref. elements A, B, C | Nonsampled   | 1.84                                   | 1.53                           | 1.64                |
| Based on conditional statistics ref. elements A, B    | Sampled      | 1.05                                   | 0.92                           | 1.01                |
| Based on conditional statistics ref. elements A, B, C | Sampled      | 1.05                                   | 0.89                           | 0.97                |

sented in which the structure of the variable-length code word changes from pel to pel, depending on the local conditional statistics of the picture. In this scheme 3-bit DPCM words are coded by assigning a variable-length code word to represent each pel as a function of its expected frequency of occurrence, given the neighbor pel values (state). We have shown that for subsampled and nonsampled 3-bit DPCM coded pictures, bit rates of 0.97 bits/pel and 1.64 bits/pel, respectively, are achievable. We therefore conclude that by using the conditional variable-length encoder it is possible to obtain bit rates below the entropy of the quantizer output.

## REFERENCES

1. H. Gharavi, "Bandwidth Compression of Digital Color Television Signals Using Block-Adaptive DPCM," *IEE Proc. E. Commun., Radar & Signal Proc.*, 127, No. 5 (October 1980), pp. 405-9.
2. A. N. Netravali and J. O. Limb, "Picture Coding—A Review," *Proc. IEEE*, 68, No. 3 (March 1980), pp. 366-406.
3. C. E. Shannon, "A Mathematical Theory of Communication," *B.S.T.J.*, 27, No. 3 (July 1948), pp. 379-423 (Part I), pp. 623-56 (Part II).
4. D. A. Huffman, "A Method for the Construction of Minimum Redundancy Codes," *Proc. IRE*, 40 (September 1952), pp. 1098-101.
5. R. Hunter and A. H. Robinson, "International Digital Facsimile Coding Standards," *Proc. IEEE*, 68, No. 7 (July 1980), pp. 830-46.
6. H. Gharavi and A. N. Netravali, "CCITT Compatible Coding of Multi-level Pictures," 62, No. 9, Part 1 (November 1983), pp. 2765-78.

## AUTHOR

**Hamid Gharavi**, B.S.E.E., 1970, Tehran Polytechnic; M.S.C., 1975 (Digital Communication), and Ph.D. (Electrical Engineering), 1979, University of Technology, Loughborough, England; University of Technology, 1979-1980; Auckland University, New Zealand, 1980-1981; AT&T Bell Laboratories, 1982-1983. Present affiliation Bell Communications Research, Inc. Before joining AT&T Bell Laboratories, Mr. Gharavi was a Research Fellow at the

University of Technology and a Lecturer at Auckland University. Mr. Gharavi has worked on problems related to digital modulations for satellite communication. He has also worked on bandwidth compression of color television signals, source coding, graphics, and pattern recognition. Member, IEEE.

## Signals Designed for Recovery After Clipping—I. Localization of Infinite Products

By B. F. LOGAN, JR.\*

(Manuscript received March 10, 1982)

It is shown for signals of the form  $s(t) = g(t) + \cos ct$ , where  $g$  is band-limited to  $[-b, b]$ ,  $0 < b < c < \infty$ , and  $(-1)^k s(k\pi/c) > 0$  (e.g., if  $|g(t)| < 1$ ), that the zeros of  $s$  in the interval  $(t - T, t + T)$  allow reconstruction of  $s(t)$  with a relative error less than  $2e^{-\lambda T}(1 - e^{-\lambda T})^{-2}$ , where  $\lambda = b - c$ . The reconstruction algorithm gives an effective way of localizing the infinite product representation for  $s(t)$ . Some practical aspects of the algorithm are discussed. The scheme offers advantages for the recovery of signals after nonlinear distortion, such as occurs, for example, in magnetic recording.

### I. INTRODUCTION

Let us assume that a signal  $s(t)$  undergoes some nonlinear distortion, generally of unknown characteristic, during transmission (or perhaps in recording), which does not alter the zero crossings. We may suppose that the reliable information we receive is just  $\text{sgn } s(t)$ , the clipped signal. We are led to ask for what class of signals  $s(t)$  can we make a reliable estimate of  $As(t)$  from  $\text{sgn } s(t)$ , i.e., from the zero crossings of  $s(t)$ .

If we assume that  $s(t)$  is a (real-valued) bandlimited signal with real simple zeros  $t_k$ , we have the formula,<sup>†</sup> assuming  $s(0) \neq 0$ ,

---

\* AT&T Bell Laboratories.

<sup>†</sup> This follows from a result of Titchmarsh,<sup>1</sup> who showed that (1) holds for  $s(t)$  that have ordinary Fourier transforms that vanish outside an interval  $[-\alpha, \alpha]$  but not outside any translate of the interval; i.e., for bandlimited functions whose spectral endpoints are centered about the origin. Then, (1) follows for bounded  $s(t)$  by considering  $s(t)(t - t_j)^{-1}(t - t_k)^{-1}$ , where  $t_j$  and  $t_k$  are either real or complex conjugates.

---

Copyright © 1984 AT&T. Photo reproduction for noncommercial use is permitted without payment of royalty provided that each reproduction is done without alteration and that the Journal reference and copyright notice are included on the first page. The title and abstract, but no other portions, of this paper may be copied or distributed royalty free by computer-based and other information-service systems without further permission. Permission to reproduce or republish any other portion of this paper must be obtained from the Editor.

$$s(t) = s(0) \prod_{k=1}^{\infty} \left(1 - \frac{t}{t_k}\right), \quad (1)$$

where the product converges (conditionally) if the zeros are ordered such that  $|t_{k+1}| > |t_k|$ . Thus, from a strictly mathematical viewpoint, we have a "formula" for recovering  $s(t)$  within a constant multiplier from  $\text{sgn } s(t)$ . However, for practical purposes the formula is worthless without additional restrictions on  $s(t)$ .

In the first place, the formula is valid only for strictly bandlimited  $s(t)$ . If the  $t_k$  are the zeros of an almost bandlimited  $s(t)$ , then the product may not even converge, or if it does, it may not even represent a bounded function, and in general cannot be expected to give a reasonable replica of  $s(t)$ .

In the second place, even if  $s(t)$  is strictly bandlimited, the infinite product representation is, in general, impractical; it is very sensitive to (correlated) perturbations of the  $t_k$  and, more important, knowledge of all the  $t_k$  is crucial to estimating  $s(t)$ , relative to  $s(0)$ , for large  $t$ . In practice, one would like to make a good estimate,  $s_T(t)$ , of  $s(t)$  just from the knowledge of the zeros of  $s$  in the interval  $(t - T, t + T)$  for some fixed  $T$  and arbitrary  $t$ ,  $(-\infty < t < \infty)$ . That is, in practice we require a *localized* reconstruction formula.

For a certain class of bandlimited  $s(t)$ , we can obtain an *exponentially localized* reconstruction formula; i.e., from a knowledge of the zeros of  $s$  in the interval  $(t - T, t + T)$ , we can make an estimate  $s_T(t)$  such that

$$|s(t) - s_T(t)| \leq |s(t)| \cdot \epsilon_T, \quad (2)$$

where

$$\epsilon_T = 0\{e^{-\lambda T}\} \quad T \rightarrow \infty$$

and  $\lambda > 0$  is an appropriate parameter in the representation of  $s(t)$ .

This class of signals, which we denote by  $S(b, c)$ , consists of signals of the form

$$s(t) = g(t) + \cos ct, \quad (3)$$

where  $g$  (real valued) is a signal whose spectrum is confined to  $[-b, b]$ ,  $0 < b < c < \infty$ , and such that

$$(-1)^k s(k\pi/c) > 0, \quad k = 0, \pm 1, \pm 2, \dots \quad (3a)$$

The alternation condition (3a) ensures that  $s(t)$  has only real simple zeros,\* one between each extremal of  $\cos ct$ . Sufficient additional

---

\* We ask the readers to accept this fact, or provide their own proof. A more general result will be given in a future paper.

conditions on  $g$  for (3a) are

$$|g(k\pi/c)| < 1 \quad k = 0, \pm 1, \pm 2, \dots \quad (3b)$$

and

$$|g(t)| < 1 \quad -\infty < t < \infty, \quad (3c)$$

the latter condition being the more practical constraint. However, (3a) allows special functions  $g$  of the form

$$g(t) = (1 + x(t))\cos ct + \hat{x}(t)\sin ct, \quad (4)$$

where  $x(t)$  is a bandpass signal (real valued) whose spectrum is confined to the disjoint intervals,  $[\lambda, \mu]$  and  $[-\mu, -\lambda]$ ,  $0 < \lambda < \mu$ ,

$$\lambda + \mu \leq 2c, \quad (4a)$$

$$x(t) > -1, \quad (4b)$$

and

$$\hat{x}(t) \text{ is the Hilbert transform of } x(t). \quad (4c)$$

The spectrum of  $g$ , defined in (4), is confined to the union of the two intervals,  $[-c + \lambda, -c + \mu]$  and  $[-\mu + c, -\lambda + c]$ . In case  $c > \mu$ , then  $g$ , defined in (4), is bandpass with spectrum confined to the disjoint intervals  $[-b, -a]$ , and  $[a, b]$ , where

$$0 < a = c - \mu < b = c - \lambda. \quad (4d)$$

In this case ( $c > \mu$ ), we may consider  $s(t)$  to be a full carrier lower-sideband signal associated with the bandpass baseband signal  $x(t)$ . Also, if  $g$  in (3) is bandpass with spectrum confined to the disjoint intervals  $[-b, -a]$ ,  $[a, b]$ , and  $0 < a < b < c$ , we can always put  $g$  in the form (4).

The important parameter associated with the class  $S(b, c)$  is

$$\lambda = c - b. \quad (5)$$

In words,  $\lambda$  is the width of the guard band between the top frequency of  $g(t)$  and the frequency of  $\cos ct$ . We will refer to  $\lambda$  as the gap frequency (rad/s). It is the presence of the gap that allows the exponential localization of the reconstruction of  $s(t)$ , giving an error of the order of  $e^{-\lambda T}$  from the knowledge of the zeros of  $s$  in the interval  $(t - T, t + T)$ . We can obtain a good approximation to  $s(t)$  for  $\lambda T$ , say, in the range  $2\pi$  to  $3\pi$ ; i.e.,  $T$  needs to be only 2 or 3 half periods (Nyquist intervals) of the gap frequency to obtain 0.1-percent error.

We should note that the signals in  $S(b, c)$  are, in effect, normalized by taking the coefficient of  $\cos ct$  to be +1. With the signals thus normalized, their zeros give a complete description of the signals.

In some applications we may think of  $s$  as a baseband signal  $g$  with

added bias ( $\cos ct$ ), and in other applications we may think of  $s$  as a lower-sideband signal with full carrier ( $\cos ct$ ).

We first present the reconstruction formulas. Subsequent sections are devoted to the derivation of the formulas. Finally, some practical aspects of the reconstruction formulas are discussed in the concluding section.

## II. THE RECONSTRUCTION FORMULAS

Here we describe an approximation,  $s_T(t)$ , determined only by the zeros of  $s$  in the interval  $(t - T, t + T)$  such that for  $s$  in  $S(b, c)$ , we have

$$|s(t) - s_T(t)| \leq \frac{2e^{-\lambda T}}{(1 - e^{-\lambda T})^2} |s(t)|, \quad -\infty < t < \infty. \quad (6)$$

The first form of the approximation is

$$s_T(t) = (1/2)\{\text{sgn } s(t)\} \cdot \exp\{\hat{h}_T(t)\}, \quad (7)$$

where

$$\hat{h}_T(t) = \sum_{-\infty}^{\infty} L_T(t - t_k) + \frac{c}{\lambda} \mu(\lambda T), \quad (7a)$$

$$L_T(t) = L_T(-t), \quad (7b)$$

$$L_T(t) = 0, \quad |t| > T, \quad (7c)$$

$$L_T(t) = - \int_t^T \frac{f(x)}{x} dx, \quad 0 < t < T, \quad (7d)$$

$$f(t) = \frac{T}{\sinh \lambda T} \frac{\sinh \lambda \sqrt{T^2 - t^2}}{\sqrt{T^2 - t^2}}, \quad (7e)$$

and

$$\mu(x) = \frac{xI_0(x)}{\sinh x} - \frac{x}{\sinh x} \cdot \frac{2}{\pi} \int_0^{\pi/2} e^{-x \sin \theta} d\theta \sim \sqrt{\frac{2x}{\pi}}, \quad x \rightarrow \infty. \quad (7f)$$

(Here  $I_0$  is the modified Bessel function.) The function  $L_T(t)$  is a sort of truncated  $\log |t/T|$ , depending both on  $\lambda$  and  $T$ , although in the notation we have suppressed the dependence on  $\lambda$ . Using the fact that  $f(0) = 1$ , we have

$$\begin{aligned} L_T(t) &= \log \left| \frac{t}{T} \right| + \int_t^T \frac{1 - f(x)}{x} dx \\ &= \log \left| \frac{t}{T} \right| + F\left(\frac{t}{T}; \lambda T\right), \quad |t| < T \\ &= 0, \quad |t| \geq T, \end{aligned} \quad (8)$$

where  $F(x; \lambda T)$  is analytic everywhere. Graphs of  $F(x; \beta)$  and  $L_T(xT)$ ,  $\beta = \lambda T = k\pi/2$  are shown in Fig. 1 for  $-1 \leq x \leq 1$ ,  $k = 1, 2, 3, \dots, 6$ . For  $\lambda T = \pi/2$ , in which case the reconstruction interval  $(t - T, t + T)$  has a length equal to only a half-period (one Nyquist interval) of the gap frequency, the function  $F$  is not significantly different from zero over the interval  $(-1, 1)$ ; so  $L_T(t) \doteq \log |t/T|$  for the case  $\lambda T = \pi/2$ . For larger  $\lambda T$ , the function  $F$  becomes significant.

In order to express  $s_T(t)$  in product form we define

$$V_T(t) = \exp L_T(t). \tag{9}$$

Here,  $V_T(t)$  is a sort of V-shaped function that we may write, using (7),

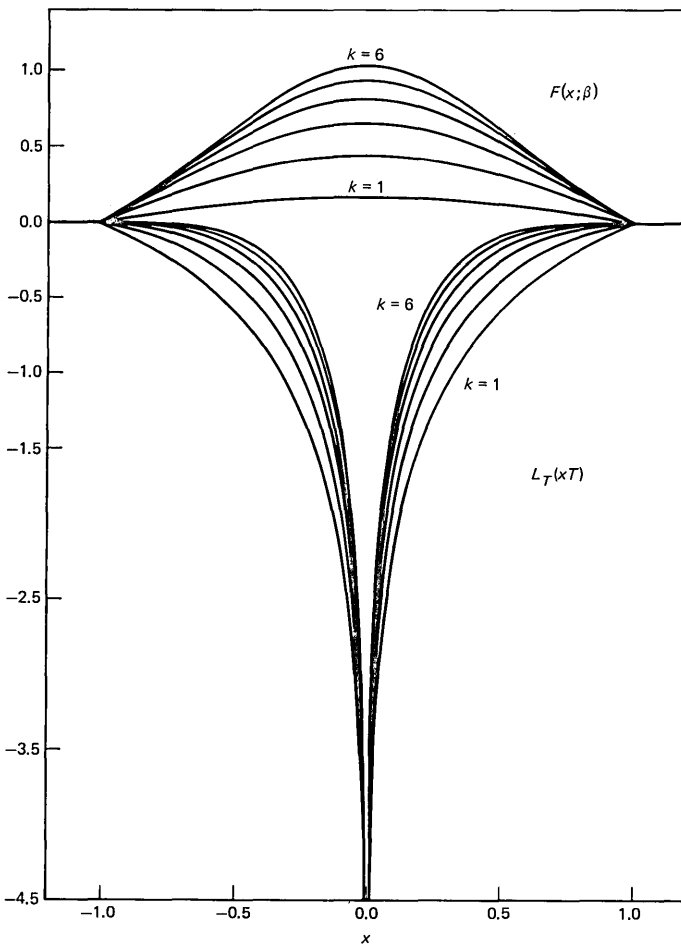


Fig. 1—The functions  $L_T(xT)$  and  $F(x; \beta)$  for  $\beta = k\pi/2$ ,  $k = 1, 2, 3, \dots, 6$ .

$$\begin{aligned}
 V_T(t) &= \left| \frac{t}{T} \right| \cdot W\left(\frac{t}{T}; \lambda T\right), & |t| < T \\
 &= 1, & |t| \geq T,
 \end{aligned} \tag{9a}$$

where

$$W(x; \lambda T) = \exp\{F(x; \lambda T)\}, \quad |x| < 1. \tag{9b}$$

We have then,

$$s_T(t) = A\{\operatorname{sgn} s(t)\} \prod_{-\infty}^{\infty} V_T(t - t_k), \tag{10}$$

where

$$A = \frac{1}{2} \exp\left\{\frac{c}{\lambda} \mu(\lambda T)\right\}. \tag{10a}$$

Graphs of the two functions,  $V_T(xT) = |x|W(x; \lambda T)$  and  $W(x; \lambda T)$ , are shown in Fig. 2 for  $-1 \leq x \leq 1$ ,  $\lambda T = \beta = k\pi/2$ , and  $k = 1, 2, 3, \dots, 6$ .

The normalization function  $\mu(\lambda T)$ , defined in (7f) and appearing in (7a) and (10a), is graphed in Fig. 3.

It should be noted in formulas (7) and (10), recalling that  $L_T(t) = 0$  for  $|t| \geq T$  and  $V_T(t) = 1$  for  $|t| \geq T$ , that the infinite sum and the infinite product involve for each  $t$  only those  $t_k$  that satisfy  $|t - t_k| < T$ ; i.e., only those  $t_k$  in the interval  $(t - T, t + T)$ . So, (10) gives the desired localization of the infinite product (1) for signals in the class  $S(b, c)$ .

The error estimate in (6) is conservative, with equality possible only at the zeros of  $s$ . At least, we have the exponential decrease of the error with  $\lambda T$ ; e.g., for  $\lambda T = 2\pi$ ,

$$\frac{2e^{-2\pi}}{(1 - e^{-2\pi})^2} \doteq 0.00375,$$

and for  $\lambda T = 3\pi$ ,

$$\frac{2e^{-3\pi}}{(1 - e^{-3\pi})^2} \doteq 0.00016.$$

So, for  $T$  somewhere between 2 and 3 half periods of the gap frequency  $\lambda$ , we get a *relative* error,  $(s_T(t) - s(t)) \div s(t)$ , amounting to no more than 0.1 percent.

Figure 4 illustrates the simplest sort of test of the algorithm in reconstructing  $s(t) = \cos t$ . Here  $g(t) = 0$ , and  $\lambda = c = 1$ . Four cases of  $s_T(t)$  are shown corresponding to  $T = \pi/2, \pi, 3\pi/2$ , and  $2\pi$ . The

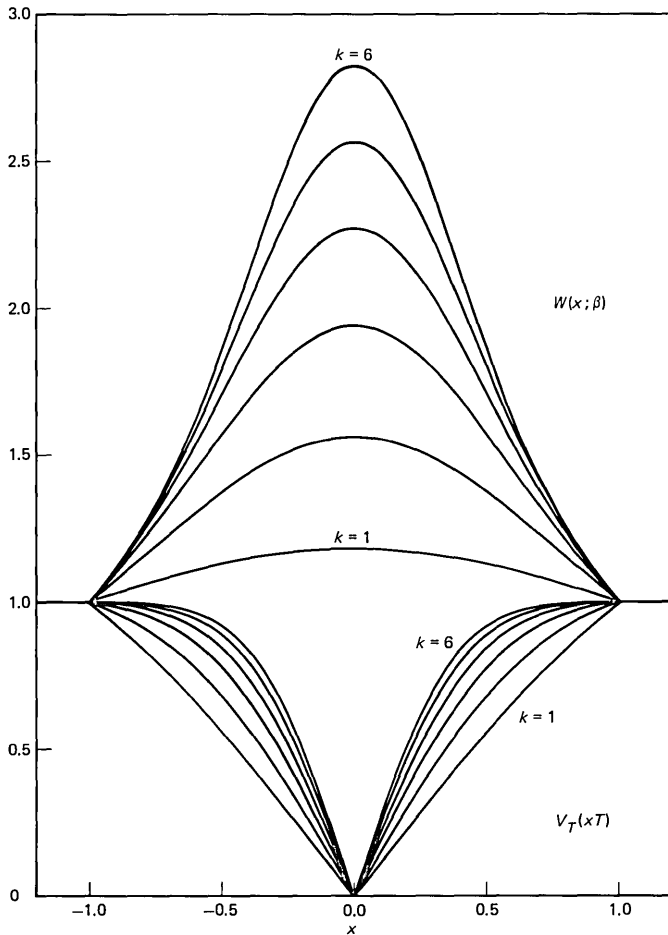


Fig. 2—The functions  $V_T(xT)$  and  $W(x; \beta)$  for  $\beta = k\pi/2, k = 1, 2, 3, \dots, 6$ .

corresponding errors and relative errors, suitably magnified, are also shown.

In the first case ( $T = \pi/2$ ), shown in Fig. 4a, only one zero of  $\cos t$  appears in the observation interval ( $t - T, t + T$ ); so, we have in this case

$$s_T(t) = A \cdot V_T(t - \pi/2) \quad \text{for } 0 \leq t \leq \pi/2.$$

Here  $V_T(t) \equiv V_T(t; \lambda T)$  with  $T = \pi/2, \lambda = 1$ . For the relatively small product,  $\lambda T = \pi/2$ , the function  $V_T(t)$  is essentially  $|t/T|$  for  $|t| < T$  (cf. Fig. 2), so that  $s_T(t)$  has a quite triangular waveform. The magnitude of the error ( $s_T(t) - s(t)$ ) in the reconstruction is maximum at  $t = 0$ , where it is approximately 0.22. The magnitude of the relative

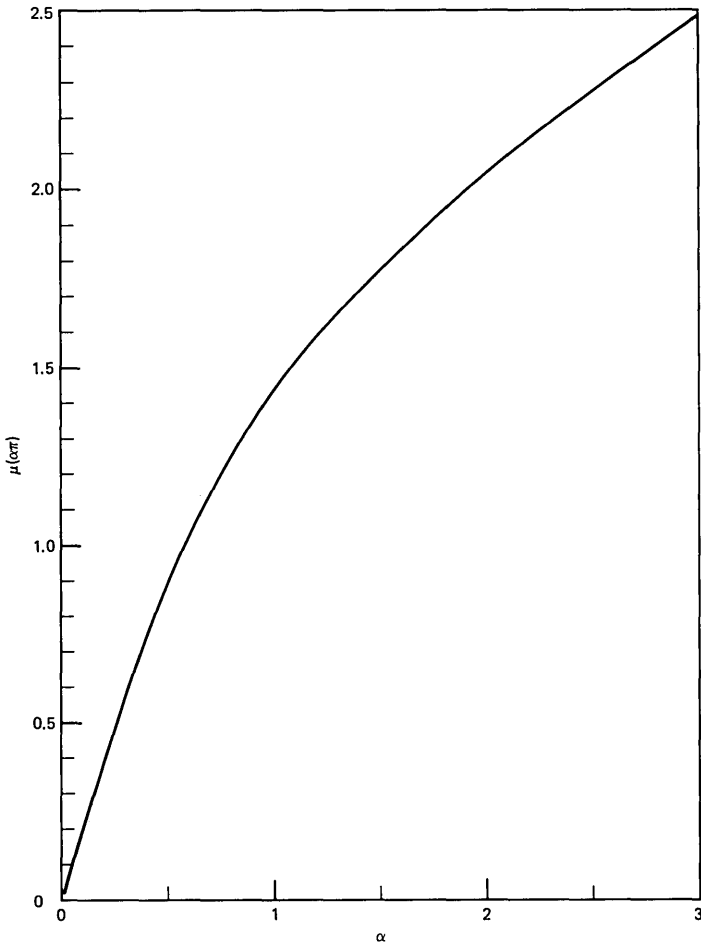


Fig. 3—Normalization function  $\mu(\lambda T)$ .

error,  $(s_T(t) - s(t)) \div s(t)$ , is also maximum at  $t = 0$  with the same value, approximately 0.22. The estimate (6) gives an upper bound for the absolute relative error in this case of approximately 0.66. The reconstruction is rather crude in this case.

The approximations become progressively better in the other cases. For example, the maximum absolute relative error in the fourth case,  $\lambda T = 2\pi$  (see Fig. 4d), is approximately 0.001, the upper bound (6) for this case being approximately 0.0037. In all cases the maximum absolute relative error is approximately one third of the upper bound, given by (6). Note that in the second and fourth cases the absolute relative error is maximum at the zeros of  $\cos t$  where the error is zero.

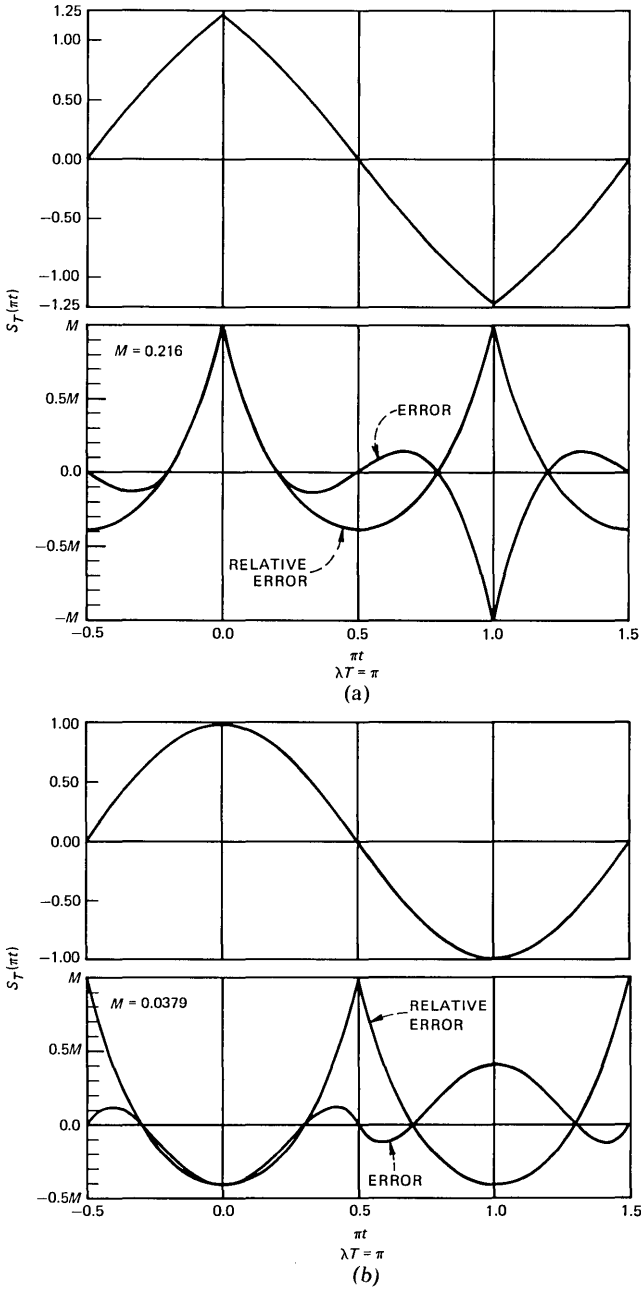


Fig. 4(a) and (b)—Reconstruction of cosine.

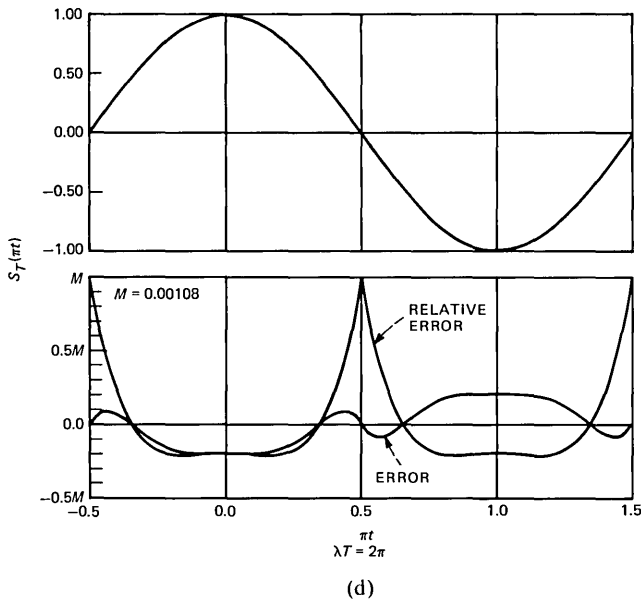
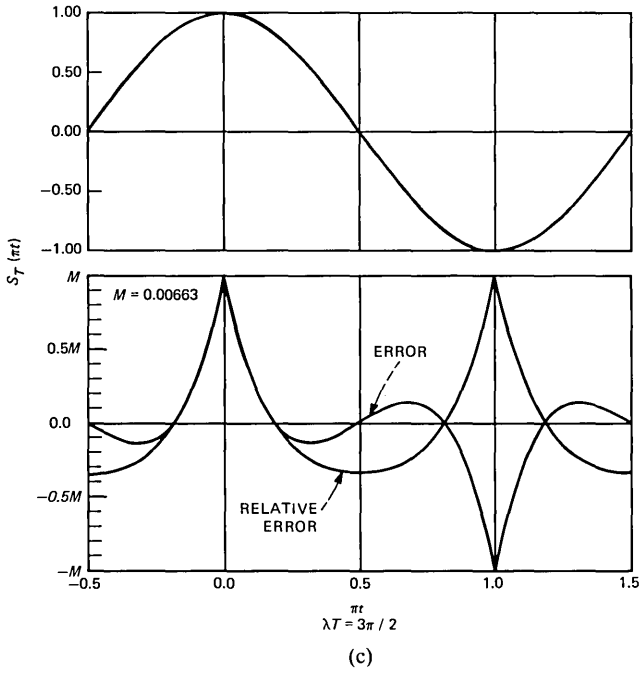


Fig. 4(c) and (d)—Reconstruction of cosine.

Note the similar character of the error waveforms in the first and third cases, where  $2T$  is an odd multiple of  $\pi$ , which is distinctly different from that of the second and fourth cases, where  $2T$  is an even multiple of  $\pi$ .

### III. THE BASIC FORMULA

Given the zeros  $\{t_k\}$  of a signal  $s(t)$  in  $S(b, c)$ , we define the following important function:

$$h(t) = J(t) - ct, \quad (11)$$

where  $J(t)$  is a jump function increasing by  $\pi$  at each zero  $t_k$  of  $s(t)$ , and

$$J(0) = 0. \quad (11a)$$

The function  $\pi^{-1}J(t)$  is just the zero-counting function of  $s(t)$ . Since there is one, and only one, zero  $t_k$  between each extremal of  $\cos ct$ , we may label the zeros such that

$$k\pi/c < t_k < (k+1)\pi/c, \quad k = 0, \pm 1, \pm 2, \dots \quad (12)$$

It is clear then that

$$h(k\pi/c) = 0, \quad k = 0, \pm 1, \pm 2, \dots \quad (13)$$

and

$$-\pi < h(t) < \pi, \quad -\infty < t < \infty. \quad (14)$$

The function  $h(t)$ , which we will refer to as the *fundamental function* associated with the zeros  $\{t_k\}$  of  $s(t)$ , may be described as a sort of meandering sawtooth function bounded between  $-\pi$  and  $\pi$ .

In this section we want to show that  $h(t)$  is a high-pass function with no spectrum in the frequency interval  $(-\lambda, \lambda)$ , where  $\lambda$  is the gap frequency ( $\lambda = c - b$ ), and therefore has a Hilbert transform  $\hat{h}(t)$ . Furthermore, we will show that

$$\log |2s(t)| = \hat{h}(t) = \frac{1}{\pi} \int_{-\infty}^{\infty} \frac{h(x)}{t-x} dx, \quad (15)$$

and thus obtain the *basic formula*

$$s(t) = (1/2)\{\operatorname{sgn} s(t)\} \exp\{\hat{h}(t)\}. \quad (16)$$

The fact that  $h(t)$  is a high-pass function allows us to make a good estimate  $\hat{h}_T(t)$  of  $\hat{h}(t)$  just from the knowledge of  $h$ , or equivalently the zeros of  $s$ , in the interval  $(t-T, t+T)$ . Later, we detail the localization of the Hilbert transform to obtain (7) from (16).

To obtain these results, we introduce the complex variable  $\tau = t + iu$ , and consider for  $s(t)$  in  $S(b, c)$  the function

$$H(\tau) = i \log\{2e^{i\tau} s(\tau)\}, \quad u > 0. \quad (17)$$

We have

$$\begin{aligned} 2e^{i\tau} s(\tau) &= 2e^{i\tau} (g(\tau) + \cos c\tau) \\ &= 1 + 2e^{i\tau} g(\tau) + e^{2i\tau}. \end{aligned} \quad (18)$$

Now  $g(\tau)$  is an entire function of exponential type  $b < c$ , real and bounded on the real line; so (cf. Ref. 2, p. 83),

$$|g(t + iu)| \leq (\cosh bu) \sup_t |g(t)|. \quad (19)$$

Hence,

$$2e^{ic(t+iu)} s(t + iu) = 1 + O(e^{-\lambda u}), \quad u \rightarrow \infty, \quad \text{where } \lambda = c - b > 0, \quad (20)$$

and therefore,

$$H(t + iu) = O(e^{-\lambda u}), \quad u \rightarrow \infty. \quad (21)$$

Also, since  $s(\tau)$  has only real zeros,  $H(\tau)$  is analytic in the upper half plane. The real part of  $H(\tau)$  is also bounded. It follows (Ref. 3, see Theorems 6.3.1 and 6.4.3) that

$$h(t) = \lim_{u \rightarrow 0^+} \operatorname{Re}\{H(t + iu)\} \quad (22)$$

and

$$\hat{h}(t) = \lim_{u \rightarrow 0^+} \operatorname{Im}\{H(t + iu)\} \quad (23)$$

are high-pass functions having no spectrum in the interval  $(-\lambda, \lambda)$ , and  $\hat{h}(t)$  is the Hilbert transform of  $h(t)$ .

We have

$$h(t) = - \lim_{u \rightarrow 0^+} \arg\{e^{i\tau} (g(\tau) + \cos c\tau)\}. \quad (24)$$

Now, for  $t = k\pi/c$  we have

$$e^{ict} (g(t) + \cos ct) = e^{ik\pi} s(k\pi/c) > 0. \quad (25)$$

Hence,  $h(k\pi/c)$  is some multiple of  $2\pi$ . We can conclude that  $h(k\pi/c) = 0$  from the fact that  $h$  is high pass and from the fact that the argument (phase) of  $s(t)$  is a decreasing function of  $t$ , decreasing by  $\pi$  at each zero of  $s$  (indent into the upper half plane around the zeros). There is one, and only one, zero between each extremal of  $\cos ct$ , and  $h'(t) = -c$  except when  $t$  is a zero of  $s(t)$ . Thus,

$$h(t) = h(0) - ct + J(t), \quad (26)$$

where  $J(t)$  is a nondecreasing staircase function (jump function),  $J(0) = 0$ , which increases by  $\pi$  at  $t_k$ , the zeros of  $s(t)$ ; i.e.,

$$\frac{k\pi}{c} < t_k < \frac{(k+1)\pi}{c}, \quad (26a)$$

$$J'(t) = 0, \quad t \neq t_k, \quad (26b)$$

and

$$J\left(\frac{k\pi}{c}\right) = k\pi. \quad (26c)$$

Thus, we have from (26) and (26c)

$$h\left(\frac{k\pi}{c}\right) = h(0) = 2n\pi, \quad k = 0, \pm 1, \pm 2, \dots \quad (27)$$

Since  $h(t)$  can increase or decrease at most by  $\pi$  in each interval  $k\pi/c < t < (k+1)\pi/c$ , we have

$$-\pi < h(t) - h(k\pi/c) < \pi$$

or

$$(2n-1)\pi < h(t) < (2n+1)\pi.$$

But,  $h(t)$  is high pass and must change sign, so we must have  $n = 0$ , and hence,

$$-\pi < h(t) < \pi \quad (-\infty < t < \infty). \quad (28)$$

In other words,  $h(0) = 0$  is the only value of  $\arg\{e^{ict}s(t)\}$  at  $t = 0$  consistent with  $H(t+iu) = 0(e^{-\lambda u})$ , where we took  $\log\{2e^{icr}s(\tau)\}$  to be the principal branch,  $\log\{1+2e^{icr}g(\tau)\} \rightarrow 2e^{icr}g(\tau)$ ,  $u \rightarrow \infty$ . Thus, we have from (17), (23), and (28)

$$\log 2|s(t)| = \frac{1}{\pi} \int_{-\infty}^{\infty} \frac{h(x)}{t-x} dx, \quad |h(x)| < \pi, \quad (29)$$

where  $h$  is the function defined in (11). Now, since  $h$  is a bounded high-pass function, we can obtain an exponential localization of the Hilbert transform in (29).

#### IV. LOCALIZATION OF THE HILBERT TRANSFORM

If the spectrum of a bounded function  $h(t)$  omits the interval  $(-\lambda, \lambda)$ , there are many equivalent representations for its Hilbert transform. We have<sup>4</sup>

$$h(t) = \int_{-\infty}^{\infty} h(x)K(t-x)dx, \quad (30)$$

where\*

$$K(t) = \frac{f(t)}{\pi t} \quad (30a)$$

and

$f(t)$  is any bandlimited function whose spectrum is confined to  $[-\lambda, \lambda]$ , satisfying (30b)

$$f(0) = 1 \quad (30c)$$

and

$$\int_{|t|>1} \frac{|f(t)|}{|t|} dt < \infty. \quad (30d)$$

Although  $\hat{h}(t)$  is not generally bounded, the singular kernel  $K(t)$  can be truncated to an interval  $(-T, T)$  giving  $K_T(t)$ , such that

$$\hat{h}_T(t) = \int_{-\infty}^{\infty} h(x)K_T(t-x)dx = \int_{-T}^T K_T(x)h(t-x)dx \quad (31)$$

is a good approximation to  $\hat{h}(t)$ ; i.e.,

$$h(t) - h_T(t) = \int_{|x|>T} \frac{f(x)}{\pi x} h(t-x)dx. \quad (32)$$

Then

$$|\hat{h}(t) - \hat{h}_T(t)| \leq M \int_{|x|>T} \frac{|f(x)|}{\pi|x|} dx, \quad (33)$$

where

$$M = \sup_t |h(t)|.$$

The bandlimited function  $f$  that minimizes the integral in (33), with  $f(0) = 1$  and spectrum confined to  $[-\lambda, \lambda]$ , is (see Ref. 4)

$$f(t) = \frac{T}{\sinh \lambda T} \frac{\sin \lambda \sqrt{t^2 - T^2}}{\sqrt{t^2 - T^2}} \quad (34)$$

or, equivalently,

$$f(t) = \frac{T}{\sinh \lambda T} \frac{\sinh \lambda \sqrt{T^2 - t^2}}{\sqrt{T^2 - t^2}}. \quad (34a)$$

---

\* Formally, the Fourier transform of  $K$  is the convolution of  $F(\omega)$ , the Fourier transform of  $f$ , with  $-i \operatorname{sgn} \omega$ , which then agrees with  $-i \operatorname{sgn} \omega$  for  $|\omega| > \lambda$ .

So, we will set

$$K_T(t) = \frac{1}{\pi t} \cdot \frac{T}{\sinh \lambda T} \frac{\sinh \lambda \sqrt{T^2 - t^2}}{\sqrt{T^2 - t^2}}, \quad |t| < T$$

$$= 0, \quad |t| \geq T. \quad (35)$$

Then, (34) in (33) gives (see Ref. 4)

$$|\hat{h}(t) - \hat{h}_T(t)| \leq \frac{2M}{\pi} \log \frac{1 + e^{-\lambda T}}{1 - e^{-\lambda T}}. \quad (36)$$

So  $K_T$ , defined in (35), gives us the desired exponential localization of the Hilbert transform.

## V. LOCALIZATION OF THE RECONSTRUCTION OF $s(t)$

Now we are prepared to obtain a good approximation to  $s(t)$  belonging to  $S(b, c)$ ,  $c - b = \lambda$ , from a knowledge of the zeros of  $s$  in  $(t - T, t + T)$ . From (29) we have

$$s(t) = (1/2)\{\text{sgn } s(t)\} \exp \hat{h}(t), \quad (37)$$

where  $\hat{h}$  is the Hilbert transform of the high-pass function  $h$  defined in (11). Now we set

$$s_T(t) = (1/2)\{\text{sgn } s(t)\} \exp \hat{h}_T(t), \quad (38)$$

where

$$\hat{h}_T(t) = \int_{-\infty}^{\infty} h(x) K_T(t - x) dx \quad (39)$$

and  $K_T$  is defined in (35). Since  $|h(x)| < \pi$ , we have from (36)

$$|\hat{h}(t) - \hat{h}_T(t)| < 2 \log \frac{1 + e^{-\lambda T}}{1 - e^{-\lambda T}}. \quad (40)$$

Owing to the special nature of  $h(x)$  (cf. [11]), we can manipulate the integral (39) into a more convenient form. We may write

$$\hat{h}_T(t) = \frac{1}{\pi} \int_{-\infty}^{\infty} dh(x) L_T(t - x) dx$$

$$= \sum_{-\infty}^{\infty} L_T(t - t_k) - \frac{c}{\pi} \int_{-\infty}^{\infty} L_T(t) dt, \quad (41)$$

where  $\{t_k\}$  are the zeros of  $s(t)$  and

$$L_T(t) = \pi \int_{-\infty}^t K_T(x) dx, \quad -\infty < t < 0, \quad (42)$$

$$L_T(t) = L_T(-t), \quad (42a)$$

$$L_T(t) = 0, \quad |t| > T, \quad (42b)$$

and

$$L_T(t) = - \int_t^T \frac{f(x)}{x} dx, \quad 0 < t < T. \quad (42c)$$

The function  $L_T(t)$  is a sort of truncated log  $|t/T|$ , depending both on  $\lambda$  and  $T$ , although in the notation we have suppressed the dependence on  $\lambda$ . Using the fact that  $f(0) = 1$ , we have

$$\begin{aligned} L_T(t) &= \log \left| \frac{t}{T} \right| + \int_t^T \frac{1-f(x)}{x} dx, \quad |t| < T \\ &= 0, \quad |t| \geq T, \end{aligned} \quad (42d)$$

and furthermore, since  $f(x) > 0$  for  $|x| \leq T$  (cf. [42c]),

$$L_T(t) \leq 0, \quad -\infty < t < \infty. \quad (42e)$$

Although it may be simpler to compute  $\hat{h}_T(t)$  from (41) and then compute  $s_T(t)$  according to (38), it is interesting to express  $s_T(t)$  in product form. So we define

$$V_T(t) = \exp L_T(t). \quad (43)$$

Here,  $V_T(t)$  is a sort of V-shaped function that we may write using (42d),

$$\begin{aligned} V_T(t) &= \left| \frac{t}{T} \right| \exp \left\{ \int_t^T \frac{1-f(x)}{x} dx \right\}, \quad |t| < T \\ &= 1, \quad |t| \geq T, \end{aligned} \quad (43a)$$

and we note that

$$V_T'(0+) = \frac{1}{T} \exp \int_0^T \frac{1-f(x)}{x} dx \quad (44)$$

and

$$V_T'(T-) = \frac{f(T)}{T} = \frac{\wedge}{\sinh \lambda T}. \quad (44a)$$

Now we may write

$$s_T(t) = A \{ \text{sgn } s(t) \} \prod_{k=-\infty}^{\infty} V_T(t - t_k), \quad (45)$$

where, from (41) and (38),

$$A = A(b, c, T) = \frac{1}{2} \exp \left\{ -\frac{c}{\pi} \int_{-\infty}^{\infty} L_T(t) dt \right\}. \quad (45a)$$

We have

$$\int_{-\infty}^{\infty} L_T(t) dt = - \int_{-\infty}^{\infty} t L_T'(t) dt = - \int_{-T}^T f(t) dt. \quad (46)$$

From a table of Fourier transforms,<sup>5</sup> we find

$$\begin{aligned} \int_{-\infty}^{\infty} \frac{\sin \lambda \sqrt{t^2 - T^2}}{\sqrt{t^2 - T^2}} \cos \omega t dt &= \pi I_0(T \sqrt{\lambda^2 - \omega^2}), & |\omega| < \lambda \\ &= 0, & |\omega| > \lambda \end{aligned} \quad (47)$$

and

$$\int_{-T}^T \frac{\cosh \lambda \sqrt{t^2 - T^2}}{\sqrt{t^2 - T^2}} \cos \omega t dt = \pi J_0(T \sqrt{\omega^2 - \lambda^2}), \quad (48)$$

where  $I_0(x) = J_0(ix)$  is the modified Bessel function. Setting  $\omega = 0$ , we have

$$\int_{-\infty}^{\infty} \frac{\sin \lambda \sqrt{t^2 - T^2}}{\sqrt{t^2 - T^2}} dt = \int_{-T}^T \frac{\cosh \lambda \sqrt{t^2 - T^2}}{\sqrt{t^2 - T^2}} dt = \pi I_0(\lambda T),$$

from which we find

$$\begin{aligned} \int_{|t|>T} \frac{\sin \lambda \sqrt{t^2 - T^2}}{\sqrt{t^2 - T^2}} dt &= 2 \int_0^T \frac{e^{-\lambda \sqrt{t^2 - T^2}}}{\sqrt{t^2 - T^2}} dt \\ &= 2 \int_0^{\pi/2} e^{-\lambda T \sin \theta} d\theta \end{aligned} \quad (49)$$

and

$$\int_{-T}^T \frac{\sinh \lambda \sqrt{T^2 - t^2}}{\sqrt{T^2 - t^2}} dt = \pi I_0(\lambda T) - 2 \int_0^{\pi/2} e^{-\lambda T \sin \theta} d\theta. \quad (50)$$

Thus,

$$\int_{-\infty}^{\infty} L_T(t) dt = -\frac{T}{\sinh \lambda T} \left\{ \pi I_0(\lambda T) - 2 \int_0^{\pi/2} e^{-\lambda T \sin \theta} d\theta \right\}, \quad (51)$$

and

$$A = A(b, c, T) = \frac{1}{2} \exp \left\{ \frac{c}{\lambda} \mu(\lambda T) \right\}, \quad (52)$$

where  $\lambda = c - b$ , and

$$\mu(x) = \frac{xI_0(x)}{\sinh x} - \frac{x}{\sinh x} \cdot \frac{2}{\pi} \int_0^{\pi/2} e^{-x \sin \theta} d\theta \sim \sqrt{\frac{2x}{\pi}},$$

$x \rightarrow \infty. \quad (52a)$

We observe, since  $V_T(t) = 1$  for  $|t| \geq T$ , that the infinite product in (45) is, in effect, for each  $t$ , a finite product. That is, we may write

$$s_T(t) = A\{\operatorname{sgn} s(t)\} \cdot \prod_{k:|t-t_k|<T} V_T(t - t_k) \quad (53)$$

to emphasize the localization of the reconstruction.

Now, to estimate the error, we write, using (37) and (38),

$$\begin{aligned} s_T(t) - s(t) &= (1/2)\{\operatorname{sgn} s(t)\}\{\exp[\hat{h}_T(t)] - \exp[\hat{h}(t)]\} \\ &= (1/2)s(t) \cdot \{\exp[\hat{h}_T(t) - \hat{h}(t)] - 1\}. \end{aligned} \quad (54)$$

Now,

$$\begin{aligned} |e^x - 1| &= \left| x + \frac{x^2}{2!} + \frac{x^3}{3!} + \dots \right| \\ &\leq \left| |x| + \frac{|x|^2}{2!} + \frac{|x|^3}{3!} + \dots \right| = e^{|x|} - 1. \end{aligned}$$

Setting  $x = \hat{h}_T(t) - \hat{h}(t)$  and using the estimate (40)

$$|\hat{h}_T(t) - \hat{h}(t)| < 2 \log \frac{1 + e^{-\lambda T}}{1 - e^{-\lambda T}},$$

we have

$$\begin{aligned} |s(t) - s_T(t)| &\leq \frac{1}{2} |s(t)| \cdot \left\{ \frac{1 + e^{-\lambda T}}{1 - e^{-\lambda T}} - 1 \right\} \left\{ \frac{1 + e^{-\lambda T}}{1 - e^{-\lambda T}} + 1 \right\} \\ &\leq \frac{2e^{-\lambda T}}{(1 - e^{-\lambda T})^2} |s(t)| \end{aligned} \quad (55)$$

with equality only for  $t = t_k$ , where  $s(t_k) = 0$ .

The error estimate in (55) is conservative since equality in (33) and (36) is attained only for (see Ref. 4)

$$\begin{aligned} h(t) &= \pm M(\operatorname{sgn} t) \cdot \{\operatorname{sgn} \sin \lambda \sqrt{t^2 - T^2}\}, \quad |t| > T \\ &= 0, \quad t \leq T. \end{aligned}$$

Here we have applied the inequality to a high-pass function  $h(t)$ , the "meandering" sawtooth function of (26) with  $h(0) = 0$ , which is quite different from the above extremal function. However, the exponent  $\lambda T$  is probably sharp.

A series for computing  $L_T(t)$  is given in the appendix.

## VI. CONCLUSION

We have seen that signals of a certain class can be reconstructed at any point  $t$  with a relative error of the order of  $e^{-\lambda T}$  from the knowledge of their zeros in an interval  $(t - T, t + T)$ . The reconstruction algorithm can be applied to practical signals of the form

$$s(t) = g_p(t) + \cos ct,$$

where  $g_p(t)$  can be closely approximated by a bandlimited signal,  $g(t)$ , whose spectrum is confined to the interval  $[-b, b]$ . We would like the zeros of  $s(t)$  not to change much when  $g_p$  is replaced by  $g$ . First, we require

$$|g_p(t)| \leq M < 1$$

for some suitable choice of  $M$ , say  $M = 0.75$ . We also need a condition on  $|g_p(t)|$  and  $|g'_p(t)|$  to ensure that  $s(t)$  has only one zero between each extremal of  $\cos ct$ , e.g.,

$$\{g_p(t)\}^2 + \{g'_p(t)/c\}^2 < 1.$$

This condition alone gives  $|g_p(t)| < 1$ , and hence,  $(-1)^k s(k\pi/c) > 0$ , from which we conclude that  $s(t)$  must have an odd number of zeros in  $(k\pi/c, (k+1)\pi/c)$ . It is sufficient to consider  $(0, \pi/c)$ . Suppose the number of zeros (counting multiplicity) in  $(0, \pi/c)$  is more than 1. Then, at some point  $x_k$  in this interval (say, the second zero), we must have  $s(x_k) = 0$  and  $s'(x_k) \geq 0$ ; i.e.,

$$g_p(x_k) = -\cos cx_k,$$

$$g'_p(x_k) \geq c \sin cx_k$$

and then

$$\{g_p(x_k)\}^2 + \{g'_p(x_k)/c\}^2 \geq 1,$$

which is a contradiction. Then, with the two above conditions, we may regard the zeros of  $s(t)$  as perturbations of the zeros of

$$s(t; b) = g(t) + \cos ct,$$

assuming that

$$|g(t) - g_p(t)| \leq \epsilon(b) < 1 - M.$$

Though the calculation is complicated, estimates can be made for the error in reconstructing  $g_p(t)$  from the zeros of  $s(t)$ . Of course, the relative error in  $|s(t) - s_T(t)|$  will not be of the order of  $e^{-\lambda T}$  but of the order of  $|g(t) - g_p(t)|$  (provided  $\lambda T$  is sufficiently large). The algorithm has much in common with the reconstruction of almost band-limited signals from their samples. That is, if we were given

$g_p(k\pi/c)$  and knew that

$$|g(t) - g_p(t)| \leq \epsilon(b),$$

we would use the fact that

$$g(t) = \frac{\pi}{c} \sum_{-\infty}^{\infty} g\left(\frac{k\pi}{c}\right) K\left(t - \frac{k\pi}{c}\right)$$

for any function  $K(t)$  of the form

$$K(t) = \frac{\sin ct}{ct} f_\lambda(t),$$

where  $f_\lambda(t)$  is a bandlimited function whose Fourier transform vanishes outside  $[-\lambda, \lambda]$ ,  $\lambda = c - b > 0$ , and  $f_\lambda(0) = 1$ . Although the series would converge conditionally for  $f(t) \equiv 1$ , it would not necessarily converge when  $g(k\pi/c)$  is replaced by  $g_p(k\pi/c)$ . So, it would be far better to take, for example,

$$f_\lambda(t) = \frac{T}{\sinh \lambda T} \frac{\sin \lambda \sqrt{t^2 - T^2}}{\sqrt{t^2 - T^2}}$$

and obtain an exponential localization in the reconstruction of  $g(t)$  from its samples and then apply the formula to  $g_p(t)$ . The basic difference in the problem solved here is that the zeros of  $s(t)$  give a *nonuniform* sampling of  $g(t)$ , but we make use of the fact that the fundamental function  $h(t)$ , given by (11), is high pass to obtain the exponential localization of the reconstruction.

We should note that the validity of the reconstruction could be extended to signals of the form (3) with implicit restrictions on  $g(t)$  such that  $s(t)$  has only real simple zeros. This does not gain us anything from a practical viewpoint since we do not have a practical way to determine all admissible functions  $g(t)$ , but it does say something interesting about the zeros of such functions, viz., that the zeros allow the exponential localization of the infinite products. The difference now is that we do not have the zeros occurring so regularly and we have to replace the upper bound for  $|h(t)|$  in (16) by something larger than  $\pi$ . This raises an interesting mathematical question: if  $s(t)$  is of the form

$$s(t) = g(t) + \cos ct$$

and  $g$  is bandlimited to  $[-b, b]$ ,  $0 < b < c < \infty$ , and such that  $s(t)$  has only real zeros, what is the longest possible zero-free interval for  $s(t)$ ? It is probably something like  $\pi/\lambda$ , where  $\lambda = c - b$ . Also, what is the optimal truncation of the Hilbert transform kernel in order to estimate  $\hat{h}(t)$  for the special class of  $h(t)$  encountered in this problem?

Once a reasonable reconstruction algorithm has been found, one can ask for the best function  $V_T(t)$ , where  $V_T(t) = 1$  for  $|t| \geq T$  and corresponding constant  $A$  such that

$$s_T(t) = A\{\text{sgn } s(t)\} \prod_{k=-\infty}^{\infty} V_T(t - t_k)$$

best approximates  $s(t)$  of the form

$$s(t) = g(t) + \cos ct$$

for some reasonably smooth class of functions  $g(t)$ ,  $|g(t)| \leq M < 1$ . For example, one might take typical speech signals  $g(t)$  and, with suitable  $c$  and  $T$ , find  $V_T$  empirically.

Some interesting applications may arise when, instead of  $s(t)$ , one transmits  $p(t)s(t)$ , where  $p(t)$  is a low-frequency positive (nonnegative) signal. Then,  $s(t)$  can be recovered by clipping  $p(t)s(t)$  and applying the reconstruction algorithm. For example, in single-sideband transmission of  $x(t)$  it is advantageous to transmit the carrier  $\cos ct$  for purposes of demodulation; i.e.,  $s(t)$  is of the form (lower sideband)

$$s(t) = (1 + x(t))\cos ct + \hat{x}(t)\sin ct,$$

where  $x(t)$  is bandpass,  $[a, b]$  and  $[-b, -a]$ ,  $0 < a < b < c$ , and  $|x(t)| < 1$ . Here, if  $x(t)$  is a speech signal, one could take  $p(t)$  to be a low-frequency (syllabic-frequency) envelope of  $x(t)$  and transmit  $p(t)s(t)$  to reduce the power in the carrier, and then recover  $s(t)$  at the receiver. The disadvantage is more sensitivity to noise, but this added sensitivity occurs only when  $p(t)$  is small, so  $p(t)$  could be detected at the receiver and used as a squelch control to mute the noise portions.

It appears feasible to construct analog circuitry for effecting the reconstruction; the singularity in  $L_T(t)$  is not bad, and for practical purposes,  $L_T(t - T)$  can be approximated by the impulse response of a realizable filter. The pulse train  $\sum \delta(t - t_k)$  can be ac coupled into the filter to obtain  $\hat{h}_T(t - T)$  at the output, since the ac coupling gives (for sufficiently large time constant) very nearly  $(\sum \delta(t - t_k) - c/\pi)$  as input to the filter. The fact that (the approximation to)  $\hat{h}_T$  remains finite means that  $\exp \hat{h}_T(t)$  is not a good approximation to  $|2s(t)|$  near the zeros of  $s(t)$ ; however, this is not important. Also, the problem of delaying  $\text{sgn } s(t)$  for multiplication by  $\exp \hat{h}_T(t - T)$  can be avoided by using a threshold circuit to detect the "near-zeros" (approximately  $t_k - T$ ) of  $\exp \hat{h}_T(t - T)$ , and then, pulses derived from the threshold circuit can be used to generate  $\text{sgn } s(t - T)$ .

It may be desirable to use a feedback circuit consisting of an operational integrating amplifier and a multiplier connected so that the output  $y(t)$  of the amplifier satisfies

$$y'(t) \doteq \hat{h}'_T(t)y(t).$$

Then,

$$y \doteq M \exp \hat{h}_T(t).$$

Here,

$$\hat{h}'_T(t) = \pi \sum K_T(t - t_k),$$

and one uses a filter whose impulse response approximates  $K_T(t - T)$ , except for  $t$  very near  $T$ . Additional means will probably have to be provided for controlling drift in the integrator (or equivalent offset in the multiplier).

Given the state of the art, a specialized digital computer may be more practical than an analog computer for effecting the reconstruction. The problem encountered here is the quantization of the location of the zeros. Some analysis is required, then, to determine admissible bounds on the quantization errors.

For practical purposes, one need only compute  $s_T(t)$  on a lattice, say  $t = k\pi/c$ . This is a good choice since  $s(k\pi/c) \neq 0$ , and so,  $\hat{h}_T(k\pi/c)$  will be more easily computed in practice. One then would compute

$$g_T(k\pi/c) = s_T(k\pi/c) - \cos(k\pi)$$

and then filter the samples to obtain an approximation to  $g(t)$ . In analog computation this method eases the problem of approximating  $\hat{h}_T(t)$  or  $L_T(t)$  since one does not require the value of  $L_T$  for small arguments.

In connection with this last method, one may be given an unknown translate of  $\text{sgn}\{s(t)\}$ , so some method is required to determine the proper phase for sampling. It can be shown that

$$\{\text{sgn } s(t)\} \cdot \{\text{sgn } \sin(ct + \theta)\} - \frac{2\theta}{\pi}, \quad \text{where } -\frac{\pi}{2} < \theta < \frac{\pi}{2},$$

is high pass, provided  $\theta$  is small enough to allow the zeros of  $s(t)$  and  $\sin(ct + \theta)$  to interlace. This implies that phase-lock circuitry can be used to adjust  $\theta$  to zero, and thus determine the proper phase for sampling, viz., at the zeros of  $\sin ct$ .

Alternatively, one could construct the fundamental function  $h(t)$  by forming an unbiased integral of

$$h'(t) = \pi \sum \delta(t - t_k) - c,$$

where  $\delta(t)$  is the Dirac delta function. An unbiased integral of a high-pass function is a particular integral that is also high pass. For practical purposes, a good approximation to  $h(t)$  can be obtained by forming a narrow pulse  $p(t - t_k)$  at each zero  $t_k$  of  $s$  and then ac coupling  $\sum p(t - t_k)$  into an RC integrator. The zeros of  $h$  that occur between

the pulses are then the proper sampling points, the zeros of  $\sin ct$  (see Refs. 11 and 27).

## VII. ACKNOWLEDGMENTS

I would like to thank D. Slepian for his valuable criticism. Also, I am grateful to Judith B. Seery and M. A. Gatto for furnishing the figures.

## REFERENCES

1. E. C. Titchmarsh, "The Zeros of Certain Integral Functions," *Proc. London Math. Soc.*, 25, 2nd series (1926), pp. 283-302.
2. R. P. Boas, Jr., *Entire Functions*, New York: Academic Press, 1974.
3. B. F. Logan, Jr., "Properties of High-Pass Signals," Doctoral Thesis, Elec. Eng. Dept., Columbia Univ., New York, 1965.
4. B. F. Logan, Jr., "Optimal Truncation of the Hilbert Transform Kernel for Bounded High-Pass Functions," *Proc. Fifth Annual Princeton Conference on Information Sciences and Systems*, Dept. of Elec. Eng., Princeton Univ., Princeton, NJ (March 1971), pp. 10-2.
5. F. Oberhettinger, *Tabellen zur Fourier Transformation*, Berlin: Springer, 1957, pp. 38-9.

## APPENDIX

### Series for Computing $L_T(t)$

Replacing  $t$  in (42d) by  $xT$ , we have

$$\begin{aligned} L_T(xT) &= \log|x| + F(x; \lambda T), & |x| < 1 \\ &= 0, & |x| > 1, \end{aligned} \quad (56)$$

where

$$F(x; \beta) = \int_x^1 \frac{\sqrt{1-t^2} - (\sinh \beta \sqrt{1-t^2})/\sinh \beta}{t\sqrt{1-t^2}} dt \quad |x| < 1. \quad (57)$$

The integral in (57) can be evaluated with the aid of the identity

$$\frac{\sinh \beta \sqrt{1-t^2}}{\beta \sqrt{1-t^2}} = \sqrt{\pi/2\beta} \sum_{n=0}^{\infty} \frac{(-\beta t^2/2)^n}{n!} I_{n+1/2}(\beta), \quad (58)$$

where

$$\begin{aligned} \sqrt{\pi/2\beta} I_{1/2}(\beta) &= \frac{\sinh \beta}{\beta}, \\ \sqrt{\pi/2\beta} I_{3/2}(\beta) &= -\frac{\sinh \beta}{\beta^2} + \frac{\cosh \beta}{\beta}, \\ \sqrt{\pi/2\beta} I_{5/2}(\beta) &= \left(\frac{3}{\beta^3} + \frac{1}{\beta}\right) \sinh \beta - \frac{3}{\beta^2} \cosh \beta, \end{aligned}$$

and, in general,

$$\sqrt{\pi/2\beta}I_{n+1/2}(\beta) = (2\beta)^{-1}\{R[n + 1/2, -\beta]e^\beta - (-1)^n R[n + 1/2, \beta]e^{-\beta}\},$$

where

$$\begin{aligned} R\left\{n + \frac{1}{2}, \beta\right\} &= 1 + \frac{(n+1)!}{1!\Gamma(n)}(2\beta)^{-1} + \frac{(n+2)!}{2!\Gamma(n-1)}(2\beta)^{-2} \\ &\quad + \dots + \frac{(2n)!(2\beta)^{-n}}{n!} \\ &= \sum_0^n \frac{(n+k)!}{k!(n-k)!}(2\beta)^{-k} \end{aligned}$$

and

$$R\{1/2, \beta\} = 1.$$

Alternatively, if we set

$$\phi_n(\beta) = \sqrt{\pi/2\beta}I_{n+1/2}(\beta) \equiv \beta^n \left(\frac{1}{\beta} \frac{d}{d\beta}\right)^n \frac{\sinh \beta}{\beta}, \quad (59)$$

we have the recurrence relation,

$$\phi_{n+1}(\beta) = \phi_{n-1}(\beta) - \frac{(2n+1)}{\beta} \phi_n(\beta). \quad (60)$$

In this notation we have

$$\frac{\sinh \beta \sqrt{1-t^2}}{(\sinh \beta) \sqrt{1-t^2}} = \sum_{n=0}^{\infty} \frac{(-\beta t^2/2)^n}{n!} \frac{\phi_n(\beta)}{\phi_0(\beta)}, \quad (61)$$

and

$$F(0, \beta) = - \sum_{n=1}^{\infty} \frac{(-\beta/2)^n}{(2n)n!} \frac{\phi_n(\beta)}{\phi_0(\beta)}, \quad (62)$$

and

$$F(x, \beta) = F(0, \beta) + \sum_{n=1}^{\infty} \frac{(-\beta x^2/2)^n}{(2n)n!} \frac{\phi_n(\beta)}{\phi_0(\beta)}. \quad (63)$$

## AUTHOR

**Benjamin F. Logan, Jr.**, B.S. (Electrical Engineering), 1946, Texas Technological College; M.S., 1951, Massachusetts Institute of Technology; Hycon-Eastern, Inc., 1955-1956; Eng.D.Sc. (Electrical Engineering), 1965, Columbia University; AT&T Bell Laboratories, 1956—. While at MIT, Mr. Logan was a research assistant in the Research Laboratory of Electronics, investigating characteristics of high-power electrical discharge lamps. Also at MIT he

engaged in analog computer development at the Dynamic Analysis and Control Laboratory. At Hycon-Eastern, Inc., he was concerned with the design of airborne power supplies. He joined AT&T Bell Laboratories as a member of the Visual and Acoustics Research Department, where he was concerned with the processing of speech signals. Currently, he is a member of the Mathematical Research Department. Member, Sigma Xi, Tau Beta Pi.



## Signals Designed for Recovery After Clipping— II. Fourier Transform Theory of Recovery

By B. F. LOGAN, JR.\*

(Manuscript received March 10, 1982)

This paper develops a Fourier transform theory for the recovery of signals of a certain class from their zeros. The class, denoted by  $S(b, c)$ , consists of real-valued signals of the form  $s(t) = g(t) + \cos ct$ , where  $g$  is bandlimited to  $[-b, b]$ ,  $0 < b < c < \infty$ , and such that  $(-1)^k s(k\pi/c) > 0$ , which is satisfied, for example, if  $|g(t)| < 1$ . A very simple method of recovery is given for the case  $c > 3b$ , and a somewhat more complicated method is given for the case  $c > 2b$ . The theory also suggests a novel method of effecting amplitude modulation, which has advantages in high-power applications.

### I. INTRODUCTION

Reference 1 shows that there is a practical way to reconstruct signals  $s(t)$  of a certain class  $S(b, c)$  from their zeros. The class  $S(b, c)$  consists of real-valued signals of the form

$$s(t) = g(t) + \cos ct, \quad (1)$$

where

$$g \text{ is bandlimited to } [-b, b], \quad 0 < b < c < \infty, \quad (1a)$$

and such that

$$(-1)^k s(k\pi/c) > 0, \quad k = 0, \pm 1, \pm 2, \dots \quad (1b)$$

The alternation condition (1b) ensures that  $s$  has only real, simple zeros, one between each extremal of  $\cos ct$ . A practical sufficient

---

\* AT&T Bell Laboratories.

---

Copyright © 1984 AT&T. Photo reproduction for noncommercial use is permitted without payment of royalty provided that each reproduction is done without alteration and that the Journal reference and copyright notice are included on the first page. The title and abstract, but no other portions, of this paper may be copied or distributed royalty free by computer-based and other information-service systems without further permission. Permission to reproduce or republish any other portion of this paper must be obtained from the Editor.

condition for (1b) is

$$|g(t)| < 1, \quad -\infty < t < \infty. \quad (1c)$$

However, (1c) is not necessary.

In Ref. 1 we introduced the so-called "fundamental function" associated with the zeros  $\{t_k\}$  of  $s \in S(b, c)$ ; viz.,

$$h(t) = J(t) - ct, \quad (2)$$

where  $J(t)$  is a jump function increasing by  $\pi$  at each zero  $t_k$ ,  $J(0) = 0$ . We showed that  $h(t)$  is a high-pass function with no spectrum in  $(-\lambda, \lambda)$ , where

$$\lambda = c - b > 0 \quad (3)$$

is the "gap frequency", i.e., the difference between the top frequency of  $g$  and the carrier or "bias" frequency. We also established that

$$-\pi < h(t) < \pi, \quad -\infty < t < \infty, \quad (4)$$

and derived the important relation

$$\log |2s(t)| = \hat{h}(t) = \frac{1}{\pi} - \int_{-\infty}^{\infty} \frac{h(x)}{t-x} dx, \quad (5)$$

where  $\hat{h}$  is the Hilbert transform of  $h$ . From (5) we obtained, using the fact that  $h$  is high-pass, an algorithm for approximating  $s(t)$  just from a knowledge of the zeros of  $s$  in the interval  $(t - T, t + T)$ , the error in the approximation being of the order of  $e^{-\lambda T}$ .

Here we want to consider alternate ways of reconstructing  $s(t)$  that involve additional facts about the Fourier transform of  $h(t)$ . Although the functions we deal with will not, in general, have Fourier transforms in the ordinary sense, we can still attach consistent meaning to the statement "the Fourier transform of  $f$  vanishes over  $E$ ," where  $E$  is the union of a finite number of disjoint intervals. To do this (see Refs. 2 and 3) we simply require  $f$  to be orthogonal to a suitable class of functions that have ordinary Fourier transforms supported on  $E$ . Then we can say that "the Fourier transforms of  $f_1$  and  $f_2$  agree over  $E$  if and only if the Fourier transform of  $(f_1 - f_2)$  vanishes over  $E$ ." We will make free use of the results derived in Ref. 2 stemming from these basic definitions and also the results in Ref. 3 pertaining especially to high-pass functions. There is too much material needed for rigorous treatment to collect here. However, the reader should be able to follow most of the arguments by supposing the functions to have ordinary Fourier transforms or else by supposing the functions to be periodic.

We need not concern ourselves with the nature of the Fourier transform of a bounded function in the sense of Schwartz distributions.

We only need the concept of the Fourier transforms of  $f_1$  and  $f_2$  agreeing over intervals, which has all the utility we require.

Our first result is that for the case of large gap frequency,  $c > 3b$ , we have

$$g(t) = -\frac{\pi}{c} \sum_{-\infty}^{\infty} (\cos ct_k) K(t - t_k), \quad (6)$$

where  $K$  is in  $L_1$  and

$$\begin{aligned} \int_{-\infty}^{\infty} K(t) e^{-i\omega t} dt &= 1, & -b \leq \omega \leq b \\ &= 0, & |\omega| \leq \lambda - b = c - 2b > b. \end{aligned} \quad (7)$$

That is, if  $c > 3b$ , we can simply sample  $-\cos ct$  at the zeros  $t_k$  and then filter the impulses to recover  $g(t)$ . Note that  $g(t_k) = -\cos ct_k$ .

We next establish that the Fourier transforms of the fundamental function  $h$  and the function  $h_n$  agree over  $(-n+1)\lambda, (n+1)\lambda$ , where

$$h_n(t) = -\text{Im} \left\{ \sum_{k=1}^n \frac{(-1)^{k+1}}{k} \gamma^k(t) \right\}, \quad n = 1, 2, \dots \quad (8)$$

and

$$\gamma(t) = 2e^{ict}g(t) + e^{2ict}. \quad (8a)$$

[In (8),  $\text{Im}$  denotes the imaginary part.] The spectrum of the function  $\gamma(t)$  is one-sided, being confined to the interval  $[\lambda, \lambda + 2b]$  and the point  $2c$ . Hence, the Fourier transform of  $\gamma^k(t)$  vanishes over  $(-\infty, k\lambda)$ ,  $k = 1, 2, \dots$ . So in the case  $2\lambda > c$ , i.e.,  $c > 2b$ , the Fourier transforms of  $h$  and  $h_1$  agree over  $(-2\lambda, 2\lambda)$ , where

$$h_1(t) = -2g(t)\sin ct - \sin 2ct. \quad (9)$$

Now low-pass filtering of  $h(t)$  is equivalent to filtering  $h_1(t)$ , provided the cutoff frequency of the filter is no greater than  $2\lambda$ . In case  $2\lambda > c$  we can filter  $h(t)$  with a sideband filter (upper vestigial) to recover a little more than the lower sideband of the signal  $-2g(t)\sin ct$ , rejecting the higher frequency nonlinear components. Then standard sideband detection techniques allow us to recover  $g(t)$ , the details being given later.

In the case  $b < c < 2b$ , nonlinear operations are required to recover  $g(t)$  or  $s(t)$  from  $h(t)$ , i.e., from the zeros of  $s$ . The methods of Analytic Modulation Systems (see Ref. 2) are used here. We may take a filtered version of the analytic signal  $H(t)$ ,

$$H(t) = h(t) + i\hat{h}(t), \quad (10)$$

namely,

$$H_v^*(t) = \int_{-\infty}^{\infty} H(x)K_v(t-x)dx, \quad (11)$$

where the filter kernel  $K_v$  belongs to  $L_1$  and

$$\int_{-\infty}^{\infty} K_v(t)e^{-i\omega t} dt = 1, \quad \lambda \leq \omega \leq \nu, \quad (11a)$$

$$\nu > c. \quad (11b)$$

Both functions here have one-sided spectrum, and since  $h$  is high-pass, the Fourier transform of  $H$  vanishes over  $(-\infty, \lambda)$ . By virtue of (11a), the Fourier transforms of  $H_v^*$  and  $H$  agree over  $(-\infty, \nu)$ .

Next we define

$$G_v^*(t) = \exp\{-iH_v^*(t)\}. \quad (12)$$

We then find that the Fourier transforms of  $G_v^*$  and  $G$  agree over  $(-\infty, \nu)$ , where

$$G(t) = \exp\{-iH(t)\} = 1 + 2e^{ict}g(t) + e^{2ict}. \quad (13)$$

Now, since  $\nu > c$ , we can filter  $G_v^*(t)$ , using a vestigial sideband filter (cutoff frequency  $\nu$ ), which is equivalent to filtering  $G(t)$ , so as to recover a little more than the lower sideband of  $2g(t)\sin ct$  (taking the imaginary part of  $G_v^*(t)$ ). Then we can proceed as before with the standard sideband detection to recover  $g(t)$ . This method allows the minimum bandwidth requirement ( $\nu > c$ ) in filtering operations on  $h$ , and thus eases the problem of obtaining the (unbounded) Hilbert transform  $\hat{h}(t)$ ; i.e.,  $h(t) + i\hat{h}(t)$  is replaced by  $h_v^*(t) + i\hat{h}_v^*(t)$ . Note, however, that in practice two filtering operations are required here,  $h \rightarrow h_v^*$  and  $h \rightarrow \hat{h}_v^*$ , to effect the operation indicated in (11).

Actually, the exponential function in (12) may be replaced by a partial sum of its power series, as detailed later. This option may be convenient in the case of moderately large gap frequencies where only a few terms are required.

The sideband detection required in the previous method can be avoided when (11b) is replaced by  $\nu > 2c$ . Then  $G_v^*(t)$  can be low-pass filtered (cutoff frequency  $\nu$ ) to obtain (all of)  $G(t) \equiv 2e^{ict}s(t)$ . Equivalently, the Fourier transforms of  $e^{-ict}G_v^*(t)$  and  $2s(t)$  agree over  $(-\mu, \mu)$ , where  $\mu = \nu - c > c$ . Denoting the real part of  $e^{-ict}G_v^*(t)$  by  $2s_\mu^*(t)$ , we have

$$s_\mu^*(t) = \frac{1}{2} \{\cos[h_v^*(t) + ct]\} \cdot \exp[\hat{h}_v^*(t)]. \quad (14)$$

This is to be compared with the *basic formula*

$$s(t) = \frac{1}{2} \{\text{sgn } s(t)\} \exp\{\hat{h}(t)\}, \quad (15)$$

which follows from (5). Defining  $J_v^*(t)$ , analogous to  $J(t)$  in (2), by

$$h_v^*(t) = J_v^*(t) - ct, \quad (16)$$

we may write

$$s_\mu^*(t) = \frac{1}{2} \{\cos[J_v^*(t)]\} \cdot \exp\{\hat{h}_v^*(t)\} \quad (17)$$

and then (15), in a similar form,

$$s(t) = \frac{1}{2} \{\cos[J(t)]\} \cdot \exp\{\hat{h}(t)\}. \quad (18)$$

The function  $s_\mu^*(t)$  may be low-pass filtered (cutoff frequency  $\mu$ ) to obtain  $s(t)$ , the resulting formula being a generalization of the basic formula (15).

Finally, a novel method of effecting amplitude modulation is suggested by the fact that for  $s$  in  $S(b, c)$ , the Fourier transforms of the two functions,  $g(t)\sin ct$  and  $(\pi/4) \{\text{sgn } s(t)\} \cdot \{\text{sgn } \sin ct\}$ , agree over  $(-2\lambda, 2\lambda)$ . The square wave then may be filtered to obtain  $g(t)\sin ct$ , provided  $2\lambda > c + b$  or  $c > 3b$ .

## II. FILTERING THE INDUCED SAMPLES OF $g(t)$ FOR THE CASE $c > 3b$

The zeros of a signal  $s$  of the form (1),  $s(t) = g(t) + \cos ct$ , induce a certain "oversampling" of  $g(t)$ . That is, if we denote the zeros of  $s$  by  $\{t_k\}$ ,  $k\pi/c < t_k < (k+1)\pi/c$ , we have

$$g(t_k) = -\cos ct_k, \quad g \text{ bandlimited to } [-b, b]. \quad (19)$$

So, in effect, the zeros  $\{t_k\}$  give us a nonuniform sampling of  $g(t)$  at the rate  $c/\pi$ , and we only need a rate slightly larger than  $b/\pi$  to pin down  $g(t)$ . However, in the general case, nonuniform sampling complicates the recovery problem.

We have given in Ref. 1 a reconstruction formula for  $s(t)$ , based on (5), which may be regarded as one *practical* way of solving the nonuniform sampling problem (19). We could apply that formula to reconstructing only the uniform samples of  $g(t)$ , say  $g(k\pi/c)$ , and then use the fact that

$$g(t) = \frac{\pi}{c} \sum_{-\infty}^{\infty} g(k\pi/c) K\left(t - k\pi/c\right), \quad (20)$$

where  $K$  is any bandlimited function belonging to  $L_1$  whose Fourier transform satisfies

$$\int_{-\infty}^{\infty} K(t)e^{-i\omega t}dt = 1, \quad -b \leq \omega \leq b$$

$$= 0, \quad |\omega| \geq 2c - b. \quad (20a)$$

In engineering terminology, we low-pass filter the uniform samples of  $g$ . The validity of (20) for bounded  $g$  whose Fourier transforms vanish outside  $[-b, b]$  may be established from the fact (see Ref. 2) that  $K$  is a reproducing kernel for  $g$ ,

$$g(t) = \int_{-\infty}^{\infty} g(x)K(t-x)dx, \quad (21)$$

and the fact that (for each  $t$ )

$$\int_{-\infty}^{\infty} g(x)K(t-x)e^{-i\omega x}dx = 0, \quad |\omega| \geq 2c, \quad (22)$$

i.e., as a function of  $x$ ,  $g(x)K(t-x)$  is a function of  $L_1$  whose Fourier transform vanishes (see Ref. 2) outside  $(-2c, 2c)$ . Then (20) follows by applying the Poisson sum formula to  $g(x)K(t-x)$ ,

$$\int_{-\infty}^{\infty} g(x)K(t-x)dx = \frac{\pi}{c} \sum_{-\infty}^{\infty} g(k\pi/c) K(t - k\pi/c). \quad (23)$$

Now we would like to show that the nonuniform samples of  $g$  at the zeros of  $s$  can be treated in the same way as uniform samples in case  $c > 3b$ .

We consider the logarithmic derivative of  $s$ ,

$$\frac{s'(\tau)}{s(\tau)} = \frac{g'(\tau) - c \sin c\tau}{g(\tau) + \cos c\tau}, \quad \tau = t + iu, \quad (24)$$

which may be written, multiplying numerator and denominator by  $2e^{ic\tau}$ , as

$$\frac{s'(\tau)}{s(\tau)} = \frac{2e^{ic\tau}g'(\tau) + ice^{2ic\tau} - ic}{2e^{ic\tau}g(\tau) + e^{2ic\tau} + 1}. \quad (24a)$$

Then, since  $g'(\tau)$  and  $g(\tau)$  grow no faster than  $A \cos b\tau$  (see Ref. 4, Theorem 6.2.6, p. 83), we have

$$\frac{s'(t + iu)}{s(t + iu)} + ic = O(e^{-\lambda u}), \quad u \rightarrow \infty. \quad (25)$$

From the infinite product representation of  $s(\tau)$  we have

$$\frac{s'(\tau)}{s(\tau)} = \sum_{-\infty}^{\infty} \frac{1}{\tau - t_k}, \quad (26)$$

where the sum converges conditionally. But if we write

$$\begin{aligned} \frac{s'(t + iu)}{s(t + iu)} &= \sum_{-\infty}^{\infty} \frac{1}{t - t_k + iu} \\ &= \sum_{-\infty}^{\infty} \frac{(t - t_k)}{(t - t_k)^2 + u^2} - i \sum_{-\infty}^{\infty} \frac{u}{(t - t_k)^2 + u^2}, \end{aligned} \quad (27)$$

the second sum converges absolutely (see Ref. 4, p. 86). For any fixed  $u > 0$  the second sum is a bounded function of  $t$ , since  $k\pi/c < t_k < (k + 1)\pi/c$ . Then (25) implies that for any fixed  $u > 0$ , the function of  $t$ ,

$$h'(t; u) = \sum_{-\infty}^{\infty} \frac{u}{(t - t_k)^2 + u^2} - c, \quad (28)$$

is a high-pass function whose Fourier transform vanishes over  $(-\lambda, \lambda)$ . The integral of each of the pulses in the sum is  $\pi$ , and the pulses concentrate around the points  $t_k$  as  $u \rightarrow 0$ . Then, if  $f$  belongs to  $L_1$  and its Fourier transform vanishes outside  $(-\lambda, \lambda)$ , we have

$$\int_{-\infty}^{\infty} f(t)h'(t; u)dt = 0, \quad u > 0. \quad (29)$$

Then, letting  $u \rightarrow 0$ , we have

$$\int_{-\infty}^{\infty} f(x)dx = \frac{\pi}{c} \sum_{-\infty}^{\infty} f(t_k). \quad (30)$$

Now if  $\lambda > 2b$ , i.e., if  $c > 3b$ , we can apply (30) to

$$f(x) = g(x)K(t - x),$$

where  $K$  is in  $L_1$  and

$$\begin{aligned} \int_{-\infty}^{\infty} K(t)e^{-i\omega t}dt &= 1, \quad -b < \omega < b \\ &= 0, \quad |\omega| > \lambda - b = c - 2b > b, \end{aligned} \quad (31)$$

to obtain

$$\begin{aligned} g(t) &= \frac{\pi}{c} \sum_{-\infty}^{\infty} g(t_k)K(t - t_k) \\ &= -\frac{\pi}{c} \sum_{-\infty}^{\infty} (\cos ct_k)K(t - t_k) \quad (c > 3b). \end{aligned} \quad (32)$$

That is, the nonuniform samples of  $g$  at the zeros of  $s$ , occurring at the rate  $c/\pi$ , may be filtered as if they were uniform samples, provided  $c > 3b$ . The rate of nonuniform sampling must be three times greater than the Nyquist rate for  $g$  in order to obtain this simple method of

recovery. We merely sample  $\cos ct$  at the zeros of  $s(t)$  and then use appropriate low-pass filtering to recover  $g(t)$ . In this connection, if the phase of the carrier, or high-frequency bias,  $\cos ct$  is not known, it can in practice be obtained from phase-lock circuitry operating on  $\text{sgn } s(t)$ . It has already been noted in Ref. 1 that [cf. eqs. (82) and (83) here]

$$\{\text{sgn } s(t)\} \cdot \{\text{sgn } \sin ct\}$$

is high-pass, which gives a proper condition for phase lock.

In connection with the necessity of the condition  $c > 3b$ , we note that no matter how small  $g$  is, provided  $g \neq 0$ , the nonuniform sampling, though almost uniform, is not perfect in the sense that (32) does not hold (exactly) unless  $c > 3b$ . We could estimate the error in (32) for  $c > b$ , which, with proper choice of  $K$ , will be small for small  $g$  (depending, of course, on how large the gap frequency is). Depending on the application, (32) may give a suitable approximation to  $g(t)$  for  $c$  only somewhat larger than  $b$ .

We note that in (28), letting  $u \rightarrow 0$ , we may write, formally,

$$h'(t; 0+) = h'(t) = \pi \sum_{-\infty}^{\infty} \delta(t - t_k) - c, \quad (33)$$

where  $\delta(t)$  is the Dirac delta function and  $h'(t)$  is interpreted as the derivative of the fundamental function  $h(t)$  defined in (2). So far we have described the Fourier transform of  $h(t)$  only as vanishing over  $(-\lambda, \lambda)$ . We give a further description next.

### III. THE FOURIER TRANSFORM OF THE FUNDAMENTAL FUNCTION

The complex-valued function,

$$H(t) = h(t) + i\hat{h}(t), \quad (34)$$

where  $h$  is the fundamental function and  $\hat{h}$  is the Hilbert transform of  $h$ , has a one-sided spectrum, i.e., its Fourier transform vanishes over  $(-\infty, \lambda)$ . Equivalently (see Ref. 2), it extends as a function analytic in the upper half-plane of the complex variable  $\tau = t + iu$ , satisfying

$$H(t + iu) = 0(e^{-\lambda u}), \quad \begin{array}{l} u \rightarrow \infty \\ (-\infty < t < \infty). \end{array} \quad (35)$$

As Ref. 1 establishes,  $H(t)$  is related to  $s(t)$  by

$$H(\tau) = i \log G(\tau), \quad (36)$$

where

$$G(\tau) = 2e^{i\tau} s(\tau), \quad (37)$$

and we take the principal branch,  $\log(1+z) \rightarrow z$  as  $z \rightarrow 0$ .

The function  $G(\tau)$  is an entire function. Let us set

$$G(\tau) = 1 + \gamma(\tau) = 1 + 2e^{icr} g(\tau) + e^{2icr}, \quad (38)$$

where

$$\gamma(t + iu) = 0\{e^{-\lambda u}\}, \quad u \rightarrow \infty. \quad (38a)$$

For sufficiently large  $u$ , say  $u > u_0$ , we will have  $|\gamma(t + iu)| < 1$  for all  $t$  so that the Taylor series for  $\log G$  converges, i.e.,

$$H(\tau) = i \left[ \gamma(\tau) - \frac{1}{2} \gamma^2(\tau) + \frac{1}{3} \gamma^3(\tau) + \dots \right], \quad (\text{Im } \tau > u_0). \quad (39)$$

The series does not converge everywhere on the real line because we do not have  $|\gamma(t)| < 1$  for  $-\infty < t < \infty$ . However, if we define

$$H_n(\tau) = i \sum_{k=1}^n \frac{(-1)^{k+1}}{k} \gamma^k(\tau), \quad n = 1, 2, \dots, \quad (40)$$

we have

$$\begin{aligned} H(\tau) - H_n(\tau) &= 0 \{ \gamma^{n+1}(\tau) \}, \quad \gamma \rightarrow 0 \\ &= 0 \{ e^{-(n+1)\lambda u} \}, \quad u \rightarrow \infty. \end{aligned} \quad (41)$$

It follows (see Ref. 2) that the Fourier transforms of  $H(t)$  and  $H_n(t)$  agree over  $(-\infty, (n+1)\lambda)$ . Also, the Fourier transforms of  $H(t)$  and  $H_n(t)$  vanish over  $(-\infty, \lambda)$ . Then for any finite  $n$  we may write

$$\begin{aligned} H(t) &= H_n(t) + R_{n+1}(t) \\ &= h_n(t) + i\hat{h}_n(t) + R_{n+1}(t), \end{aligned} \quad (42)$$

where the Fourier transform of  $R_{n+1}(t)$  vanishes over  $(-\infty, (n+1)\lambda)$ , and  $\hat{h}_n$  is the Hilbert transform of  $h_n$ .

So, despite the fact that the infinite series in (39) does not converge for  $u = 0$ , we can still equate the Fourier transforms of  $H(t)$  and the partial sums  $H_n(t)$  of the series over the frequency interval  $(-\infty, (n+1)\lambda)$ . Here again we see the importance of a positive gap frequency  $\lambda$ . Since

$$\gamma(t) = 2e^{ict}g(t) + e^{2ict}, \quad (43)$$

we have an effective way of describing the Fourier transforms of  $h(t)$  and  $\hat{h}(t)$  over intervals  $(-(n+1)\lambda, (n+1)\lambda)$ ; i.e., they agree with the Fourier transforms of  $h_n(t)$  and  $\hat{h}_n(t)$ , respectively, over such intervals. These functions in turn are simply related to  $g$  through  $\gamma$ . For example,

$$\begin{aligned} H_1(t) &= i\gamma(t) \\ &= 2ie^{ict}g(t) + ie^{2ict}, \end{aligned} \quad (44)$$

$$\begin{aligned}
 h_1(t) &= \frac{1}{2} H_1(t) + \frac{1}{2} \bar{H}_1(t) \\
 &= -2g(t)\sin ct - \sin 2ct,
 \end{aligned} \tag{45}$$

$$\begin{aligned}
 \hat{h}_1(t) &= \frac{1}{2i} H_1(t) - \frac{1}{2i} \bar{H}_1(t) \\
 &= 2g(t)\cos ct + \cos 2ct.
 \end{aligned} \tag{46}$$

Thus the Fourier transforms of  $h(t)$  and  $-2g(t)\sin ct$  agree over the frequency interval  $(-2\lambda, 2\lambda)$ . Similarly, the Fourier transform of  $\hat{h}(t) = \log 2|s(t)|$  agrees over  $(-2\lambda, 2\lambda)$  with the Fourier transform of  $2g(t)\cos ct$ . Since the Fourier transform of  $g(t)\sin ct$  vanishes outside  $[-b-c, b+c]$ , we see that in case  $2\lambda > b+c$ , i.e.,  $c > 3b$ , we can recover  $-2g(t)\sin ct$  by appropriate filtering of  $h(t)$ . Actually, in case  $c > 3b$ , it is simpler to recover  $g(t)$  by the sampling technique of the previous section.

Next we consider the case  $2\lambda > c$ , i.e.,  $c > 2b$ , in which case there is a relatively simple way of recovering  $g(t)$  from  $h(t)$ .

#### IV. A LINEAR RECOVERY METHOD FOR THE CASE $c > 2b$

Here we need only be concerned with the case  $2b < c \leq 3b$ , since for  $c > 3b$  we have a simpler recovery method. However, in case  $c > 2b$  we still have a method requiring only linear operations.

We have seen that the Fourier transform of the fundamental function  $h(t)$ , defined in (2), agrees over  $(-2\lambda, 2\lambda)$  with that of  $h_1(t)$  in (45) and hence, agrees over  $(-2\lambda, 2\lambda)$  with that of  $-2g(t)\sin ct$ . In case  $2\lambda > c$ , i.e.,  $c > 2b$ , the band  $(-2\lambda, 2\lambda)$  includes the lower sideband of  $-2g(t)\sin ct$  and at least a part of the upper sideband. Then, with proper filtering of  $h(t)$  and subsequent demodulation, we can recover  $g(t)$  by linear operations. In the first place the filtering must eliminate everything outside the band  $(-2\lambda, 2\lambda)$ ; i.e., the higher-order nonlinear terms  $h_n(t)$ ,  $n \geq 2$ , defined in (42). There is nothing in the band  $(-\lambda, \lambda)$  since the Fourier transform of  $h_1$  vanishes over  $(-\lambda, \lambda)$ . So let  $K_1$  denote the kernel (impulse response) of a bandpass filter, where we first require

$$\int_{-\infty}^{\infty} K_1(t)e^{-i\omega t} dt = 0, \quad |\omega| \geq 2\lambda, \tag{47}$$

$$\int_{-\infty}^{\infty} |K_1(t)| dt < \infty, \tag{47a}$$

and define

$$f_1(t) = \int_{-\infty}^{\infty} h(x)K_1(t-x)dx, \quad (48)$$

which is equivalent to

$$\begin{aligned} f_1(t) &= - \int_{-\infty}^{\infty} 2g(x)\sin cx K_1(t-x)dx \\ &= - \int_{-\infty}^{\infty} K_1(x)2g(t-x)\sin \{c(t-x)\}dx. \end{aligned} \quad (48a)$$

Now if we multiply  $f_1(t)$  by  $-\sin ct$  and band limit the result, we should obtain a filtered version of  $g(t)$ . The spectrum of  $f_1$  is confined to the intervals  $[\lambda, 2\lambda]$  and  $[-2\lambda, -\lambda]$ . Then, defining

$$f_2(t) = -f_1(t)\sin ct, \quad (49)$$

we see that the spectrum of  $f_2$  is confined to the union of the intervals  $[\lambda + c, 2\lambda + c]$ ,  $[\lambda - c, 2\lambda - c]$ ,  $[-2\lambda - c, -\lambda - c]$ , and  $[-2\lambda + c, -\lambda + c]$ . (Recall that  $\lambda = c - b$ .) The innermost intervals are the second and fourth; viz.,  $[-b, c - 2b]$  and  $[-c + 2b, b]$ . The outer intervals are  $[2c - b, 3c - 2b]$  and  $[-3c + 2b, -2c + b]$ . We are interested in the case  $2b < c \leq 3b$  and want to retain the spectrum in the inner intervals and eliminate the spectrum in the outer intervals by low-pass filtering. We have ample room for this. So let  $K_2$  be a kernel (impulse response) of a low-pass filter, satisfying

$$\int_{-\infty}^{\infty} K_2(t)e^{-i\omega t}dt = 0, \quad |\omega| \geq 2c - b > 3b \quad (50)$$

$$\int_{-\infty}^{\infty} |K_2(t)|dt < \infty, \quad (50a)$$

and then define

$$g_1(t) = \int_{-\infty}^{\infty} f_2(x)K_2(t-x)dx. \quad (51)$$

We have

$$\begin{aligned} g_1(t) &= - \int_{-\infty}^{\infty} \sin cx f_1(x)K_2(t-x)dx \\ &= - \int_{-\infty}^{\infty} \sin cx K_2(t-x)dx \int_{-\infty}^{\infty} K_1(y)2g(x-y)\sin\{c(x-y)\}dy. \end{aligned}$$

The requirements (47a) and (50a) allow us to interchange the order of integration. Then

$$\begin{aligned} & \int_{-\infty}^{\infty} K_2(t-x)g(x-y)2 \sin cx \sin\{c(x-y)\}dx \\ &= \int_{-\infty}^{\infty} K_2(t-x)g(x-y) \{\cos cy - \cos(cx-cy)\}dx \\ &= (\cos cy) \int_{-\infty}^{\infty} K_2(t-x)g(x-y)dx, \end{aligned} \tag{51a}$$

the other term dropping out since, for each  $y$ , the Fourier transform of  $g(x-y)\cos(2cx-cy)$  vanishes over  $(-2c+b, 2c-b)$ . Thus we have

$$g_1(t) = \int_{-\infty}^{\infty} g(x)K_3(t-x)dx, \tag{52}$$

where

$$K_3(t) = \int_{-\infty}^{\infty} \{K_1(y)\cos cy\} \cdot K_2(t-y)dy. \tag{52a}$$

So  $g_1(t)$  is in fact a filtered version of  $g(t)$ . Denoting by  $\overset{\sim}{K}_i(\omega)$  the Fourier transform of  $K_i(t)$ , the overall filter response is given by

$$\overset{\sim}{K}_3(\omega) = \frac{1}{2} \left\{ \overset{\sim}{K}_1(\omega+c) + \overset{\sim}{K}_1(\omega-c) \right\} \cdot \overset{\sim}{K}_2(\omega). \tag{53}$$

So, if in addition to the requirements (47) and (50) we require

$$\frac{1}{2} \left\{ \overset{\sim}{K}_1(\omega+c) + \overset{\sim}{K}_1(\omega-c) \right\} \cdot \overset{\sim}{K}_2(\omega) = 1, \quad |\omega| < b, \tag{54}$$

then we will have, with  $g_1$  defined in (51),

$$g_1(t) = g(t). \tag{55}$$

Conceptually, the simplest way to satisfy (54) is to require  $K_1$  to be a vestigial sideband filter with linear cutoff characteristic, i.e., assuming  $2b < c \leq 3b$ ,

$$\begin{aligned} \overset{\sim}{K}_1(\omega) &= \frac{1}{2} \cdot \frac{2\lambda - \omega}{2\lambda - c}, \quad |\omega - c| \leq c - 2b \\ &= 1, \quad \lambda \leq \omega \leq 2b, \end{aligned} \tag{56}$$

and, of course,

$$\begin{aligned}\tilde{K}_1(\omega) &= \tilde{K}_1(-\omega) \\ \tilde{K}_1(\omega) &= 0, \quad |\omega| > 2\lambda.\end{aligned}$$

Then  $K_2$  is a low-pass filter with gain of 2 in the passband; i.e.,

$$\begin{aligned}\tilde{K}_2(\omega) &= 2, \quad |\omega| \leq b \\ &= 0, \quad |\omega| \geq 2c - b > 3b.\end{aligned}\tag{57}$$

We should note that the multiplication of  $f_1(t)$  by  $-\sin ct$  in (49) can be replaced by multiplication with  $-\pi/4 \operatorname{sgn}\{\sin ct\}$ , since the additional high-frequency terms drop out in (51a). That is, a switch-type multiplier may be used in the demodulation process, thereafter making appropriate gain corrections.

## V. A GENERAL RECOVERY METHOD

In case  $\lambda$  is not greater than  $b$ , i.e.,  $c$  is not greater than  $2b$ , nonlinear operations are required to recover  $s(t)$  or  $g(t)$ . The general method here, which makes further use of the ideas developed in the Theory of Analytic Modulation Systems (see Ref. 2), affords an alternative to the method in Ref. 1. In effect, the method here allows the Hilbert transform in (11) to be replaced by a filtered version. This modification must be taken into account in subsequent operations.

The method is best explained in terms of the functions with one-sided spectrum, i.e., the functions  $G$  and  $H$  in (36),

$$H(t) = i \log G(t) = i \log[1 + \gamma(t)] = h(t) + i\hat{h}(t),\tag{58}$$

where

$$G(t) = 2e^{ict}s(t)$$

and

$$\gamma(t) = 1 + 2e^{ict}g(t) + e^{2ict}.$$

We have already noted that the Fourier transforms of  $H(t)$  and  $H_n(t)$ , defined by

$$H_n(t) = i \sum_{k=1}^n \frac{(-1)^{k+1}}{k} \gamma^k(t),\tag{59}$$

vanish over  $(-\infty, \lambda)$  and agree over  $(-\infty, (n+1)\lambda)$ .

Let us denote by  $H_\nu^*(t)$  any function such that the Fourier transforms of  $H(t)$  and  $H_\nu^*(t)$  agree over  $(-\infty, \nu)$ . In particular,  $H_\nu^*$  may be any function of the form

$$H_\nu^*(t) = \int_{-\infty}^{\infty} H(x)K_\nu(t-x)dx,\tag{60}$$

where  $K_\nu$ , in the interesting case  $\nu > \lambda$ , satisfies

$$\int_{-\infty}^{\infty} K_\nu(t) e^{-i\omega t} dt = 1, \quad \lambda \leq \omega \leq \nu, \quad (61)$$

with

$$\int_{-\infty}^{\infty} |K_\nu(t)| dt < \infty. \quad (61a)$$

Or we may take  $H_\nu^*(t)$  to be any function of the form

$$H_\nu^*(t) = i \sum_{k=1}^{\infty} a_k \gamma^k(t), \quad (62)$$

where the  $a_k$  decrease rapidly enough and

$$a_k = \frac{(-1)^{k+1}}{k} \text{ for } 1 \leq k \leq n, \quad \text{where } (n+1)\lambda \geq \nu. \quad (62a)$$

Now let us denote by  $G_\nu^*(t)$  any function such that the Fourier transforms of  $G(t)$  and  $G_\nu^*(t)$  agree over  $(-\infty, \nu)$ . Since

$$G(t) = 1 + 2e^{ict}g(t) + e^{2ict},$$

and  $g(t)$  is real, we can recover  $g(t)$  from any such function  $G_\nu^*(t)$  provided  $\nu > c$ , which is to say all we need is a little more than the lower sideband of  $g(t)\sin ct$  or  $g(t)\cos ct$ .

We have the inverse relation between  $G(t)$  and  $H(t)$ ; viz.,

$$G(t) = \exp\{-iH(t)\}, \quad (63)$$

and as shown in Ref. 2, the Fourier transforms of  $G(t)$  and  $\exp\{-iH_\nu^*(t)\}$  agree over  $(-\infty, \nu)$ . So we may take

$$G_\nu^*(t) = \exp\{-iH_\nu^*(t)\}, \quad \nu > c, \quad (64)$$

where  $H_\nu^*(t)$  is any function of the form (50).

Since the Fourier transforms of  $H(t)$  and  $H_\nu^*(t)$  vanish over  $(-\infty, \lambda)$ , the Fourier transform of the  $n$ th power of  $H_\nu^*(t)$  vanishes over  $(-\infty, n\lambda)$ . So we may take, if we prefer,

$$G_\nu^*(t) = \sum_{k=0}^n \frac{1}{k!} [-iH_\nu^*(t)]^k, \quad (n+1)\lambda \geq \nu > c. \quad (65)$$

This last form may be preferable to (64) for moderately large gap frequencies, for example,  $3\lambda > c$ . For small gap frequencies there would appear to be no practical reason for preferring a large-degree polynomial in (65) to the exponential in (64). In general, if  $2\lambda \leq c$ , then nonlinear operations are required to obtain a suitable  $G_\nu^*(t)$ . We can modify this statement in case  $g(t)$  itself has a spectral gap about the

origin. Then we could recover  $g(t)$  from  $G_v^*(t)$  when  $\nu$  is slightly less than  $c$ . For example, in this case if  $2\lambda = c$ , we could take  $n = 1$  in (65).

Whether we choose (64) or (65), we have the Fourier transforms of  $-\text{Im}\{G_v^*(t)\}$  and  $-2g(t)\sin ct$  agreeing over  $(-\nu, \nu)$ ,  $\nu > c$ . Then the recovery problem is essentially that of Section IV, except there the Fourier transforms of  $h(t)$  and  $-2g(t)\sin ct$  agree over  $(-2\lambda, 2\lambda)$ ,  $2\lambda > c$ . So, with obvious modifications of the cutoff frequencies of the filters, the recovery process in Section III applies to the general case when  $h(t)$  is replaced by  $-\text{Im}\{G_v^*(t)\}$ ,  $\nu > c$ .

We have

$$H_v^*(t) = h_v^*(t) + i\hat{h}_v^*(t). \quad (66)$$

So the general recovery method allows  $\hat{h}(t)$  to be replaced by a function  $\hat{h}_v^*(t)$ , whose Fourier transform agrees with that of  $\hat{h}(t)$  only over the interval  $(-\nu, \nu)$ ,  $\nu > c$ . In particular,  $\hat{h}_v^*(t)$  could be bandlimited to a larger interval. Alternatively,  $\hat{h}_v^*(t)$  could be obtained from  $h(t)$  by a transversal filter having the appropriate periodic frequency response.

In practice, all the required operations can only be approximated. As contrasted to the method in Ref. 1, complexity in the recovery method here is exchanged for simplicity in approximating the Hilbert transform of  $h(t)$ .

We now want to specialize to the case  $\nu \geq 2c$  and obtain a formula for  $s(t)$  analogous to that in Ref. 1.

## VI. A GENERALIZATION OF THE BASIC FORMULA

From (5) we have

$$s(t) = \frac{1}{2} \{\text{sgn } s(t)\} \cdot \exp\{\hat{h}(t)\}. \quad (67)$$

We call this the basic formula for recovery of  $s(t)$  from  $\text{sgn } s(t)$  or, equivalently, from the fundamental function  $h(t)$  defined in (2).

In Ref. 1, the practicality of (67) was demonstrated by using the fact that the Fourier transform of  $h(t)$  vanishes over  $(-\lambda, \lambda)$ . Here we give a generalization of (67), which may be preferred in analog implementations.

We take  $H_v^*(t)$  to be any function of the form (60) where  $\nu > 2c$ , and set

$$G_v^*(t) = \exp\{-iH_v^*(t)\}, \quad (68)$$

as in (64). Now we have the Fourier transforms of  $G(t)$  and  $G_v^*(t)$  agreeing over  $(-\infty, \nu)$  where  $\nu > 2c$ . Recall that

$$G(t) = 2e^{ict}s(t),$$

and, therefore, its Fourier transform vanishes outside  $[0, 2c]$ . So we

can multiply  $G_\nu^*(t)$  by  $e^{-ict}$  and then, with appropriate filtering, recover  $2s(t)$ .

Let us define then

$$2s_\mu^*(t) = \text{Re}\{e^{-ict}G_\nu^*(t)\}. \quad (69)$$

Since  $s(t)$  is real, the Fourier transforms of  $s(t)$  and  $s_\mu^*(t)$  agree over the interval  $(-\mu, \mu)$  where  $\mu = \nu - c > c$ .

In (68) we set

$$H_\nu^*(t) = h_\nu^*(t) + ih_\nu^*(t),$$

and then write (69) as

$$s_\mu^*(t) = \frac{1}{2} \{\cos[h_\nu^*(t) + ct]\} \cdot \exp\{\hat{h}_\nu^*(t)\}, \quad (70)$$

and note the similarity to (67). To carry this a bit further, we recall the definition (2) of  $h$ ,

$$h(t) = J(t) - ct, \quad (71)$$

where  $J(t)$  is a jump function increasing by  $\pi$  at each zero of  $s(t)$ ,  $J(0) = 0$ . We may define  $J_\nu^*(t)$  in an analogous way by setting

$$h_\nu^*(t) = J_\nu^*(t) - ct. \quad (72)$$

Since  $h_\nu^*(t)$  is a filtered version of  $h(t)$ , their Fourier transforms agreeing over  $(-\nu, \nu)$ , we may think of  $J_\nu^*(t)$  as a filtered version of  $J(t)$ , although the corresponding convolution with  $J(t)$  alone need not make sense.

Now we may write

$$s_\mu^*(t) = \frac{1}{2} \{\cos[J_\nu^*(t)]\} \cdot \exp\{\hat{h}_\nu^*(t)\}, \quad (73)$$

and observing that  $\{\text{sgn } s(t)\} = \cos[J(t)]$ ,

$$s(t) = \frac{1}{2} \{\cos[J(t)]\} \cdot \exp\{\hat{h}(t)\}. \quad (74)$$

This is the analogy we seek. Now  $s(t)$  may be obtained by bandlimiting  $s_\mu^*(t)$ ; i.e.,

$$s(t) = \int_{-\infty}^{\infty} s_\mu^*(x)K_{c,\mu}(t-x)dx, \quad (75)$$

where  $K_{c,\mu}(t)$  belongs to  $L_1$  and satisfies

$$\begin{aligned} \int_{-\infty}^{\infty} K_{c,\mu}(t)e^{-i\omega t}dt &= 1, & |\omega| &\leq c \\ &= 0 & |\omega| &\geq \mu > c. \end{aligned} \quad (76)$$

We may regard (74) as a limiting case ( $\mu \rightarrow \infty$ ) of (75). That is, (75) is a generalization of (74).

## VII. NOTE ON HIGH-POWER AMPLITUDE MODULATION

Compared to conventional modulators, switching-type modulators have the advantage that little power is dissipated in the switches (e.g., transistors). Of course they also have the advantage of easily effecting linear modulation. The disadvantage is the introduction of high-frequency components, which must be removed by filtering. However, if the filter has low losses, the high-frequency energy is, for the most part, stored in the reactive elements of the filter, resulting in an efficient modulation system.

If  $g(t)$  is bandlimited to  $[-b, b]$  and we wish to modulate  $\sin ct$  with  $g(t)$ , then a straightforward method to do this with a switching-type modulator is to form

$$\begin{aligned} f(t) &= g(t) \{\text{sgn} \sin ct\} \\ &= \frac{4}{\pi} \left[ g(t) \sin ct + \frac{1}{3} g(t) \sin 3ct + \dots \right], \end{aligned} \quad (77)$$

and then, assuming  $c > b$ , an output filter may be designed to deliver  $4/\pi g(t) \sin ct$  to the load.

In high-power applications, the disadvantage of this method is that the input  $g(t)$  to the switches must furnish the power to the load. That is, high-power baseband amplifiers are required. An interesting alternative is suggested by the results in Section III.

There we showed that the Fourier transforms of  $h(t)$  and  $-2g(t) \sin ct$  agree over  $(-2\lambda, 2\lambda)$  where  $\lambda = c - b$ .

Recall that

$$h(t) = J(t) - ct, \quad (78)$$

where  $J(t)$  is a jump function with  $J(0) = 0$ , which increases by  $\pi$  at each zero of the function  $s(t)$ ,

$$s(t) = g(t) + \cos ct. \quad (79)$$

Now denote by  $\sigma(t)$  the periodic sawtooth function,

$$\begin{aligned} \sigma(t) &= \frac{\pi}{2} - ct, \quad 0 < t \leq \pi/c \\ \alpha \left( t + \frac{\pi}{c} \right) &= \sigma(t). \end{aligned} \quad (80)$$

This function, associated with  $\log(1 - e^{i2ct})$ , has the Fourier series

$$\sigma(t) = \sum_{n=1}^{\infty} \frac{1}{n} \sin 2nct. \quad (81)$$

Since  $s(t)$  has one and only one zero between each extremal of  $\cos ct$ , we have

$$J(k\pi/c) = k\pi, \quad k = 0, \pm 1, \pm 2, \dots$$

Now the function  $\phi(t)$ , defined by

$$\phi(t) = h(t) - \sigma(t) = J(t) - ct - \sigma(t), \quad (82)$$

is a pure step function increasing by  $\pi$  at the zeros  $\{t_k\}$  of  $s(t)$  and decreasing by  $\pi$  at the zeros of  $\sin ct$ . We see that  $\phi(0+) = -\pi/2$  and since the zeros of  $s(t)$  and  $\sin ct$  interlace, it is easy to see that we can express  $\phi(t)$  in the form

$$\phi(t) = -\frac{\pi}{2} \{\text{sgn } s(t)\} \cdot \{\text{sgn } \sin ct\}. \quad (83)$$

Clearly, from (81) and (82), the Fourier transforms of  $\phi(t)$  and  $h(t)$  agree over  $(-2c, 2c)$ , and hence, the Fourier transforms of  $\phi(t)$  and  $-2g(t)\sin ct$  agree over  $(-2\lambda, 2\lambda)$ , since  $2c > 2\lambda = 2(c - b)$ .

In order to filter out  $-2g(t)\sin ct$  from  $\phi(t)$  we require  $c + b < 2\lambda$  or  $c > 3b$ . Thus, if  $c > 3b$  we can use (83) as a keying or switching voltage and generate

$$\begin{aligned} f(t) &= M \{\text{sgn } s(t)\} \cdot \{\text{sgn } \sin ct\} \\ &= \frac{4M}{\pi} g(t)\sin ct + \text{hi-freq}, \end{aligned} \quad (84)$$

where  $M$  represents a constant voltage that furnishes power to the load and "hi-freq" represents components of  $f(t)$  outside the band  $(-2\lambda, 2\lambda)$  that may be removed by filtering.

Thus, if we add  $\cos ct$  to  $g(t)$ , and simply require  $|g(t)| \leq 1$ , with  $c > 3b$ , where  $b$  is the "top-frequency" of  $g$  (i.e., add a high-frequency bias larger than  $|g(t)|$ ) and then clip the result to obtain  $\{\text{sgn } s(t)\}$  and then multiply by  $\{\text{sgn } \sin ct\}$ , we obtain a square wave, which we may use to switch transistors alternately between  $\pm M$ , the output having the desired "in-band" component  $(4M/\pi) g(t)\sin ct$ .

Alternatively, we may multiply  $s(t)$  by  $\{\text{sgn } \sin ct\}$  and then clip the result to obtain the keying or switching voltage.

This method clearly has an advantage over the straightforward method of (77) in high-power applications. The disadvantage of both methods is that filters capable of handling high power are required. Conceivably, in some applications (audio) the filtering may not be required.

## VIII. DISCUSSION AND CONCLUSION

Here we have, in essence, detailed the remarkable properties of the zeros  $\{t_k\}$  of any function  $s(t)$  of the form (1). We may regard the description of the Fourier transform of the fundamental function  $h(t) = J(t) - ct$  as summarizing the properties of the zeros  $\{t_k\}$ .

The rude property is that the Fourier transform of  $h$  vanishes over  $(-\lambda, \lambda)$ , where  $\lambda$  is the gap frequency in (1). This means that

$$\frac{1}{\pi} h'(t) = \sum_{-\infty}^{\infty} \delta(t - t_k) - c/\pi,$$

is high-pass, and so provides a quadrature formula for functions  $f$  in  $L_1$  and bandlimited to  $(-\lambda, \lambda)$ , i.e.,

$$\int_{-\infty}^{\infty} g(t) dt = \frac{\pi}{c} \sum_{-\infty}^{\infty} f(t_k).$$

This formula is the basis of the simple recovery procedure for  $c > 3b$ , which is not an uninteresting case, e.g., in recording applications, where  $c$  is the bias frequency.

In the first stage of refinement, the zeros  $\{t_k\}$  have the property that, insofar as regards spectrum in the interval  $(-2\lambda, 2\lambda)$ , the transformation  $s(t) \rightarrow h(t)$  or  $s(t) \rightarrow \sum_{-\infty}^{\infty} \delta(t - t_k)$  is linear. Then, when  $2\lambda > c$ , i.e.,  $c > 2b$ , we have a linear recovery method that we would use in case  $c$  were not larger than  $3b$ . What is involved here is essentially vestigial sideband detection.

In further stages of refinement, the zeros  $\{t_k\}$  have the property that we can equate the Fourier transform of  $h(t)$  (or the pulse train) over frequency intervals  $(-(n+1)\lambda, (n+1)\lambda)$  to the Fourier transform of a finite sum involving no more than the  $n$ th power of  $g(t)$ . For recovery of  $g(t)$  in case  $c < 2b$  the theory of analytic modulation and detection after bandlimiting as developed in Ref. 2 comes into play. The theory given there is specialized here to detection of analytic signals  $z(t)$  of the special form  $z(t) = 2e^{ict}s(t) \equiv G(t)$ , where  $s(t)$  is a real-valued bandlimited signal of still more special form. The analytic "modulation law"  $f(z)$  in this case is  $i \log z$ . We are given

$$h(t) = \text{Re}[i \log\{z(t)\}],$$

and then can obtain  $z(t)$  from

$$z(t) = \exp\{-iH(t)\}, \quad H(t) = h(t) + i\hat{h}(t).$$

This is essentially the basic formula in Ref. 1. However, to allow us as much latitude as possible in approximating  $\hat{h}(t)$ , we assume, in effect, that we are given  $h_v^*(t)$ , a function whose Fourier transform agrees with that of  $h(t)$  over the frequency interval  $(-\nu, \nu)$ . We only require

$\nu > c$ , half the bandwidth of  $z(t)$ , because of the special form of  $z(t)$ . The general recovery method assumes no more than  $\nu > c$ , which requires the vestigial sideband detection techniques in recovery of  $g(t)$  from

$$z_v^*(t) \equiv G_v^*(t) = \exp\{-iH_v^*(t)\}, \quad H_v^*(t) = h_v^*(t) + i\hat{h}_v^*(t).$$

The general recovery method is interesting from a mathematical viewpoint, since we assume no more than is necessary. However, the simplification obtained by requiring  $\nu > 2c$ , as in Section VI, appears to be well worth the price paid in filter requirements, i.e., the filters are required to have prescribed characteristics over the band  $(-\nu, \nu)$ . The resulting recovery formula may be preferred to the basic formula given in Ref. 1, especially for analog implementation.

#### REFERENCES

1. B. F. Logan, Jr., "Signals Designed for Recovery after Clipping—I. Localization of Infinite Products," AT & T Bell Lab. Tech. J., this issue.
2. B. F. Logan, Jr., "Theory of Analytic Modulation Systems," B.S.T.J., 57, No. 3 (March 1978), pp. 491-576.
3. B. F. Logan, Jr., "Properties of High-Pass Signals," doctoral thesis, Elec. Eng. Dept., Columbia Univ., New York, 1965.
4. R. P. Boas, Jr., *Entire Functions*, New York: Academic Press, 1954.

#### AUTHOR

**Benjamin F. Logan, Jr.**, B.S. (Electrical Engineering), 1946, Texas Technological College; M.S., 1951, Massachusetts Institute of Technology; Eng.D.Sc. (Electrical Engineering), 1965, Columbia University; AT&T Bell Laboratories, 1956—. While at MIT, Mr. Logan was a research assistant in the Research Laboratory of Electronics, investigating characteristics of high-power electrical discharge lamps. Also at MIT he engaged in analog computer development at the Dynamic Analysis and Control Laboratory. From 1955 to 1956 he worked for Hycon-Eastern, Inc., where he was concerned with the design of airborne power supplies. He joined AT&T Bell Laboratories as a member of the Visual and Acoustics Research Department, where he was concerned with the processing of speech signals. Currently, he is a member of the Mathematical Research Department. Member, Sigma Xi, Tau Beta Pi.

## Integrated Voice/Data Services on Fasnet

By J. W. MARK\* and J. O. LIMB†

(Manuscript received July 8, 1983)

Fasnet is a high-speed local area network with a pair of unidirectional communication channels. While individual stations control their own access to the medium, global scheduling of the medium for various types of traffic is controlled centrally. Centralized scheduling permits a slot to be endowed with a type, so it is feasible to integrate synchronous and asynchronous traffic services on Fasnet. In this paper we describe a policy for admitting new voice calls into the system and an approximate analysis of the queueing behaviour of data packets in an integrated voice and data services environment. Queueing behaviour can also be studied by means of simulation, which is, however, an expensive undertaking, particularly at high transmission rates, for example, at 100 Mb/s. The approximate method described in this paper allows the performance evaluation for high-speed local area networks.

### I. INTRODUCTION

Packet-switching technology has enhanced the potential for complete integration of different types of traffic on a common transmission facility, more particularly within a local environment where signal propagation delays are relatively small. Over the past decade a number of papers have been published on the integration of voice and data.<sup>1-8</sup>

We will address the problem of integrated voice and data services using a specific local area network (LAN), Fasnet,<sup>9</sup> as the backbone support. The techniques explored and evaluated here would carry over

---

\* University of Waterloo, Waterloo, Ontario, Canada. † AT&T Bell Laboratories; present affiliation Bell Communications Research, Inc.

---

Copyright © 1984 AT&T. Photo reproduction for noncommercial use is permitted without payment of royalty provided that each reproduction is done without alteration and that the Journal reference and copyright notice are included on the first page. The title and abstract, but no other portions, of this paper may be copied or distributed royalty free by computer-based and other information-service systems without further permission. Permission to reproduce or republish any other portion of this paper must be obtained from the Editor.

to other related systems (e.g., certain implicit token-passing systems and some ring networks) with small modifications.

Fasnet is a dual-channel, packet-switched LAN. Channel time is partitioned into contiguous slots, each of a duration long enough to transmit one packet of data plus the necessary overhead to allow for access control, addressing, error checking, etc. A voice source, engaged in a conversation, may be silent (either listening to the other party in the conversation or in a short pause between speech spurts) or active (producing a speech spurt). An active voice source is partitioned into segments, each of length  $T$  seconds. Each segment of voice is mapped into one information packet. The length of an information packet is thus determined by the code rate of the incoming voice source and the transmission rate of Fasnet. To maintain voice continuity, it is necessary to transmit one voice packet of the same source every  $T$  seconds. From the LAN's point of view, to maintain an approximate continuous service, it must offer service to voice once every  $T$  seconds. The initial portion of the  $T$ -second interval will be devoted to serving voice calls. The interval  $T$  between consecutive starts of voice service will be referred to as a service cycle. The service cycle period can be expressed in terms of the number of slots, and it is conceivable that the number of voice sources connected to Fasnet is larger than the number of slots in one service cycle. Obviously, the system cannot accommodate more simultaneously "active" voice source than the number of slots available in one service cycle without degrading the signal in some way; some kind of admission control needs to be exercised.

In this paper we assume that a station may be handling voice, data, or both. If we consider voice only, a station that is not in a voice session will be referred to as *idle*. A *nonidle* station producing a speech spurt (talk spurt) will be referred to as *active*; it will be referred to as *silent* if its voice session is in a silent condition.

From an operational point of view, calls already in progress, whether they be in a talk spurt or in a silent interval, must be guaranteed channel time when needed. Since data can be buffered and voice needs continuity, voice will be given a higher priority than data. New calls that are not admitted will be blocked. In the event that a subscriber is blocked, an appropriate tone (short busy) is returned to the subscriber and he/she would try again at a later time. (Of course a satisfactory system design would provide sufficient channel capacity that such an event would occur with no more than a prespecified probability.) On the other hand, unused voice capacity is available to data traffic until there is an increase in voice traffic. In this paper we propose an admission policy for new calls under the constraint that ongoing sessions are guaranteed channel access and that the average number of active voice calls is controlled to within a small neighbour-

hood of the target operating value,  $N_t$ . (Due to statistical variations in the number of active voice calls and the fact that ongoing voice sessions cannot be dropped, the mean number of active voice calls can only be controlled to within a neighbourhood of  $N_t$ .) We evaluate the performance of data under this admission policy. An alternative strategy has been explored in Ref. 10, in which data traffic is guaranteed a minimum capacity. Voice stations returning from the silent state to the active state are not guaranteed a voice slot, and clipping of a speech spurt can occur as experienced in an overloaded Time Assignment Speech Interpolation (TASI) system.<sup>11</sup> The maximum voice load is thus determined by the amount of clipping that may be tolerated. The study showed that, in the distributed environment of the LAN, performance approached very closely that of an ideal TASI system.

The priority admission mechanism and the data queueing behaviour in Fasnet are similar to those in Welnet.<sup>8</sup> The difference lies in the media access control, the network architecture, and the method of switching from one traffic type to another. In Fasnet, a "dead time", referred to as a sojourn time, usually accompanies switching from one type of service to another. In Welnet, provided the packet transmission time is greater than the propagation delay, there is no dead time due to switching of traffic type. Otherwise, the service disciplines of Fasnet and Welnet are similar.

Allowing voice sessions to capture the channel when needed will cause the service rate for data to fall below the data arrival rate during some epochs when the system is heavily loaded with voice and data. When such an event takes place, the traffic intensity, defined as the ratio of data arrival rate to service rate, will temporarily exceed unity. In this mode of operation, the aggregate data queue will experience a sustained growth with a nonstationary distribution, and the queueing process will be temporarily unstable. An approximate analysis method, based on a periodic switching single-server model and the fluid approximation method,<sup>12</sup> was developed in Ref. 8 to analyze the data queueing behaviour for integrated voice and data services on Welnet. The approximate analysis method involves a decomposition of the queueing process into stationary and nonstationary queues and a determination of the mean queue contribution from each of the operational modes. With a suitable modification to account for the sojourn time, the approximate analysis method developed in Ref. 8 is used to analyze the data queueing behaviour for integrated voice and data services on Fasnet.

This paper is organized as follows: Section II briefly describes the Fasnet architecture, which includes a description of the frame format of a Fasnet slot and the concept of a voice cycle. Section III discusses the evolution of the state equation for voice, which leads to the

proposal of an ad hoc admission policy for new calls in Section IV. Fasnet provides centralized control of classes of traffic, where a class may be a traffic type, a priority, or some combination. However, access by individual stations is a distributed function, being determined by the station itself. It is important to assure that the centralized control is implemented in such a way that service to each traffic type remains fair. (We define a fair system as one in which all active stations have an equal chance to access the common channel.) In Section V we evaluate the performance of data for a "fair" Fasnet, under the new voice admission policy introduced in Section IV and the constraint that ongoing voice calls are guaranteed service.

## II. FASNET ARCHITECTURE

Fasnet uses two channels with unidirectional signal propagation in each.<sup>9</sup> The first station (the head station in Fig. 1a) in each channel exercises centralized access control. In the event the first station malfunctions, the second station senses the lack of timing information and assumes the role of the first station. Since there is complete symmetry in the two channels, we will consider the information flow in one of them only.

Each channel has  $M$  taps, each of which supports a signal processor that handles both transmit and receive functions. The processor will be referred to as a station. Each station will support a number of user machines or processes. The first station permits access to each class by issuing a slot of a given type. A new class of traffic may be admitted

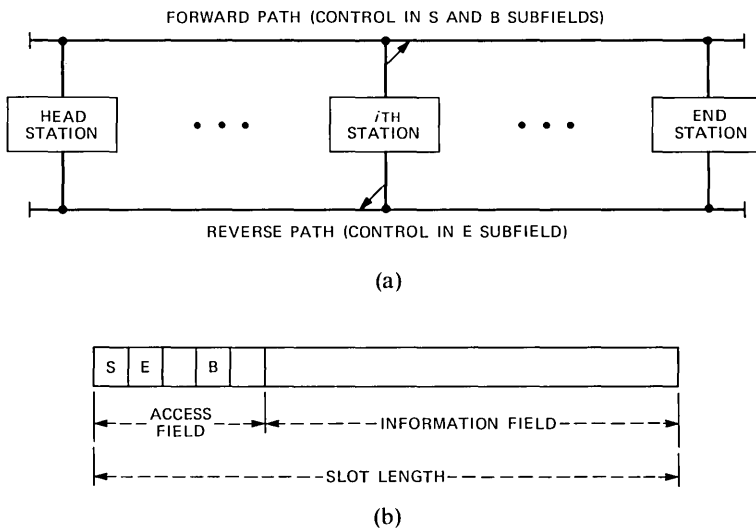


Fig. 1—Fasnet: (a) topology; (b) frame format.

by sending a request to the first station, which, in turn, upgrades its traffic classification to accommodate the new class.

### 2.1 Fasnet frame format

Channel time is divided into slots, each of a duration sufficiently long to transmit an information packet plus control, addressing, and cyclic redundancy checking information. A Fasnet slot comprises an access field and an information field in a manner depicted in Fig. 1. The access field is endowed with an S (Start), an E (End), and a B (Busy) subfield. The S subfield contains a code that designates the start of a sequence of slots of a particular traffic type. The B subfield is a single-bit subfield that indicates whether the information field is full or empty. Individual stations have the capability to read and write into the B bit. Guard times on either side of the B subfield allow for the read and write deliberations. As shown in Fig. 1, the contents of the information field are under the control of the individual stations. A slot is initiated with an empty information field and the content of the B subfield is a "0". If B = "1", the slot is busy; if B = "0", the slot is free. Stations can only write into free slots of the correct type.

### 2.2 Channel occupancy

Let  $r$  in b/s be the code rate of a voice source,  $R$  in b/s be the network transmission rate, and  $H$  be the number of overhead bits.  $H$  includes the access field, the source/destination addresses, control, and Cyclic Redundancy Check (CRC). Then, the slot length in bits is given by

$$F = H + rT \text{ bits/slot.} \quad (1)$$

The number of bits transmitted by the system in  $T$  seconds is  $RT$ , and the number of bits in an information packet is  $rT$ . The voice cycle length,  $L$ , in slots, is then

$$L = \frac{RT}{H + rT} \text{ slots.} \quad (2)$$

Let  $C = 1$  be the normalized channel capacity, i.e., the channel can be utilized to transmit at most one packet per slot. Since a slot is longer than the time necessary to transmit one information packet, the maximum channel occupancy,  $U_{\max}$ , is

$$U_{\max} \equiv \frac{rT}{H + rT} \text{ slots.} \quad (3)$$

The capacity required to coordinate packet transmission,  $C_s$ , is

$$C_s \equiv C - U_{\max}. \quad (4)$$

### 2.3 Code designations of priority scheduling

A voice cycle repeats every  $L$  slots. All admitted voice sessions are guaranteed one slot per voice cycle. It is expected that the number of slots taken by voice calls during any voice cycle will be less than  $L$  slots so that there will be slots available for data transmissions on a per-cycle basis. The concept of a voice cycle is depicted in Fig. 2, with a single slot expanded to emphasize the characteristics of the access field. The access field of each slot has three subfields, namely, S, E, and B. As indicated in Fig. 1a, the first (or head) station issues slots in the forward path, and the last (or end) station echoes acknowledgment in the reverse path. The S subfield contains a code word that designates the traffic type for that slot. The B subfield contains a token bit to indicate whether the slot is full or empty. The code word in the S subfield is set by the head station when the slot is issued. The B bit is to be set by the transmitting station. The end station observes whether a slot, after traversing the entire channel, is full or empty. If the slot is empty, then every station with the designated type of traffic has transmitted the permitted number of packets. The status of an empty slot is indicated (by the end station) in the E subfield. The occurrence of an empty slot signals the end of one type of service and the start of a new service type. The dead time associated with the circulation of an empty slot, as indicated to the head station by the marked E subfield, has been referred to earlier as the sojourn time.

The S subfield, which takes on one of the code words H, G, V, D, and C, determines the mode of the slot. To ensure "fairness", admission

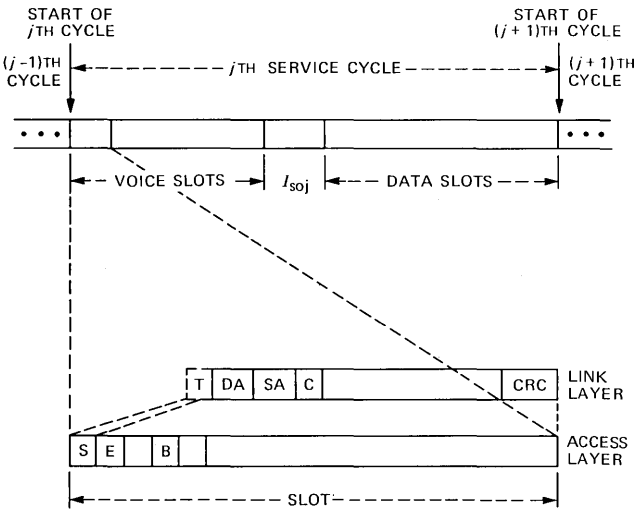


Fig. 2—Service cycle.

of new voice is carried out in two stages. Upon arrival, a new call enters the *wait* state. When the new voice in the wait state sees an H in the S subfield, it transits to the *hold* state and ultimately transmits when a visiting slot is free. The station model for new voice admission is depicted in Fig. 3. The code words H, G, V, D, and C have the following connotation:

- H is a type designation that allows new voice in the wait state to transit to the hold state and to start competing for a slot
- G allows new voice in the hold state to start competing for a slot
- V allows old "active" voice to start competing for a slot

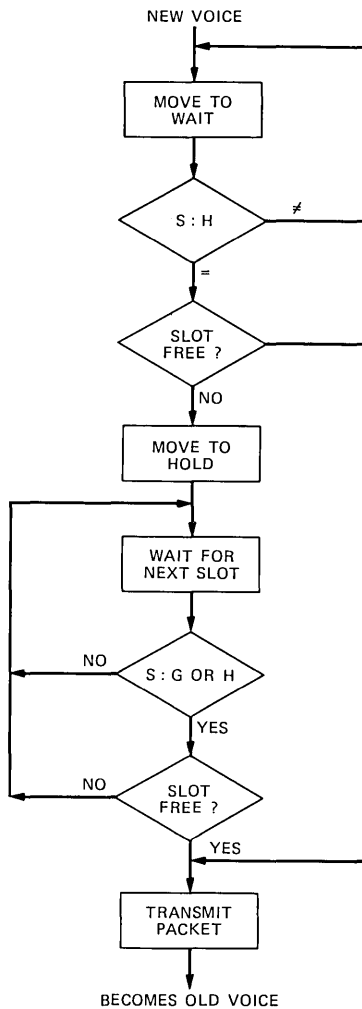


Fig. 3—New voice admission algorithm.

- D allows "active" data stations to transit from the wait state to the hold state and to start competing for a slot
- C allows active data stations in the hold state to start competing for a slot.

A data subcycle differs from a voice subcycle. Since a data subcycle may be interrupted by a voice subcycle, a data subcycle may span more than one service cycle. The access control code, D, starts a new data subcycle after all data stations in the wait state have been served so as to maintain fairness amongst the data stations. There are basically three types of services, namely, new voice calls, old voice calls, and data. Both H and G admit new voice calls, and both D and C allow data stations to transmit. However, each H (D) slot is issued at most once per voice (data) subcycle. That is, an H slot is followed by a string of G slots and a D slot is followed by a string of C slots. Fig. 4 shows the flowchart for the issuance of slots by the head station using feedback information, denoted by an asterisk, that arrives from the end station, after one channel propagation delay. The quantity  $\Omega_j$ , determined in Section IV, is the number of new voice calls to be admitted in the  $j$ th admission cycle.

### III. EVOLUTION OF STATE EQUATION

Consider just the voice subcycle. A station can be either in a voice session or idle. A voice session can be in a talk spurt or silent. Figure 5 shows the state diagram of a voice source.

Figure 5 depicts the state transitions at the start of the  $j$ th service cycle [or at the completion of the  $(j - 1)$ th cycle]. The symbols used have the following notations:

- $n_{j-1}$  denotes the number of *active* voice stations in the  $(j - 1)$ th cycle
- $d_{j-1}$  denotes the number of stations moving to the *silent* state after the completion of the  $(j - 1)$ th cycle
- $D_{j-1}$  denotes the number of stations terminating their voice sessions at the completion of the  $(j - 1)$ th cycle
- $b_j$  denotes the number of stations moving from the silent to the active state during the  $(j - 1)$ th cycle
- $B_j$  denotes the number of stations with new calls that are admitted in the  $j$ th voice cycle
- $G_j$  denotes the number of new calls arriving in the  $j$ th voice cycle.

Then, the number of calls not accepted in the  $j$ th voice cycle is  $G_j - B_j$ . The state equation at the beginning of the  $j$ th voice cycle is

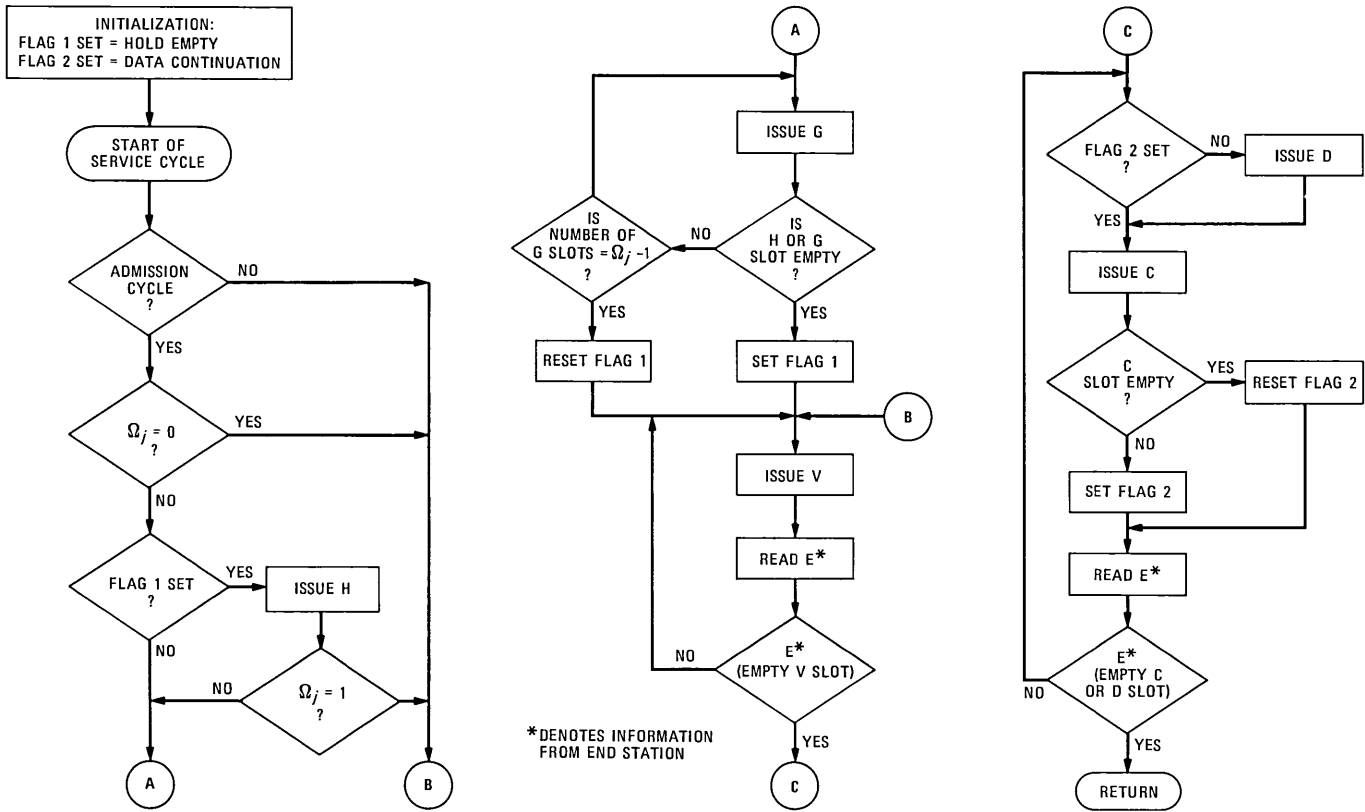


Fig. 4—Flow chart for slot issuance by head station with feedback from end station.

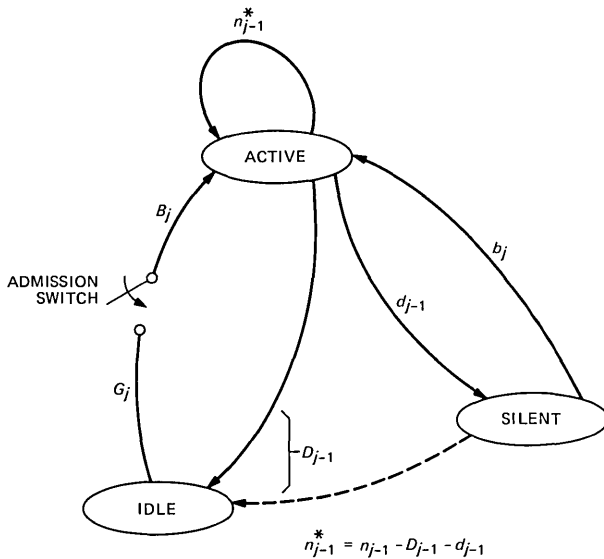


Fig. 5—State transition diagram for voice at start of  $j$ th service cycle, assuming deaths occur while in active state.

$$n_j = n_{j-1} - d_{j-1} - D_{j-1} + b_j + B_j. \quad (5)$$

Under the access control mechanism described in Section 2.1,  $n_{j-1}$  is the only known quantity in the above equation. (It is possible to obtain information about  $D_{j-1}$  and  $d_{j-1}$  by the incorporation of a more complex access control mechanism.) We will describe, in the next section, an admission policy for new calls under the Fasnet structure described in Section II and the state development in eq. (5).

#### IV. NEW VOICE ADMISSION CONTROL

It is desirable to maintain an equilibrium operating state such that the mean number of active voice sessions (in talk spurt) will be  $\bar{n} \approx N_t$ , where  $N_t$  is the target number of active voice sessions. Let  $N$  be the total number of voice sessions to be supported and  $p$  be the fraction of voice sessions that are active. Then,  $\bar{n} = pN$ . In this paper, we let  $p = 0.4$ , i.e., 40 percent of the time a (nonidle) voice source is in talk spurt.

Suppose we call each run of identically designated slots, i.e., H, G, V, D, and C, a sequence denoted by  $S_x$ ,  $x \in \{H, G, V, D, C\}$ . The termination of a sequence is detected by the last station whenever it sees the first empty slot. Before a new sequence of slots can be initiated, a sojourn time,  $I_{soj}$ , elapses.  $I_{soj}$  equals one slot time plus one round trip propagation delay. (The round trip propagation delay equals

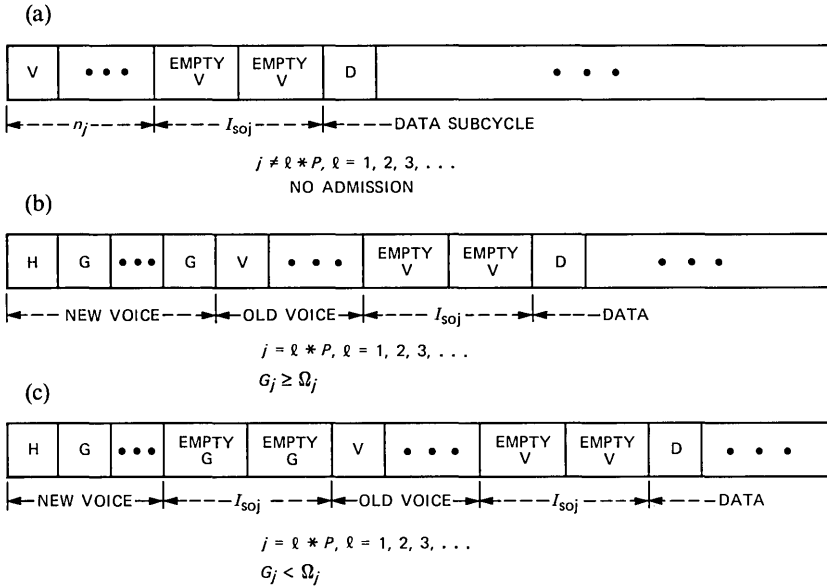


Fig. 6—Concept of sojourn time in  $j$ th cycle.

2.  $\lceil \delta \rceil$  where  $\delta$ , measured in slots, is the propagation delay in one direction, if the starts occur at the same instant in each channel, and the symbol  $\lceil \cdot \rceil$  denotes the integer greater than or equal to its argument.)

At the start of a new service cycle, the first station issues a sequence,  $S_G$ , of  $\Omega_j$  H- or G-designated slots (see Fig. 4). The number actually admitted is

$$B_j = \begin{cases} G_j & \text{if } G_j < \Omega_j \\ \Omega_j & \text{if } G_j \geq \Omega_j. \end{cases} \quad (6)$$

The format of a voice cycle is shown in Fig. 6. A sequence  $S_V$  will follow  $S_G$ . If  $G_j \geq \Omega_j$ , there will be no sojourn time separating  $S_G$  and  $S_V$ . Otherwise, there will be a sojourn time  $\leq I_{soj}$  slots separating  $S_G$  and  $S_V$ . Also note from Fig. 6 that there is at least one sojourn time between an  $S_V$  and an  $S_C$  sequence within a service cycle, where  $S_C$  denotes a sequence of D or C starts.

Admission of new voice calls is controlled by the design parameter  $N_t$ . Since a cycle time is quite short, it is only necessary to admit new voice calls once every  $P$  cycles. Let  $\Delta_j$  be the accumulated number of calls that left the system since the last admission cycle. Then  $\Delta_j$  may be estimated by

$$\hat{\Delta}_j = \sum_{i=j-P+1}^j \frac{n_i}{p} \frac{T}{T_h}, \quad (7)$$

where  $T$  is the cycle length in seconds,  $T_h$  is the holding time of a voice session, and  $p$  is the probability that a voice session is in talk spurt. The value  $n_j/p$  is an estimate of the total number of voice sessions in the system in the  $j$ th cycle. On the assumption that, at steady state, the net movement from silent to talk spurt and vice versa is zero, the maximum number of active voice in the  $j$ th admission cycle can be approximated as

$$n_j = n_{j-P} + B_j - \hat{\Delta}_j. \quad (8)$$

The objective is to drive the system to operate at a point such that the average number of active voice approximately equals the design parameter  $N_t$ . We propose to compute a running average  $\bar{n}_j$  by the following recursive formula:

$$\bar{n}_j = \gamma \bar{n}_{j-1} + (1 - \gamma)n_j, \quad (9)$$

where  $\gamma$ , in the range  $0 < \gamma < 1$ , is a constant factor that determines the relative weighting of the last running average and the current number of active voice. The constant  $\gamma$  also fades the memory of the recursive process and hence affects the size of the moving average window. To have a relatively large window,  $\gamma$  should only be slightly less than unity, e.g.,  $\gamma = 0.98$ . Thus, during start-up,  $\bar{n}_j$  will be small. By the same token, the number admitted is expected to be considerably larger than the number that leaves the system. Then, during start-up, the number of new voice already admitted should play an important role in controlling the admission process. When the system attains an equilibrium condition, the running average will approximately equal  $N_t$  and should assume primary control of the admission process. That is, at equilibrium, the number admitted should balance the number that left the system.

Let  $c_j$  be the parameter that accounts for the difference between the number admitted and the number that left. The number admitted in the past admission cycles should only be remembered until the system attains steady state, i.e., until  $\bar{n}_j$  attains a value close to  $N_t$ . It is proposed to compute the control variable  $c_j$  by a recursive equation of the form

$$c_j = \eta c_{j-1} + B_j - \hat{\Delta}_j, \quad (10)$$

where  $0 < \eta < 1$  is chosen to fade the memory at an appropriate rate.  $\eta$  should be related to the time constant with which the system attains steady state from start-up. In fact, the combination of (9) and (10) forms a robust iterative algorithm so that an optimum choice of  $\eta$  is

not critically important. The strategy is to admit new voice calls whenever  $\bar{n}_j + c_j < N_t$ . The number to be admitted in the  $j$ th cycle is governed by the equation

$$\Omega_j = \max(0, N_t - \bar{n}_j - c_j). \quad (11)$$

We have run numerous tests of the admission control algorithm described in this section. In all cases, the system quickly locks onto a small neighbourhood of the target operating point,  $N_t$ . It is noted that admission control takes effect only when the total number of active voice exceeds  $N_t$ . If the total number of voice calls is fewer than  $N_t$ , so that the total number of active voice in the system is fewer than  $N_t$ , no admission control would be needed, and all calls would be admitted into the system.

## V. QUEUEING ANALYSIS OF DATA PACKETS

Although the topology and the media access protocol of Fasnet<sup>9</sup> differ from those of Welnet,<sup>8</sup> the operational features of the two systems are similar. That is, each of these two systems has a deterministic media access protocol, which allows for priority scheduling and a bounded packet delivery time. With appropriate modifications, the periodic switching model and the mean value approximation method used in Ref. 8 to analyze the data buffer queueing behaviour are applicable here. The queueing analysis described below assumes that the procedure for admitting new voice calls is able to maintain

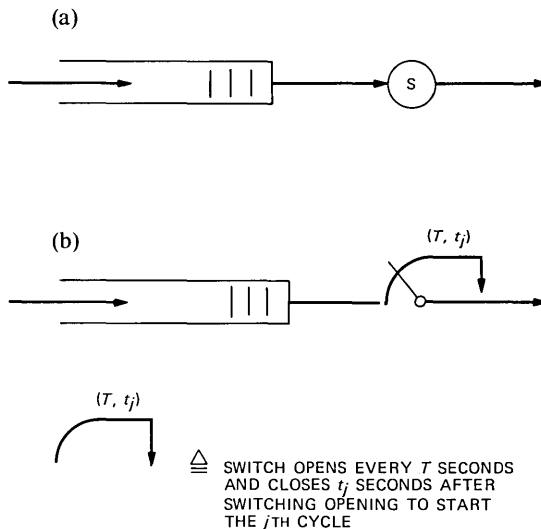


Fig. 7—(a) Single-server model. (b) Periodic switching model.

the voice service operating at the target value  $N_t$ , i.e., the mean number of active voice in the system approximately equals  $N_t$ .

The periodic switching model shown in Fig. 7 opens every  $T$  seconds and closes  $t_j$  seconds after the opening of the switch at the start of the  $j$ th service cycle. Here,  $t_j$  is the time needed to serve  $n_j$  active voice plus the total (i.e., including also those sojourns occurring in the data subcycles) sojourn time incurred in the  $j$ th service cycle. We have hitherto used  $n_j$  to represent the number of active voice calls. Since each active voice occupies one slot per cycle, in what follows,  $n_j$  will also denote the number of slots occupied by voice in the  $j$ th cycle.

Let  $m_j$  denote the number of sojourns in the  $j$ th cycle. We then have

$$t_j = \frac{(n_j + m_j I_{\text{soj}})T}{L}, \text{ in seconds,} \quad (12)$$

where  $T$ ,  $L$ , and  $I_{\text{soj}}$  are as previously defined. The time available for servicing data packets in the  $j$ th cycle is then  $T - t_j$  seconds or  $(L - n_j - m_j I_{\text{soj}})$  slots. Since the transmission of each packet requires one slot time  $(L - n_j - m_j I_{\text{soj}})$ , data packets can be transmitted in the  $j$ th cycle. We define

$$\mu_k = \frac{L - (n_j = k) - m_j I_{\text{soj}}}{T} \text{ packets/s} \quad (13)$$

to be the service rate available to data in the  $j$ th cycle. The mean service rate is then

$$\mu_d = \frac{L - \bar{n} - \bar{m} I_{\text{soj}}}{T} \text{ packets/s.} \quad (14)$$

Let  $\lambda_d$  be the aggregate data arrival rate in packet/s. The data utilization,  $\rho_d$ , is defined by

$$\begin{aligned} \rho_d &= \frac{\lambda_d}{\mu_d} \\ &= \frac{\lambda_d T}{L - \bar{n} - \bar{m} I_{\text{soj}}}. \end{aligned} \quad (15)$$

For stable operation, it is required that  $\rho_d < 1$ . For a given total number of voice calls in the system,  $N$ , there is a small probability (caused by the statistical fluctuation in the number of active voice calls in the  $j$ th cycle) that, in a certain  $j$ th cycle,  $\lambda_j > [(L - (n_j = k) - m_j I_{\text{soj}})]/T$  and the system is said to experience temporary overload, where  $\lambda_j$  is the number of arrivals in the  $j$ th cycle. Under the fluid approximation model to be discussed below, we approximate  $\lambda_j$  by  $\lambda_d$ , the mean arrival rate, and define the data utilization in the  $j$ th cycle by

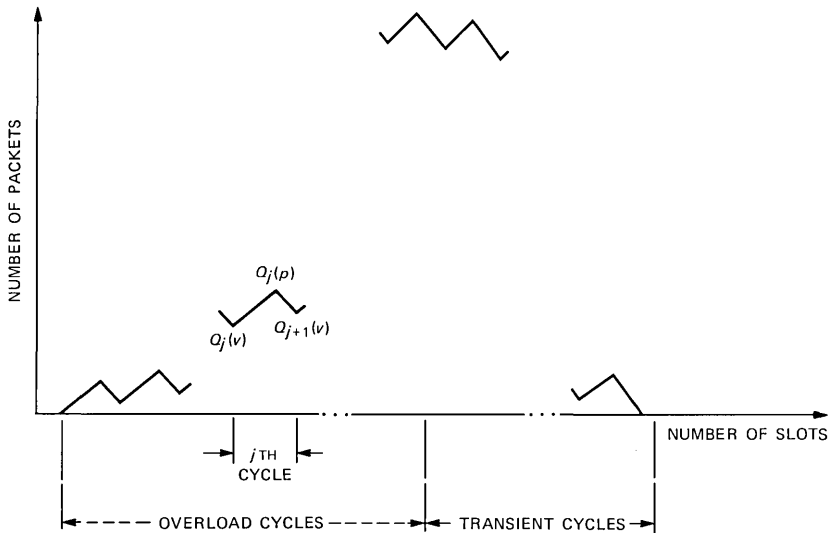


Fig. 8—Fluid approximation model for the  $j$ th cycle.

$$\rho_k = \frac{\lambda_d T}{L - (n_j = k) - m_j I_{soj}} \quad (16)$$

Depending on the value of  $k$ ,  $\rho_k$  can exceed unity.

The mean value, or fluid, approximation method<sup>12</sup> is depicted in Fig. 8, where  $N_c(v)$  is the critical number of active voice at which the service available to data in the fluid approximation model equals the number of data packets that have arrived in the same cycle. The  $j$ th cycle is on the verge of overload when the combination of voice, sojourn time, and data is such that the queue at the end is the same as at the beginning of the  $j$ th cycle, i.e.,  $Q_{j+1} = Q_j$ . At this operating point, the number of active voice is  $N_c(v)$ . If  $n_j > N_c(v)$ , there is a net growth in the queue and  $Q_{j+1} > Q_j$ . The queueing process temporarily becomes unstable and the system experiences overload. Since the number of voice in talk spurt obeys a binomial distribution and since the mean time between transitions from silent to talk spurt, and vice versa, is long compared to a cycle time (e.g., 1.50 seconds compared to 10 ms), once the system enters an overload state, there is every likelihood that it will stay in the overload state for many consecutive service cycles.

To analyze the queueing behaviour, we separate the service cycles into two sets, a stable set in which the queueing process is stationary and an overload set in which the queueing process is nonstationary. In addition, during the interval when the system is servicing voice only, new data arrivals will have to be scheduled for transmission. Let

$\Omega_s$  and  $\Omega_o$  be the sets of stable and overload states, respectively. The average queue in the system is given by the sum of the contributions from the stable and overload states and the temporary queueing due to scheduling:

$$\bar{Q} = \bar{Q}(s) + \bar{Q}(o) + \bar{Q}_{sch}, \quad (17a)$$

where

$$\bar{Q}(s) = E[Q | k \in \Omega_s] \cdot \Pr(k \in \Omega_s) \quad (17b)$$

is the contribution from the stable states,

$$\bar{Q}(o) = E[Q | k \in \Omega_o] \cdot \Pr(k \in \Omega_o) \quad (17c)$$

is the contribution from the overload state, and  $\bar{Q}_{sch}$  is mean queue due to scheduling of the data packets during a service cycle.

An approximate queueing analysis method, based on a decomposition of stable and overload operational modes, was developed in Ref. 8 for the queueing analysis of integrated voice/data services on Welnet. Functionally, the media access protocols of Fasnet and Welnet differ only in that Fasnet may incur a sojourn time whenever a change in the type of traffic to be served takes place. With the incorporation of the sojourn time into the analysis model, the method developed in Ref. 8 can be used to analyze the data queueing behaviour on Fasnet.

When the number of active data stations is small (at light loads), there will be many data subcycles within one service cycle and consecutive data subcycles will be separated by a sojourn time. While the existence of sojourn time represents a loss of channel capacity, not every occurrence of a sojourn affects the data queueing process. The ultimate limit occurs when every data station has packets to be transmitted (as is likely to happen in an overload state). We define the mean number of sojourn times per service cycle, which represents a loss in channel capacity, by

$$\bar{m} = \frac{L - \bar{n}(o) - \bar{m} \cdot I_{soj}}{M \cdot P_{max}} + 1, \quad (18a)$$

where the 1 in the right-hand side of (18a) represents the sojourn between the end of the voice subcycle and the beginning of the data subcycle,  $\bar{n}(o)$  is the mean number of active voice in the overload state,  $M$  is the number of data stations, and  $P_{max} \geq 1$  is the maximum number of packets that an active data station is permitted to send per data subcycle. A value of  $P_{max} > 1$  is beneficial for small  $M$ , so that the mean number of sojourn times in the overload state is a minimum. For  $M > L - N_c(v)$ , a value of  $P_{max} = 1$  suffices. The expression for  $\bar{m}$  can be rearranged to yield

$$\bar{m} = \frac{L - \bar{n}(o) + M \cdot P_{\max}}{M \cdot P_{\max} + I_{\text{soj}}}. \quad (18b)$$

It can be shown that the mean number of voice while in the overload state,  $\bar{n}(o)$ , is given by Ref. 8:

$$\bar{n}(o) = \frac{\sum_{k=N_c(v)+1}^N (n_j = k) \cdot \Pr(n_j = k)}{\sum_{k=N_c(v)+1}^N \Pr(n_j = k)}. \quad (19)$$

From Fig. 8, we deduce that

$$\lambda_d T = L - N_c(v) - \bar{m} I_{\text{soj}}. \quad (20)$$

That is, when the number of active voice  $n_j = N_c(v)$ , the number of packets arrived in the  $j$ th cycle equals the number of packets served in the same cycle. The above equation can be rearranged to yield

$$N_c(v) = L - \lambda_d T - \bar{m} I_{\text{soj}}.$$

Substituting  $\lambda_d T$  by  $\rho_d(L - \bar{n} - \bar{m} I_{\text{soj}})$  from (20) and rearranging, we have

$$N_c(v) = L(1 - \rho_d) + \rho_d \cdot \bar{n} - \bar{m} \cdot I_{\text{soj}}(1 - \rho_d). \quad (21)$$

The parameters  $\bar{m}$  and  $N_c(v)$  are related by a set of transcendental equations.  $\bar{m}$  and  $N_c(v)$  can be computed by the following algorithm:

1. Substitute  $N_c(v)$  for  $\bar{n}(o)$  in (18b) and then combine the result with (21) to obtain

$$N_c(v) = \frac{[L(1 - \rho_d) + \bar{n}\rho_d](M \cdot P_{\max} + I_{\text{soj}}) - I_{\text{soj}}(1 - \rho_d)(L + M \cdot P_{\max})}{I_{\text{soj}}(1 - \rho_d)(L + M \cdot P_{\max})}.$$

2. Calculate  $N_c(v)$ .
3. Using this value of  $N_c(v)$ , calculate  $\bar{n}(o)$  by eq. (19).
4. Calculate  $\bar{m}$  using (18b).
5. Recalculate  $N_c(v)$  using (21).

The approximate analysis model developed in Ref. 8 is based on the fact that the number of active voice obeys a binomial distribution and that the system (for voice) is at equilibrium when the number of active voice equals the mean,  $\bar{n} = pN$ , where  $p$  is the probability that a voice call is in talk spurt and  $N$  is the total number of voice calls in the system. When the number of active voice calls deviates from  $\bar{n}$ , there is a tendency for the system to move towards the equilibrium point.

Define  $d_k$  to be the net drift toward the equilibrium point. Then, at any operating point  $n_j = k$ , the net drift,  $d_k$ , is given by Ref. 8:

$$d_k = \alpha \cdot T \cdot (n_j = k) - \beta \cdot T \cdot (N - (n_j = k)) | k \in \Omega_o \text{ slots/cycle}, \quad (22)$$

where  $\alpha^{-1}$  and  $\beta^{-1}$  are, respectively, the mean holding times of a talk spurt and a silent event and  $T$ , as previously defined, is the cycle length in seconds. With probability  $\text{Pr}[\text{overload}] = \text{Pr}[k \in \Omega_o] = \text{Pr}[n_j > N_c(v)]$ , the system is in the overload state. Once it enters the overload state, the mean time that the system spends in the overload state is a function of the net drift  $d_k$  given by (22). The mean and second moment of the duration that the system spends in the overload state is given by Ref. 8:

$$\begin{aligned} \tau_o &= \frac{\sum_{k=N_c(v)+1}^N \frac{(N - (n_j = k))\text{Pr}(n_j = k)}{d_k}}{\sum_{k=N_c(v)+1}^N (N - (n_j = k))\text{Pr}(n_j = k)} \\ &= \frac{\sum_{k=N_c(v)+1}^N \frac{(N - (n_j = k))\text{Pr}(n_j = k)}{\alpha \cdot T \cdot (n_j = k) - \beta \cdot T \cdot (N - (n_j = k))}}{\sum_{k=N_c(v)+1}^N (N - (n_j = k))\text{Pr}(n_j = k)}, \quad (23) \end{aligned}$$

and

$$s_o = \frac{\sum_{k=N_c(v)+1}^N \frac{(N - (n_j = k))\text{Pr}(n_j = k)}{[\alpha \cdot T \cdot (n_k = k) - \beta \cdot T \cdot (N - (n_j = k))]^2}}{\sum_{k=N_c(v)+1}^N (N - (n_j = k))\text{Pr}(n_j = k)}. \quad (24)$$

The coefficient of variation of the duration in the overload state is then given by

$$C_o^2 \equiv \frac{s_o}{[\tau_o]^2} - 1. \quad (25)$$

It turns out that  $C_o \ll 1$ . This is a consequence of the fact that the increase in the number of active voice, which drives the data queuing process into an overload condition, is a slowly fluctuating process. Thus, the second moment of the overload duration has negligible effect on the queuing behaviour when the system is in the overload state.

As observed in Ref. 8 and depicted in Fig. 9, a transient state always follows an overload state. The chain of service cycles depicted in Fig. 9 will be referred to as an "overload/transient" chain. The contribution to the average queue in the system from an overload/transient chain is given by the queue in a typical overload/transient chain multiplied

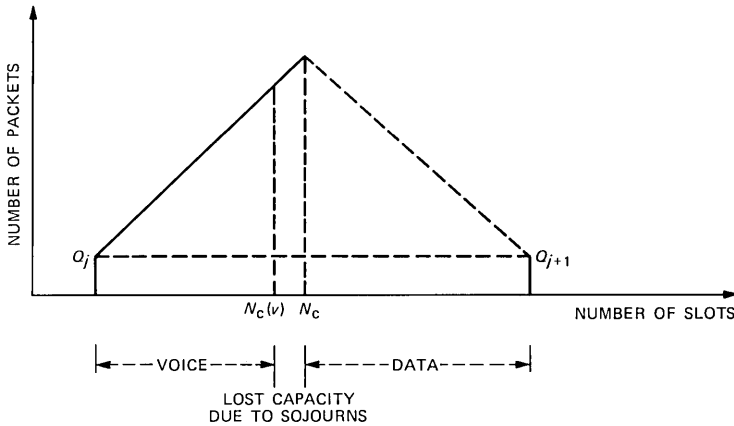


Fig. 9—Chaining of overload/transient cycles.

by the probability of the occurrence of an overload/transient chain. The mean duration of the overload portion of the chain depicted in Fig. 9 is  $\tau_o$ . The queue growth in the overload state is given by the difference of the queue size at the ends of consecutive service cycles, i.e.,  $\Delta Q_j = q_{j+1}(v) - Q_j(v)$ . The average queue growth per cycle will be denoted by  $E[\Delta Q]$ . The average queue growth in an overload state is then given by an accumulation of the growth per cycle over the overload duration, i.e.,

$$\sum_{i=1}^{[\tau_o]} iE[\Delta Q],$$

where  $[x]$  denotes the integer part of  $x + 0.5$ , plus  $\lambda_d N_c(v) P/2R$ , which is the average growth in the cycle when the system enters the transient state. The queue shrinkage will be slightly faster than the queue growth so that the mean duration in the transient state is nominally shorter than  $\tau_o$ . This is due to the fact that the number of active voice while the system is in the overload state is larger than that when the system is in the transient state. The average number of slots available for data per overload cycle is  $L - \bar{n}(o) - \bar{m} \cdot I_{soj}$ ; that per transient cycle is  $L - \bar{n}(t) - \bar{m} \cdot I_{soj}$ , where  $\bar{n}(o)$  and  $\bar{n}(t)$  are the mean number of active voice in the overload and transient states, respectively.  $\bar{n}(o)$  is given by (19), and  $\bar{n}(t) \leq N_c(v)$ . For convenience, we approximate  $\bar{n}(t)$  by  $N_c(v)$  and define

$$h = \frac{L - \bar{n}(o) - \bar{m} \cdot I_{soj}}{L - N_c(v) - \bar{m} \cdot I_{soj}} \leq 1 \quad (26)$$

to be the fractional contribution from the transient portion to the

queue size in an overload/transient chain. Then, the number of packets in an average overload/transient chain is given by Ref. 8:

$$E[Q | k \in \Omega_o] = (1 + h) \left\{ \frac{[\tau_o] \cdot ([\tau_o] + 1)}{2} E[\Delta Q] + \frac{\lambda_d \cdot \bar{n}(o) \cdot P}{2R} \right\}, \quad (27)$$

where

$$E[\Delta Q] = \lambda_d T - \{L - \bar{n}(o) - \bar{m} \cdot I_{soj}\} \quad (28)$$

is the average queue growth per cycle when the system is in an overload state. The average queue contribution from the overload/transient chain is then given by

$$\bar{Q}(o) = E[Q | k \in \Omega_o] \cdot \Pr[k \in \Omega_o]. \quad (29)$$

The stationary contribution can be written as

$$\bar{Q}(s) = \sum_{k=0}^{N_c(v)-1} E[Q | n_j = k] \Pr(n_j = k), \quad (30)$$

where  $E[Q | n_j = k]$  is the mean number of packets in the system given the number of voice in the  $j$ th cycle is less than  $N_c(v)$  and, for Poisson arrivals, is given by the M/G/1 formula:

$$E[Q | n_j = k] = \rho_k + \frac{\rho_k^2(1 + C_d^2)}{2(1 - \rho_k)}. \quad (31)$$

$\rho_k$  is the utilization defined by (16) and  $C_d^2$  is the squared coefficient of variation of service time. Since voice changes slowly compared to a cycle time,  $C_d^2 \ll 1$ .

The Pollaczek-Khinchin M/G/1 formula describes the queueing effect at the imbedded points of the service process which, in our case, correspond to the ends of service cycles. During the initial part of the service cycle when the system is serving voice stations, the data stations experience a temporary queueing. The average temporary queue per cycle corresponds to a delay during which a typical data packet is scheduled for channel access. Depending on the state of the system, the number served in a given cycle may be fewer than the number that has arrived during the same cycle. The queueing of those new arrivals that are not served in the same cycle is accounted for by the M/G/1 formula. To compute the queueing due to scheduling, it is only necessary to consider new arrivals when the system is in the stable mode. Consider the fluid approximation model depicted in Fig. 10. The total number of packets that need to be queued temporarily

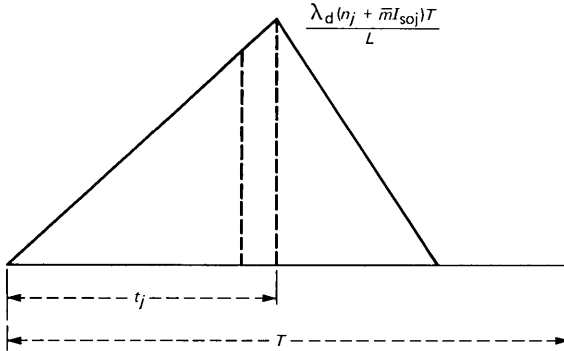


Fig. 10—Fluid approximation model for the evaluation of mean queue due to scheduling.

in the  $j$ th cycle is given by the area under the triangle; the average number of packets in the temporary queue is given by the area divided by the base. Thus, the average number of packets in the temporary queue due to scheduling during one cycle is given by

$$\bar{Q}_{\text{sch}} = \frac{\lambda_d T}{2L} \sum_{k=0}^{N_c^{(v)}} [(n_j = k) + \bar{m} \cdot I_{\text{soj}}] \cdot \Pr(n_j = k). \quad (32)$$

The mean number of packets in the system is then given, as indicated in (17a), by the sum of  $\bar{Q}(o)$ ,  $\bar{Q}(s)$ , and  $\bar{Q}_{\text{sch}}$ , which are prescribed respectively by (29), (30), and (32).

## VI. NUMERICAL RESULTS

Recognizing the difficulty with an exact analysis of the data queueing behaviour in an integrated voice and data service environment, we have introduced an approximate analysis in Section V. Another approach to evaluating the system performance is by means of computer simulation or emulation. Emulation portrays all the steps involved in the actual system. The drawback in an emulation process is that it is extremely time-consuming and that it is not feasible to emulate a high-rate system. We compare the approximate analysis results with those obtained by means of computer emulation. Based on the closeness of the approximate analysis results to those obtained from emulation on a 10-Mb/s Fasnet, we conjecture that the performance results obtained for a high-rate Fasnet (e.g., 100 Mb/s) using the approximate analysis method are reasonable portrayals of system performance.

## 6.1 Simulation

The simulation consisted of an emulation at the packet level. We assume the system operates at 10 Mb/s. The length of the line was assumed to be 2.5 km, resulting in normalized propagation and signal processing delay for a single line of 0.2 slot. Data and voice stations were randomly positioned along the line. We assumed that 142 voice station pairs were in conversation with an additional 20 active data stations. The other parameters used in the simulation are  $r = 64$  kb/s,  $T = 10$  ms, and  $P = 700$  b/packet.

An ongoing voice conversation is modeled as a two-state Markov process. It spends 40 percent of the time in the active state and 60 percent in the silent state (activity factor = 0.4). The average talk spurt duration is 1.5 seconds and the average silent interval is 2.25 seconds, both with an exponential length distribution. All data stations generated traffic at the same mean rate and each station transmits a maximum of three packets from its queue during one data subcycle ( $P_{\max} = 3$ ). Data packets arrive at each station according to a Poisson distribution.

Each simulation run was for 500,000 packets, corresponding to a duration of 35 seconds. The simulation started with voice conversations assigned to talk and silent stations in the same proportion as the steady-state distribution. To ensure that the steady state was reached before data were recorded, statistics were not gathered until after the first 20,000 packets.

Performance is measured in terms of the average number of packets in the system. In a given service cycle, there is temporary queueing when the system is serving the voice stations. The queue at the end of each cycle is smaller than it is during the cycle. The simulation results shown in Fig. 11 reflect the effects of temporary queueing due to scheduling during one service cycle.

For each data point shown in Fig. 11, the results for between five and twenty independent runs were combined. At lower data rates, the variance is small and few runs were required to obtain accurate measures of the mean data queue. At higher data rates, the variance was significantly larger. The simulation did not guarantee that the average amount of voice traffic would be equal to the value used to calculate the theoretical results. This affects the measurement of the average queue size for data since the channel capacity available for data depends directly on the capacity taken by the voice stations. To improve the estimate of the mean queue for data, the average number of active voice conversations (which was measured for each run) was regressed against mean queue and, from this regression, the value at 56.8 ( $0.4 \times 142$ ) active calls (the value used in the calculations) was estimated. An example of this is shown in Fig. 12, where the experi-

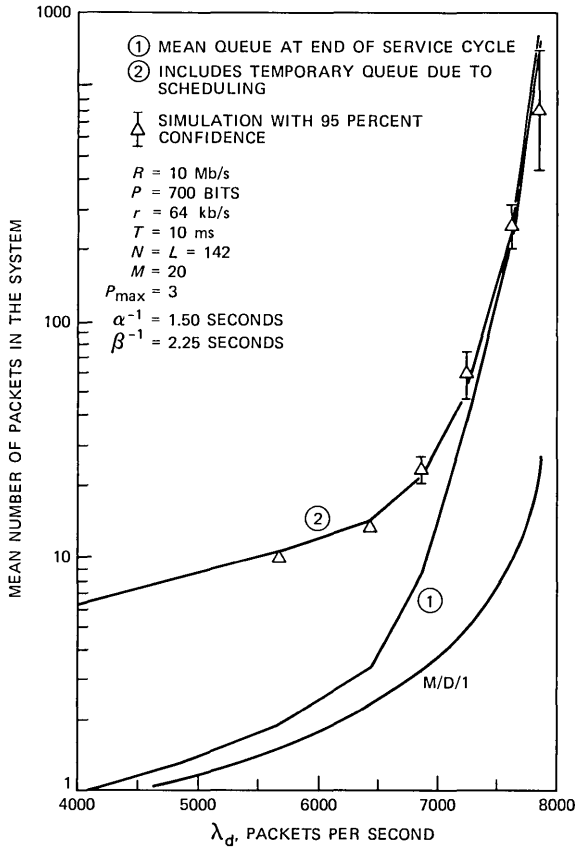


Fig. 11—Data queueing characteristics.

mental points, regression line, and 95-percent confidence interval are shown.

## 6.2 Calculation

The same parameters used in the simulation were employed to calculate the average queue contributions from the stable and overload modes and channel access scheduling, using the equations developed in Section V. The calculated results are tabulated in Table I. For comparison purposes, the mean number of packets in the system is plotted in Fig. 11 for the cases with and without the mean scheduling queue per cycle. Inspection of Fig. 11 shows that the calculated results closely approximate those obtained from simulation.

The data arrival rate in packets/slot is expressible as  $\lambda_d T/L$ . Then, by Little's formula,<sup>13</sup> the mean packet delay is given by

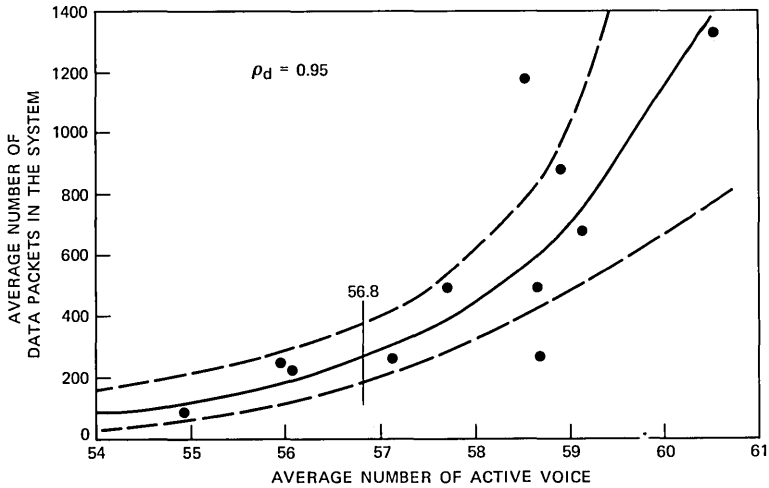


Fig. 12—Regression analysis of mean data queue vs. mean number of active voice with 95-percent confidence.

Table I—Mean number of packets in the system as a function of the arrival rate  $\lambda_d$  in packets/s\*

| $\rho_d$ | $\lambda_d$ | $N_c(v)$ | $\bar{m}$ | Pr[over-load] | $\bar{Q}_{sch}$ | $\bar{Q}(s)$ | $\bar{Q}(o)$ | $\bar{Q}$ |
|----------|-------------|----------|-----------|---------------|-----------------|--------------|--------------|-----------|
| 0.50     | 4091.80     | 97.72    | 1.68      | 2.6449e-12    | 5.19            | 1.01         | —            | 6.21      |
| 0.60     | 4891.12     | 89.43    | 1.82      | 1.6032e-08    | 6.86            | 1.38         | —            | 8.24      |
| 0.70     | 5691.21     | 81.19    | 1.95      | 1.4707e-05    | 8.78            | 1.96         | —            | 10.73     |
| 0.80     | 6483.12     | 73.01    | 2.08      | 2.3096e-03    | 11.02           | 3.25         | 0.23         | 14.51     |
| 0.85     | 6877.15     | 68.94    | 2.15      | 2.3249e-02    | 12.01           | 4.71         | 4.31         | 21.03     |
| 0.90     | 7269.90     | 64.88    | 2.21      | 9.4180e-02    | 12.16           | 6.86         | 30.56        | 49.58     |
| 0.95     | 7895.67     | 60.83    | 2.28      | 2.6206e-01    | 10.54           | 8.64         | 228.68       | 247.86    |
| 0.98     | 7895.67     | 58.41    | 2.32      | 3.8351e-01    | 8.02            | 6.30         | 1512.02      | 1526.34   |

\*  $R = 10$  Mb/s,  $r = 64$  kb/s,  $H = 60$  bits,  $P = 700$  b/packet,  $\alpha^{-1} = 1.50$  seconds,  $\beta^{-1} = 2.25$  seconds,  $L = 142$  slots,  $N = L$ ,  $M = 20$ ,  $P_{max} = 3$ ,  $I_{soj} = 2$ .

$$\bar{d} = \bar{Q}L/\lambda_d T.$$

The analysis and simulation results of the delay-throughput characteristics are shown in Fig. 13. These curves are an alternative presentation of the results shown in Fig. 11.

To demonstrate the effects on data queuing when the number of voice calls is reduced, we compare in Fig. 14 the cases for  $N = 128$ , 136, and 142. It is observed that at a relatively high data rate, the average queue decreases significantly when the number of voice calls is reduced by approximately 5 percent, i.e., from 142 to 136. The improvement in queuing comes from the fact that a reduction in the number of voice calls is accompanied by a relatively large reduction in the probability that the system is in the overload state.

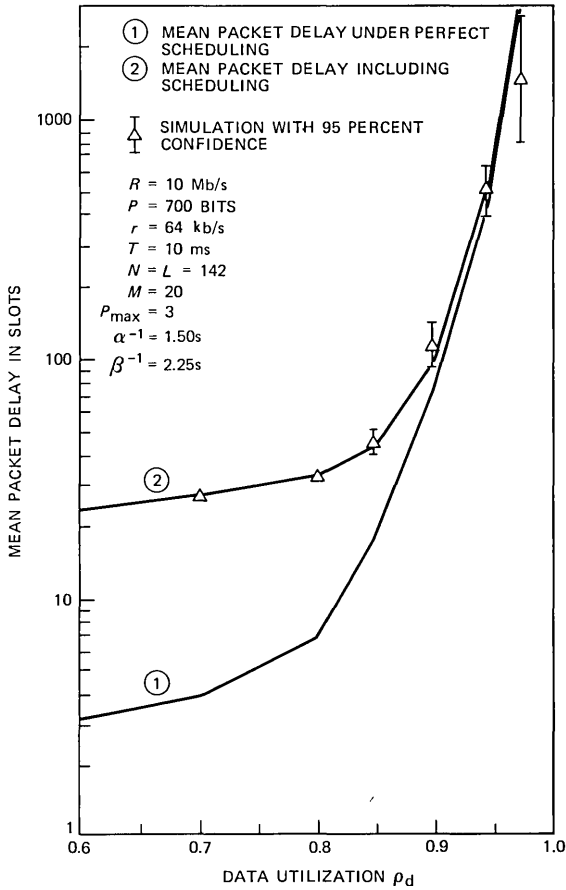


Fig. 13—Mean data packet delay characteristics.

As the voice arrival rate  $r$  decreases or the network transmission rate increases, the number of slots in a cycle increases. For example, with  $R = 100 \text{ Mb/s}$ ,  $r = 64 \text{ kb/s}$ ,  $P = 700 \text{ b/packet}$ , and  $T = 0.01$  second, the number of slots per cycle is approximately 1408. For  $r = 32 \text{ kb/s}$  and  $P = 380 \text{ b/packet}$  ( $H = 60$  bits in each case), the number of slots per cycle is approximately 2624. Letting the number of voice calls  $N = L$ , the average number of data packets in the system as a function of the traffic intensity  $\rho_d$  is plotted in Fig. 15. It is noted that the mean contribution to the queue due to scheduling is the same for the two cases, since the packet length for the  $r = 64 \text{ kb/s}$  case is 1.8421 times longer than that of the  $r = 32 \text{ kb/s}$  case. The longer cycle length (due to a shorter packet length) case exhibits better long-term queuing performance (excluding scheduling queuing). Consider for

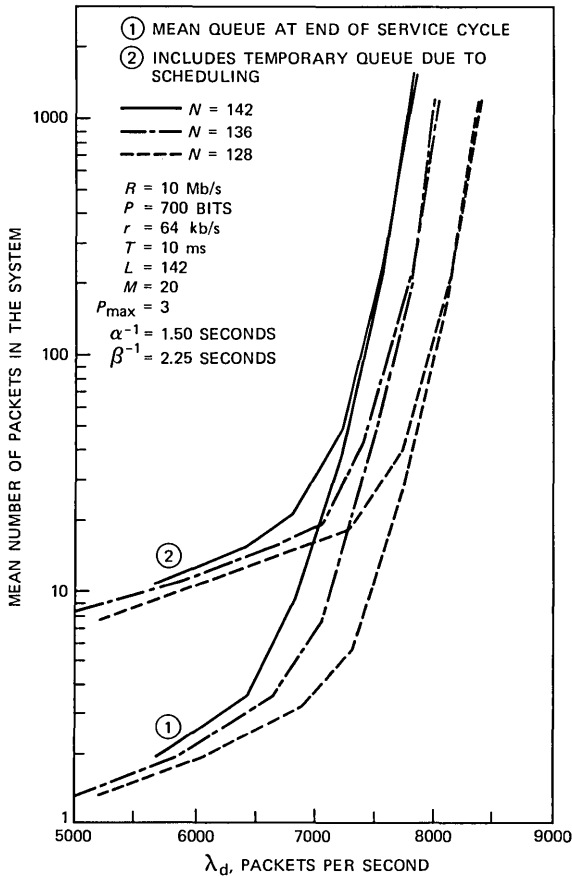


Fig. 14—Effects on queuing with a decrease in the total number of voice stations.

example, at  $\rho_d = 0.95$ , the average number in the system (excluding scheduling queuing) is 18.21 packets for the  $r = 64 \text{ kb/s}$  case and 12.72 packets for  $r = 32 \text{ kb/s}$ . Since the relative packet length ratio is  $700/380$ , the effective mean queue for the  $64 \text{ kb/s}$  case is 2.64 times that of the shorter packet case. Thus, the mean queue for the case where  $P = 700$  bits is equivalent to 33.58 380-bit packets at  $\rho_d = 0.95$  compared to 12.72 380-bit packets for the  $32 \text{ kb/s}$  case at the same utilization.

For comparison purposes, the M/D/1 curve is also plotted in Figs. 11 and 15. The M/D/1 result is based strictly on a stationary distribution, i.e., ignoring the statistical variations associated with the speech spurts. At light loads where the system always operates in a stable mode, the M/D/1 represents a reasonable lower bound. At heavy loads where the system experiences a reasonable percentage of

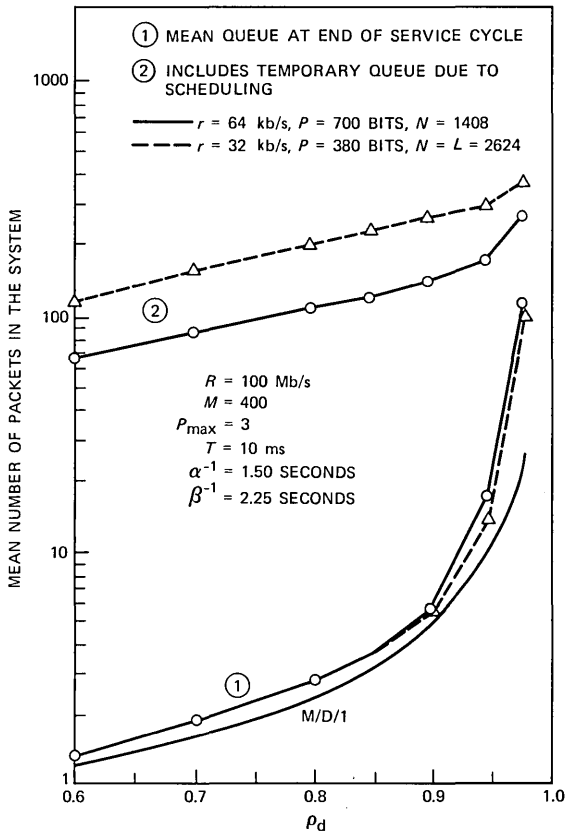


Fig. 15—Queueing characteristics for different packet lengths.

overload, the  $M/D/1$  curve serves no useful comparison (see Fig. 11). Of significance are the numerical results shown in Fig. 15, in which the perfect scheduling Fasnet results deviate from the  $M/D/1$  curve by almost a constant amount up to 95-percent data utilization. This is a consequence of the fact that, at the higher speed ( $R = 100$  Mb/s), overload does not become significant until the data utilization approaches unity. The discrepancy between the  $M/D/1$  and the perfect scheduling Fasnet curves can be attributed to the presence of sojourn time in the Fasnet access discipline.

## VII. DISCUSSIONS AND CONCLUSIONS

In previous work, Limb and Flamm<sup>10</sup> described a scheme for accommodating voice and data that differs from the present method in that calls returning from idle may get clipped. New calls are accepted until an unacceptable level of clipping is approached, whereupon they are

blocked. Unused voice capacity may be utilized by data, although a sojourn time is required to switch between the voice subcycle and the data subcycle unless the voice subcycle is full.

A direct comparison between the two schemes is difficult because of the different way in which the voice traffic is treated—the new calls admission policy and the clipping of talk spurts in one case and the absence of clipping in the other. However, a couple of observations can be made: Both systems have comparable performance since they both utilize the available slots efficiently when traffic is heavy; clipping may be undesirable in certain instances, for example, where a number of Fasnet links are connected in tandem. A speech spurt could be clipped more than once, leading to a noticeable degradation. In this instance, the present method would be preferable.

The global access control that is enabled by the endowment of each slot with a type designation renders Fasnet particularly suitable for integrated services. We have described the ramifications for integrated voice and data services on Fasnet and a policy for admitting new voice into the system. Once admitted, a voice station is guaranteed service when needed. Voice stations are served on a periodic basis, so that each voice source sees almost synchronous service, i.e., the service is synchronous within the statistical variations dictated by the binomial distribution of the silent and talk spurt intervals in a voice process. The mean interpacket delay can be expected to be negligibly small. Note that the service discipline described will not clip any voice packets from a talk spurt.

Since data traffic can be buffered, it is not necessary to maintain continuous service for data. During intervals when the system is servicing voice stations, data stations are temporarily locked out and have to be buffered. Depending on the data input load relative to the service time available for data during one service cycle, the temporary queues may be cleared entirely at the end of the service cycle, or some residual packets will carry over from one cycle to the next. If the latter phenomenon occurs over many consecutive cycles, the system will sustain a net growth in its queues. Under this condition the system experiences overloading, and the data utilization during these cycles will exceed unity for a short period and the data queues will experience significant growth.

The conventional approach to analyzing the queueing behaviour is the generating function analysis method. However, the size of the state space in a practical network renders the generating function method impractical. An approximate analysis method, based on a merge of a periodic service single-server model and a fluid approximation method, has been developed in Ref. 8 to analyze the queueing behaviour for integrated voice and data services on Welnet, a local

area network in which the service discipline is functionally similar to that of Fasnet. With a suitable modification to account for the sojourn time that accompanies each switch in the type of service by the Fasnet access control, the approximate analysis method introduced in Ref. 8 was used to analyze the data buffer queueing behaviour for integrated voice and data services on Fasnet.

System performance may also be evaluated by means of computer simulation. Simulation is time-consuming and it is impractical to simulate high transmission rate systems. In this study, we simulated a 10-Mb/s Fasnet and measured performance in terms of the mean queue in the system as a function of the data input load. The analytic results closely approximate those obtained from simulation. It is conjectured that the analysis method yields reasonably accurate results. Analytical results for a 100-Mb/s Fasnet have been presented. An interesting observation is that the larger bandwidth has the effect of reducing the system overload probability.

In this paper we used an approximate model to analyze the network performance. We verified the reasonableness of the approximate model. An alternative approach is to approximate the correlated voice source by a memoryless process, e.g., a birth-and-death process. The validity of such an approximation needs to be shown. An analysis of the backlog in the buffers for a birth-and-death process is discussed in Ref. 14.

## REFERENCES

1. K. Kummerle, "Multiplex Performance of Integrated Line and Packet-Switched Traffic," Proc. 2nd Int. Conf. Comp. Commun., Stockholm, Sweden, August 1974, pp. 517-23.
2. M. J. Fischer and T. C. Harris, "A Model for Evaluating the Performance of an Integrated Circuit-and Packet-Switched Multiplex Structure," IEEE Trans. Commun., *COM-24* (February 1976), pp. 195-202.
3. C. J. Weinstein, M. K. Malpass, and M. J. Fischer, "Data Traffic Performance of an Integrated Circuit-and Packet-Switched Multiplex Structure," IEEE Trans. Commun., *COM-28* (June 1980), pp. 873-7.
4. B. Maglaris and M. Schwartz, "Performance Evaluation of a Variable Frame Multiplexer for Integrated Switched Networks," IEEE Trans. Commun., *COM-29* (June 1981), pp. 800-7.
5. I. Gitman, W-N. Hsieh, and B. J. Occhiogross, "Analysis and Design of Hybrid Switching Networks," IEEE Trans. Commun., *COM-29* (September 1981), pp. 1290-1300.
6. B. R. Iyer and J. B. Sinclair, "Analysis of Data Delays in an Integrated Data-Voice Link," Technical Report 8204, Electrical Engineering Department, Rice University, Houston, Texas, April 1982.
7. A. Leon-Garcia, R. H. Kwong, and G. F. Williams, "Performance Evaluation Methods for an Integrated Voice/Data Link," IEEE Trans. Commun., *COM-30* (August 1982), pp. 1848-58.
8. J. W. Mark, "Priority Scheduling for Integrated Voice/Data Services in Local Area Networks," CCNG Report E-111, Computer Communication Networks Group, University of Waterloo, Waterloo, Ont., Canada, March 1983.
9. J. O. Limb and C. Flores, "Description of Fasnet—A Unidirectional Local Area Communications Network," B.S.T.J., 61, No. 7, Part 1 (September 1982), pp. 1413-40.

10. J. O. Limb and L. E. Flamm, "A Distributed Local Area Network Packet Protocol for Combined Voice and Data Transmission," GLOBECOM '82 Conf. Rec., November 29-December 2, 1982, Miami, Florida, pp. B2.5.1-6.
11. C. J. Weinstein, "Fractional Speech Loss and Talker Activity Model for TASI Packet-Switched Speech," IEEE Trans. Commun., COM-26 No. 8 (August 1978), pp. 1253-7.
12. G. F. Newell, *Applications of Queueing Theory*, London: Chapman and Hall Ltd., 1972, Chapter 2.
13. J. D. C. Little, "A Proof of the Queueing Formula  $L = \lambda W$ ," Oper. Res., 9 (May 1961), pp. 383-7.
14. S. Halfin, "The Backlog of Data in Buffers with Variable Input and Output Rates," Proc. of the Second International Symposium on Performance of Computer-Communications Systems, Zurich, March 21-23, 1984.

## AUTHORS

**John O. Limb**, B.E.E., 1963, Ph.D. (Electrical Engineering), 1967, University of Western Australia, Nedlands; Research Laboratory, Australian Post Office, 1966-1967; AT&T Bell Laboratories, 1967-1983. Present affiliation Bell Communications Research, Inc. At AT&T Bell Laboratories, Mr. Limb worked for a number of years on the coding of color and monochrome picture signals to reduce channel capacity requirements, and has published widely in this area. He is now manager of the Communication Research Department in Bell Communications Research, Inc. His current research interest is wideband, local area networks. Fellow, Institute of Electrical and Electronics Engineers; member, Association for Computing Machinery, Association for Research in Vision and Ophthalmology, Optical Society of America.

**Jon W. Mark**, B.A. Sc., 1962, University of Toronto; M.Eng., 1968, Ph.D., 1970, McMaster University; Canadian Westinghouse, 1962-1968; IBM, Thomas Watson Research Center, 1976-1977; AT&T Bell Laboratories, 1982-1983; University of Waterloo, 1970—. At the IBM Research Center Mr. Mark was a visiting scientist. At AT&T Bell Laboratories, he was a consultant to the Computer Technology Research Laboratory. He worked for a number of years in the areas of radar and sonar signal processing, equalization, data compression, and spread spectrum communication. At present, Mr. Mark is a Professor of Electrical Engineering at the University of Waterloo. His current research interests are network modeling and performance evaluation, satellite networks, and local area networks. Senior Member, IEEE.

## Experimental Ion-Implanted Bubble Memory Device With $16\text{-}\mu\text{m}^2$ Cell

By T. J. NELSON,\* D. J. MUEHLNER,\* V. V. S. RANA,\*  
B. J. ROMAN,\* and G. P. VELLA-COLEIRO\*

(Manuscript received April 1, 1983)

This paper describes a  $4\text{-}\mu\text{m}$ -period ( $16\ \mu\text{m}^2/\text{bit}$ ) magnetic bubble device based on ion-implanted propagation patterns. Single-layer LaSmLuBiGa-IG films were implanted with  $\text{Ne}^+$  and  $\text{He}^+$  ions using densified photoresist masking patterns. Coarse (three eighths of a period) minimum features were used in the Permalloy and Al-Cu levels. A 21-Oe overlap bias range was obtained for generation, propagation, transfer, and detection at 55-Oe drive. Generation and detection were demonstrated to have a 39-Oe bias range at 44-Oe drive, and a 39-Oe bias range for minor-loop propagation was obtained at  $\geq 33$ -Oe drive.

### I. INTRODUCTION

Using proposed scaling laws for Permalloy†-based magnetic bubble devices, Kyrder<sup>1</sup> has concluded that  $6 \times 10^6$  b/cm<sup>2</sup>,  $1\text{-}\mu\text{m}$  bubble devices should be achievable. Fontanta et al.<sup>2</sup> have studied devices using  $4.75 \times 5.25\text{-}\mu\text{m}^2$  cells and  $0.75\text{-}\mu\text{m}$  gaps fabricated with 10X reduction, direct step on wafer projection printing. Quasistatic gate operation was achieved at 70-Oe drive field. Recently, Yanase et al.<sup>3</sup> demonstrated propagation on  $4\text{-}\mu\text{m}$  "club foot" circuits with  $1\text{-}\mu\text{m}$  gaps at

---

\* AT&T Bell Laboratories.

† Permalloy is a trademark of the Allegheny Ludlum Steel Corporation.

---

Copyright © 1984 AT&T. Photo reproduction for noncommercial use is permitted without payment of royalty provided that each reproduction is done without alteration and that the Journal reference and copyright notice are included on the first page. The title and abstract, but no other portions, of this paper may be copied or distributed royalty free by computer-based and other information-service systems without further permission. Permission to reproduce or republish any other portion of this paper must be obtained from the Editor.

drive fields above 45 Oe. It appears, therefore, that Permalloy-based bubble devices are already near their anticipated density limit.

One-micrometer bubble devices with  $30\text{-}\mu\text{m}^2$  cell area have been operated<sup>4</sup> at 150 kHz, using Ion-Implanted Propagation Patterns<sup>5</sup> (I2P2s) instead of Permalloy. And Komenou et al.<sup>6</sup> have reported promising results using  $16\text{-}\mu\text{m}^2$  I2P2 cells. Because of their extreme simplicity (a sine-wave-shaped track will propagate, for example), I2P2 devices can be resolved with three-eighths of a period minimum features, which, together with a  $0.75\text{-}\mu\text{m}$  optical lithography limit, imply a possible density of  $2.5(10)^7$  b/cm<sup>2</sup>.

This paper describes magnetic bubble material and test-circuit design and characterizes generation, propagation, transfer, and detection in  $4\text{-}\mu\text{m}$ -period devices based on ion-implanted propagation patterns (see Fig. 1).<sup>\*</sup> With one exception, the minimum features in the Permalloy and Al-Cu levels were coarsened to three-eighths of a period. We have continued to use single-layer garnet films, and the layers processed on the chip were unchanged, except that the Permalloy thickness was reduced from 500 AU to 375 AU.

## II. MATERIAL FOR $4\text{-}\mu\text{m}$ -PERIOD BUBBLE DEVICES

Films of the nominal composition  $(\text{LaSmLu})_3(\text{FeGa})_5\text{O}_{12}$ , with and without Bi, were used in the present study. Propagation at  $4\text{-}\mu\text{m}$  period in films of  $(\text{LaSmLuCa})_3(\text{FeGe})_5\text{O}_{12}$  composition was previously reported.<sup>7</sup> However, this composition required a high magnetic moment ( $4\pi M_s = 784\text{G}$ ) to produce  $1.1\text{-}\mu\text{m}$ -sized bubbles. The saturation magnetization ( $4\pi M_s$ ) is given by  $4\pi M_s = \sqrt{32\pi A Q / \ell^2}$ , where  $\ell$  is the material length parameter,  $Q$  is the quality factor, and  $A$  is the exchange constant. Hence, a similar bubble size (same  $\ell$ , and  $Q$ ) can be obtained at a lower  $4\pi M_s$  by going to a composition having a lower exchange constant. Since  $A$  scales with the Curie temperature,<sup>7</sup> the required  $4\pi M_s$  can be lowered by going to a composition having a lower Curie temperature. In the present work we have used Ga substitution, instead of CaGe, to reduce the  $4\pi M_s$  and, possibly, the minimum drive field. The desired anisotropy was obtained from the SmLu site selectively. The bubble mobility was improved by making use of the Lanthanum effect;<sup>7,8</sup> i.e., the Sm content was kept low and the uniaxial anisotropy was increased by increasing the Lu content and using La to match the film lattice parameter to that of the substrate, La having no effect on the uniaxial anisotropy.

---

<sup>\*</sup> The contents of this paper were presented by T. J. Nelson in the Fourth International Conference on Magnetic Bubbles held September 24–27, 1980, in Tokyo.

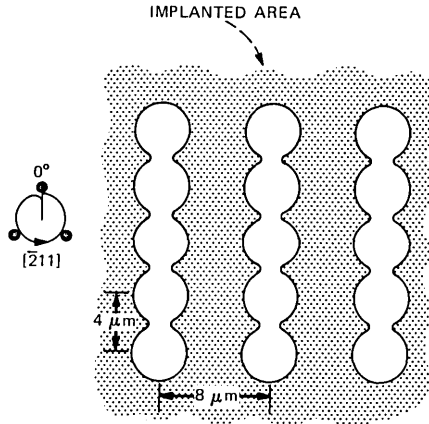


Fig. 1—Minor-loop ion-implanted propagation patterns and orientation with respect to wafer, preferred positions, and rotating field conventions.

Films were grown from  $\text{PbO}-\text{B}_2\text{O}_3$  flux by the Liquid Phase Epitaxy (LPE) technique on 50-mm diameter (111)  $\text{Gd}_3\text{Ga}_5\text{O}_{12}$  substrates by horizontal dipping with a unidirectional rotation of 100 rpm. The growth temperatures ranged from  $872^\circ$  to  $880^\circ\text{C}$ . Table I lists the properties of typical films. The film thickness and demagnetized stripe width intentionally exceed the  $0.9\ \mu\text{m}$  desired for  $4\text{-}\mu\text{m}$  period to allow for the thickness of the implant.  $H_o$  is the collapse field. The domain wall mobility ( $\mu$ ) was calculated from the resonance line width using standard Ferromagnetic Resonance (FMR) technique. Initially, films were grown without bismuth (type A). The bubble visibility in these films was poor because of the low Faraday rotation ( $\theta_F$ ). The addition of Bi was made (film type B) to produce an enhanced (and reversed) Faraday rotation to improve the bubble visibility.

The anisotropy of the implanted films was determined from microwave resonance using the method described in Ref. 9. Measurements were made at 11.85 GHz on 50-mm diameter wafers after removing the film on the back side by etching in phosphoric/sulfuric acid. Figure 2 shows the derivative microwave absorption vs. field of a film (type A). This film was implanted with 80/Ne/1E14, 270/Ne/2E14, and 130/He/6E15 followed by a  $300^\circ\text{C}$  anneal. (The implantations are referred to in a shorthand form representing energy in keV/ion species/dose in ions/cm<sup>2</sup>.) The anisotropy fields of both the film and its implant can be read from Fig. 2. For this film,

$$Q = 1 + \frac{770}{664} = 2.16.$$

A sufficiently large change in anisotropy of about  $6(10)^4$  ergs/cm<sup>3</sup> was

Table I—Properties of (LaSmLu)<sub>3</sub>(FeGa)<sub>5</sub>O<sub>12</sub> films

|   | Type       | Property                |                         |                             |               |                   |               |                        |   |
|---|------------|-------------------------|-------------------------|-----------------------------|---------------|-------------------|---------------|------------------------|---|
|   |            | th<br>( $\mu\text{m}$ ) | sw<br>( $\mu\text{m}$ ) | $\ell$<br>( $\mu\text{m}$ ) | $H_o$<br>(Oe) | $4\pi M_s$<br>(G) | $H_K$<br>(Oe) | $\mu$<br>(cm/<br>s/Oe) | $\theta_F$<br>(at<br>5000Å)<br>(degrees/<br>cm) |
| A | Without Bi | 1.39                    | 1.08                    | 0.11                        | 378           | 664               | 1435          | 485                    | 1400  |
| B | With Bi    | 1.22                    | 1.07                    | 0.11                        | 365           | 655               | 1650          | 400                    | -4500   |

caused by the implantation. Figure 3 shows the visually obtained minor-loop bias margins vs. drive field on another film (type B). This film was implanted with 80/Ne/1E14 (no pattern) and 270/Ne/2E14 + 130/He/4E15 patterned implants. This sample was subjected to full processing, which included vacuum anneal at about 350°C for 1 hour prior to the Permalloy evaporation. The demagnetized strip width in the implanted region after processing was 0.85  $\mu\text{m}$ , sufficiently close to the desired value.

### III. PROCESSING OF 4- $\mu\text{m}$ -PERIOD BUBBLE DEVICES

This study employed contact printing using chrome masters on glass. The test devices were originally encoded with 0.5- $\mu\text{m}$  address steps at 8- $\mu\text{m}$  period. For this study they were shrunk to 0.25- $\mu\text{m}$  steps at 4- $\mu\text{m}$  period using an Electron Beam Exposure System (EBES)<sup>10</sup> option. Scanning Electron Microscope (SEM) photographs of the propagate patterns are shown in Fig. 4a as printed in AZ1350J photoresist in the ordinary way and Fig. 4b as transferred to densified AZ1350J by trilevel<sup>11</sup> method. The latter lithographic technique permits the transfer of a high-resolution image, which is more easily achieved in a thin resist layer, into a thick polymerized layer that is dimensionally stable under extreme implantation conditions. Plasma-deposited SiO<sub>2</sub> separates the thin and thick organic layers and, after plasma etching through the primary resist pattern, serves as a reactive ion-etch mask to complete the image transfer process. Because of the highly anisotropic etching, trilevel patterns have vertical edge profiles and were used exclusively to guarantee edge integrity for the implanted patterns in this study.

The processing after implantation consisted of 2000 AU of plasma-deposited SiO<sub>2</sub> (P-SiO<sub>2</sub>), 375 AU of Permalloy, and an additional 2000 AU of P-SiO<sub>2</sub> and 5000 AU of Al-Cu. Via holes were plasma etched into the second SiO<sub>2</sub> layer to connect the Permalloy sensors to their Al-Cu pads. The devices received no additional passivation. The Permalloy and Al-Cu layers were patterned with contact printing and ion-beam milling. As will be discussed below, the minimum features in the metal layers, except in the generator, were coded to be 1.5  $\mu\text{m}$ .

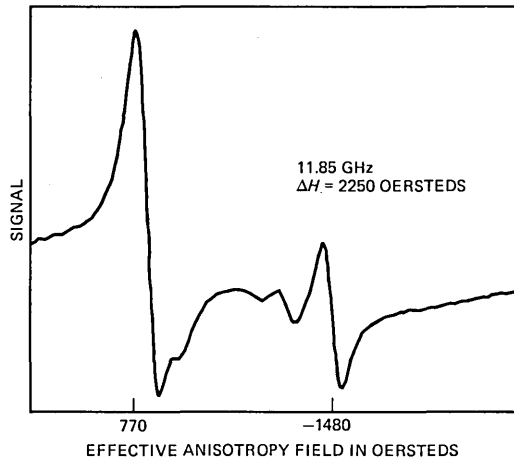


Fig. 2—FMR absorption (derivative) as a function of field of a  $(\text{LaSmLu})_3(\text{GaFe})_5\text{O}_{12}$  film implanted with 80/Ne/1E14, 270/Ne/2E14, and 130/He/6E15.

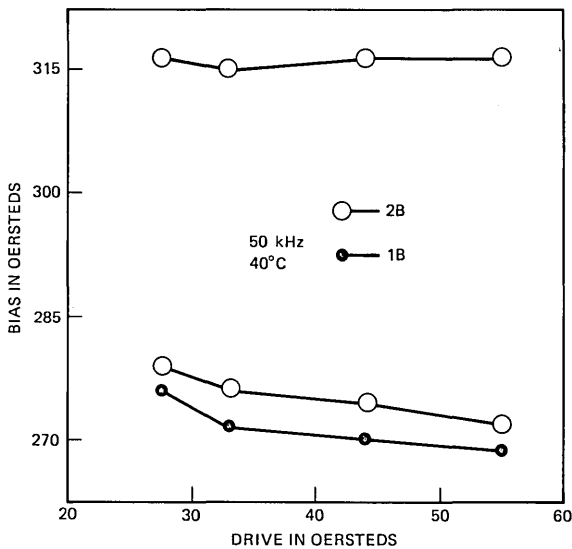
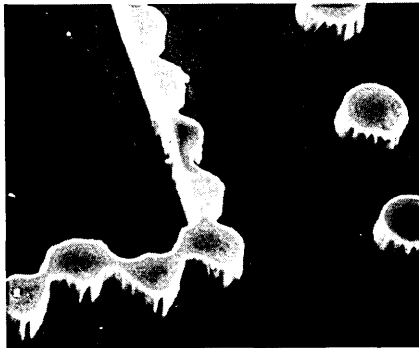


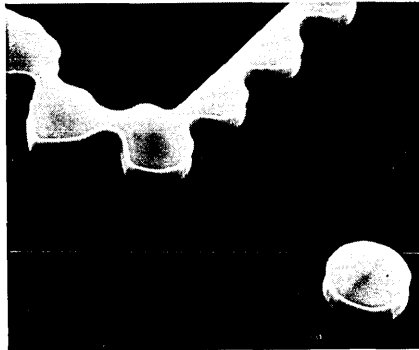
Fig. 3—Minor-loop propagation margins vs. drive field at 40°C using 80/Ne/1E14 (unpatterned) + 270/Ne/2E14 + 130/He/4E15. Open circles refer to two bubbles in adjacent positions.

#### IV. LAYOUT AND OPERATION OF 4-μ-PERIOD BUBBLE DEVICE

Figure 5 shows the components and layout used in this study. The generator consists of a simple Al-Cu hairpin, much like that used in Permalloy devices. Between the generator and detector, a line of clover-leaf-shaped features was interpolated. These features were sep-



(a)



(b)

Fig. 4—SEM photographs of 4- $\mu\text{m}$ -period resist patterns (a) with contact-printed AZ1350J resist and (b) using trilevel resist.

arated by 1- $\mu\text{m}$  merge gaps.<sup>12</sup> The clover-leaf features have threefold symmetry, except for small EBES address effects, and so provide strong-side propagation all around. The transfer-enable was designed to frustrate propagation of bubbles by the merge gap and send them through the gaps and around the cover-leaf features. In this way, a block of bubbles coming from the generator may, when properly positioned, be brought to the transfer ports for insertion into the minor loops. The trapping-transfer gates<sup>13</sup> operate by confining bubbles within the lower slot of the conductor and between the two implant boundaries. Bubbles transfer from one path to the other after being trapped for approximately 180° of field rotation. When a group of bubbles is transferred out from the minor loops to the tops of the clover-leaf features, each bubble propagates around through the merge gap to the path between the generator and detector. Once the block is thus assembled, the bubbles propagate towards the detector with the same bit order as originally generated. The detector consists of an Al-Cu conductor hairpin to stretch the bubbles and a Permalloy stripe to

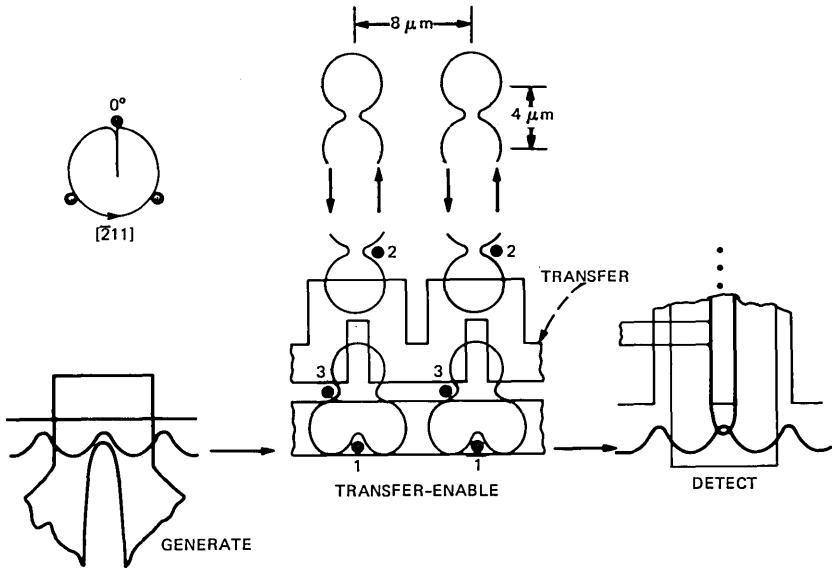


Fig. 5—Test-circuit layout used in design study at 4- $\mu\text{m}$  period. Minimum feature was 1  $\mu\text{m}$  in the implant level and 1.5  $\mu\text{m}$  in the Permalloy and Al-Cu levels.

sense them. The bubbles are collapsed by a second current pulse to restore the detector for the next bubble.

The minimum coded feature used in the implant level was 1  $\mu\text{m}$ , which was the distance between implanted regions through the narrowest place on the minor loops or the width of the implanted region in the gaps between clover-leaf features. Except for the generator, the minimum feature in the metal levels was coded to be 1.5  $\mu\text{m}$ , which was the line width of the Permalloy sensor and the gap width in the Al-Cu hairpins. The Al-Cu line width in the transfer gates was made 2.5  $\mu\text{m}$ , which is the maximum permitted by the 8- $\mu\text{m}$  interloop spacing and the 1.5- $\mu\text{m}$  gap width.

The experimental 4- $\mu\text{m}$ -period devices (film type B) were operated on a microscope-based test set under microprocessor control. The temperature of the chips was unregulated, but as the duty factor for the drive coils was small and the bias magnet was water cooled, it was less than 25°C. All testing was carried out at 50 kHz with sine-wave currents in the drive coils. Figure 5 shows positions 1 through 3 where bubbles were stopped during the tests. A typical test consisted of (1) generation and propagation to 1; (2) propagation with transfer-enable and transfer-in to 2; (3) propagation around the minor loop back to 2; (4) propagation and transfer-out to 3; and, finally, (5) propagation and detection. The test was automatically repeated at 3-Oe bias intervals. The data pattern generated was compared with that actually detected,

and the exclusive OR of the two was printed for each test. The bias ranging could be restricted to a single component of the test, in which case the other components were performed at a fixed bias. All current pulsers were triggered at  $0^\circ$  in the appropriate cycles by the computer, and delays, widths, and amplitudes were manually adjusted on the pulsers.

## V. DEVICE COMPONENTS AT 4- $\mu\text{m}$ PERIOD

### 5.1 Generation

The generator design, shown in more detail in Fig. 6, was included in a serial test circuit also present on the chip. Ordinary ungapped propagation patterns were employed in the serial test circuit, which was used to obtain the generator and detector data given in Figs. 7, 9, and 10. A reduction in upper bias margin with increased pulse width was observed. At 100-ns pulse width, the full bias range was obtained with generator current varied almost by a factor of 2, from 110 to 200 mA.

### 5.2 Detection

Figure 8 shows the detector design employed. The Al-Cu hairpin was pulsed to remove the bubble from the strong-side track and simultaneously stretch it along the Permalloy at a drive-field angle of  $90^\circ$ . At this time the magnetization in the Permalloy switches from up to down. A decreased resistance is observed when a stripped-out bubble is present, indicating increased cross-magnetization. Figure 9 shows the stretch-current amplitude dependence of the bias margins for the approximately 50- $\mu\text{m}$ -long detector in the serial test circuit. Good bias margins were obtained between 50 mA and 90 mA. Figure

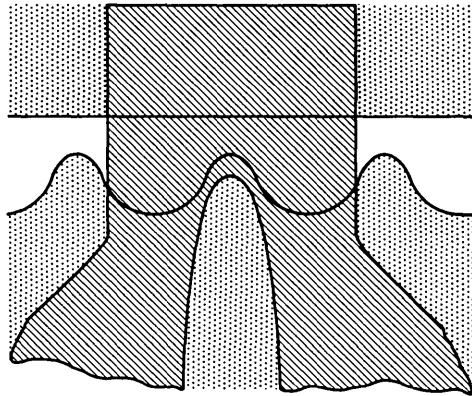


Fig. 6—Generator design using 1.5- $\mu\text{m}$  slot width and 2.5- $\mu\text{m}$  line width in the Al-Cu level.

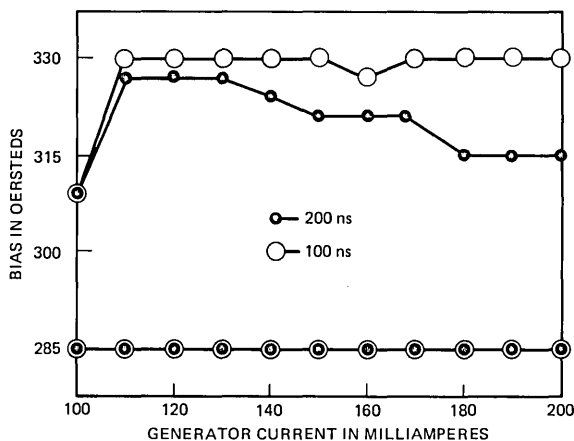


Fig. 7—Bias range at 55-Oe drive and 25°C for generation at 0° as a function of current.

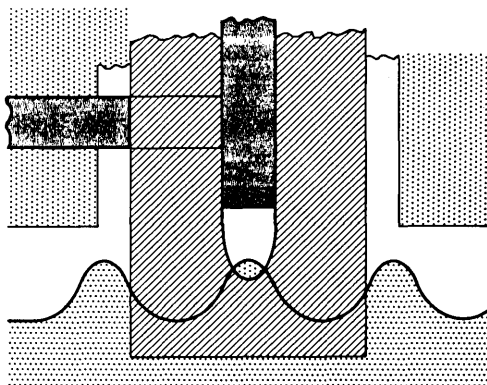


Fig. 8—Destructive Read Out detector design using 1.5- $\mu\text{m}$  Permalloy line width and 2.5- $\mu\text{m}$  Al-Cu line width at 4- $\mu\text{m}$  period.

10 shows the bias-range dependence on collapse current amplitude. The collapse pulse was applied typically quite late, which stroboscopic observation (at 8- $\mu\text{m}$  period) suggests gives the strip time to contract to a bubble before the collapse pulse is applied. Therefore, the collapse pulse is thought to collapse only a bubble, not a strip. Figure 11 shows the bias range vs. drive field for generation, strong-side propagation and detection. The bias range has opened up at 44-Oe drive, though operation was possible down to 33 Oe with some loss of low bias margin. The data presented in Figs. 7, 9, and 10 were taken at 55-Oe drive to be compatible with the transfer results given below.

Figure 12 shows the differential voltage between detector and

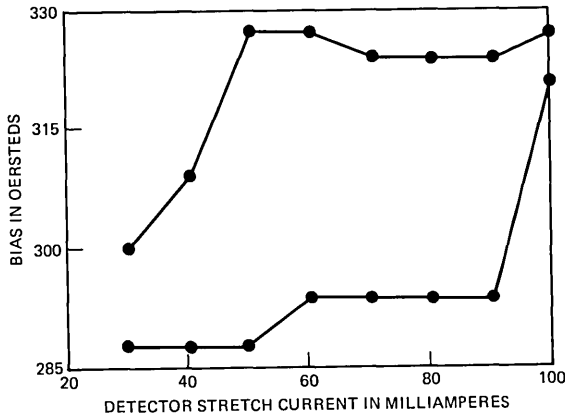


Fig. 9—Bias range vs. detector stretch current at 55-Oe drive field with pulse active between 72° and 126°.

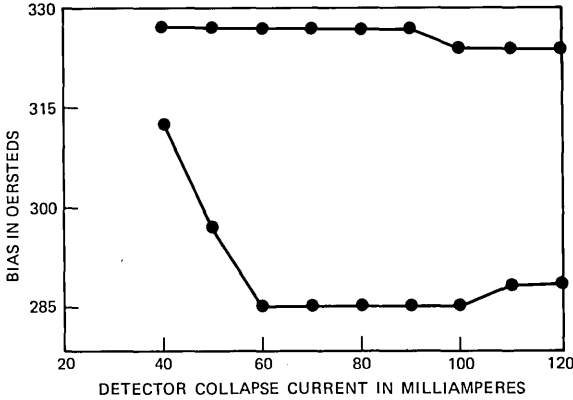


Fig. 10—Bias range vs. collapse pulse current at 55-Oe drive field with pulse timing 252° to 288°.

dummy, amplified by 10. This waveform was obtained at 55-Oe drive with the circuit for which transfer and minor-loop margins are given below. Reliable detection with this longer (100  $\mu\text{m}$  compared to 50  $\mu\text{m}$  in the serial test circuit) detector required earlier phasing for the stretch pulse, about 54° instead of 72°. In this particular circuit a higher collapse current was also needed. The 500 $\Omega$  detector gave about 6 mV at 2.5 mA, corresponding to a figure of merit of  $\delta V/V \approx 0.5$  percent.

### 5.3 Transfer-enable

The transfer-enable and trapping-transfer ports are drawn to larger scale in Fig. 13. The major line is composed of the bottoms of the

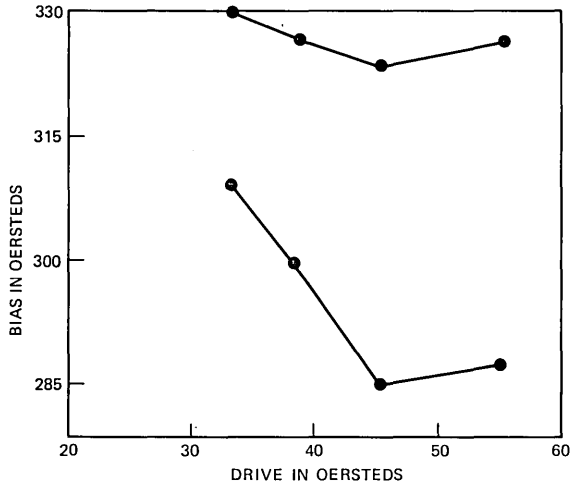


Fig. 11—Bias range for generation, strong-side propagation, and detection at 25°C vs. drive field.

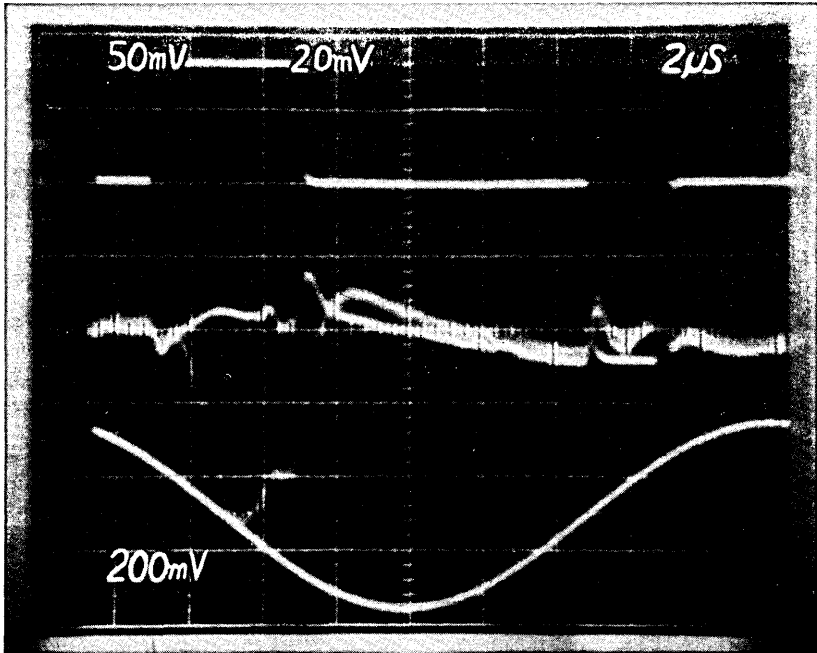


Fig. 12—Differential detector output with bubble and no bubble traces superimposed. Gain is 10 for the signal and 1 mV/mA for the stretch and collapse pulses. Positive peak of the sine wave is at 0°.

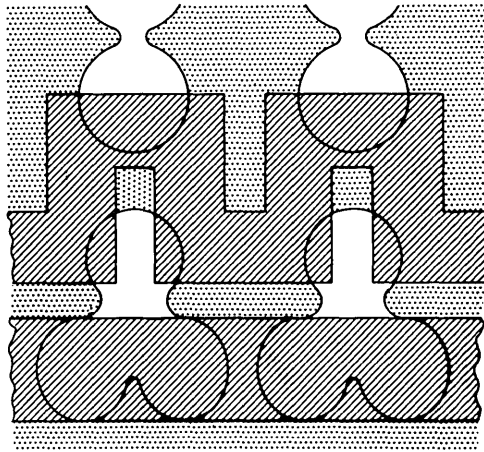


Fig. 13—Transfer-enable and trapping-transfer designs used to communicate between minor loops and gapped major line.

clover-leaf features. While bubbles propagated past the gaps at lower drive, at least 50 Oe was needed to propagate bubbles away from the clover-leaf cusps. The data reported below were obtained with 55-Oe sine-wave drive. Transfer-enable bias range vs. pulse current is shown in Fig. 14. Four bubbles, aligned with four ports, were made to pass through the merge gaps by a pulse active near a rotating field phase of  $0^\circ$ . The bubbles started from the cusps on the major line, passed through the gaps at the end of the first cycle, and propagated three steps around the clover leaf. A 33-Oe bias range was obtained for 25 through 45 mA pulses active from  $-72^\circ$  to  $36^\circ$ . Some variation has been seen with other chips of the same wafer. In other tests, for example, the low bias limit increased with increasing current instead of being independent of current as in Fig. 14.

#### 5.4 Trapping transfer

Figure 13 also shows trapping-transfer gates linking the tops of the clover-leaf features with the bottoms of the minor loops. For the data presented in Figs. 15 through 20, a single bubble was loaded into each of three adjacent 73-step minor loops. Note that the trapping-transfer conductor slot opens away from the minor loops. This means that the pulse increases the bias on neighboring positions in the minor loops. In this work, the effect of the pulse current on neighboring positions was investigated by pulsing one cycle before and one cycle after the bubbles propagated by the gates within the minor loops. The open circles in Figs. 15 through 20 represent, with these extra pulses, both transfer-in and transfer-out. The slot orientation was chosen to avoid

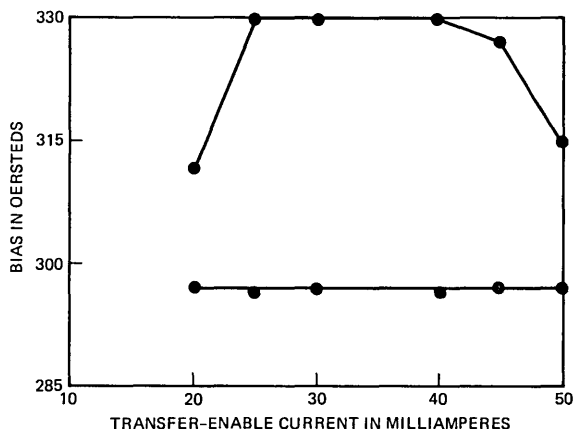


Fig. 14—Bias range vs. transfer-enable current at 55-Oe drive with pulse active from  $-72^{\circ}$  to  $36^{\circ}$ .

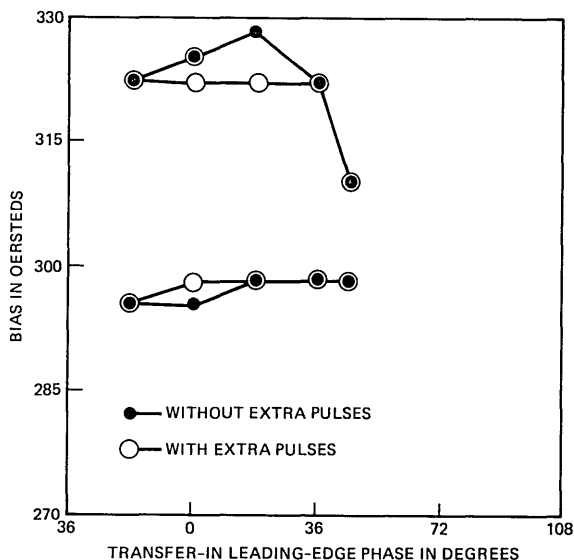


Fig. 15—Bias range vs. transfer-in leading-edge phase at 55 Oe. Trailing edge was held constant at  $144^{\circ}$  and the current was 35 mA.

the bad conductor crossings that developed after passivation in 8- $\mu$ m trapping-transfer gates. In the present design, the bad crossing would be expected if the conductor slot extended past the implant boundary of the bottom of the minor loop. In the 8- $\mu$ m-period gates, the crossings were still good after passivation when the slot stopped short, as in Fig. 13, and left continuous metal over the bubble path.

Figure 15 shows bias range vs. leading-edge phase of the transfer-in pulse. The pulse could be started as late as  $+36^\circ$ ; thereafter, the upper bias margin dropped abruptly. The bias range was fairly constant for earlier phases. Transfer-in trailing-edge phase was varied to produce Fig. 16. Figure 17 shows the bias range vs. transfer-in current, with the lowest current for reliable operation at 30 mA. The high bias effect of the pulse on neighboring positions in the minor loop was most noticeable in this plot. The overall margins were limited by transfer-in at low bias, which improved as the current was lowered. Figure 18 shows the bias range vs. transfer-out leading-edge phase. Figure 19 shows that a higher upper bias limit exists for trailing-edge phases near  $360^\circ$ . Such phasing, however, loses high bias margin when the effect on bubbles in adjacent cycles is considered. This high bias failure mode is also clearly evident in Fig. 20, which shows the bias range vs. transfer-out current. The overall margins were in fact limited at high bias by transfer-out.

## VI. OVERALL BIAS RANGE AND CONCLUSIONS

Figure 21 shows the bias ranges for individual device components at 55-Oe drive. These results were obtained with the chip also used to produce the data shown in Figs. 14 through 20. The enable, transfer, and detector designs have been discussed above. The generator in the major-minor test circuit had  $1\text{-}\mu\text{m}$  gap and  $1.75\text{-}\mu\text{m}$  coded line widths.

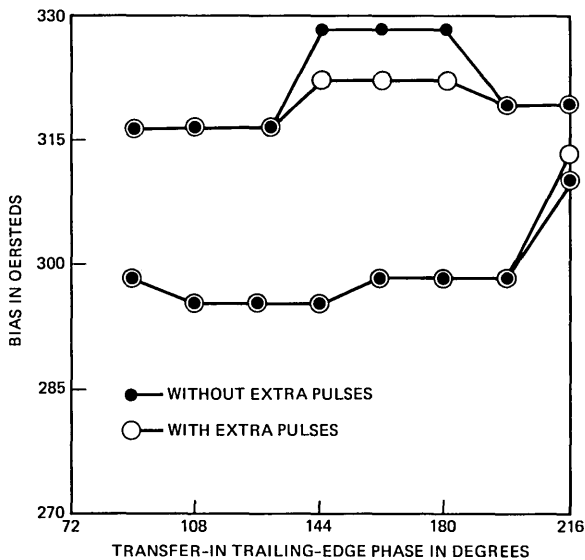


Fig. 16—Bias range vs. transfer-in trailing-edge phase at 55 Oe with leading edge at  $0^\circ$  and the current at 35 mA.

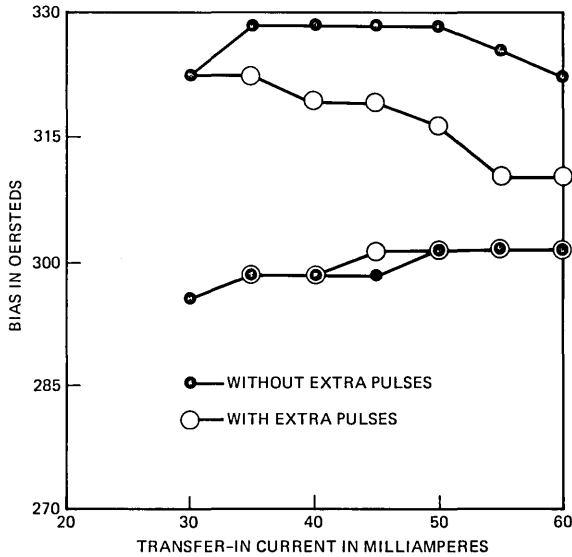


Fig. 17—Bias range vs. transfer-in current at 55 Oe with pulse active from 0° to 144°.

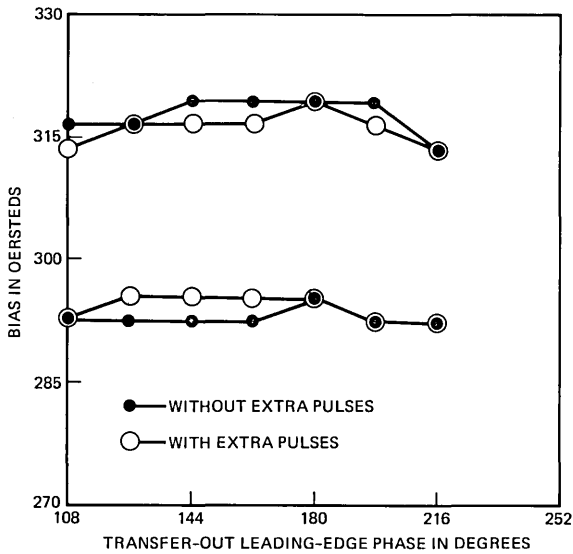


Fig. 18—Bias range vs. transfer-out leading-edge phase at 55 Oe. Pulse current was 45 mA and lasted until 306°.

In other work we have found 1.5- $\mu$ m gaps to be satisfactory for generation at 4- $\mu$ m period. A generator pulse of 105 mA, lasting 80 ns, worked well on the chip of Figs. 14 through 21. In other nominally identical chips, higher currents, over 200 mA, were required for gen-

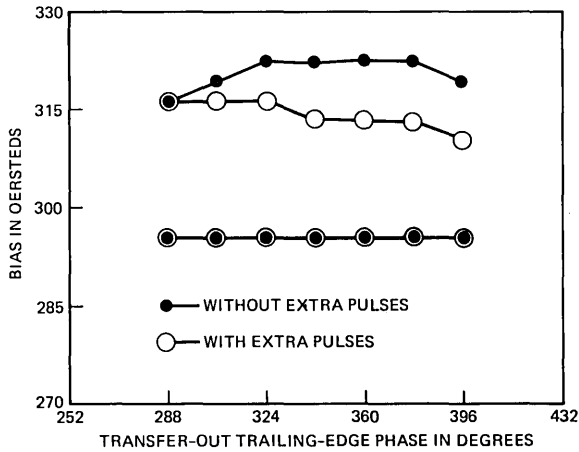


Fig. 19—Bias range vs. transfer-out trailing-edge phase at 55 Oe. The leading-edge phase was 180° and the current was 45 mA.

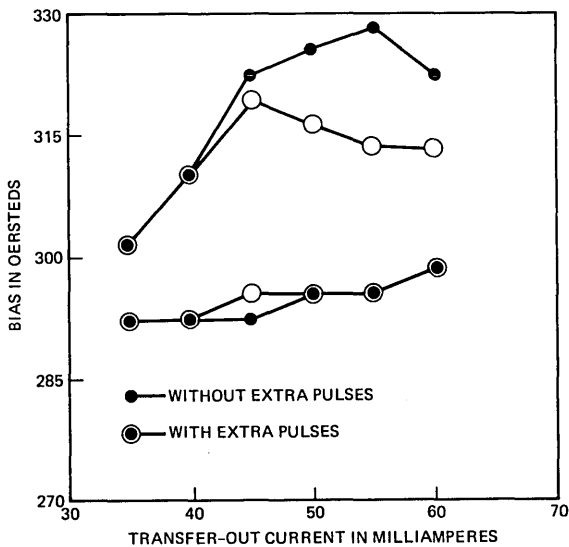


Fig. 20—Bias range vs. transfer-out current at 55 Oe with pulse active from 180° to 306°.

eration. The wide minor-loop margins indicate that low end failure due to stripping or hopping between loops is not the limiting problem at 55 Oe. However, Fig. 3 shows that the low bias limit for minor-loop propagation would increase if the drive could be decreased. Transfer-out limited the overall range at high bias. Figure 20 shows that the high end loss in transfer-out limited is due to interference with bubbles

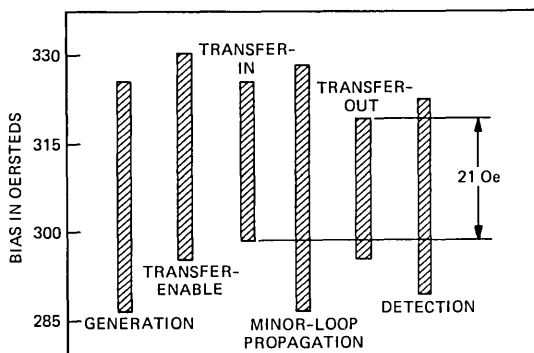


Fig. 21—Bias range for test components at 55 Oe. The generator pulse was 105 mA and 80 ns wide and occurred at  $0^\circ$ . Transfer-enable lasted from  $-72^\circ$  to  $+36^\circ$  at 35 mA. Transfer-in was 35 mA from  $0^\circ$  to  $144^\circ$ . Transfer-out was 45 mA from  $180^\circ$  to  $306^\circ$ .

in adjacent minor-loop positions. The next limit at high bias was due to detection. The low bias limit was caused by transfer-in. Since the low bias limit increases with increasing transfer-in current, some sort of stripping is indicated. The low drive limit, 50 Oe, was caused by bubbles sticking in the cusps of the clover-leaf-shaped major path features.

In summary, an experimental  $4\text{-}\mu\text{m}$ -period functional major-minor bubble device has been operated at 55-Oe drive with 21-Oe bias range. Generation and detection were demonstrated to have a good bias range down to 44-Oe drive, and good minor-loop propagation was obtained as low as 33 Oe.

## VII. ACKNOWLEDGMENTS

It is a pleasure to thank A. J. Perneski, S. L. Blank, P. I. Bonyhard, J. E. Geusic, and C. J. Mogab for helpful comments and suggestions. We also thank our colleagues R. C. LeCraw, R. D. Pierce, and J. F. Dillon, Jr. for various measurements during the course of this work. H. C. Alder provided expert technical assistance.

## REFERENCES

1. M. H. Kryder, "Magnetic Bubble Device Scaling and Density Limits," *IEEE Trans. Magn.*, *MAG-15*, No. 3 (May 1979), pp. 1009-16.
2. R. E. Fontana, Jr., D. C. Bullock, and S. K. Singh, "Characteristics of a 1Mbit/ $1\text{ cm}^2$  Magnetic Bubble Memory," *IEEE Trans. Magn.*, *MAG-16*, No. 5 (September 1980), pp. 1101-5.
3. T. Yanase, S. Orihara, and K. Yamagishi, "Design Consideration for a  $4\text{ }\mu\text{m}$  Period Permalloy Bubble Device," Paper No. DB-01, 3rd Joint Intermag-MMM Conference, Montreal, Canada, 20-23 July 1982.
4. Y. S. Lin et al., "Self-Aligned Contiguous Disk Chip Using  $1\text{ }\mu\text{m}$  Bubbles and Charged-Wall Functions," *IEEE Trans. Magn.*, *MAG-15*, No. 6 (November 1979), pp. 1642-7.

5. R. Wolfe et al., "Ion-Implanted Patterns for Magnetic Bubble Propagation," AIP Conf. Proc., 10 (November 1972), pp. 339-43.
6. K. Komenou et al., "Development of an Ion Implanted Bubble Device with 4  $\mu\text{m}$  Period," IEEE Trans. Magn., MAG-17 (November 1981), pp. 2908-13.
7. S. L. Blank et al., "Design and Development of Single-Layer, Ion-Implantable Small Bubble Materials for Magnetic Bubble Devices," J. Appl. Phys., 50, No. 3, Part II (March 1979), pp. 2155-60.
8. R. C. LeCraw et al., "Effect of Lanthanum on Growth-Induced Anisotropy in LPE Bubble Garnet Films," IEEE Trans. Magn., MAG-13, No. 5 (September 1977), pp. 1092-4.
9. G. P. Vella-Coleiro, "Measurement of Magnetostriction Coefficients of Epitaxial Garnet Films," Rev. Sci. Instrum., 50, No. 9 (September 1979), pp. 1130-2.
10. J. G. Skinner, "Life with EBES," Kodak Microelectronics Seminar Proceedings, Interface '76 (October 1976), pp. 92-9.
11. J. M. Moran and D. Maydan, "High Resolution, Steep Profile Resist Patterns," B.S.T.J. 58, No. 5 (May-June 1979), pp. 1027-36.
12. T. J. Nelson et al., "Design of Bubble Device Elements Employing Ion-Implanted Propagation Elements," B.S.T.J., 59, No. 2 (February 1980), pp. 229-57.
13. T. J. Nelson et al., "Ion-Implanted Bubble Circuit Function Design," IEEE Trans. Magn. MAG-17, No. 1 (January 1981), pp. 1134-41.

## AUTHORS

**Dirk J. Muehler**, A.B. (Physics), 1965, University of California at Berkeley; Ph.D. (Physics), 1970, Massachusetts Institute of Technology; Instructor and Assistant Professor (Physics), M.I.T., 1970-1979; AT&T Bell Laboratories, 1979—. At M.I.T. Mr. Muehler worked first on far infrared studies of cosmic background radiation and later on infrared nonlinear optics. Since joining AT&T Bell Laboratories he has worked on high-density magnetic bubble memories.

**Terence J. Nelson**, B.S. (Electrical Engineering), 1961, Iowa State University; M.E.E., 1963, New York University; AT&T Bell Laboratories, 1961-1963; Ph.D. (Physics), 1967, Iowa State University; AEC Postdoctoral Fellow, 1967-1969, Iowa State University and Lawrence Radiation Laboratory, Berkeley, California; AT&T Bell Laboratories, 1969—. During his first stay at AT&T Bell Laboratories, Mr. Nelson worked on ultrasonic delay lines and digital light deflection. In his doctoral and postdoctoral work, he specialized in mathematical physics, especially relativistic wave equations. He is coauthor of a graduate textbook on electric and magnetic fields. When he returned to AT&T Bell Laboratories, Mr. Nelson studied mode locking in lasers, and later he became involved with magnetic bubble device development. His interests in bubble technology have included bubble nucleation, single-level devices, optimized chevron detectors, and bubble devices based on ion-implanted propagation patterns. Member, Eta Kappa Nu, Sigma Xi, Phi Kappa Phi, American Physical Society.

**Virendra V. S. Rana**, B. Tech, 1967 (Metallurgical Engineering), Indian Institute of Technology, Kharagpur; M.S., 1971 (Materials Science), State University of New York, Stony Brook; Ph.D., 1977 (Materials Science), University of Southern California, Los Angeles; AT&T Bell Laboratories, 1979—. Before joining AT&T Bell Laboratories, Mr. Rana worked as a Research Scientist in the Materials Science Department at the University of Southern California. His research interests included work in the fracture of materials, liquid-phase sintering of ceramics, and investigation of defects in compound semiconductors. At AT&T Bell Laboratories he has been involved with developing new materials for magnetic bubble devices and investigating

the crystal growth aspects of the liquid-phase epitaxial technique. Currently, he is working on processes and technology for producing silicon integrated circuits.

**Bernard J. Roman**, B.S. (Physics), 1962, Carnegie-Mellon University; Ph.D. (Physics), Northwestern University, Evanston, Illinois; AT&T Bell Laboratories, 1969—. At AT&T Bell Laboratories, Mr. Roman has been responsible for the development of many processing techniques related to magnetic bubble device fabrication and for the successful transfer of these techniques into manufacture at AT&T Technologies, Inc. His current interests include the investigation of various high-density, fine-line lithography approaches to magnetic bubble fabrication.

**George P. Vella-Coleiro**, B.Sc. (Science), 1961, Royal University of Malta; M.A. (Physics), 1963, Ph.D. (Physics), 1967, Oxford University; AT&T Bell Laboratories, 1967—. At AT&T Bell Laboratories, Mr. Vella-Coleiro has been investigating the fundamental properties of magnetic bubble materials. Rhodes Scholar, 1961–64; Member, American Physical Society, IEEE.



# Theoretical Design of Single-Layer Antireflection Coatings on Laser Facets

By G. EISENSTEIN\*

(Manuscript received November 19, 1982)

Single-layer antireflection coating films are used to transform semiconductor injection lasers into different kinds of active devices such as superluminescent diodes or optical amplifiers. In this paper, optimum film parameters (thickness  $h$  and index of refraction  $n$ ) are established for a wide range of InGaAsP lasers emitting at  $1.3 \mu\text{m}$ . Optimum film parameters are different for the TE and TM polarizations. The minimum theoretical power reflectivity is higher for the TM polarization than the minimum reflectivity for the TE polarization by a factor of about three. Both are very low, on the order of  $10^{-6}$ . Tolerances in film parameters for a power reflectivity  $R \leq 10^{-3}$  (which is acceptable for most practical applications) are calculated for a typical laser having a spot size  $a = 0.5 \mu\text{m}$ . The tolerances are  $\Delta h \cong \pm 50 \text{\AA}$  and  $\Delta n/n \cong \pm 3$  percent for the TE polarization and  $\Delta h \cong \pm 43 \text{\AA}$  and  $\Delta n/n \cong \pm 2.4$  percent for the TM polarization. Processing of high-quality antireflection coating films on InGaAsP devices is possible according to these tolerances by using sputtered  $\text{Si}_3\text{N}_4$ , which allows a very slow deposition rate (on the order of  $75 \text{\AA}/\text{min}$ ) and the tailoring of the film index by adjusting the nitrogen pressure in the plasma.

## I. INTRODUCTION

Single-layer antireflection (AR) coating films can be very useful in transforming semiconductor injection lasers into different kinds of active devices. For example, a laser whose emitting facet reflectivities (one or both) are reduced to zero is transformed into a superlumines-

---

\* AT&T Bell Laboratories.

---

Copyright © 1984 AT&T. Photo reproduction for noncommercial use is permitted without payment of royalty provided that each reproduction is done without alteration and that the Journal reference and copyright notice are included on the first page. The title and abstract, but no other portions, of this paper may be copied or distributed royalty free by computer-based and other information-service systems without further permission. Permission to reproduce or republish any other portion of this paper must be obtained from the Editor.

cent diode<sup>1</sup> or an amplifier-modulator,<sup>2</sup> respectively. Such matching layers are analyzed in this paper. The purpose of the analysis is to

1. Establish the optimum parameters (thickness and index of refraction) of a matching layer for a given laser
2. Estimate the minimum theoretical reflection from a matching layer
3. Calculate the allowed tolerances of the film parameters for an acceptable reflectivity
4. Compare the reflectivities of TE and TM polarized light for possible explanation of the observed preferential polarization in practical devices.<sup>1</sup>

## II. THEORY

The device shown in Fig. 1 is assumed to have the properties described in the following paragraphs.

The laser diode's index of refraction is  $n_1 = 3.52$ , which is that of the InGaAsP active region in which the field is largely confined. We ignore the step in the index due to the cladding material to simplify the calculations. Kaplan and Deimel have shown that in most cases this simplification has a very small effect on the resulting reflectivity.<sup>3</sup> In some cases, however, this index step cannot be ignored and one should use a weighted average of the indices or resort to the rigorous calculation presented in Ref. 3.

The emitted beam is assumed to be Gaussian in both transverse directions. A Gaussian functional form is a good approximation to the emitted beam of practical devices<sup>1</sup> and enables us to characterize the laser in terms of a measurable parameter, the spot size. The spot size measured is that of the emitted beam and is slightly different from the spot size of the field inside the device. This is because of the

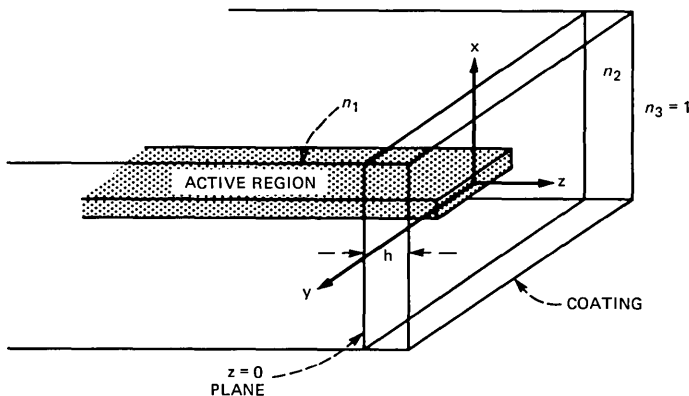


Fig. 1—Geometry of the laser and AR film.

angular-dependent reflection coefficient of the AR film. The difference between the two is negligible however.

The spot size in the direction perpendicular to the junction (X direction) is assumed to be much smaller than the corresponding spot size in the Y direction. Therefore, it is reasonable to analyze a two-dimensional model in the XZ plane (see Fig. 2). This model is valid for most lasers with the possible exception of buried structure lasers, which emit a nearly circular beam. The electric field is assumed to be linearly polarized along the Y, or along the X directions (TE or TM polarization, respectively.) The problem at hand is approached in a manner similar to the problem of calculating the modal reflectivity of a laser.<sup>4,5</sup> There, a narrow guided beam is impinging on a semiconductor-air interface, while here, the same guided beam impinges on an AR matching layer.

The technique used is that of the angular plane wave spectrum representation.<sup>6</sup> The calculation is an extension of two previous papers by R. H. Clarke,<sup>7,8</sup> and details are given in the appendix.

### III. RESULTS

The power reflectivity  $R$  of an optimum AR layer was calculated for a wide range of laser spot sizes. Detailed results for a  $0.5\text{-}\mu\text{m}$  spot size, typical of practical devices, are shown in Figs. 3, 4, and 5. (The spot size is defined as the electric field radius at its  $1/e$  point.)

The reflected power in the case of TE polarization is shown either in Fig. 3a as a function of film thickness assuming optimum film index  $n_2 = 1.8346$ , or in Fig. 3b as a function of film index assuming optimum normalized thickness  $hn_2/\lambda = 0.2606$ . Similar results are shown in Figs. 4a and b for the TM polarization. The optimum index and thickness are  $n_2 = 1.9361$  and  $hn_2/\lambda = 0.2511$ , respectively. In these expressions  $\lambda$  is the free-space wavelength =  $1.3\ \mu\text{m}$ .

The minimum reflectivity under the theoretically optimum conditions is very low ( $R < 10^{-6}$ ). This extremely low reflectivity is of little importance, however, since achieving it in practice would require tolerances too stringent for the film parameters. Assuming, for ex-

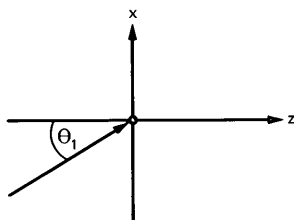


Fig. 2—Definition of the coordinate system and the angle of incidence.

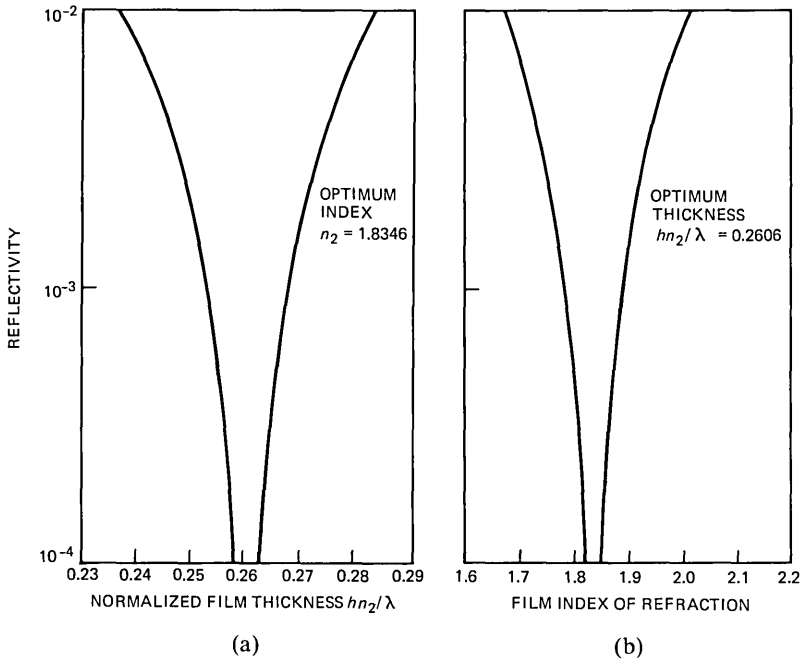


Fig. 3—Reflectivity: (a) as a function of film thickness (with optimum index), and (b) as a function of index (with optimum thickness) in the TE case for spot size  $a = 0.5 \mu\text{m}$  and  $\lambda = 1.3 \mu\text{m}$ .

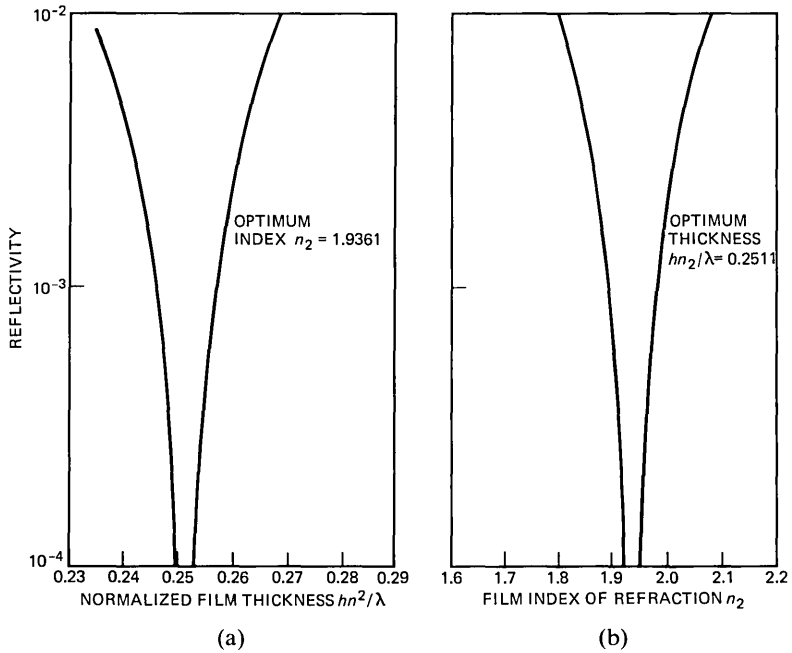


Fig. 4—Reflectivity as a function of: (a) thickness (with optimum index), and (b) as a function of index (with optimum thickness) in the TM case for spot size  $a = 0.5 \mu\text{m}$  and  $\lambda = 1.3 \mu\text{m}$ .

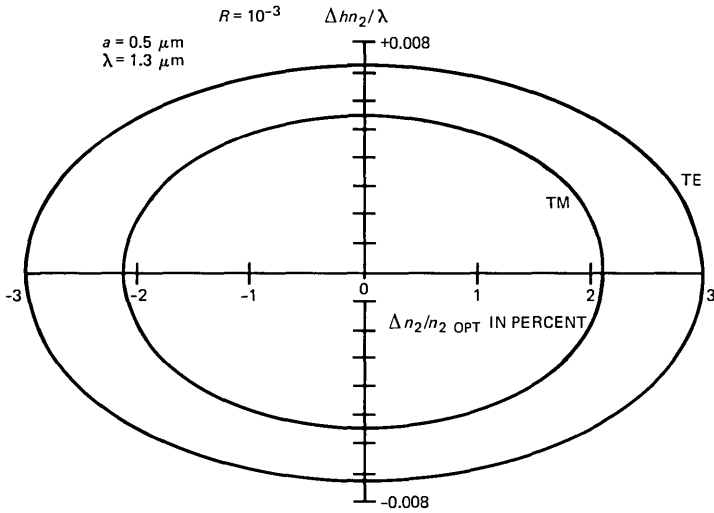


Fig. 5—Tolerances in thickness and index of refraction for  $R = 10^{-3}$  for TE and TM polarizations.

ample, that a reflectivity  $R \leq 10^{-3}$  is acceptable, we deduce from Fig. 5 the tolerances in the film parameters to achieve this reflectivity. They are assuming  $n_2 = 1.8346$  and  $hn_2/\lambda = 0.2606$ ,  $\Delta hn_2/\lambda \cong \pm 0.00744$  ( $\Delta h \cong \pm 50\text{\AA}$ ) and  $\Delta n_2/n_2 \cong \pm 3$  percent for the TE polarization, and assuming  $n_2 = 1.9361$  and  $hn_2/\lambda = 0.2511$ ,  $\Delta hn_2/\lambda \cong \pm 0.0064$  ( $\Delta h \cong \pm 43\text{\AA}$ ) and  $\Delta n_2/n_2 \cong \pm 2.4$  percent for the TM polarization. The tolerances in film thickness and index can be traded for each other according to the contours described in Fig. 5.

Similar calculations were performed for a wide range of laser spot sizes. Optimum film parameters as a function of laser spot size are shown in Figs. 6a and b for the TE and TM polarizations, respectively. In both cases spot sizes  $a > 3.5 \mu\text{m}$  (for  $\lambda = 1.3 \mu\text{m}$ ) approach the condition of a plane wave, i.e.,  $hn_2/\lambda = 0.25$  and  $n_2 = \sqrt{n_1}$ . Small spot sizes, however, deviate significantly from these asymptotic conditions. Figure 6 should be used as a design curve for optimum AR films for a given laser.

#### IV. DISCUSSION

The reflectivity of AR matching layers on the emitting facet of an injection laser was calculated for a wide range of laser spot sizes. The calculation assumes that the optical field is Gaussian and that the spot size in the direction perpendicular to the junction is much smaller than the corresponding spot size in the direction parallel to the junction. This allows for a two-dimensional model that is valid for

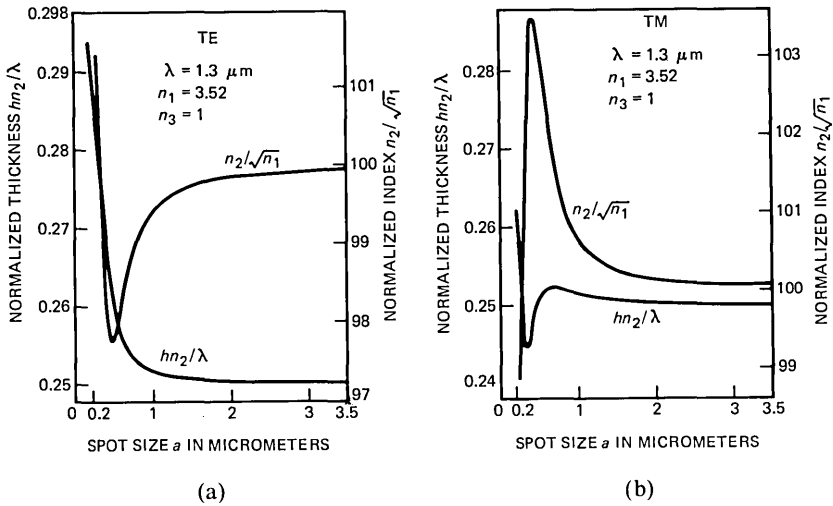


Fig. 6—Optimum film parameters as a function of spot size for: (a) TE polarization and (b) TM polarization.

most lasers. For lasers with an essentially circular spot the results presented here can be used only qualitatively.

Optimum film index and thickness were calculated, as well as the allowed tolerances, to ensure a reflectivity  $R = 10^{-3}$ , which is an acceptable reflectivity for most practical applications. Optimum film parameters for TE and TM polarizations were found to differ slightly. The minimum reflectivity for TM polarization is slightly higher than for TE polarization. Moreover, the tolerances for the TE case are higher. Therefore, we can assume that in practical devices, the reflectivity for the TM component of the optical field is higher than for the TE component. However, a practical superluminescent diode has most of its power polarized TE (more than 75 percent).<sup>1</sup> We have to conclude, therefore, that this observed preferential polarization is not due to the reflectivity but rather due to differences in internal gain and losses.

The reflectivity of practical AR films on superluminescent diodes was found to be on the order of  $10^{-4}$  to  $10^{-3}$  (see Refs. 9 and 10). This reflectivity is quite realistic according to the tolerances calculated.

Finally, the tolerances calculated tell us that the use of sputtered  $\text{Si}_3\text{N}_4$  on InGaAsP devices can result in high-quality AR coatings. Indeed, the slow deposition rate (on the order of  $75\text{\AA}/\text{min}$ ) and the possibility of tailoring the film index by adjusting the nitrogen pressure in the plasma allow the processing of films with the required tolerances.

## REFERENCES

1. I. P. Kaminow, G. Eisenstein, L. W. Stulz, and A. G. Dentai, "Lateral Confinement InGaAsP Superluminescent Diode at 1.3 Micron," *J. Quantum Elec.*, *QE-19*, No. 1 (January 1983), pp. 78-82.
2. D. Marcuse, "Computer Model of an Injection Laser Amplifier," *J. Quantum Elec.*, *QE-19*, No. 1 (January 1983), pp. 63-73.
3. D. Kaplan and P. Deimel, unpublished work.
4. E. I. Gordon, "Mode Selection in GaAs Injection Lasers Resulting from Fresnel Reflection," *IEEE J. Quantum Elec.*, *QE-9* (July 1973), pp. 772-6.
5. F. K. Reinhart, I. Hayashi, and M. B. Panish, "Mode Reflectivity and Waveguide Properties of Double Heterostructure Injection Lasers," *J. Appl. Phys.*, *42* (October 1971), pp. 4466-79.
6. R. H. Clarke and J. Brown, *Diffraction Theory and Antennas*, New York: John Wiley and Sons, 1980.
7. R. H. Clarke, "Theoretical Limit of Antireflection Coating for a Diode Laser Amplifier," *Int. J. Elec.*, *53*, No. 5 (November 1982), pp. 495-9.
8. R. H. Clarke, "Theory of Reflection from Antireflection Coatings, B.S.T.J.", *62*, No. 10, Part 1 (December 1983), pp. 2885-91.
9. I. P. Kaminow, G. Eisenstein, and L. W. Stulz, "Measurement of the Modal Reflectivity of an Antireflection Coating on a Superluminescent Diode," *J. Quantum Elec.*, *QE-19*, No. 4 (April 1983), pp. 493-5.
10. G. Eisenstein and L. W. Stulz, "High Quality Antireflection Coatings on Laser Facets by Sputtered Silicon Nitride, *App. Optics* (January 1984).
11. Born and Wolf, *Principles of Optics*, 5th Ed., New York: Pergamon, 1975.

## APPENDIX

### Calculation of Modal Reflectivity

We assume a Gaussian beam (with spot size  $a$ ) to the left of the laser facet ( $Z = 0$ )

$$E(X, 0) = \exp(-X^2/a^2). \quad (1)$$

A time-variation  $\exp(i\omega t)$  is assumed throughout. This field can be represented as an angular spectrum of plane waves incident at different angles  $\Theta$  (see Fig. 2):

$$F_i(s) = \frac{n_2}{\lambda} \int_{-\infty}^{\infty} E(x, 0) \exp\left(i \frac{2\pi n_1}{\lambda} sx\right) dx, \quad (2)$$

where  $s = \sin\Theta$  and  $\lambda =$  free space wavelength  $= 1.3 \mu\text{m}$ . Equation 2 becomes

$$F_i(s) = \frac{\sqrt{\pi}an_1}{\lambda} \exp\left(-\frac{s^2}{\left(\frac{\lambda}{\pi an_1}\right)^2}\right). \quad (3)$$

The amplitude reflection coefficient  $r(s)$  for each plane wave incident on the AR film (thickness  $h$ , index of refraction  $n_2$ ), followed by a semi-infinite region ( $n_3 = 1$ ) is<sup>11</sup>

$$r(s) = \frac{r_{12} + r_{23}\exp(-2i\beta)}{1 + r_{12}r_{23}\exp(-2i\beta)}, \quad (4)$$

where

$$\beta = \frac{2\pi hn_2}{\lambda} \sqrt{1 - \left(\frac{n_1 s}{n_2}\right)^2} \quad (5)$$

and  $r_{12}(s)$ ,  $r_{23}(s)$  are the well-known Fresnel reflection coefficients at the first and second boundaries, respectively. (Note that the Fresnel coefficients for the TE or TM polarizations are different from one another.)

The reflected wave  $F_r(s)$  is easily found to be

$$F_r(s) = r(s)F_i(s). \quad (6)$$

The power reflection coefficient of the film  $R$  is found by calculating the portion of the reflected wave that is coupled back into the laser mode and the proper normalization, i.e.,

$$R = \frac{\left| \int_{-\infty}^{\infty} r(s)Q(s) \exp\left(-\frac{2s^2}{\left(\frac{\lambda}{n_1\pi a}\right)^2}\right) ds \right|^2}{\left| \int_{-\infty}^{\infty} \exp\left(-\frac{2s^2}{\left(\frac{\lambda}{n_1\pi a}\right)^2}\right) ds \right|^2}, \quad (7)$$

where  $Q = \cos\theta$  in the TE case and  $Q = (\cos\theta - \sin^2\theta)/\cos\theta$  in the TM case.<sup>8</sup> The integration range is from  $s = -\infty$  to  $s = \infty$ . The corresponding angle is real for  $|s| < 1$  and becomes complex for  $|s| > 1$ ; its value is  $\theta = \pm\pi/2 \pm i\psi$ .  $\psi$  varies from 0 to  $\infty$  as  $|s|$  varies from 1 to  $\infty$ . The integrals in eq. (7) are solved numerically and the results are plotted in Figs. 3, 4, 5, and 6.

#### AUTHOR

**Gadi Eisenstein**, BSC, University of Santa Clara, California, 1975, MSC and Ph.D., University of Minnesota, 1977 and 1980, respectively, all in Electrical Engineering; AT&T Bell Laboratories, 1980—. Mr. Eisenstein is a Member of Technical Staff in the Photonic Circuits Research Department. His work is in the area of high-speed lasers and electro-optic devices.

## Polarization Quality of High-Birefringence Single-Mode Fibers

By F. M. SEARS\* and J. R. SIMPSON\*

(Manuscript received May 31, 1983)

Coherent optical communications, integrated optics, and interferometric sensors require that single-mode fibers maintain a stable state of polarization. With a broadband source, wavelength averaging of the power in either orthogonally polarized  $HE_{11}$  mode permits a simple measurement of the power transfer to the cross-polarized state (the  $h$  value). Polarization-holding quality was measured on several single-mode fibers with strain birefringence that had been induced by a new preform deformation method or a gas-phase etching technique. The fibers exhibited  $h$  values from  $2.3 \times 10^{-5} \text{ m}^{-1}$  (average polarization-holding to  $-24 \text{ dB}$ ) to  $8.9 \times 10^{-4} \text{ m}^{-1}$  with beat lengths (at  $\lambda = 632.8 \text{ nm}$ ) from 1.7 to 10 mm when the power is wavelength averaged over the 800- to 1100-nm range.

### I. INTRODUCTION

Coherent optical communications,<sup>1</sup> integrated optics, and interferometric sensors require that single-mode fibers maintain a stable state of polarization over long propagation lengths. Environmental perturbations are one cause of cross-polarization coupling of the two orthogonally polarized  $HE_{11}$  modes<sup>2-4</sup> resulting in an unstable state of polarization. The birefringent properties of polarization-maintaining fibers should be designed to be insensitive to environmental changes.

An important characteristic of single-polarization fibers is the average rate at which power is coupled into the cross-polarization state.

---

\* AT&T Bell Laboratories.

---

Copyright © 1984 AT&T. Photo reproduction for noncommercial use is permitted without payment of royalty provided that each reproduction is done without alteration and that the Journal reference and copyright notice are included on the first page. The title and abstract, but no other portions, of this paper may be copied or distributed royalty free by computer-based and other information-service systems without further permission. Permission to reproduce or republish any other portion of this paper must be obtained from the Editor.

With a broadband source, wavelength averaging of the power in either mode can allow a simple measurement of the power transfer to the cross-polarized mode.<sup>5</sup> Following that approach, a statistically determined polarization-holding parameter,  $h$ , and beat lengths (at  $\lambda = 632.8$  nm) were measured for several single-mode fibers. The strain birefringence was induced by a preform deformation method<sup>6</sup> or a gas-phase etching<sup>7</sup> technique. The power is wavelength averaged over the 800- to 1100-nm spectral range.

## II. RATE OF TRANSFER OF CROSS-POLARIZATION

One parameter commonly used in describing birefringent fibers is the mode beat length defined by

$$L_p = \frac{2\pi}{\delta\beta} = \frac{\lambda}{B}, \quad (1)$$

where  $\delta\beta$  is the difference between the propagation constants for the slow- and fast-polarization eigenmodes,  $\lambda$  is the wavelength of light, and  $B$  is the modal or normalized linear birefringence. The modal birefringence can be separated into a stress anisotropy component,  $B_s$ , and a geometrical, or shape, component,  $B_G$ .

Kaminow<sup>2</sup> obtained an analytical expression for the ensemble averages of the relative powers in the two polarization modes. Rashleigh<sup>5</sup> et al. extended the random-coupling theory to incorporate a finite range of wave numbers on a single fiber since the random-coupling theory requires measurements of a large number of fibers. The rate of transfer of cross-polarization in a single-mode fiber is defined by

$$\zeta \equiv \{P_y\}/\{P\} = 1/2[1 - \exp(-2hL)], \quad (2)$$

where  $P_y$  indicates the power in the cross-polarization mode,  $P = P_x + P_y$  is the total power,  $P_x$  is the power in the excited mode, and  $L$  is the fiber length. The inverse of the parameter  $h$  describes the characteristic distance for power transfer to the cross-polarization state.

The ensemble of  $N$  statistically equivalent fibers is directly proportional to the bandwidth  $\delta\lambda$  of a broad bandwidth light source;<sup>5</sup> i.e.,

$$N \approx \sigma L \delta\lambda \approx L/\Delta \ell, \quad (3)$$

where  $\Delta \ell$  represents one member of an ensemble of equivalent fibers and

$$\sigma = \frac{1}{c} \frac{d(\delta\beta)}{dk_o} \equiv \frac{1}{c} \left[ \frac{\delta\beta}{k_o} + k_o \frac{d(\delta\beta/k)}{dk_o} \right] \quad (4)$$

is the polarization-mode dispersion, the group delay difference between orthogonally polarized modes. The relative standard deviation of the

rate of power transfer to the cross-polarization state is of the order  $N^{-1/2}$ .

### III. EXPERIMENTAL TECHNIQUE

Figure 1 shows a schematic for the measurement of the rate of power transfer to the cross-polarization state. The source for these experiments is white light from a xenon arc lamp that is chopped and then filtered by Corning glass filters 5-56 and 2-58. The combined filters produce a bandwidth of 800 to 1100 nm. The filtered light is linearly polarized and focused into the single-mode test fiber. Cladding-mode strippers are used to ensure that the light being examined is guided along the fiber core. The polarized fiber output light is focused through a linear analyzer and detected by a silicon avalanche photodiode. The detected signal is input to a lock-in amplifier and referenced to a synchronizing signal from the chopper. The lock-in function-output voltage is digitized and sent to a computer where  $P_x$  and  $P_y$  are averaged in time.

Stolen and Turner<sup>8</sup> showed that the best polarization-holding azimuthal angle in a fiber can be determined by rotating the polarizer and analyzer until the detected power is minimum. At the minimum power, the measured output is in the cross-polarization state. To examine the power in the excited mode, the linear analyzer is rotated 90 degrees.

### IV. RESULTS AND DISCUSSION

The rate of power transfer to the cross-polarization state and beat lengths (at  $\lambda = 632.8$  nm) were measured and are presented in Table

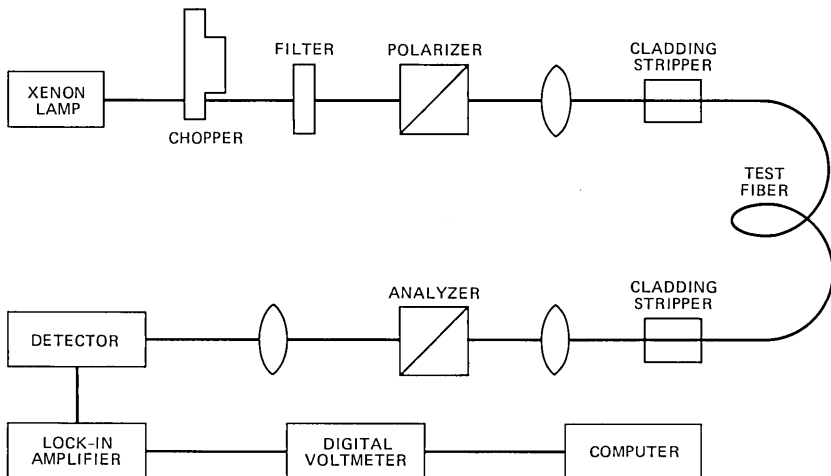


Fig. 1—Measurement system for the rate of power transfer to the cross-polarization state.

I. Table I also shows the average polarization holding in decibels defined as  $10 \cdot \log_{10} (h \cdot \text{fiber length})$ . The measured fibers were all single mode for wavelengths longer than 800 nm.

Fibers 2 through 4 were fabricated with a cladding refractive index below that of the silica support tube (depressed index or W-type fiber design). The ellipticity of the stress-applying region (shown in Fig. 2) immediately surrounding the core gives rise to the birefringence observed. The stress resulting from this structure has been analyzed in detail by Stolen.<sup>9</sup> Fibers 2 through 4 contain an  $\text{Al}_2\text{O}_3\text{-SiO}_2$  core,  $\text{B}_2\text{O}_3\text{-P}_2\text{O}_5\text{-SiO}_2$  stress region, and a fluorine-doped  $\text{SiO}_2$  cladding. Two modes were present in these fibers at a wavelength of  $0.63 \mu\text{m}$ , and a high fundamental mode tunneling loss was observed in the  $1.0\text{-}\mu\text{m}$  wavelength region.

Fiber 1 (shown in Fig. 3) was made by a gas-phase etching technique.<sup>8</sup> It contained a  $\text{GeO}_2\text{-SiO}_2$  core, a fluorine-doped silica stress region, and a  $\text{SiO}_2$  cladding. This fiber has a core diameter of  $3.6 \mu\text{m}$ , and was multimode at  $0.63 \mu\text{m}$ . The long wavelength, leaky-mode loss edge was beyond  $1.5 \mu\text{m}$ .

The  $h$  values for the fibers listed in Table I vary from  $2.3 \times 10^{-5} \text{ m}^{-1}$  to  $8.9 \times 10^{-4} \text{ m}^{-1}$  with the beat lengths varying from 1.7 mm to 10 mm. There was no correlation between the changes in the  $h$  values and the beat lengths. This agrees with other results in the litera-

Table I—Average polarization-holding quality over 800- to 1100-nm spectral range

| Fiber Number | Fiber Length (m) | $h$ ( $\text{m}^{-1}$ ) | $L_p$ (mm) | Polarization Holding (dB) | Core Diameter ( $\mu\text{m}$ ) |
|--------------|------------------|-------------------------|------------|---------------------------|---------------------------------|
| 1            | 96               | $6.2 \times 10^{-4}$    | 10         | -12.2                     | 3.6                             |
| 2            | 50               | $8.9 \times 10^{-4}$    | 2.6        | -13.5                     | $4.3 \times 11$                 |
| 3            | 450              | $1.5 \times 10^{-4}$    | 3          | -11.7                     | 5.8                             |
| 4            | 174              | $2.3 \times 10^{-5}$    | 4.3        | -24                       | 6                               |

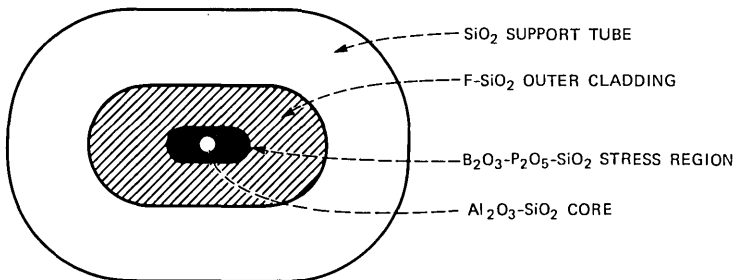


Fig. 2—Single-mode birefringent fiber cross section fabricated by a preform deformation.

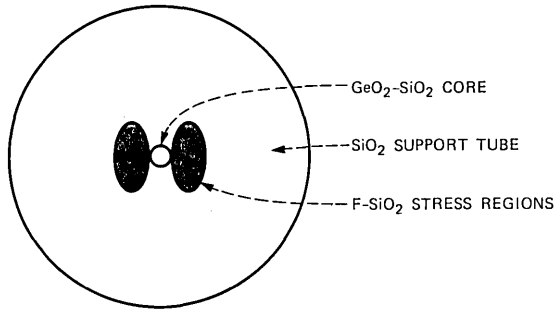


Fig. 3—Single-mode birefringent fiber cross section fabricated by a gas-phase etching technique.

ture.<sup>5-7</sup> The fiber-core diameters are listed in Table I. Fiber 2 has shape-induced birefringence due to the elliptical core, but this effect is small compared to the stress-induced birefringence.

The coherence length,  $\Delta \ell$ , for lightwaves in a fiber is

$$\Delta \ell = \frac{\Delta \tau}{\sigma}, \quad (5)$$

where  $\Delta \tau = \lambda_o^2 / c \delta \lambda$  is the coherence time of the source and  $\lambda_o$  is the mean wavelength for the spectral width  $\delta \lambda$ . Using the definition for  $\sigma$  from eq. (4) and neglecting the second term (small for stress-induced birefringence), eq. (5) becomes

$$\Delta \ell = \frac{\lambda_o}{\delta \lambda} L_p. \quad (6)$$

As an example, fiber 1 has a beat wavelength,  $L_p = 10$  mm, which results in a coherence length,  $\Delta \ell = 3.2$  cm, for a source whose spectral width is  $\delta \lambda = 300$  nm centered about  $\lambda_o = 950$  nm. For fiber 1 in Table I, this measurement represents an average of  $N \approx 3000$  independent samples with a relative standard deviation of  $N^{-1/2} \sim 0.018$ .

It has been shown that birefringent multimode fibers preserve the state of polarization.<sup>10</sup> The observation was that in fibers supporting a moderate number of modes, all modes maintain linear polarization with the exception of one mode near cutoff. Multimode polarization holding measurements were made in the wavelength region from 500 to 900 nm. The multimode results for fiber 1 indicate polarization holding to  $-27$  dB, corresponding to an  $h$  value of  $2.2 \times 10^{-5} \text{ m}^{-1}$ .

A 1-km length of high-birefringence fiber fabricated by Hitachi Cable Ltd. was reported in the literature<sup>11</sup> to have an  $h$ -value of  $5.5 \times 10^{-6} \text{ m}^{-1}$  for an average polarization holding to  $-22$  dB. These values are in the same range as those measured here. However, low-loss high-birefringence fibers have been reported to hold polarization to better than  $-30$  dB.<sup>12</sup>

## V. CONCLUSION

In conclusion, the polarization quality of high-birefringence single-mode fibers has been evaluated using a broadband source. The birefringent fibers were fabricated by a preform deformation method and a gas-phase etching technique. A statistical determination of the rate of power transfer to the cross-polarized state was made by wavelength averaging. The  $h$  values measured in the single-mode regime of the fibers varied from  $2.3 \times 10^{-5} \text{ m}^{-1}$  to  $8.9 \times 10^{-4} \text{ m}^{-1}$  with beat lengths from 1.7 mm to 10 mm. Polarization preservation was found in the multimode regime supporting a moderate number of modes, but it is not yet understood how mode mixing affects polarization performance.

## VI. ACKNOWLEDGMENTS

We would like to thank K. L. Walker and R. Csencsits for providing the etched-preform-type fiber and acknowledge valuable discussions with L. G. Cohen and R. H. Stolen.

## REFERENCES

1. Y. Yamamoto and T. Kimura, "Coherent Optical Fiber Transmission System," *IEEE J. Quant. Electr.*, *QE-17* (June 1981), pp. 919-35.
2. I. P. Kaminow, "Polarization in Optical Fibers," *IEEE J. Quant. Electr.*, *QE-17* (January 1981), pp. 15-22.
3. T. Okoshi, "Single-Polarization Single-Mode Optical Fibers," *IEEE J. Quant. Electr.*, *QE-17* (June 1981), pp. 879-84.
4. D. N. Payne, A. J. Barlow, and J. J. Ramskov Hansen, "Development of Low- and High-Birefringence Optical Fibers," *IEEE J. Quant. Electr.*, *QE-18* (April 1982), pp. 477-88.
5. S. C. Rashleigh et al., "Polarization Holding in Birefringent Single-Mode Fibers," *Optics Letters*, *7* (January 1982), pp. 40-2.
6. R. H. Stolen, W. Pleibel, and J. R. Simpson, unpublished work.
7. K. L. Walker and R. Csencsits, unpublished work; R. D. Birch, D. N. Payne, and M. P. Vardham, "Fabrication of Polarization Maintaining Fibres Using Gas-Phase Etching," *Electron. Lett.*, *18* (November 1982), pp. 1036-8.
8. R. H. Stolen and E. H. Turner, "Faraday Rotation in Highly Birefringent Optical Fibers," *Appl. Optics*, *19* (March 1980), pp. 842-5.
9. R. H. Stolen, "Calculation of Stress Birefringence in Fibers by a Infinitesimal Element Method," *J. Lightwave Tech.*, *LT-1*, No. 2 (June 1983), pp. 297-301.
10. R. E. Wagner, R. H. Stolen, and W. Pleibel, "Polarization Preservation in Multimode Fibres," *Electron. Lett.*, *17* (March 1981), pp. 177-8.
11. S. C. Rashleigh and M. J. Marrone, "Polarization-Holding in a High-Birefringence Fibre," *Electron. Lett.*, *18* (April 1982), pp. 326-7.
12. T. Katsuyama, H. Matsumura, and T. Sukanuma, "Low Loss Single-Polarization Fibre," *Electron. Lett.*, *17* (June 1981), pp. 473-4.

## AUTHORS

**Frederick M. Sears**, S.B. and S.M. (Mechanical Engineering), 1975, Massachusetts Institute of Technology; Ph.D. (Mechanical Engineering), 1980, University of California at Berkeley; Lawrence Livermore National Laboratory, 1978-1980; AT&T Bell Laboratories, 1980—. At the Lawrence Livermore National Laboratory, Mr. Sears developed experimental and theoretical techniques for digital ultrasonic testing of geologic materials to examine their anelastic properties. At AT&T Bell Laboratories, he is currently pursuing

research and development on optical-fiber characterization techniques as a Member of Technical Staff. Recent investigations include fiber interferometry, single-polarization fibers, polarization-maintaining fibers, polarization mode dispersion, and optical time-domain reflectometry. Member, Optical Society of America, the American Geophysical Union, and the National Technical Association.

**J. R. Simpson**, B.S. (Glass Science), 1972, Alfred University, Alfred, NY; M.S. (Ceramic Science), 1978, Rutgers University; AT&T Bell Laboratories, 1976—. At AT&T Bell Laboratories, Mr. Simpson's research has included the characterization of optical fibers for fiber preform development and methods of increasing deposition rates in the Modified Chemical Vapor Deposition (MCVD) process. As a Member of Technical Staff, he has pursued the study of alternate dopants for the MCVD process and for making single-mode single-polarization optical fiber.



# PAPERS BY BELL LABORATORIES AUTHORS

## COMPUTING/MATHEMATICS

- Dodd S. L., **Shape-Preserving Spline Interpolation for Specifying Bivariate Functions on Grids.** IEEE Comp G 3(6):70-79, 1983.
- Fishburn P. C., **Packing Graphs With Odd and Even Trees.** J Graph Th 7(3):369-383, 1983.
- McConkey J., **The 2nd-Annual-Symposium on Small Computers in the Arts (Editorial).** Comput Mus 7(3):25-30, 1983.

## ENGINEERING

- Alles D. S., **Direct Electron-Beam Lithography (Editorial).** Sol St Tech 26(9):125, 1983.
- Beni G., Hackwood S., Hornak L. A., Jackel J. L., **Dynamic Sensing for Robots—An Analysis and Implementation.** Int J Rob R 2(2):51-61, 1983.
- Bank R. E., Rose D. J., Fichtner W., **Numerical-Methods for Semiconductor-Device Simulation.** IEEE Device 30(9):1031-1041, 1983.
- Chen C. Y., Alavi K., Cho A. Y., Garbinski P. A., Pang Y. M. **New Ga<sub>0.47</sub>In<sub>0.53</sub>As Sheet-Charge Field-Effect Transistor for Long-Wavelength Optoelectronic Integration.** Electr Lett 19(19):791-792, 1983.
- Chu T. S., **An Imaging Beam Waveguide Feed.** IEEE Antenn 31(4):614-619, 1983.
- Coughran W. M., Grosse E., Rose D. J., **CAZM—A Circuit Analyzer With Macro-modeling.** IEEE Device 30(9):1207-1213, 1983.
- Cox D. C., **Time-Division Adaptive Retransmission for Reducing Signal Impairments in Portable Radiotelephones.** IEEE Veh T 32(3):230-238, 1983.
- Farrow R. C. **A Model for Microcomputer Control of the Scanning Electron-Microscope Used in Basic Research.** Scan Elec M1983(P2):479-488, 1983.
- Fichtner W., Rose D. J., **Special Issue on Numerical-Simulation of VLSI Devices—Foreword (Editorial).** IEEE Device 30(9):967, 1983.
- Fichtner W., Rose D. J., Bank R. E., **Semiconductor-Device Simulation.** IEEE Device 30(9):1018-1030, 1983.
- Goodman D. J., Sundberg C. E., **Quality of Service and Bandwidth Efficiency of Cellular Mobile Radio With Variable Bit-Rate Speech Transmission.** IEEE Veh T 32(3):211-217, 1983.
- Hackwood S., Beni G., Hornak L. A., Wolfe R., Nelson T. J., **A Torque-Sensitive Tactile Array for Robotics.** Int J Rob R 2(2):46-50, 1983.
- Iannuzzi M., **Bias Humidity Performance and Failure Mechanisms of Nonhermetic Aluminum SICs in an Environment Contaminated With Cl<sub>2</sub>.** IEEE Compon 6(2):191-201, 1983.
- Lamorte M. F., Abbott D. H., **AlGaAs/GaAs Cascade Solar-Cell Computer Modeling Under High Solar Concentration.** Solar Cells 9(4):311-326, 1983.
- Liou K. Y., **Single-Longitudinal-Mode Operation of Injection-Laser Coupled to a Grinrod External Cavity.** Electr Lett 19(19):750-751, 1983.
- Mayo J. S., **Design Automation—Lessons of the Past, Challenges for the Future.** IEEE Comp G 3(6):13-18, 1983.
- Penumalli B. R., **A Comprehensive (2)-Dimensional VLSI Process Simulation Program, Biceps.** IEEE Device 30(9):986-992, 1983.
- Petersen W. P., Fichtner W., Grosse E. H., **Vectorized Monte-Carlo Calculation for the Transport of Ions in Amorphous Targets.** IEEE Device 30(9):1011-1017, 1983.
- Pini R. et al., **Ultraviolet Four-Photon Mixing in a Multimode Silica Fiber Raman Amplifier.** Opt Commun 47(3):226-229, 1983.
- Shashaty A. J., **Nonlinear and Hysteretic Twisting Effects in Ocean Cable Laying.** J Energ Res 105(3):341-345, 1983.

## MANAGEMENT/ECONOMICS

Luss H., **An Inspection Policy Model for Production Facilities.** *Manag Sci.* 29(9):1102-1109, 1983.

## PHYSICAL SCIENCES

Ashkin A., Gordon J. P., **Stability of Radiation-Pressure Particle Traps—An Optical Earnshaw Theorem.** *Optics Lett* 8(10):511-513, 1983.

Aur S., Kofalt D., Waseda Y., Egami T., Wang R., Chen H. S., Teo B. K., **Local-Structure of Amorphous  $\text{Mo}_{50}\text{Ni}_{50}$  Determined by Anomalous X-Ray-Scattering Using Synchrotron Radiation.** *Sol St Comm* 48(2):111-115, 1983.

Auston D. H., Smith P. R., **Generation and Detection of Millimeter Waves by Picosecond Photoconductivity.** *Appl Phys L* 43(7):631-633, 1983.

Bjorkholm J. E., Ballman A. A., **Localized Wet-Chemical Etching of InP Induced by Laser-Heating.** *Appl Phys L* 43(6):574-576, 1983.

Cage M. E., Dziuba R. F., Field B. F., Williams E. R., Girvin S. M., Gossard A. C., Tsui D. C., Wagner R. J., **Dissipation and Dynamic Nonlinear Behavior in the Quantum Hall Regime.** *Phys Rev L* 51(15):1374-1377, 1983.

Carroll P. J., Patterson G. D., Cullerton S. A., **Light-Scattering Photography of Polymers Near the Glass-Transition.** *J Pol Sc PP* 21(10):1889-1896, 1983.

Chraplyvy A. R., Stone J., Burrus C. A., **Optical Gain Exceeding 35 dB at 1.56  $\mu\text{m}$  Due to Stimulated Raman-Scattering by Molecular  $\text{D}_2$  in a Solid Silica Optical Fiber.** *Optics Lett* 8(7):415-417, 1983.

Feibelman P. J., Hamann D. R., **Electronic-Structure of Metal Overlayers on Rhodium.** *Phys Rev B* 28(6):3092-3099, 1983.

Goodby J. W., **Relationships Between Miscibility Grouping and Smectic Mesophase Structure.** *Molec Cryst* 92(6):171-177, 1983.

Johnson P. D., Smith N. V., **Production of Circularly Polarized-Light From Synchrotron Radiation in the Vacuum Ultraviolet Region.** *Nucl Instru* 214(2-3):505-508, 1983.

Khanarian G., Tonelli A. E., **Non-Linear Electrooptic and Dielectric Properties of Flexible Polymers (Review).** *ACS Symp S* 1983(233):235-244, 1983.

Lovinger A. J., **Ferroelectric Transition in a Co-Polymer of Vinylidene Fluoride and Tetrafluoroethylene.** *Macromolec* 16(9):1529-1534, 1983.

Luther L. C., Kometani T. Y., **Chemical-Analysis of Bi-Containing Magnetic-Bubble Garnet-Films.** *J Am Ceram* 66(9):619-622, 1983.

Ostermayer F. W., Kohl P. A., Burton R. H., **Photo-Electrochemical Etching of Integral Lenses on InGaAsP/InP Light-Emitting-Diodes.** *Appl Phys L* 43(7):642-644, 1983.

Ota Y., **Silicon Molecular-Beam Epitaxy (Review).** *Thin Sol Fi* 106(1-2):3-136, 1983.

Pang Y. M., Chen C. Y., Gardinski P. A., **1.5 GHz Operation of an  $\text{Al}_x\text{Ga}_{1-x}\text{As}$  GaAs Modulation-Doped Photoconductive Detector.** *Electr Lett* 19(18):716-717, 1983.

Patterson G. D., Carroll P. J., **Photon-Correlation Spectroscopy of Polymers in the Glassy State.** *J Pol Sc PP* 21(10):1897-1902, 1983.

Pulito V. L., Miller D. L., Sassa S., Yamane T., **DNA Fragments in Friend-Erythroleukemia Cells Induced by Dimethyl-Sulfoxide.** *P Nas Biol* 80(19):5912-5915, 1983.

Rowe M. W., Gallagher P. K., Gyorgy E. M., **Establishing the Absence of Any Influence by an External Magnetic-Field Upon the Intrinsic Rate of Reduction of Magnetite by Hydrogen.** *J Chem Phys* 79(7):3534-3536, 1983.

Schneider M. V., Cho A. Y., Kollberg E., Zipath H., **Characteristics of Schottky Diodes with Microcluster Interface.** *Appl Phys L* 43(6):558-560, 1983.

Tell B., Bjorkohm J. E., Beebe E. D., **Subnanosecond Pulsed Laser Annealing of Se-implanted InP.** *Appl Phys L* 43(7):655-657, 1983.

Tsang W. T., Olsson N. A., **Enhanced Frequency-Modulation in Cleaved-Cou-**

**pled-Cavity Semiconductor-Lasers With Reduced Spurious Intensity Modulation.** Appl Phys L 43(6):527-529, 1983.

Valley J. F., Slusher R. E., **Acoustic-Wave Calibration for Co<sub>2</sub>-Laser Scattering Experiments.** Rev Sci Ins 54(9):1157-1162, 1983.

Wertheim G. K., Disalvo F. J., Buchanan D. N., **Site Inequivalence in Fe<sub>1-x</sub>Nb<sub>3-x</sub>Se<sub>10</sub>.** Phys Rev B 28(6):3335-3338, 1983.

White J. C., Henderson D., **Anti-Stokes Raman Laser-Emission at 149-nm in Atomic Bromine.** Optics Lett 8(10):520-522, 1983.

Yamada M., Tien P. K., Martin R. J., Nahory R. E., Ballman A. A., **Double Zinc Diffusion Fronts in InP—Theory and Experiment.** Appl Phys L 43(6):594-596, 1983.

Yan M. F., Cannon R. M., Bowen H. K., Chowdhry U., **Effect of Grain-Size Distribution on Sintered Density.** Mater Sci E 60(3):275-281, 1983.

Zucker J. E., Pinczuk A., Chemla D. S., Gossard A., Wiegmann W., **Raman-Scattering Resonant With Quasi-Two-Dimensional Excitons in Semiconductor Quantum Wells.** Phys Rev L 51(14):1293-1296, 1983.

## SOCIAL AND LIFE SCIENCES

Frauenthal J. C., Swick K. E., **Limit-Cycle Oscillations of the Human-Population.** Demography 20(3):285-298, 1983.

Kiger J. I., Glass A. L., **The Facilitation of Lexical Decisions by a Prime Occurring After the Target.** Mem Cognit 11(4):356-365, 1983.

Ortony A., Turner T. J., Antos S. J., **A Puzzle About Affect and Recognition Memory.** J Exp Psy L 9(4):725-729, 1983.



## **CONTENTS, MARCH 1984**

**Signals Designed for Recovery After Clipping—III: Generalizations**

**B. F. Logan, Jr.**

**Click Modulation**

**B. F. Logan, Jr.**

**Design Diagrams for Depressed Cladding Single-Mode Fibers**

**W. T. Anderson and P. F. Glodis**

**Single GRIN-Lens Directional Couplers**

**F. H. Levinson and S. W. Granlund**

**The DTWP: An LPC-Based Dynamic Time-Warping Processor for Isolated Word Recognition**

**M. K. Brown, R. T. Thorkildsen, Y. H. Oh, and S. S. Ali**

**On the Application of Embedded Training to Connected-Letter Recognition for Directory Listing Retrieval**

**L. R. Rabiner, J. G. Wilpon, and S. G. Terrace**

**An Improved Word-Detection Algorithm for Telephone-Quality Speech Incorporating Both Syntactic and Semantic Constraints**

**J. G. Wilpon, L. R. Rabiner, and T. Martin**

**Performance of Cross-Polarized M-ary QAM Signals Over Nondispersive Fading Channels**

**M. Kavehrad**







**AT&T BELL LABORATORIES TECHNICAL JOURNAL** is abstracted or indexed by *Abstract Journal in Earthquake Engineering*, *Applied Mechanics Review*, *Applied Science & Technology Index*, *Chemical Abstracts*, *Computer Abstracts*, *Current Contents/Engineering, Technology & Applied Sciences*, *Current Index to Statistics*, *Current Papers in Electrical & Electronic Engineering*, *Current Papers on Computers & Control*, *Electronics & Communications Abstracts Journal*, *The Engineering Index*, *International Aerospace Abstracts*, *Journal of Current Laser Abstracts*, *Language and Language Behavior Abstracts*, *Mathematical Reviews*, *Science Abstracts (Series A, Physics Abstracts; Series B, Electrical and Electronic Abstracts; and Series C, Computer & Control Abstracts)*, *Science Citation Index*, *Sociological Abstracts*, *Social Welfare, Social Planning and Social Development*, and *Solid State Abstracts Journal*. Reproductions of the Journal by years are available in microform from University Microfilms, 300 N. Zeeb Road, Ann Arbor, Michigan 48106.



**AT&T**  
Bell Laboratories